Quantum Studies on Low-Dimensional Coupled Electron-Nuclear Dynamics

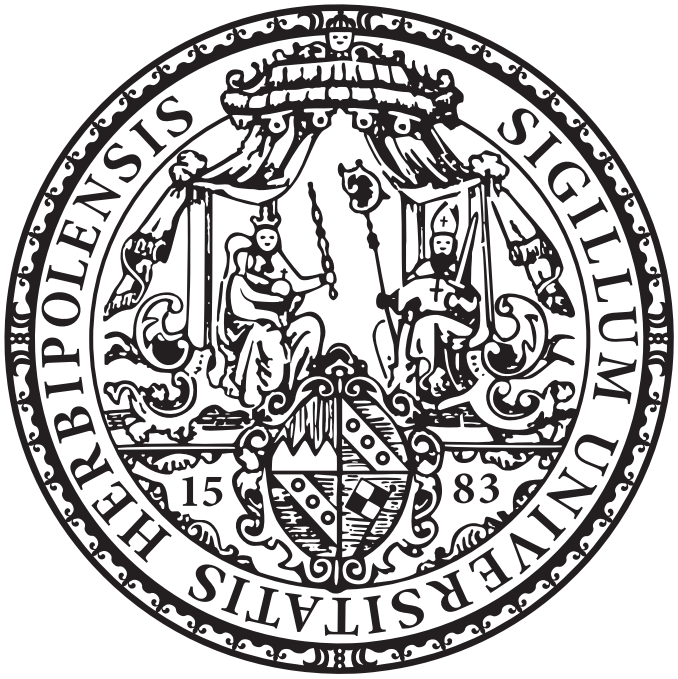

Doctoral Dissertation (Thesis)

to obtain the degree of
"Doktor der Naturwissenschaften"
(Dr. rer. nat.)

awarded by the
Julius-Maximilians-Universität Würzburg

submitted by

Julian Albert

from Würzburg

Würzburg 2017

Submitted to the Faculty of Chemistry and Pharmacy on

.....

Evaluators of the written Dissertation (Thesis)

Supervisor - 1. Evaluator: .....

2. Evaluator: .....

Examiners of the Public Defense

1. Examiner .....

2. Examiner .....

3. Examiner .....

Date of the Public Defense .....

Doctoral Certificate awarded on .....

Contents

Chapter 1

Introduction

Based on the programm of the research unit FOR 1809 regarding light-induced dynamics in molecular aggregates [1–4], this work addresses the fundamental questions related to excited state dynamics in quantum systems. Aggregates are promising systems of importance in, e.g., organic semi-conductors [5–9]. The main goal of the FOR is to understand the arrangement of molecular building blocks in aggregates and to understand the resulting functionality controlled by light-induced dynamics [10–12].

The latter is strongly connected with excited state dynamics [13–15]. This is still a challange to quantum dynamics as the size of molecular systems and also aggregates is large, and therefore, computational predictions are necessarily limited. The situation is even more complex in case of environmental effects [16, 17].

Mixed classical-quantum methods are able to tackle high-dimensional systems and predict reaction pathways; however, these methods rely on quantum chemical calculations which have to be optimized for the regarded quantum system as well as to be numerically efficent [18–20].

Leaving such rather complex systems aside, this work takes a step back and regards the fundamental understanding of wave-packet dynamics in a low-dimensional quantum system, the Shin-Metiu model [21, 22]. With the reduction of complexity, it becomes possible to investigate coupled electron-nuclear dynamics within

the frame of a numerically exact calculation. The conclusions drawn from these observations might help to understand molecular quantum systems of higher dimensionality.

This work concentrates on the fundamental dynamical properties revealed by an exact treatment of a coupled electron-nuclear wave-packet dynamic. This motion is compared to the nuclear dynamics within the adiabatic and diabatic representation. Several key questions are addressed. In section 4.2, the influence of non-adiabatic coupling on the eigenfunctions is regarded. Section 4.4 addresses the distinction of electronic and vibrational coherences in two-dimensional spectra [23]. Furthermore, in section 4.5 the question is addressed of how can a system with strong electron-nuclear coupling be treated using classical mechanics [24]. This is followed in section 4.6 by the calculation of the electron flux within the Born-Oppenheimer approximation [25]. Finally, in chapter 5 the coupled electron-nuclear dynamics in the vicinity of a conical intersection (CoIn) is regarded [26].

Chapter 2

Theoretical Background

2.1 Eigenvalue Equation

An eigenvalue equation in a coordinate space $\vec{\tau}$ is given in eq. (2.1). Here $\vec{\tau} \in \mathbb{R}^n$, where $n \in \mathbb{N}$ is the dimension of the configuration space [27]:

$$\hat{O}(\vec{\tau})\ \phi(\vec{\tau}) = a\ \phi(\vec{\tau}). \tag{2.1}$$

In this equation, $\hat{O}(\vec{\tau})$ is a hermitian Operator acting on the eigenstate $\phi(\vec{\tau}) \in \mathfrak{H}$ with the corresponding eigenvalue a, where $\mathfrak{H}$ is a Hilbert space. Because $\hat{O}(\vec{\tau})$ is a hermitian operator, the eigenvalue is real: $a \in \mathbb{R}$. The set of the eigenvalues of $\hat{O}(\vec{\tau})$ are called the spectrum of the operator [28].

2.2 Postulates of Quantum Mechanics

In 1926, E. Schrödinger formulated a theory describing a non-relativistic quantum system. Here, the basic postulates of Schrödinger's quantum theory will be repeated shortly [29–32].

2.2.1 State Expression and Normalization

The first postulate is the description of a quantum system by a wave function $\phi(\vec{\tau}, t)$, with $t \in \mathbb{R}$. The probability density $\varrho(\vec{\tau}, t)$ at time t and at position $\vec{\tau}$ is given as $|\phi(\vec{\tau}, t)|^2$. The density of the state integrated over configuration space $\vec{\tau}$ has to be [33]:

$$\int_{\mathbb{R}^n} d\vec{\tau}\ |\phi(\vec{\tau}, t)|^2 = 1, \quad \forall\ t, \tag{2.2}$$

which is known as the normalization condition. Thus, $\phi(\vec{\tau}, t)$ has to be a function of twice integrable function space $\mathbb{L}^2$ [34].

2.2.2 Observables and Expectation Values

Measurable observables correspond to eigenvalues of hermitian operators, see eq. (2.1). The average of experimentally determined observables is formulated as an expectation value as [27, 35]:

$$\langle \hat{O}(\vec{\tau}) \rangle(t) = \int_{\mathbb{R}^n} \psi^*(\vec{\tau}, t)\ \hat{O}(\vec{\tau})\ \psi(\vec{\tau}, t)\ d\vec{\tau}\ , \tag{2.3}$$

where $\psi(\vec{\tau}, t) \in \mathfrak{H}$ is not necessarily an eigenfunction of $\hat{O}(\vec{\tau})$.

2.2.3 Time-Evolution

The temporal evolution of $\psi(\vec{\tau}, t)$ is given by the time-dependent Schrödinger equation [27]:

$$i\hbar\ \frac{\partial}{\partial t}\psi(\vec{\tau}, t) = \hat{H}(\vec{\tau})\ \psi(\vec{\tau}, t), \tag{2.4}$$

where i is the imaginary unit and $\hbar$ is Planck's constant. $\hat{H}(\vec{\tau}) \in \mathfrak{H}$ is a hermitian operator corresponding to the total energy of the described quantum system. It will be seen that the time-dependent Schrödinger equation is a linear homogeneous partial differential equation [36]. Therefore, the superposition principle [33] holds

for the quantum state description.

Before the properties of the Schrödinger equation are discussed in detail, first a Dirac-based notation which shortens the formalism of quantum mechanics is introduced in the following.

2.3 Dirac-Based Notation

Dealing with wave functions expressing quantum states, which are dependent on several variables, the notation for the complex scalar product for $\chi(\vec{\tau},t)^* \in \mathfrak{H}^*$ and $\psi(\vec{\tau},t) \in \mathfrak{H}$ in $\vec{\tau}$ space is written as:

$$\langle \chi(\vec{\tau},t) \,|\, \psi(\vec{\tau},t) \rangle_{\vec{\tau}} = \int_{-\infty}^{\infty} \chi(\vec{\tau},t)^* \psi(\vec{\tau},t)\; d\vec{\tau}, \tag{2.5}$$

which is the definition of an algebraic complex scalar product in an unitary space. This notation is strongly related to the Dirac *braket* notation introduced in 1939 [37]. From now on, this Dirac–based notation is applied solely.

2.4 Schrödinger Equation

The Schrödinger equation is the central equation to describe non-relativistic quantum mechanical systems [29]. In this work, a planar quantum system consisting of only one electron and three protons in a plane, with two of the protons being fixed in position is studied. Then, the Schrödinger equation reads:

$$i\hbar\, \frac{\partial}{\partial t} |\psi(\vec{r},\vec{R},t)\rangle = \hat{H}(\vec{r},\vec{R})\; |\psi(\vec{r},\vec{R},t)\rangle. \tag{2.6}$$

The vector $\vec{r} \in \mathbb{R}^2$ refers to the coordinate vector of the electron, and $\vec{R} \in \mathbb{R}^2$ refers to the mobile proton. $|\Psi(\vec{r},\vec{R},t)\rangle$, describes a quantum state in Hilbert space $\mathfrak{H}$. As a result, for the quantum system the hamiltonian $\hat{H}(\vec{r},\vec{R})$ with electron mass m_e and proton mass M reads as:

$$\hat{H}(\vec{r},\vec{R}) = -\frac{\hbar^2}{2M}\vec{\nabla}^2_{\vec{R}} - \frac{\hbar^2}{2m_e}\vec{\nabla}^2_{\vec{r}} + V(\vec{r},\vec{R}), \tag{2.7}$$

with $\vec{\nabla}_{\vec{R}} = \begin{pmatrix} \frac{\partial}{\partial R_x} \\ \frac{\partial}{\partial R_y} \end{pmatrix}$ and $\vec{\nabla}_{\vec{r}} = \begin{pmatrix} \frac{\partial}{\partial x} \\ \frac{\partial}{\partial y} \end{pmatrix}$.

The time-dependent Schrödinger equation is a linear partial differential equation of second order which, in case of $|\Psi(\vec{r},\vec{R},t)\rangle$ being an eigenfunction, is separable in space $\vec{r},\vec{R}$ and time t via the following product ansatz [27]:

$$|\Psi(\vec{r},\vec{R},t)\rangle = \xi(t)|\psi(\vec{r},\vec{R})\rangle. \tag{2.8}$$

The solution and initial conditions for $|\Psi(\vec{r},\vec{R},t)\rangle$ will be regraded in the following subsection.

2.4.1 Solution of the Time-Dependent Schrödinger Equation

A separation of variables, namely $\vec{r},\vec{R}$ and t, leads to the following form of the Schrödinger equation:

$$\begin{aligned} \mathrm{i}\hbar\frac{\dot{\xi}(t)}{\xi(t)} &= \hat{H}(\vec{r},\vec{R})\frac{|\psi(\vec{r},\vec{R})\rangle}{|\psi(\vec{r},\vec{R})\rangle} \\ \mathrm{i}\hbar\frac{\dot{\xi}(t)}{\xi(t)} &= E. \end{aligned} \tag{2.9}$$

Neither the left part of the equation is dependent on the right part of the equation and vice versa. This leads to the conclusion that both parts must be constant [27]. This can be expressed by the constant E, namely the eigenenergy of the quantum state, described by $\xi(t)|\psi(\vec{r},\vec{R})\rangle$.

Solving now eq. (2.9) for $\xi(t)$ leads to the following time-dependence for $\xi(t_0)$ as an initial condition:

$$\xi(t) = \xi(t_0)e^{-\frac{\mathrm{i}}{\hbar}Et}. \tag{2.10}$$

As a result, the total wave function has the time-dependence:

$$|\psi(\vec{r},\vec{R})\rangle\xi(t) = |\psi(\vec{r},\vec{R})\rangle\xi(t_0)e^{-\frac{\mathrm{i}}{\hbar}Et}. \tag{2.11}$$

Summarizing, one initial condition for $|\psi(\vec{r},\vec{R})\rangle\xi(t)$ at $t = 0$ is needed, and by knowledge of the eigenenergy E, the temporal evolution of the system is given. Still, one is left with the conditions which are put on $|\psi(\vec{r},\vec{R})\rangle$, but this will be explained in the following subsections for a case with four degrees of freedom using one electron and one proton, moveable in a plane as mentioned earlier. It should be noted that propagators are used for the time-evolution of wave packets. These propagators are introduced in section 2.5.

2.4.2 Solution of the Time-Independent Schrödinger Equation in Four Dimensions for Screened Coulomb Potentials

In general, it is not possible to solve the Schrödinger equation for many particle systems analytically. So, one is forced to use numerical methods like imaginary time-propagation (ITP) to solve the differential equations numerically [38].
Despite the complexity, one can find different representations which partially solve the time-independent Schrödinger equation step by step and, therefore, shed some light on the quantum mechanical system. In the following, two different state representations are given to characterize the multi-particle system encountered in this work. With these representations the coordinate space is reduced by first solving the electronic Schrödinger equation and treating the proton coordiante $\vec{R}$ afterwards [39]. Using atomic units, unless otherwise stated, the total hamiltonian $\hat{H}(\vec{r},\vec{R})$ reads as:

$$\hat{H}(\vec{r},\vec{R}) = \underbrace{\underbrace{-\frac{\vec{\nabla}^2_{\vec{R}}}{2M}}_{\hat{T}_N(\vec{R})}\underbrace{-\frac{\vec{\nabla}^2_{\vec{r}}}{2}}_{\hat{T}_e(\vec{r})}\underbrace{-\frac{1}{|\vec{r}-\vec{R}|}-\sum_{k=1}^{2}\frac{1}{|\underline{\vec{R}_k}-\vec{r}|}}_{\hat{V}_{eN}(\vec{r},\vec{R})}+\underbrace{\sum_{k=1}^{2}\frac{1}{|\underline{\vec{R}_k}-\vec{R}|}}_{\hat{V}_N(\vec{R})}}_{\hat{H}_{el}(\vec{r},\vec{R})}. \tag{2.12}$$

Note that $\underline{\vec{R}_1}$ and $\underline{\vec{R}_2}$, both being $\in \mathbb{R}^2$, are the positions of the two fixed protons. The hamiltonian can be decomposed in the kinetic energy operator for the mobile proton $\hat{T}_N(\vec{R})$ and the electronic hamiltonian $\hat{H}_{el}(\vec{r},\vec{R})$ consisting of the kinetic energy operator of the electron $\hat{T}_e(\vec{r})$, the interaction between electron and protons $\hat{V}_{eN}(\vec{r},\vec{R})$ and the static repulsive interaction between the protons $\hat{V}_N(\vec{R})$ [27, 40]. This decomposition leads to the ability of a partial solution of the Schrödinger equation [39].

It should be noted that in this study screened Coulomb potentials are used later on for numerical and practical reasons [41, 42] .

It must be emphasized that the total hamiltonian and the total wave function $|\psi(\vec{r},\vec{R})\rangle$ depend on the electron and proton coordinate. Solving this equation exactly for all coordinates, a discrete set of eigenfunctions $\{|\tilde{\varphi}_n(\vec{r},\vec{R})\rangle e^{ic_n}\} \in \mathbb{C}$, and a corresponding spectrum of eigenvalues $E_n \in \mathbb{R}$ is obtained. The eigenfunctions are unique, up to a phase factor $e^{ic_n} \in \mathbb{C}$, which has no impact on the energetic eigenvalues. For simplicity, $c_n = c_r$ is chosen in the way that the eigenfunctions are real [27].

$$|\varphi_n(\vec{r},\vec{R})\rangle = |\tilde{\varphi}_n(\vec{r},\vec{R})e^{ic_r}\rangle \in \mathbb{R}, \tag{2.13}$$

and finally

$$\hat{H}(\vec{r},\vec{R})\ |\varphi_n(\vec{r},\vec{R})\rangle = E_n\ |\varphi_n(\vec{r},\vec{R})\rangle. \tag{2.14}$$

2.4.2.1 Adiabatic Representation

In order to solve the time-independent Schrödinger equation (eq. (2.14)) partially and expand it into the adiabatic representation, adiabatic electronic eigenfunctions are needed. The idea behind this is to solve the electronic Schrödinger equation:

$$\left[\hat{H}_{el}(\vec{r};\vec{R}) - u_{nn}(\vec{R})\right]|\phi_n(\vec{r};\vec{R})\rangle = 0. \tag{2.15}$$

As a result, one obtains electronic energetic eigenvalues $u_{nn}(\vec{R})$ parametrically dependent on the nuclear geometry $\vec{R}$. The eigenfunctions define a normalized orthogonal complete set $\left\{|\phi_n(\vec{r};\vec{R})\rangle\right\}$ at each nuclear geometry $\vec{R}$ [27].
It is important to know that the phase matching between two adiabatic electronic eigenfunctions of adjacent nuclear geometries must be fulfilled. This means that $|\phi_n(\vec{r};\vec{R})\rangle$ must be continuous and twice differentiable along the nuclear geometry coordinate $\vec{R}$. This is crucial in dealing with the adiabatic eigenfunctions in the context of the total Schrödinger equation.
The expansion of the total wave function $|\psi(\vec{r},\vec{R})\rangle$ into the basis set $\left\{|\phi_n(\vec{r};\vec{R})\rangle\right\}$ is given as [43, 44]:

$$|\psi(\vec{r},\vec{R})\rangle = \sum_n |\phi_n(\vec{r};\vec{R})\rangle \underbrace{\langle\phi_n(\vec{r};\vec{R})\,|\,\psi(\vec{r},\vec{R})\rangle_{\vec{r}}}_{|\chi_n(\vec{R})\rangle}. \tag{2.16}$$

As a result of the expansion into the electronic basis set, functions $|\chi_n(\vec{R})\rangle$ depending on the proton coordiante $\vec{R}$ are obtained. Inserting the adiabatic expansion eq. (2.16) into the total Schrödinger equation, yields [39]:

$$
\begin{aligned}
0 =& \left(\hat{H}(\vec{r},\vec{R}) - E\right) \sum_n |\phi_n(\vec{r};\vec{R})\rangle |\chi_n(\vec{R})\rangle \\
=& \left(\hat{T}_N(\vec{R}) + \hat{H}_{el}(\vec{r};\vec{R}) - E\right) \sum_n |\phi_n(\vec{r};\vec{R})\rangle |\chi_n(\vec{R})\rangle \\
=& \langle\phi_k(\vec{r};\vec{R})| \left(\hat{T}_N(\vec{R}) + \hat{H}_{el}(\vec{r};\vec{R}) - E\right) \sum_n |\phi_n(\vec{r};\vec{R})\rangle_{\vec{r}} |\chi_n(\vec{R})\rangle \\
=& \sum_n \left\{ \underbrace{\langle\phi_k(\vec{r};\vec{R})|\hat{T}_N(\vec{R})|\phi_n(\vec{r};\vec{R})\rangle_{\vec{r}}}_{\hat{\Omega}_{kn}(\vec{R})} + \left[u_{nn}(\vec{R})\delta_{kn} - E\right] \right\} |\chi_n(\vec{R})\rangle. \qquad (2.17)
\end{aligned}
$$

Thus, the Schrödinger equation is transformed into a coupled system of n equations for the nuclear wave functions $|\chi_n(\vec{R})\rangle$, where $n \in \mathbb{N}$ numbers the basis state and the coupling elements are denoted as $\hat{\Omega}_{kn}(\vec{R})$. The coupling operators are calculated as:

$$
\begin{aligned}
\hat{\Omega}_{kn}(\vec{R}) &= \langle\phi_k(\vec{r};\vec{R}) \,|\, \hat{T}_N(\vec{R}) \,|\, \phi_n(\vec{r};\vec{R})\rangle_{\vec{r}} \\
&= \langle\phi_k(\vec{r};\vec{R}) \,|\, -\frac{\vec{\nabla}^2_{\vec{R}}}{2M} \,|\, \phi_n(\vec{r};\vec{R})\rangle_{\vec{r}} \\
&= -\frac{1}{2M} \underbrace{\langle\phi_k(\vec{r};\vec{R}) \,|\, \vec{\nabla}^2_{\vec{R}} \,|\, \phi_n(\vec{r};\vec{R})\rangle_{\vec{r}}}_{\hat{\omega}_{kn}(\vec{R})}. \qquad (2.18)
\end{aligned}
$$

These kinetic coupling elements depend on the proton mass M and on $\hat{\omega}_{kn}(\vec{R})$. Putting the focus on the modified kinetic nuclear matrix element $\hat{\omega}_{kn}(\vec{R})$, the coupling strength is determined by the change of electronic eigenfunctions for the nuclear geometry [27].

$$
\begin{aligned}
\hat{\omega}_{kn}(\vec{R}) =& \langle \phi_k(\vec{r};\vec{R})|\vec{\nabla}_{\vec{R}}[\vec{\nabla}_{\vec{R}}|\phi_n(\vec{r};\vec{R})\rangle_{\vec{r}}] \\
=& \underbrace{\langle \phi_k(\vec{r};\vec{R})|\vec{\nabla}^2_{\vec{R}}|\phi_n(\vec{r};\vec{R})\rangle_{\vec{r}}}_{\tau^{(2)}_{kn}(\vec{R})} + 2\underbrace{\langle \phi_k(\vec{r};\vec{R})|\vec{\nabla}_{\vec{R}}|\phi_n(\vec{r};\vec{R})\rangle_{\vec{r}}}_{\vec{\tau}_{kn}(\vec{R})}\vec{\nabla}_{\vec{R}} \\
&+ \underbrace{\langle \phi_k(\vec{r};\vec{R})\,|\,\phi_n(\vec{r};\vec{R})\rangle_{\vec{r}}}_{\mathbb{1}\text{ or }\delta_{kn}}\vec{\nabla}^2_{\vec{R}},
\end{aligned}
\tag{2.19}
$$

following the rearrangement of $\hat{\omega}_{kn}(\vec{R})$, eq. (2.17) can be written in matrix form. In what follows, $\vec{\tau}_{kn}(\vec{R})$ and $\tau^{(2)}_{kn}(\vec{R})$ will be called NACT [39], standing for non-adiabatic coupling element.

$$
\begin{aligned}
&-\frac{\vec{\nabla}^2_{\vec{R}}}{2M}|\chi_k(\vec{R})\rangle + \left(u_{kk}(\vec{R}) - E\right)|\chi_k(\vec{R})\rangle \\
&-\frac{1}{2M}\sum_n \left(2\vec{\tau}_{kn}(\vec{R})\vec{\nabla} + \tau^{(2)}_{kn}(\vec{R})\right)|\chi_n(\vec{R})\rangle = 0.
\end{aligned}
\tag{2.20}
$$

Using the following divergence condition [45–47]:

$$
\tau^{(2)}(\vec{R}) = \vec{\tau}^{\,2}(\vec{R}) + \vec{\nabla}_{\vec{R}}\cdot\vec{\tau}(\vec{R}),
\tag{2.21}
$$

eq. (2.20) can be rewritten as [48–51]:

$$
-\frac{1}{2M}\sum_n \left[\vec{\nabla}_{\vec{R}}\delta_{kn} + \vec{\tau}_{kn}(\vec{R})\right]^2|\chi_n(\vec{R})\rangle + \left(u_{kk}(\vec{R}) - E\right)|\chi_k(\vec{R})\rangle = 0.
\tag{2.22}
$$

The latter equation is the Schrödinger equation in the adiabatic representation. The electronic Schrödinger equation is now solved, and the electron coordinate is integrated out. The information about the electron is now completely incorporated in the NACT $\vec{\tau}_{kn}(\vec{R})$ and in the adiabatic potential $u_{kk}(\vec{R})$.

On the other hand, it is also possible to define a diabatic representation with electronic eigenfunctions which do not depend on the nuclear geometry and are,

therefore, constant for each geometry. Now, the question arises under what condition this can be transformed into the Schrödinger equation within the diabatic representation. In what follows, the diabatic representation will be given, and afterwards, the transformation from a diabatic to an adiabatic picture for the nuclear and electronic wave function will be discussed.

2.4.2.2 Diabatic Representation

Within the diabatic picture, the electronic Schrödinger equation is solved only for a single discrete geometry ($\underline{\vec{R}}$) [46, 49, 52–56]:

$$\left[\hat{H}_{el}(\vec{r};\underline{\vec{R}}) - \tilde{u}_{nn}(\underline{\vec{R}})\right] |\tilde{\phi}_n(\vec{r};\underline{\vec{R}})\rangle = 0. \tag{2.23}$$

This is exactly the same as taking the adiabatic ansatz at one specific nuclear geometry. The eigenfunctions built a complete orthonormal set at the reference geometry $\underline{\vec{R}}$. Expanding the total wave function into the diabatic basis set at a given geometry, one obtains:

$$|\psi(\vec{r},\vec{R})\rangle = \sum_n |\tilde{\phi}_n(\vec{r};\underline{\vec{R}})\rangle \underbrace{\langle\tilde{\phi}_n(\vec{r};\underline{\vec{R}}) \,|\, \psi(\vec{r},\vec{R})\rangle_{\vec{r}}}_{|\tilde{\chi}_n(\vec{R};\underline{\vec{R}})\rangle}. \tag{2.24}$$

Inserting the diabatic expression into the Schrödinger equation yields:

$$-\frac{1}{2M}\vec{\nabla}^2_{\vec{R}}|\tilde{\chi}_k(\vec{R};\underline{\vec{R}})\rangle + \sum_n \left(\tilde{u}_{kn}(\vec{R};\underline{\vec{R}}) - E\right)|\tilde{\chi}_n(\vec{R};\underline{\vec{R}})\rangle = 0, \tag{2.25}$$

where $\tilde{u}_{kn}(\vec{R};\underline{\vec{R}}) = \langle\tilde{\phi}_k(\vec{r};\underline{\vec{R}}) \,|\, \hat{H}_{el}(\vec{r};\vec{R}) \,|\, \tilde{\phi}_n(\vec{r};\underline{\vec{R}})\rangle_r$. This is the Schrödinger equation within the diabatic representation for a certain nuclear geometry $\underline{\vec{R}}$. The information about the electron does not appear as a kinetic coupling but as a potential coupling with elements $\tilde{u}_{kn}(\vec{R};\underline{\vec{R}})$, with $k \neq n$. Here, the picture arises

of a nuclear wave packet being driven on diabatic potential energy surfaces which are coupled to other surfaces via diabatic potential coupling elements.

Now, the question arises under what condition the diabatic representation of the Schrödinger equation can be transformed into the adiabatic representation. If one takes the Schrödinger equation within the adiabatic representation eq. (2.22):

$$-\frac{1}{2M}\sum_{n}\left[\vec{\nabla}_{\vec{R}}\delta_{kn}+\vec{\tau}_{kn}(\vec{R})\right]^{2}|\chi_{n}(\vec{R})\rangle+\left(u_{kk}(\vec{R})-E\right)|\chi_{k}(\vec{R})\rangle=0, \tag{2.26}$$

then an orthogonal transformation matrix $A(\vec{R};\underline{\vec{R}})\in\mathbb{R}^{n\times n}$ is considered, with $\sum_{m}(A^{-1})_{km}(\vec{R};\underline{\vec{R}})A_{mn}(\vec{R};\underline{\vec{R}})=\delta_{kn}$, that transforms like [45, 47, 48, 50]:

$$|\tilde{\chi}_{n}(\vec{R};\underline{\vec{R}})\rangle=\sum_{m}A_{nm}(\vec{R};\underline{\vec{R}})|\chi_{m}(\vec{R})\rangle. \tag{2.27}$$

and

$$|\chi_{n}(\vec{R})\rangle=\sum_{m}(A^{-1})_{nm}(\vec{R};\underline{\vec{R}})|\tilde{\chi}_{m}(\vec{R};\underline{\vec{R}})\rangle. \tag{2.28}$$

This transformation is path-dependent, as the nuclear geometry $\underline{\vec{R}}$ of the diabatic basis representation is arbitrary. Additionally, the transformation is carried out from $\underline{\vec{R}}$ to the continuous variable $\vec{R}$ and vice versa. So, in general this transformation depends on the path Γ between $\underline{\vec{R}}$ and $\vec{R}$. Inserting eq. (2.27) and eq. (2.28) into eq. (2.26) yields [39]:

$$\begin{aligned}&-\frac{1}{2M}\sum_{k,n}A_{ok}(\vec{R};\underline{\vec{R}})\left[\vec{\nabla}_{\vec{R}}\delta_{kn}+\vec{\tau}_{kn}(\vec{R})\right]^{2}\sum_{m}(A^{-1})_{nm}(\vec{R};\underline{\vec{R}})A_{mn}(\vec{R};\underline{\vec{R}})|\chi_{n}(\vec{R})\rangle\\&+\sum_{k,n}A_{ok}(\vec{R};\underline{\vec{R}})\left(u_{kn}(\vec{R})\delta_{kn}-E\right)\sum_{m}(A^{-1})_{nm}(\vec{R};\underline{\vec{R}})A_{mn}(\vec{R};\underline{\vec{R}})|\chi_{n}(\vec{R})\rangle=0.\end{aligned} \tag{2.29}$$

This can be rewritten in the form, see appendix A:

$$
\begin{aligned}
&-\frac{1}{2M}\vec{\nabla}^2_{\vec{R}}|\tilde{\chi}_o(\vec{R};\underline{\vec{R}})\rangle+\\
&2\sum_{k,m,n}\left[A_{ok}(\vec{R};\underline{\vec{R}})\underbrace{\left(\vec{\nabla}_{\vec{R}}\delta_{kn}(A^{-1})_{nm}(\vec{R};\underline{\vec{R}})+\vec{\tau}_{kn}(A^{-1})_{nm}(\vec{R};\underline{\vec{R}})\right)}_{=0}\right]\vec{\nabla}_{\vec{R}}|\tilde{\chi}_m(\vec{R};\underline{\vec{R}})\rangle\\
&+\sum_{k,m,n,s}A_{ok}(\vec{R};\underline{\vec{R}})\times\\
&\left[\left(\vec{\nabla}_{\vec{R}}\delta_{ks}+\vec{\tau}_{ks}(\vec{R})\right)\underbrace{\left(\vec{\nabla}_{\vec{R}}\delta_{sn}(A^{-1})_{nm}(\vec{R};\underline{\vec{R}})+\vec{\tau}_{sn}(A^{-1})_{nm}(\vec{R};\underline{\vec{R}})\right)}_{=0}\right]\times\\
&|\tilde{\chi}_m(\vec{R};\underline{\vec{R}})\rangle+\sum_m\left(\tilde{u}_{om}(\vec{R};\underline{\vec{R}})-E\right)|\tilde{\chi}_m(\vec{R};\underline{\vec{R}})\rangle=0.
\end{aligned}
\tag{2.30}
$$

As far as $\sum_n \vec{\nabla}_{\vec{R}}\delta_{kn}(A^{-1})_{nm}(\vec{R};\underline{\vec{R}})+\vec{\tau}_{kn}(\vec{R})(A^{-1})_{nm}(\vec{R};\underline{\vec{R}})=0\ \ \forall k,m$, the transformation from the adiabatic representation to the diabatic representation can be achieved. In case the extended curl condition [45]:

$$
0=\frac{(\partial\vec{\tau}_{kn}(\vec{R}))_{R_x}}{\partial R_y}-\frac{(\partial\vec{\tau}_{kn}(\vec{R}))_{R_y}}{\partial R_x}-\left[(\vec{\tau}_{kn}(\vec{R}))_{R_x}(\vec{\tau}_{kn}(\vec{R}))_{R_y}-(\vec{\tau}_{kn}(\vec{R}))_{R_y}(\vec{\tau}_{kn}(\vec{R}))_{R_x}\right]
\tag{2.31}
$$

is satisfied, one can find a solution for the transformation matrix [39]:

$$
(A^{-1})_{km}(\vec{R};\underline{\vec{R}})=\sum_n\left(e^{-\int_{\underline{\vec{R}}}^{\vec{R}}\vec{\tau}(\vec{R}')\cdot\partial\vec{R}'}\right)_{kn}(A^{-1})_{nm}(\underline{\vec{R}},\underline{\vec{R}}).
\tag{2.32}
$$

The line integral $-\int_{\underline{\vec{R}}}^{\vec{R}}\vec{\tau}_{kn}(\vec{R}')\cdot\partial\vec{R}'=\varphi_{kn}(\vec{R};\underline{\vec{R}})$ gives the mixing angle $\varphi_{kn}(\vec{R};\underline{\vec{R}})\in\mathbb{R}$ between involved states which are coupled via $\vec{\tau}_{kn}(\vec{R})$.

Then, for example, for a two-level system $\vec{\tau}_{21}(\vec{R})=-\vec{\tau}_{12}(\vec{R})$ [39] and the rotation matrix is given as $e^{Q(\vec{R};\underline{\vec{R}})}$, with:

$$Q(\vec{R};\underline{\vec{R}}) = \varphi(\vec{R};\underline{\vec{R}}) \begin{bmatrix} 0 & -1 \\ 1 & 0 \end{bmatrix}. \tag{2.33}$$

Now one can calculate:

$$Q^2(\vec{R};\underline{\vec{R}}) = -\varphi(\vec{R};\underline{\vec{R}})^2 \mathbb{1}. \tag{2.34}$$

Then:

$$Q^3(\vec{R};\underline{\vec{R}}) = -\varphi(\vec{R};\underline{\vec{R}})^3 \begin{bmatrix} 0 & -1 \\ 1 & 0 \end{bmatrix}. \tag{2.35}$$

and

$$Q^4(\vec{R};\underline{\vec{R}}) = -\varphi(\vec{R};\underline{\vec{R}})^2 Q^2(\vec{R};\underline{\vec{R}}) = \varphi(\vec{R};\underline{\vec{R}})^4 \mathbb{1}, \tag{2.36}$$

and so on. Then:

$$e^{Q(\vec{R};\underline{\vec{R}})} = \sum_{n=0}^{\infty} \frac{(-1)^n}{2n!} \varphi(\vec{R};\underline{\vec{R}})^{2n} \begin{bmatrix} 1 & 0 \\ 0 & 1 \end{bmatrix} + \sum_{n=0}^{\infty} \frac{(-1)^n}{(2n+1)!} \varphi(\vec{R};\underline{\vec{R}})^{2n+1} \begin{bmatrix} 0 & -1 \\ 1 & 0 \end{bmatrix}. \tag{2.37}$$

Finally, the transfomation for a two-level system can be written as rotation matrix of the following form:

$$A^{-1}(\vec{R};\underline{\vec{R}}) = \begin{pmatrix} \cos(\varphi(\vec{R};\underline{\vec{R}})) & -\sin(\varphi(\vec{R};\underline{\vec{R}})) \\ \sin(\varphi(\vec{R};\underline{\vec{R}})) & \cos(\varphi(\vec{R};\underline{\vec{R}})) \end{pmatrix} A^{-1}(\underline{\vec{R}},\underline{\vec{R}}), \tag{2.38}$$

with $k, n, m = 1, 2$. This is a rotation matrix $A^{-1}(\vec{R};\underline{\vec{R}})$ which transforms the diabatic representation via an abstract mixing angle to the adiabatic representation. Depending on its geometry, the value of the mixing angle will be different.

This mixing angle can be directly connected to the transformation from the diabatic electronic eigenfunctions to the adiabatic electronic eigenfunctions in incremental $\Delta\vec{R}$ steps [39]:

$$\begin{aligned} |\phi_k(\vec{r};\underline{\vec{R}}+\Delta\vec{R})\rangle &= \sum_n \left(\delta_{kn} - \Delta\vec{R}\cdot\vec{\tau}_{kn}(\vec{R})\right)|\phi_n(\vec{r};\underline{\vec{R}})\rangle \\ \frac{|\phi_k(\vec{r};\underline{\vec{R}}+\Delta\vec{R})\rangle - |\phi_k(\vec{r};\underline{\vec{R}})\rangle}{\Delta\vec{R}} &= -\sum_n \vec{\tau}_{kn}(\vec{R})|\phi_n(\vec{r};\underline{\vec{R}})\rangle \\ \sum_n \vec{\nabla}_{\vec{R}}\delta_{kn}|\phi_n(\vec{r};\vec{R})\rangle + \vec{\tau}_{kn}(\vec{R})|\phi_n(\vec{r};\vec{R})\rangle &= 0. \end{aligned} \tag{2.39}$$

From the solution of eq. (2.39), one can recast the transformation expression for the diabatic transformation to the adiabatic transformation of the electronic eigenfunctions.

$$\begin{aligned} |\phi_k(\vec{r};\vec{R})\rangle &= \sum_n \left(e^{-\int_{\underline{\vec{R}}}^{\vec{R}}\vec{\tau}(\vec{R}')\cdot\partial\vec{R}'}\right)_{kn}|\phi_n(\vec{r};\underline{\vec{R}})\rangle \\ |\phi_k(\vec{r};\vec{R})\rangle &= \sum_{n,m}\left(e^{-\int_{\underline{\vec{R}}}^{\vec{R}}\vec{\tau}(\vec{R}')\cdot\partial\vec{R}'}\right)_{kn}\underbrace{(A^{-1})_{nm}(\underline{\vec{R}},\underline{\vec{R}})}_{\delta_{nm}}|\phi_m(\vec{r};\underline{\vec{R}})\rangle \\ |\phi_k(\vec{r};\vec{R})\rangle &= \sum_m (A^{-1})_{km}(\vec{R};\underline{\vec{R}})|\phi_m(\vec{r};\underline{\vec{R}})\rangle. \end{aligned} \tag{2.40}$$

This exemplifies that the transformation from the diabatic to the adiabatic representation and vice versa is equivalent for the electronic eigenfunctions, the nuclear

wave function, and the reduced Schrödinger equation. The solution of the transformation matrix is path-dependent and strongly related to the non-adiabatic coupling elements.

$$(A^{-1})_{km}(\vec{R};\underline{\vec{R}}) = \sum_n \left(e^{-\int_{\underline{\vec{R}}}^{\vec{R}} \vec{\tau}(\vec{R}')\cdot\partial\vec{R}'} \right)_{kn} (A^{-1})_{nm}(\underline{\vec{R}},\underline{\vec{R}}). \tag{2.41}$$

Another possibility to gain the transformation matrix $A^{-1}(\vec{R};\underline{\vec{R}})$ is to define the diabatic electronic basis functions out of the adiabatic electronic eigenfunctions at a certain geometry $\underline{\vec{R}}$. Then, the adiabatic electronic eigenfunctions are expanded into the diabatic basis set.

$$\begin{aligned} |\phi_k(\vec{r};\vec{R})\rangle &= \sum_n |\tilde{\phi}_n(\vec{r};\underline{\vec{R}})\rangle\langle\tilde{\phi}_n(\vec{r};\underline{\vec{R}})\,|\,\phi_k(\vec{r};\vec{R})\rangle_{\vec{r}} \\ &= \sum_n (A^{-1})_{kn}(\vec{R};\underline{\vec{R}})|\tilde{\phi}_n(\vec{r};\underline{\vec{R}})\rangle. \end{aligned} \tag{2.42}$$

2.5 Quantum Wave-Packet Dynamics

2.5.1 Exact Propagation

The time-dependence of a wave packet can be calculated via the system propagator $\hat{U}(\vec{r},\vec{R},t,t_0)$. This propagator arises from the solution of the time-dependent Schrödinger equation. One initial condition needs to be fulfilled. This is the initial wave packet $|\psi(\vec{r},\vec{R},t_0)\rangle$. Then, by knowledge of the full time-independent hamiltonian $\hat{H}(\vec{r},\vec{R})$, the evolution of the wave packet is given by the propagator [27]:

$$\hat{U}(\vec{r},\vec{R},t,t_0) = e^{-i\int_{t_0}^{t} \hat{H}(\vec{r},\vec{R})\ dt'}. \tag{2.43}$$

The time-dependence for the wave packet is then given as:

$$\begin{aligned}|\psi(\vec{r},\vec{R},t)\rangle &= \hat{U}(\vec{r},\vec{R},t,t_0)|\psi(\vec{r},\vec{R},t_0)\rangle \\ &= e^{-i\int_{t_0}^{t}\hat{H}(\vec{r},\vec{R})\ dt'}|\psi(\vec{r},\vec{R},t_0)\rangle \\ &= \sum_n c_n(t_0)|\varphi_n(\vec{r},\vec{R})\rangle\ e^{-iE_n(t-t_0)},\end{aligned} \tag{2.44}$$

where the picture arises of a spectral superposition of eigenstates being driven in phase by their corresponding eigenenergies. This superposition depends on the state coefficients $c_n(t_0)$ of the composition of the wave packet.

2.5.2 Propagation in the Adiabatic Framework

Besides the exact propagation, a propagation in the adiabatic representation can also be done. This is a reduction down to nuclear coordinates which are propagated only. In case the non-adiabatic coupling elements $\vec{\tau}_{kn}(\vec{R})$ can also be regarded within the dynamical description, this representation is also an exact one. The coupled equations of motion then read:

$$i\frac{\partial}{\partial t}|\chi_k(\vec{R},t)\rangle = -\frac{1}{2M}\sum_n\left[\vec{\nabla}_{\vec{R}}\delta_{kn}+\vec{\tau}_{kn}(\vec{R})\right]^2|\chi_n(\vec{R},t)\rangle + u_{kk}(\vec{R})|\chi_k(\vec{R},t)\rangle. \tag{2.45}$$

The time-dependence for a nuclear wave packet $|\chi_k(\vec{R},t)\rangle$ within the adiabatic electronic eigenstates $|\phi_k(\vec{r};\vec{R})\rangle$ is then given by:

$$|\chi_k(\vec{R},t)\rangle = \sum_n\left(e^{-i\left(-\frac{1}{2M}\left[\vec{\nabla}_{\vec{R}}+\vec{\tau}(\vec{R})\right]^2+u(\vec{R})\right)(t-t_0)}\right)_{kn}\sum_j c_{nj}(t_0)|\Pi_{nj}(\vec{R})\rangle, \tag{2.46}$$

where $|\chi_n(\vec{R},t)\rangle = \sum_j c_{nj}(t_0)|\Pi_{nj}(\vec{R})\rangle$ is the nuclear wave packet in the n-th

adiabatic state.

Often, these NACTs can not be treated within a numerical calculation, thus, the dynamical description gets unprecise. In certain cases, one can neglect the NACTs, which is well known as the Born-Oppenheimer approximation [43, 44]. In this case a quite good result for the dynamics is achieved. Then the equations of motion are given as:

$$i\frac{\partial}{\partial t}|\chi_k(\vec{R},t)\rangle = \left[-\frac{1}{2M}\vec{\nabla}^2_{\vec{R}} + u_{kk}(\vec{R})\right]|\chi_k(\vec{R},t)\rangle. \tag{2.47}$$

$$|\chi_k(\vec{R},t)\rangle = e^{-i\left(-\frac{1}{2M}\vec{\nabla}^2_{\vec{R}}+u_{kk}(\vec{R})\right)(t-t_0)}\sum_j c_{kj}(t_0)|\Pi_{kj}(\vec{R},t_0)\rangle. \tag{2.48}$$

2.5.3 Propagation in the Diabatic Framework

Last but not least, it is also possible to propagate in the diabatic state representation. The coupling elements appear as off-diagonal coupling elements $\tilde{u}_{kn}(\vec{R};\underline{\vec{R}})$, with $k \neq n$. The coupled equations of motion read:

$$i\frac{\partial}{\partial t}|\tilde{\chi}_k(\vec{R};\underline{\vec{R}},t)\rangle = \sum_n \left\{-\frac{\vec{\nabla}^2_{\vec{R}}}{2M}\delta_{kn} + \tilde{u}_{kn}(\vec{R};\underline{\vec{R}})\right\}|\tilde{\chi}_n(\vec{R};\underline{\vec{R}},t)\rangle. \tag{2.49}$$

Then the temporal evolution of a nuclear wave packet is given within the diabatic states as:

$$|\tilde{\chi}_k(\vec{R};\underline{\vec{R}},t)\rangle = \sum_n \left(e^{-i\left(-\frac{1}{2M}\vec{\nabla}^2_{\vec{R}}+\tilde{u}(\vec{R};\underline{\vec{R}})\right)(t-t_0)}\right)_{kn}\sum_j c_{nj}(t_0)|\tilde{\Pi}_{nj}(\vec{R};\underline{\vec{R}},t_0)\rangle. \tag{2.50}$$

2.6 Wave Packet in the Wigner Representation

A wave packet in coordinate space $R \in \mathbb{R}$ can be described by a wave function $|\psi(R,t)\rangle$ at time $t \in \mathbb{R}$. This wave packet can also be described by a pure state in density formalism by the operator [27]:

$$\hat{\varrho}(R,t) = |\psi(R,t)\rangle\langle\,\psi(R,t)|. \tag{2.51}$$

The Wigner representation connects the quantum mechanical density operator with the classical distribution in phase space. The Wigner function of the density operator is defined via:

$$\varrho_w(R,P,t) = \int_R ds\langle R + \frac{s}{2} \mid \hat{\varrho}(R,t) \mid R - \frac{s}{2}\rangle e^{-iPs}. \tag{2.52}$$

P is the momentum variable. For the density operator, the time-evolution is similar to wave functions given by the Liouville-von Neumann equation:

$$i\frac{\partial\hat{\varrho}(R,t)}{\partial t} = \left[\hat{H}(R), \hat{\varrho}(R,t)\right]. \tag{2.53}$$

Inserting the Liouville-von Neumann equation into the Wigner representation of the density operator and multiplying eq. (2.52) by the imaginary unit yields:

$$\frac{\partial\varrho_w(R,P,t)}{\partial t} = \{H(R,P), \varrho_w(R,P,t)\} - \frac{1}{24}\frac{\partial^3 V(R)}{\partial R^3}\frac{\partial^3\varrho_w(R,t)}{\partial R^3} + \dots\,. \tag{2.54}$$

Here, the time-evolution equation for the density operator in the Wigner representation is given [57]. The temporal derivation of this quantity is then determined by the Poisson bracket $\{H(R,P), \varrho_w(R,P,t)\}$ known from classical mechanics and additional correction terms. These correction terms will disappear when harmonic

potentials $V(R)$ are used within the system's description. In this case, the equation of motion for the density operator in the Wigner representation reads:

$$\frac{\partial \varrho_w(R,P,t)}{\partial t} = \{H, \varrho_w(R,P,t)\}\,. \tag{2.55}$$

According to this, $\varrho_w(R,P,t)$ can be built up of trajectories [58, 59]:

$$\varrho_w(R,P,t) = \sum_{R_i}\sum_{P_i} \rho(R_i,P_i)\delta(R-R_i)\delta(P-P_i), \tag{2.56}$$

and these trajectories can be propagated using Newton's equation of motion [60]:

$$m_i \frac{d^2}{dt^2} R_i = F_i^{(ex)} + \sum_{i\neq j} F_{ij} \tag{2.57}$$

where $F_i^{(ex)}$ is the force acting on the i-th particle. F_{ij} is the force acting between the i-th and j-th particle. Thus, a wave packet can be approximated as a swarm of trajectories in classical phase space as long as the driving system's potential is harmonic.

2.7 Non-Linear Polarization

Light-matter interaction can be described in a perturbative approach. Here, for the calculation of linear absorption spectra and two-dimensional spectra one is interested in the induced polarization of first and third order by one and three light-matter interactions [61].

Formulating the components of the polarization to the final signal is done in the density matrix representation. Therefore, the description of quantum states in the Liouville space $\mathfrak{L}$ is used here. In Liouville space, the contribution of the polarization to the detection signal can be demonstratively derived [62].

It should be noted that the calculations later on are done in Hilbert space.

2.7.1 Liouville Space

In Liouville space [63], the expression of the density matrix is replaced by a vector in double *braket* notation [62]. Then, for the set of eigenfunctions $\{|\varphi_n(\vec{r},\vec{R})\rangle\}$ follows:

$$|\rho(t)\rangle\rangle = \sum_{n,m} \rho_{nm}(t)|nm\rangle\rangle = \sum_{n,m} \rho_{nm}(t)|\varphi_n(\vec{r},\vec{R})\rangle\langle\,\varphi_m(\vec{r},\vec{R})|. \tag{2.58}$$

Analogously the complex conjugate density matrix is defined as:

$$\langle\langle\rho(t)| = \sum_{n,m} \rho^*_{nm}(t)\langle\langle nm| = \sum_{n,m} \rho_{mn}(t)|\varphi_m(\vec{r},\vec{R})\rangle\langle\,\varphi_n(\vec{r},\vec{R})|. \tag{2.59}$$

Of course, then the extended orthonormality relation holds:

$$\langle\langle nm\,|\,jk\rangle\rangle = \boldsymbol{Tr}_{\vec{r},\vec{R}}\,[|\varphi_m(\vec{r},\vec{R})\rangle\langle\varphi_n(\vec{r},\vec{R})\,|\,\varphi_j(\vec{r},\vec{R})\rangle_{\vec{r},\vec{R}}\langle\varphi_k(\vec{r},\vec{R})|] = \delta_{k,m}\delta_{j,n}, \tag{2.60}$$

and expectation values are calculated by:

$$\langle\langle \hat{O} \,|\, \rho(t) \rangle\rangle = \boldsymbol{Tr}_{\vec{r},\vec{R}} \left[\hat{O}(\vec{r},\vec{R}) \sum_{n,m} \rho_{nm}(t) |\varphi_n(\vec{r},\vec{R})\rangle\langle\, \varphi_m(\vec{r},\vec{R})| \right] = \langle \hat{O} \rangle(t). \quad (2.61)$$

The evolution of a state defined in Hilbert space is described via the time-dependent Schrödinger equation. As density matrix expressions are used, one is forced to extend the formalism. Then, the temporal evolution of the density is expressed via the time-dependent Liouville-von Neumann equation

$$\frac{\partial \rho_{kl}(t)}{\partial t} = -i \sum_{m} [\hat{H}_{km}\rho_{ml}(t) - \rho_{km}(t)\hat{H}_{ml}]. \quad (2.62)$$

The hamilton operator $\hat{H}_{km}$ is written in the system basis set spanned by $\{|\varphi_n(\vec{r},\vec{R})\rangle\}$ in Hilbert space. The expression $\hat{H}_{km}\rho_{ml}(t) - \rho_{km}(t)\hat{H}_{ml}$ can be replaced by one single superoperator $\hat{L}_{kl,mn}$ in Liouville space $\mathfrak{L}$ acting on the matrix vector $|nm\rangle\rangle$. Then, the time-dependent Liouville-von Neumann equation in Liouville space reads:

$$\frac{\partial \rho_{kl}(t)}{\partial t} = -i \sum_{m,n} \hat{L}_{kl,mn}\ \rho_{mn}(t). \quad (2.63)$$

Starting from this equation, the expression for spectroscopic signals is derived. In what follows, light-matter interactions are described via time-dependent perturbation theory [64] in Liouville space.

2.7.2 Light-Matter Interaction

Light-matter interactions are described in a semi-classical approach. Therefore, classical electro-magnetic fields are used. The magnetic component of the field is neglected, as the interaction between matter and the magnetic component is weak [65, 66]. Then, the electric field is defined as a classical transversal wave $\vec{E}(\vec{R}_e,t) \in \mathbb{R}^2$ in coordinate space $\vec{R}_e \in \mathbb{R}^2$, with an amplitutde $\vec{\zeta} = 2\vec{\epsilon} \in \mathbb{R}^2$, a wave momentum $\vec{k} \in \mathbb{R}^2$, and a frequency $\omega \in \mathbb{R}$. Additionally, on the basis

of experimental techniques [67–69] using short laser pulses, the electric field is characterized as a short Gaussian pulse being described by an additional Gaussian envelope expression:

$$\vec{E}(\vec{R}_e,t) = \vec{\zeta}\,\cos(\vec{k}\cdot\vec{R}_e-\omega t)e^{-\alpha t^2} = \vec{\epsilon}\,\left(e^{-i\{\vec{k}\cdot\vec{R}_e-\omega t\}} + e^{+i\{\vec{k}\cdot\vec{R}_e-\omega t\}}\right)e^{-\alpha t^2}, \quad (2.64)$$

with $\alpha \in \mathbb{R}^+$. Here, α is connected to the Gaussian standard deviation $\sigma \in \mathbb{R}_0^+ \setminus \{\infty\}$ via $\alpha = \frac{1}{2\sigma^2}$ [34].
Only systems are regarded with a size much smaller than the wave length $\lambda = \frac{2\pi}{|\vec{k}|}$ of the used classical fields. Therefore, expanding the space-dependent component of the electric field in a power series and terminating after the zeroth-order term yields:

$$e^{i\vec{k}\cdot\vec{R}_e} = 1 + i\vec{k}\cdot\vec{R}_e + ... \approx 1. \quad (2.65)$$

This is known as dipole approximation [70]. From now on, only electric fields are regarded where the spatial dependence is omitted.

$$\vec{E}(t) = \vec{\zeta}\,\cos(\omega t) = \vec{\epsilon}\,\left(e^{-i\omega t} + e^{+i\omega t}\right)e^{-\alpha t^2}. \quad (2.66)$$

Applying the rotating wave approximation [71], one can distinguish $\vec{\epsilon}\,e^{-i\omega t}e^{-\alpha t^2}$ to prompt an excitation within a quantum system, and $\vec{\epsilon}\,e^{+i\omega t}e^{-\alpha t^2}$ to prompt a stimulated emission [62].
The finite pulse sequence of $n \in \mathbb{N}$ interactions is written as one composite electric field $\vec{E}(t)$:

$$\vec{E}(t) = \sum_{n=1}^{m}\vec{E}_n(t-t_n) = \sum_{n=1}^{m}\vec{E}_n^{(+)}(t-t_n) + \vec{E}_n^{(-)}(t-t_n), \quad (2.67)$$

with

$$\vec{E}_n^{(\pm)}(t) = \vec{\epsilon} e^{\mp i\omega_n(t-t_n)} e^{-\alpha(t-t_n)^2}. \tag{2.68}$$

t_n is the center of the n-th Gaussian pulse. The dipole-moment operator for the system is given by:

$$\hat{\vec{\mu}}(\vec{r}, \vec{R}) = -\hat{\vec{r}} + \hat{\vec{R}}, \tag{2.69}$$

and in the transition dipole matrix elements as:

$$\hat{\vec{\mu}}_{nm}(\vec{R}) = \langle \phi_n(\vec{r}, \vec{R}) \,|\, -\hat{\vec{r}} + \hat{\vec{R}} \,|\, \phi_m(\vec{r}, \vec{R}) \rangle_{\vec{r}}. \tag{2.70}$$

The transition dipole matrix in the exact basis state representation is given as:

$$\vec{\mu}_{nm} = \langle \varphi_n(\vec{r}, \vec{R}) \,|\, -\hat{\vec{r}} + \hat{\vec{R}} \,|\, \varphi_m(\vec{r}, \vec{R}) \rangle_{\vec{r},\vec{R}}. \tag{2.71}$$

Furthermore, one defines for the operator in Liouville space:

$$\hat{\vec{\mu}}_{jk,nm} = \vec{\mu}_{jn}\delta_{km} - \vec{\mu}^*_{km}\delta_{jn}. \tag{2.72}$$

The polarization is given as the expectation value of the dipole-moment operator [72]:

$$\vec{P}(t) = \langle \hat{\vec{\mu}} \rangle(t) = \langle\langle \hat{\vec{\mu}} \;|\, \rho(t) \rangle\rangle. \tag{2.73}$$

In the following, the vector notation is omitted because the polarization is regarded parallel to the direction of the electric field $\left(\vec{P}(t) \parallel \vec{\epsilon}\right)$ [65]. As the description is in the complete eigenstate basis $\{|\varphi_n(\vec{r}, \vec{R})\rangle\}$, the spatial notation of the light-matter interaction is also suppressed. Making now a perturbative approach for the polarization, it is composed of contributions of order $q \in \mathbb{N}$ [73–75]:

$$P(t) = \sum_{l}^{q} P^{(l)}(t) = \sum_{l}^{q} \langle\langle \hat{\vec{\mu}} \mid \rho^{(l)}(t) \rangle\rangle. \tag{2.74}$$

Following S. Mukamel [62], the time-dependence for $\rho^{(l)}_{nm}(t)$ can be derived in the time-dependent perturbative picture as:

$$\begin{aligned} \rho^{(l)}_{nm}(t) =& i^l \int_0^\infty dt_l \int_0^\infty dt_{l-1} \cdots \int_0^\infty dt_1 E_l(t-t_l) E_{l-1}(t-t_l-t_{l-1}) \cdots \times \\ & E_1(t-t_l-t_{l-1} \cdots - t_1) G_{nm,nm}(t_l) \sum_{\substack{e,f,c,\\ d,\ldots,a,b}} \hat{\mu}_{nm,ef} \times \\ & G_{ef,ef}(t_{l-1}) \hat{\mu}_{ef,cd} G_{cd,cd}(t_{l-2}) \ldots G_{ab,ab}(t_1) \hat{\mu}_{ab,00} \rho_{00}(t_0), \end{aligned} \tag{2.75}$$

where

$$G_{nm,nm}(t_l) = \Theta(t_l) \hat{U}_{nm,nm}(t_l) = \Theta(t_l) e^{-i \hat{L}_{nm,nm}\ t_l} \tag{2.76}$$

is the Green's function, propagating the unperturbed system [76–78]. With the perturbative expansion of the density, the time-dependent perturbative polarization can finally be written as:

$$\begin{aligned} P^{(l)}(t) =& i^l \int_0^\infty dt_l \int_0^\infty dt_{l-1} \cdots \int_0^\infty dt_1 \sum_{\substack{n,m,e,f,\\ c,d,\ldots,a,b}} \times \\ & \langle\langle \hat{\mu} \mid nm \rangle\rangle G_{nm,nm}(t_l) \hat{\mu}_{nm,ef} G_{ef,ef}(t_{l-1}) \hat{\mu}_{ef,cd} G_{cd,cd}(t_{l-2}) \times \\ & \ldots G_{ab,ab}(t_1) \hat{\mu}_{ab,00}\ \rho_{00}(t_0) \times \\ & E_l(t-t_l) E_{l-1}(t-t_l-t_{l-1}) \ldots E_1(t-t_l-t_{l-1} \cdots - t_1). \end{aligned} \tag{2.77}$$

The following expression for $S^{(l)}(t_l, t_{l-1}, \ldots, t_1)$ out of the polarization function can be extracted and denoted as response function:

$$
\begin{aligned}
S^{(l)}(t_n, t_{l-1}, \ldots, t_1) =& i^l \sum_{\substack{n,m,e,f,\\ c,d,\ldots,a,b}} \langle\langle \hat{\mu} \,|\, mn \rangle\rangle G_{nm,nm}(t_l) \hat{\mu}_{nm,ef} \times \\
& G_{ef,ef}(t_{l-1}) \hat{\mu}_{ef,cd} G_{cd,cd}(t_{l-2}) \times \\
& \ldots G_{ab,ab}(t_1) \hat{\mu}_{ab,00} \rho_{00}(t_0).
\end{aligned} \tag{2.78}
$$

With this expression, the contributions to a one-dimensional spectrum [79–81], e.g. an absorption spectrum, can be derived. This is a process with one single light-matter interaction. As a result, the response function is of first order: $S^{(1)}(t_1)$ is depending on one single interaction at a certain time t_1.

$$
S^{(1)}(t_1) = i \sum_a \langle\langle \hat{\mu} \,|\, a0 \rangle\rangle G_{a0,a0}(t_1) \hat{\mu}_{a0,00} \ \rho_{00}(t_0). \tag{2.79}
$$

This can be further expanded in Hilbert space to finally come to the form:

$$
S^{(1)}(t_1) = i\{\mu_{a0} \rho_{00}(t_0) \mu_{0a}(t_1) - \mu_{a0}(t_1) \rho_{00}(t_0) \mu_{0a}\}, \tag{2.80}
$$

where there are two contributions to the total response function. One, where the light-matter interaction takes place upon the *ket*-elements of the density matrix, calling $J(t_1)$ and $J^*(t_1)$ for the interaction on the *bra*-elements of the density matrix.

$$
S^{(1)}(t_1) = i\{J(t_1) - J^*(t_1)\}. \tag{2.81}
$$

Similarly, for the three-photon interaction for the two-dimensional spectrum a response function with three interactions is obtained:

$$
\begin{aligned}
S^{(3)}(t_3,t_2,t_1) =& i^3\Theta(t_1)\Theta(t_2)\Theta(t_3)\{R_1(t_3,t_2,t_1) - R_1^*(t_3,t_2,t_1) \\
&+ R_2(t_3,t_2,t_1) - R_2^*(t_3,t_2,t_1) + R_3(t_3,t_2,t_1) \\
&- R_3^*(t_3,t_2,t_1) + R_4(t_3,t_2,t_1) - R_4^*(t_3,t_2,t_1)\},
\end{aligned} \tag{2.82}
$$

with the eight contributions $R_n(t_3,t_2,t_1)$ and $R_n^*(t_3,t_2,t_1)$, with $n = 1,2,3,4$:

$$
R_1(t_3,t_2,t_1) = \sum_{a,b,c,d} \mu_{ca}\mu_{0a}(t_1)\mu_{cb}(t_1+t_2+t_3)\mu_{b0}(t_1+t_2)\ \rho_{00}(t_0), \tag{2.83}
$$

$$
R_2(t_3,t_2,t_1) = \sum_{a,b,c,d} \mu_{bc}\mu_{0c}(t_1+t_2)\mu_{ba}(t_1+t_2+t_3)\mu_{a0}(t_1)\ \rho_{00}(t_0), \tag{2.84}
$$

$$
R_3(t_3,t_2,t_1) = \sum_{a,b,c,d} \mu_{0a}(t_1)\mu_{ab}(t_1+t_2)\mu_{bc}(t_1+t_2+t_3)\mu_{c0}\ \rho_{00}(t_0), \tag{2.85}
$$

and

$$
R_4(t_3,t_2,t_1) = \sum_{a,b,c,d} \mu_{0c}(t_1+t_2+t_3)\mu_{ba}(t_1+t_2)\mu_{a0}(t_1)\mu_{bc}\ \rho_{00}(t_0). \tag{2.86}
$$

Chapter 3

Numerical Methods

3.1 Numerics on a Grid

3.1.1 Discretization in Coordinate Space

Regarding a spatial coordinate $r \in \mathbb{R}$ with $r \in [r_0; r_{end}]$, one defines the increment

$$dr = \frac{(r_{end} - r_0)}{n_g - 1}, \tag{3.1}$$

where $n_g \in \mathbb{N}$ is the number of sampling points. Discrete values of the coordinate are given as:

$$r_n = dr \cdot (n - 1) + r_0, \tag{3.2}$$

with $n \in [1; n_g]$. Any function is represented by its values at the grid points r_n. For example, a wave function then assumes the discrete values $\Psi_n(r_n)$. The extension to several spatial degrees of freedom is straight-forward [82].

3.1.2 Discretization in Momentum Space

Discretizing the coordinate space wave function at $(n_g - 1)$ sampling points, the momentum wave function representation is [34]:

$$\Psi(k_j) = \frac{1}{2\pi n_g} \sum_{m=0}^{n_g-1} \Psi(r_m) e^{-ik_j r_m}. \tag{3.3}$$

The momentum increment is [82]:

$$dk = \frac{k_+ - k_-}{n_g - 1}, \tag{3.4}$$

where $k_+ \in \mathbb{R}$ is the maximal momentum in positive direction, and $k_- \in \mathbb{R}$ is the maximal momentum in negative direction. Due to the periodicity of momentum space, the maximal momentum component is given as:

$$k_+ = \underbrace{\frac{\pi}{dr}}_{k_{max}} - dk, \tag{3.5}$$

and the maximal momentum in negative direction is given as:

$$k_- = \underbrace{-\frac{\pi}{dr}}_{-k_{max}} . \tag{3.6}$$

Inserting these two relations in eq. (3.4), yields for the incremental momentum expression:

$$dk = \frac{2\pi}{dr\, n_g}. \tag{3.7}$$

Finally, one can symmetrically span the discretized momentum space in the following form [65]:

$$k_n = \begin{cases} (n-1)\frac{2\pi}{n_g dr} & , \text{if } n = 1, 2, \ldots, \frac{n_g}{2} + 1 \\ -(n_g + 1 - n)\frac{2\pi}{n_g dr} & , \text{if } n = \frac{n_g}{2} + 2, \ldots, n_g \ . \end{cases} \tag{3.8}$$

3.2 Short-Time Propagator

In section 2.5, the formal solution of the time-dependent Schrödinger equation with time-independent hamiltonian has already been encountered, where the time-evolution depends on the propagator $U(r, t, t_0)$:

$$\hat{U}(r, t, t_0) = e^{-i\hat{H}(r)\cdot(t-t_0)}. \tag{3.9}$$

In order to numerically evaluate this expression, a discretization of the time-coordinate is needed, where one uses a time-incremet of $\Delta t \in \mathbb{R}$.

$$\Delta t = \frac{t - t_0}{N}. \tag{3.10}$$

$N \in \mathbb{N}$ is the total number of time-steps. With this incremental description one can formulate the short-time propagator in exponential form [83]:

$$\hat{U}\left(r, t_0 + \Delta t, t_0\right) = e^{-i\hat{H}(r)\Delta t}. \tag{3.11}$$

Consequently, the expression for eq. (3.9) is:

$$\hat{U}(r, t, t_0) = \hat{U}\left(r, t_0 + N(\Delta t), t_0\right) = \prod_{j=1}^{N} e^{-i\hat{H}(r)\Delta t}. \tag{3.12}$$

3.3 Split-Operator Method

The short-time propagation scheme mentioned above is used. For this numerical method, one has to evaluate the following expression for the system's short-time propagator $\hat{U}\left(r, t_0 + N(\Delta t), t_0\right)$ approximately [84, 85]:

$$|\Psi(r, t + \Delta t)\rangle = e^{-i\hat{H}(r)\Delta t}|\Psi(r, t)\rangle. \tag{3.13}$$

The hamiltonian $\hat{H}(r)$ has derivatives of r, as has already been seen in previous chapters. A straight-forward numerical evaluation of these derivatives in spatial representation is not recommended.

The key is to evaluate the derivative components of the hamiltonian in the momentum space. There, they appear as multiplicatives of the momentum coordinate k. So, the challenge is to split up $\hat{H}(r)$ into a propagation scheme that allows to switch between coordinate space representation and momentum space representation.

This form is known from section 2.4.2, and one can proceed with a splitting into a kinetic and a potential part of the hamiltonian:

$$\hat{H} = \hat{T} + \hat{V}. \tag{3.14}$$

Then in a straight-forward scheme one would evaluate the following expression for the short-time propagator:

$$e^{-i\hat{H}\Delta t} = e^{-i\hat{T}\Delta t}e^{-i\hat{V}\Delta t}; \tag{3.15}$$

then the expression for a short-time propagation of the wave function is:

$$|\Psi(r, t + \Delta t)\rangle = \mathfrak{F}^{-1}\ e^{-i\hat{T}(k)(\Delta t)}\ \mathfrak{F}\ \left\{e^{-i\hat{V}(r)(\Delta t)}|\Psi(r, t)\rangle\right\}, \tag{3.16}$$

where the discrete Fourier transform $\mathfrak{F}$ [86] is used to switch between space and momentum representation.

Note that eq. (3.15) is not correct because $[\hat{T}, \hat{V}] \neq 0$.

The split-operator technique aims at reducing the error produced by the non-commutivity of the kinetic energy operator and potential energy operator.

Given two arbitrary operators $\hat{A}$ and $\hat{B}$ which do not commute, the product of

exponents containing $\hat{A}$ and $\hat{B}$ is:

$$\exp\hat{A}\exp\hat{B} = \mathbb{1} + \hat{A} + \hat{B} + \frac{\hat{A}^2 + 2\hat{A}\hat{B} + \hat{B}^2}{2} + \dots \ . \tag{3.17}$$

This, however, is not the same expression in second order as one obtains for:

$$\exp\left[\hat{A} + \hat{B}\right] = \mathbb{1} + \hat{A} + \hat{B} + \frac{\hat{A}^2 + \hat{A}\hat{B} + \hat{B}\hat{A} + \hat{B}^2}{2} + \dots \ . \tag{3.18}$$

Therefore, one uses the following splitting. Here, derivations appear in the second order term already:

$$\begin{aligned}\exp\frac{\hat{A}}{2}\exp\hat{B}\exp\frac{\hat{A}}{2} =& \mathbb{1} + \frac{\hat{A}}{2} + \frac{\hat{A}^2}{4} + \hat{B} + \frac{\hat{B}\hat{A}}{2} + \dots + \frac{\hat{B}^2}{2} \\ &+ \dots + \frac{\hat{A}}{2} + \frac{\hat{A}^2}{4} + \dots + \frac{\hat{A}\hat{B}}{2} + \dots \ .\end{aligned} \tag{3.19}$$

Thus, this splitting reproduces $e^{\hat{A}+\hat{B}}$ correctly up to second order. Using the splitting, the time-evolution of the wave function is now:

$$|\Psi(r, t+\Delta t)\rangle = e^{-i\frac{\hat{V}(r)}{2}(\Delta t)}\ \mathfrak{F}^{-1}\ e^{-i\hat{T}(k)(\Delta t)}\ \mathfrak{F}\ \left\{e^{-i\frac{\hat{V}(r)}{2}(\Delta t)}|\Psi(r,t)\rangle\right\}. \tag{3.20}$$

For small time-steps Δt in the propagation scheme, one can neglegt the contributions of third and higher order.

3.4 Coupled Propagation

The split-operator method can also be applied for the propagation of coupled systems. Regarding, for example, a two-state problem with nuclear coordinate $R \in \mathbb{R}$ in the diabatic representation, where the hamiltonian is of the following form:

$$\begin{pmatrix} -\frac{1}{2M}\nabla_R^2 + \tilde{u}_{00}(R,\underline{R}) & \tilde{u}_{01}(R,\underline{R}) \\ \tilde{u}_{10}(R,\underline{R}) & -\frac{1}{2M}\nabla_R^2 + \tilde{u}_{11}(R,\underline{R}) \end{pmatrix}. \tag{3.21}$$

Due to the coupling $\tilde{u}_{01}(R,\underline{R}) = \tilde{u}_{10}(R,\underline{R})$ the potential energy operator is not diagonal but the exponential operator containing the potential can be written as:

$$e^{-i\hat{V}\Delta t} = \exp\left\{ \underbrace{\begin{pmatrix} -i\tilde{u}_{00}(R,\underline{R})\Delta t & 0 \\ 0 & -i\tilde{u}_{11}(R,\underline{R})\Delta t \end{pmatrix}}_{-i\hat{\tilde{V}}\Delta t} + \underbrace{\begin{pmatrix} 0 & -i\tilde{u}_{01}(R,\underline{R})\Delta t \\ -i\tilde{u}_{01}(R,\underline{R})\Delta t & 0 \end{pmatrix}}_{-i\hat{W}\Delta t} \right\}. \tag{3.22}$$

The term $e^{-i\hat{W}\Delta t}$ can be evaluated as follows:

$$\begin{aligned} e^{-i\hat{W}\Delta t} &= \exp\begin{pmatrix} 0 & -i\tilde{u}_{01}(R,\underline{R})\Delta t \\ -i\tilde{u}_{01}(R,\underline{R})\Delta t & 0 \end{pmatrix} \\ &= \sum_{n=0}^{\infty} \frac{(-i\Delta t)^n}{n!}\hat{W}^n \\ &= \sum_{n=0}^{\infty} \frac{(-1)^n(\Delta t)^{2n}}{2n!}\tilde{u}_{01}(R,\underline{R})^{2n}\mathbb{1} \\ &\quad - i\sum_{n=0}^{\infty} \frac{(-1)^n(\Delta t)^{2n+1}}{(2n+1)!}\tilde{u}_{01}(R,\underline{R})^{2n+1}\begin{pmatrix} 0 & 1 \\ 1 & 0 \end{pmatrix} \\ &= \begin{pmatrix} \cos\left(\tilde{u}_{01}(R,\underline{R})\Delta t\right) & -i\sin\left(\tilde{u}_{01}(R,\underline{R})\Delta t\right) \\ -i\sin\left(\tilde{u}_{01}(R,\underline{R})\Delta t\right) & \cos\left(\tilde{u}_{01}(R,\underline{R})\Delta t\right) \end{pmatrix}. \end{aligned} \tag{3.23}$$

According to split-operator technique, the extended propagation scheme is:

$$\begin{pmatrix} |\tilde{\chi}_1(R,t+\Delta t)\rangle \\ |\tilde{\chi}_0(R,t+\Delta t)\rangle \end{pmatrix} = e^{-i\frac{\hat{W}(R,\underline{R})}{4}(\Delta t)} e^{-i\frac{\hat{\tilde{V}}(R,\underline{R})}{2}(\Delta t)} e^{-i\frac{\hat{W}(R,\underline{R})}{4}(\Delta t)} \mathfrak{F}^{-1} \; e^{-i\hat{T}(k)(\Delta t)} \times$$
$$\mathfrak{F} \left\{ e^{-i\frac{\hat{W}(R,\underline{R})}{4}(\Delta t)} e^{-i\frac{\hat{\tilde{V}}(R,\underline{R})}{2}(\Delta t)} e^{-i\frac{\hat{W}(R,\underline{R})}{4}(\Delta t)} \begin{pmatrix} |\tilde{\chi}_1(R,t)\rangle \\ |\tilde{\chi}_0(R,t)\rangle \end{pmatrix} \right\}. \tag{3.24}$$

3.5 Using Short-Time Propagation for Time-Dependent Perturbation Theory

Time-dependent perturbation theory is used to describe multi-photon processes. The Δt incremental time-evolution of a perturbed wave function $|\Psi(r,t)\rangle$ in a system hamiltonian of the form $\hat{H}(r,t) = \hat{H}_0(r) + \hat{W}(t)$ with the time-dependent interaction $\hat{W}(t)$ and the unperturbed system hamiltonian $\hat{H}_0(r)$, can be described by [27, 64]:

$$|\Psi(r,t)\rangle_I = |\Psi(r,t_0)\rangle_I - i\int_{t_0}^{t} dt' \hat{W}_I(t') |\Psi(r,t')\rangle_I, \tag{3.25}$$

where $\hat{W}_I(t')$ is the time-dependent interaction and $|\Psi(r,t)\rangle_I$ is the wave function in the interaction picture. A transformation to the Schrödinger picture and a description in incremental time-steps leads to:

$$\begin{aligned} |\Psi(r,t+\Delta t)\rangle = & e^{-i\hat{H}_0(r)\Delta t} |\Psi(r,t)\rangle \\ & - i\int_{t}^{t+\Delta t} dt' e^{-i\hat{H}_0(r)(t+\Delta t-t')} \hat{W}(t') |\Psi(r,t')\rangle. \end{aligned} \tag{3.26}$$

The time-increment Δt is adjusted to the short-time propagation time-step. As far as this incremental step is short, one can approximate the integral expression

by a left Rieman sum:

$$|\Psi(r,t+\Delta t)\rangle = e^{-i\hat{H}_0(r)\Delta t}|\Psi(r,t)\rangle - i(\Delta t)\hat{W}(t+\Delta t)|\Psi(r,t+\Delta t)\rangle. \tag{3.27}$$

This recursive equation is evaluated iteratively. Starting from a temporal unperturbed system, one can define this as $|\Psi^{(0)}(r,t)\rangle$ which means zeroth-order perturbed wave function. Higher orders of perturbation are then obtained by iteratively applying eq. (3.27). So for the nth-order, one uses the expression [87, 88]:

$$\begin{aligned}|\Psi^{(n)}(r,t+\Delta t)\rangle =& e^{-i\hat{H}_0(r)\Delta t}|\Psi^{(n)}(r,t)\rangle \\ & - i(\Delta t)\hat{W}(t+\Delta t)|\Psi^{(n-1)}(r,t+\Delta t)\rangle.\end{aligned} \tag{3.28}$$

3.6 Imaginary-Time Propagation

In section 2.4.2, the solution of the stationary Schrödinger equation was discussed. Here a numerical method for the determination of the eigenfunctions of the hamiltonian $\hat{H}(\vec{r},\vec{R})$ with screened Coulomb potentials, is given [38].
Remembering the short-time evolution of an arbitrary wave function $|\psi(\vec{r},\vec{R},t)\rangle \in \mathfrak{H}$ from previous sections,

$$|\psi(\vec{r},\vec{R},t+dt)\rangle = e^{-i\hat{H}(\vec{r},\vec{R})dt}|\psi(\vec{r},\vec{R},t)\rangle, \tag{3.29}$$

a substitution of $dt = -id\tau$ leads to:

$$|\psi(\vec{r},\vec{R},\tau+d\tau)\rangle = |\psi(\vec{r},\vec{R},\tau)\rangle\ e^{-\hat{H}(\vec{r},\vec{R})d\tau}, \tag{3.30}$$

which is the imaginary-time evolution of the wave function. Expanding the wave function in terms of the eigenfunctions of the hamiltonian leads to:

$$|\psi(\vec{r},\vec{R},\tau+d\tau)\rangle = \sum_n e^{-E_n d\tau} c_n(\tau)|\varphi_n(\vec{r},\vec{R})\rangle. \tag{3.31}$$

Thus, different terms are exponentially damped differently. As far as the ground state has the lowest eigenenergy, this is the only state which is left after the eigenenergy has converged. The duration of the imaginary propagation is specified via a threshold energy, which is the energy difference between two imaginary-time steps because the wave function's energy at time τ, is given by:

$$E(\tau) = -\frac{1}{2\ d\tau} \ln\left(\frac{\langle\psi(\vec{r},\vec{R},\tau+d\tau)\,|\,\psi(\vec{r},\vec{R},\tau+d\tau)\rangle_{\vec{r},\vec{R}}}{\langle\psi(\vec{r},\vec{R},\tau)\,|\,\psi(\vec{r},\vec{R},\tau)\rangle_{\vec{r},\vec{R}}}\right). \tag{3.32}$$

For long times one converges to the ground state energy for an initial wave function which should contain all relevant symmetries and should at least contain the ground state.

$$\lim_{\tau\to\infty} E(\tau) = E_0. \tag{3.33}$$

It should be noticed that because the imaginary time-evolution is not norm conserving, thus, one is forced to renormalize the wave function after each imaginary-time step. Higher eigenfunctions can be obtained by projecting out lower eigenfunctions $|\varphi_n(\vec{r},\vec{R})\rangle$ already found during the damping procedure.

$$|\varphi_m(\vec{r},\vec{R})\rangle = \lim_{\tau\to\infty}\left\{|\psi(\vec{r},\vec{R},\tau)\rangle - \sum_{n=1}^{m-1}\langle\varphi_n(\vec{r},\vec{R})\,|\,\psi(\vec{r},\vec{R},\tau)\rangle|\varphi_n(\vec{r},\vec{R})\rangle\right\}. \tag{3.34}$$

3.7 Velocity Verlet Algorithm

In section 2.6, classical trajectories were introduced. These trajectories are propagated numerically by the Velocity Verlet Algorithm [89, 90]. According to the classical Newtonian equations of motion, the spatial coordinate can be obtained for a small time-step Δt by:

$$x(t + \Delta t) = x(t) + v(t)\Delta t + \frac{1}{2}(\Delta t)^2 a(t), \tag{3.35}$$

where the trajectories velocity at time t is given as $v(t)$. The acceleration $a(t)$ also determines the spatial coordinate. Parallelly, the velocity is obtained by the acceleration:

$$v(t + \Delta t) = v(t) + \frac{a(t) + a(t + \Delta t)}{2}\Delta t. \tag{3.36}$$

Chapter 4

Adiabatic and Non-Adiabatic Dynamics within the Shin-Metiu Model

The one-dimensional Shin-Metiu model has been used to characterize non-adiabatic quantum dynamics [21, 22]. With the help of this model, coupled and uncoupled electron-nuclear wave-packet motion was investigated [91]. Kinetic coupling elements were calculated, and their impact on the quantum dynamical properties of the system in the weak and strong coupling case was examined. In additional studies, the case of an intermediate coupling case was considered. The dynamical properties were characterized by photoelectron spectra documenting that this observable is able to monitor coupled electron-nuclear dynamics [66, 92, 93].

Based on this work, the investigation of the Shin-Metiu model is continued here in order to identify the basics of coupled electron-nuclear motion. The coupling strongly influences the spectral properties of the system [91]. Therefore, in the following the eigenfunctions in the weak coupling case are compared to the eigenfunctions in the strong coupling case. On the gathered indications of an alternative state representation, a diabatization is performed in the case of strong non-adiabatic coupling. After this, two-dimensional spectroscopy, which is known

to reveal coupled dynamics [67], is used to further distinguish the two different coupling cases. Furthermore, a comparison of classical and quantum dynamics will be presented. Finally, the electron flux within the weak coupling case is examined.

4.1 The One-Dimensional Shin-Metiu Model

The particle configuration of the Shin-Metiu model [21, 22] is depicted in fig. 4-1. It is a H_3^{2+} system and consists of two fixed protons, a mobile proton and a mobile electron. The coordinate of the mobile proton is denoted as R_x, and the coordinate of the electron is denoted as x. Both are able to move in one dimension.

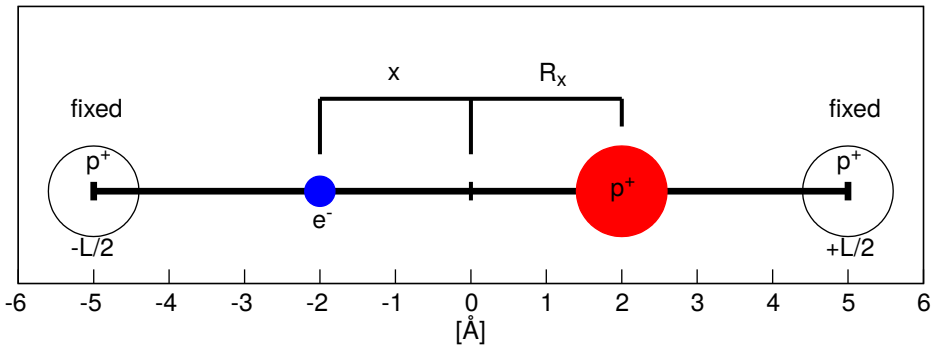

Figure 4-1: **One-Dimensional Shin-Metiu Model**. The model consists of two fixed protons (p^+) on the left and the right at $-\frac{L}{2} = -5.0$ Å and $\frac{L}{2} = 5.0$ Å. The two internal degrees of freedom are defined by x and R_x for the electron and the mobile-proton coordinate.

This model describes a one-dimensional quantum system with two internal degrees of freedom (x,R_x). The model hamiltonian $\hat{H}(x, R_x)$ is given by:

$$\hat{H}(x, R_x) = -\frac{1}{2M}\frac{\partial^2}{\partial R_x^2} - \frac{1}{2}\frac{\partial^2}{\partial x^2} + \hat{V}(x, R_x), \tag{4.1}$$

with the proton mass M and

$$\hat{V}(x,R_x) = +\frac{1}{\left|\frac{L}{2}-R_x\right|}+\frac{1}{\left|\frac{L}{2}+R_x\right|}-\frac{\operatorname{erf}\left(\frac{|L/2-x|}{R_f}\right)}{\left|\frac{L}{2}-x\right|}-\frac{\operatorname{erf}\left(\frac{|L/2+x|}{R_f}\right)}{\left|\frac{L}{2}+x\right|} - \frac{\operatorname{erf}\left(\frac{|R_x-x|}{R_c}\right)}{|R_x-x|}+E_{off}. \tag{4.2}$$

This hamiltonian consists of the kinetic operators for the mobile proton and the electron and screened and unscreened Coulomb-interactions between the particles. The screened Coulomb potentials [41, 42] are of the form $V^{\pm}(q)$:

$$V^{\pm}(q) = \pm\frac{\operatorname{erf}\left(\frac{|q|}{A}\right)}{|q|}, \tag{4.3}$$

where q is an arbitrary one-dimensional coordinate, and A is an arbitrary shielding parameter. The sign of the expression determines whether the potential is attractive $(-)$ or repulsive $(+)$. These potentials have the property to screen the attraction between the electron and the protons which can be followed in fig. 4-2.

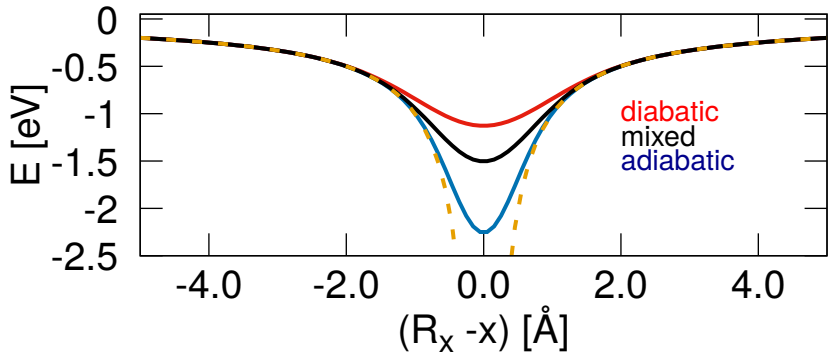

Figure 4-2: **Screened Coulomb Potentials**. Three different screened Coulomb potentials are schematically sketched. A Coulomb potential is indicated by the dashed yellow curve.

The screening parameter R_f controls the attraction between the fixed protons, at $-\frac{L}{2} = -5.0$ Å and $\frac{L}{2} = 5.0$ Å, and the electron; at the same time R_c controls the

attraction between the electron and the mobile proton. The energy E_{off} shifts the minimum of the potential to the origin of the energy scale and has a value of 11.58 eV in the weak coupling case and 10.01 eV in the strong coupling case.

The model parameters are summarized in table 4.1. It is distinguished between the weak coupling case with $R_c = 1.5$ Å and strong coupling case with $R_c = 2.5$ Å. For the particle distances and the shielding parameters, the units are changed to Å. For the energy, the unit is set to eV.

Table 4.1: **Model Parameters.**

symbol:	description:	value
$[R_{x_{min}}; R_{x_{max}}] \in \mathbb{R}$	range in R_x-space	[-6;6]Å
$[x_{min}; x_{max}] \in \mathbb{R}$	range in x-space	[-50;50]Å
$N_R \in \mathbb{N}$	grid points in R_x-direction (p^+)	256
$N_x \in \mathbb{N}$	grid points in x-direction (e^-)	256
$M \in \mathbb{R}$	proton mass	1836.15 a.u.
$\delta\tau \in \mathbb{R}$	time-step ITP	0.5 a.u.
$R_f \in \mathbb{R}$	shielding: e^- and p^+_{fixed}	1.5 Å

For the two coupling cases, the potential $V(x, R_x)$ is depicted in fig. 4-3. In the left panel the potential for the weak coupling case is given as a contour plot. Characteristic for this potential are two minima which are connected by a reaction path along the diagonal of the coordinate axes where the reaction path exhibits a small barrier. The potential for the strong coupling case is depicted in the right panel of fig. 4-3 and exhibits two separate minima being elongated parallely to the R_x-axis.

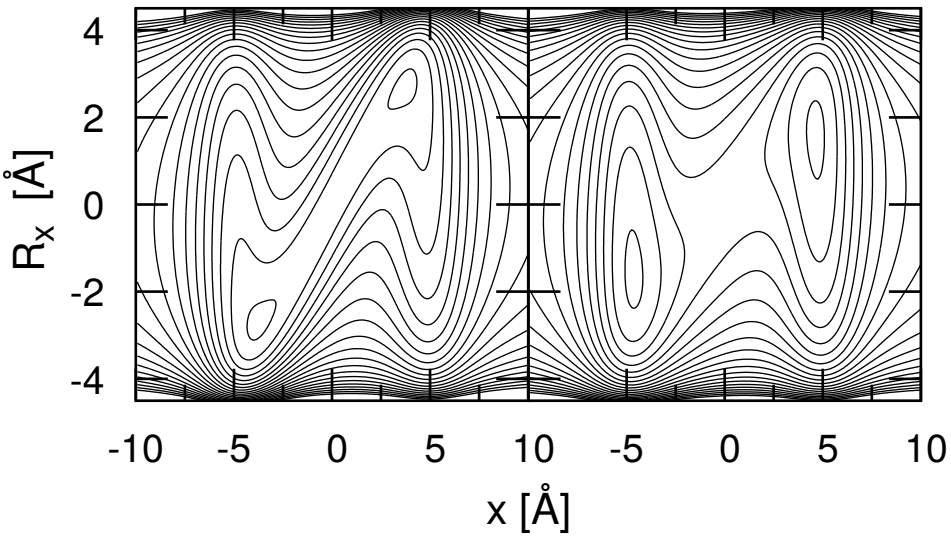

Figure 4-3: **Potential for the Weak and Strong Coupling Case**. The potential $V(x, R_x)$ exhibits for the weak coupling two minima at approximately ($x = -3.5$, $R_x = -2.5$) Å and ($x = +3.5$, $R_x = +2.5$) Å and a diagonally elongated valley connecting both minima. In case of strong coupling, the two minima are approximately at ($x = -4.5$, $R_x = -1.8$) Å and ($x = +4.5$, $R_x = +1.8$) Å. The two minima are further apart from each other compared to the weak coupling case [91]. Energetically, the lines are separated by 0.05 eV. The first line corresponds to a value of 0.01 eV.

4.2 Eigenfunctions

The eigenfunctions are regarded for weak and strong coupling. In what follows the eigenfunctions are obtained by first regarding the adiabatic eigenfunctions and the corresponding adiabatic potentials. This aspect has already been investigated by M. Erdmann and M. Falge [66, 91], but it is shortly given here for clarity and completeness in order to justify the results of the exact eigenfunctions.

4.2.1 Weak Coupling

4.2.1.1 Adiabatic Electronic Eigenfunctions in the Weak Coupling Case

For this study, the adiabatic representation in section 2.4.2.1 is applied. First, the solutions of the electronic Schrödinger equation are regarded. Solving the electronic Schrödinger equation

$$\left[-\frac{1}{2}\frac{d^2}{dx^2} + \hat{V}(x, R_x)\right] |\phi_n(x; R_x)\rangle = u_{nn}(R_x)|\phi_n(x; R_x)\rangle, \tag{4.4}$$

real adiabatic electronic eigenfunctions $|\phi_n(x; R_x)\rangle$ are obtained which are parametrically dependent on R_x.

The first two adiabatic electronic eigenfunctions $|\phi_n(x; R_x)\rangle$ with $n = 0, 1$ are shown in fig. 4-4.

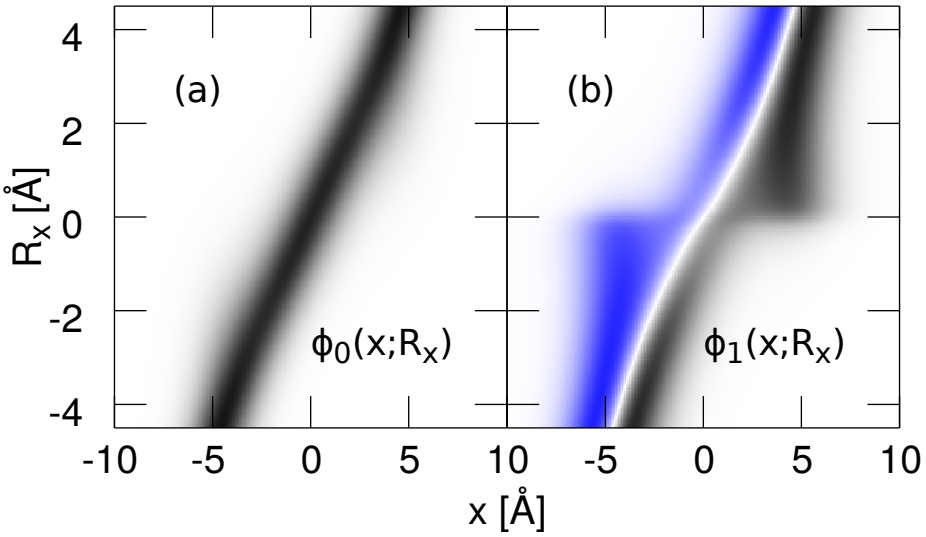

Figure 4-4: **Adiabatic Electronic Eigenfunctions of the Weak Coupling Case**. (a) corresponds to the adiabatic ground state and (b) is the adiabatic first excited state. The black color shows positive values, and the blue color shows negative values of the wave function.

In the left panel, the ground state adiabatic electronic eigenfunction is depicted.

It has no nodal structure in x and evolves almost constantly in shape along the nuclear coordinate R_x. Additionally, the localization of the electronic wave function moves diagonally, along the R_x parameter, from negative to positive values of x. This describes the shift of the electron probability density with the displacement of the proton and suggests the non-adiabatic coupling elements (NACTs) from the adiabatic electronic ground state $|\phi_0(x; R_x)\rangle$ to other adiabatic states $|\phi_n(x; R_x)\rangle$ to be small. As a result, the ground state decouples from the other adiabatic electronic excited states.

The first excited state $|\phi_1(x; R_x)\rangle$ has a clear nodal structure along the x-coordinate. In R_x-direction, changes in the shape of the electronic eigenfunction are seen, indicating that this adiabtic electronic eigenfunction is coupled to the next higher adiabatic state.

Here, in the following, only the two lowest adiabatic electronic states with $n = 0, 1$ are regarded. An arrangement of the corresponding adiabatic potentials $u_{00}(R_x)$ and $u_{11}(R_x)$ is given in fig. 4-5.

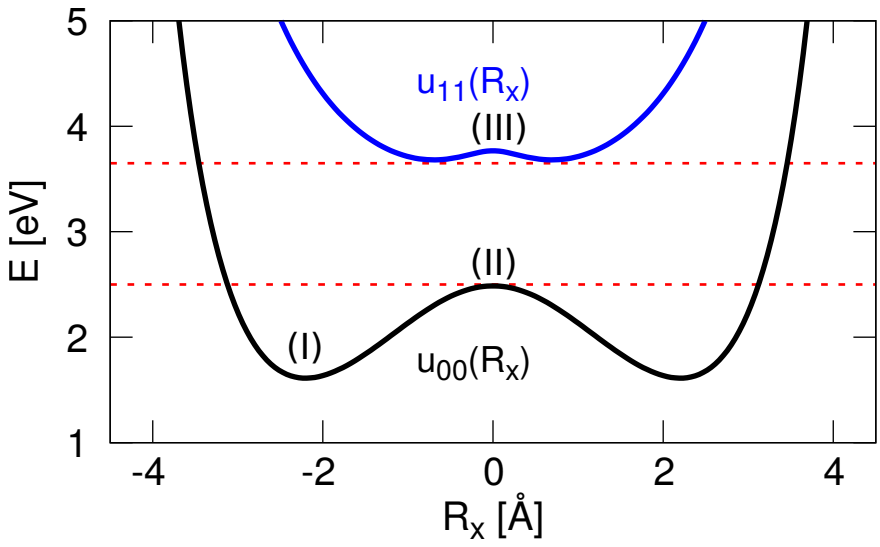

Figure 4-5: **Adiabatic Potentials - Weak Coupling Case**. The black curve represents the adiabatic electronic ground state, and the blue curve represents the adiabatic electronic excited state. (I), (II) and (III) mark the energetic regions where the character of the nuclear component of the exact eigenfunctions changes.

The energetic difference between $u_{00}(R_x)$ and $u_{11}(R_x)$ exemplifies that these electronic eigenfunctions are weakly coupled to each other, see here the following equation for the non-adiabatic coupling element [94]:

$$\tau_{10}(R_x) = \frac{\langle \phi_1(x;R_x) \,|\, \nabla_{R_x} \hat{H}_{el}(x;R_x) \,|\, \phi_0(x;R_x) \rangle}{|u_{11}(R_x) - u_{00}(R_x)|}. \tag{4.5}$$

This theorem suggests, for energetically well separated adiabatic electronic eigenstates, the denominator of eq. (4.5) to become large, and the coupling elements to become accordingly small.

Besides eq. (4.5), the NACTs can be explicitly calculated. They are shown in fig. 4-6. These non-adiabatic coupling elements are indeed small in contrast to the strong coupling case, which is discussed in the next section. These findings confirm eq. (4.5).

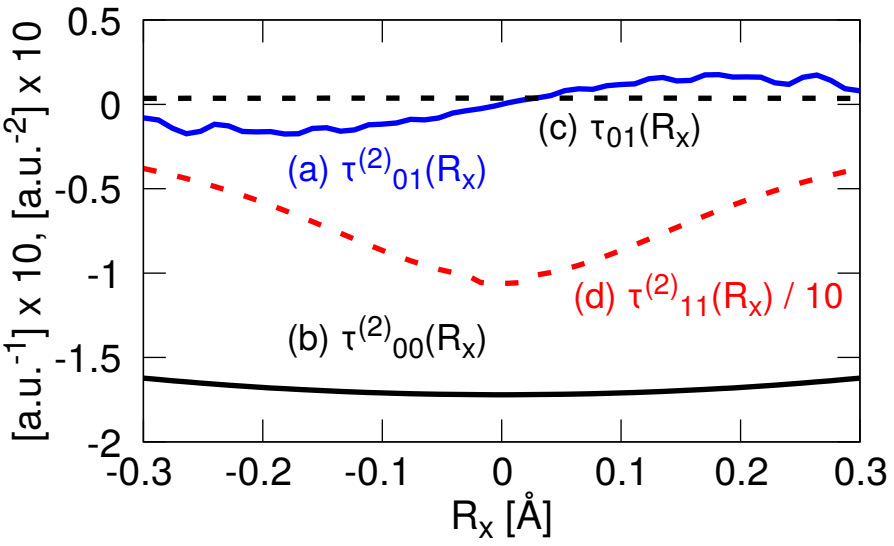

Figure 4-6: **Non-Adiabatic Coupling Elements of the Weak Coupling Case**. Depicted are the non-adiabatic coupling elements which are negligible as they take up only small values compared to the strong coupling case which will be seen later on. Note that curve (d) is divided by a factor of 10.

The total hamiltonian $\hat{H}(x, R_x)$ can be written in the adiabatic representation [39]:

$$\hat{H}_{nn,adi}(R_x;R_x) = \langle \phi_n(x;R_x) \,|\, \hat{H}(x,R_x) \,|\, \phi_n(x;R_x) \rangle_x. \tag{4.6}$$

Writing the hamiltonian of the subsystem in the adiabtic representation of the two adiabatic electronic eigenstates $|\phi_n(x;R_x)\rangle$, with $n = 0, 1$, yields:

$$\begin{pmatrix} \hat{H}_{00,adi}(R_x;R_x) & \hat{H}_{01,adi}(R_x;R_x) \\ \hat{H}_{10,adi}(R_x;R_x) & \hat{H}_{11,adi}(R_x;R_x) \end{pmatrix} = \\ \begin{pmatrix} \frac{1}{2M}(\tau^{(2)}_{00}(R_x) - \nabla^2_{R_x}) + u_{00}(R_x) & \frac{1}{2M}\tau^{(2)}_{01}(R_x) + \frac{1}{M}\tau_{01}\nabla_{R_x} \\ \frac{1}{2M}\tau^{(2)}_{10}(R_x) + \frac{1}{M}\tau_{10}\nabla_{R_x} & \frac{1}{2M}(\tau^{(2)}_{11}(R_x) - \nabla^2_{R_x}) + u_{11}(R_x) \end{pmatrix}. \tag{4.7}$$

Neglecting the kinetic-coupling elements $\tau^{(2)}_{nn}(R_x)$, $\tau^{(2)}_{nm}(R_x)$ and $\tau_{nm}(R_x)$ with $n, m = 0, 1$, yields:

$$\begin{pmatrix} -\frac{1}{2M}\nabla^2_{R_x} + u_{00}(R_x) & 0 \\ 0 & -\frac{1}{2M}\nabla^2_{R_x} + u_{11}(R_x) \end{pmatrix} \begin{pmatrix} |\chi_0(R_x)\rangle \\ |\chi_1(R_x)\rangle \end{pmatrix} = \\ \begin{pmatrix} E & 0 \\ 0 & E \end{pmatrix} \begin{pmatrix} |\chi_0(R_x)\rangle \\ |\chi_1(R_x)\rangle \end{pmatrix}. \tag{4.8}$$

In this case, the Born-Oppenheimer adiabatic approximation [43, 44] is valid for treating the ground state as a subsystem. For the adiabatic electronic ground state, the time-independent Schrödinger equation can be approximated as:

$$\left[-\frac{1}{2M}\nabla^2_{R_x} + u_{00}(R_x) \right] |\chi_0(R_x)\rangle = E|\chi_0(R_x)\rangle, \tag{4.9}$$

and the adiabatic first excited state can be approximated as:

$$\left[-\frac{1}{2M}\nabla^2_{R_x} + u_{11}(R_x)\right]|\chi_1(R_x)\rangle = E|\chi_1(R_x)\rangle. \tag{4.10}$$

4.2.1.2 Eigenfunctions in the Weak Coupling Case

Regarding the division of the total hamiltonian in the adiabatic representation with the separation of the adiabatic ground state, eigenfunctions are expected which have a pure electronic character from either the adiabatic ground state or the adiabatic excited state. The eigenfunctions of three different energetic regions (I), (II) and (III), shown in the adiabatic potential in fig. 4-5, are studied. (I) as the energetic region of a double minimum potential, (II) as the energetic region above the double minimum barrier and finally (III) as the energetic region where a new electronic-eigenstate characteristic begins.

4.2.1.3 (I) - Double Minimum Potential

The adiabatic electronic ground state is weakly coupled to other electronic states, therefore, a specific quantum number for the electronic state is chosen. Taking the eigenfunctions in the adiabatic representation, the electronic quantum number for the electronic ground state is $n = 0$ and m is selected for the quantum number of nuclear wave function components:

$$|\psi_{0,m}(x, R_x)\rangle = |\phi_0(x; R_x)\rangle \cdot |\chi_{0,m}(R_x)\rangle. \tag{4.11}$$

The exact eigenfunctions for values of m are depicted in fig. 4-7, and the correspondent reference of quantum number and panels of the figure are found in table 4.2.

Table 4.2: **Nuclear Quantum Numbers for Exact Eigenfunctions.**

panel:	(a)	(b)	(c)	(d)	(e)	(f)	(g)	(h)	(i)
m:	0	1	2	3	4	5	6	7	8
$E_{0m}[eV]$:	1.649	1.649	1.721	1.721	1.793	1.793	1.863	1.863	1.933

In fig. 4-7 panel (a), the lowest vibrational and electronic ground state can be found with $n = 0$ and $m = 0$. There, the exact eigenfunction exhibits two amplitudes with opposite phase. The amplitudes appear at each minimum of the double minimum potential as expected, see fig. 4-3.

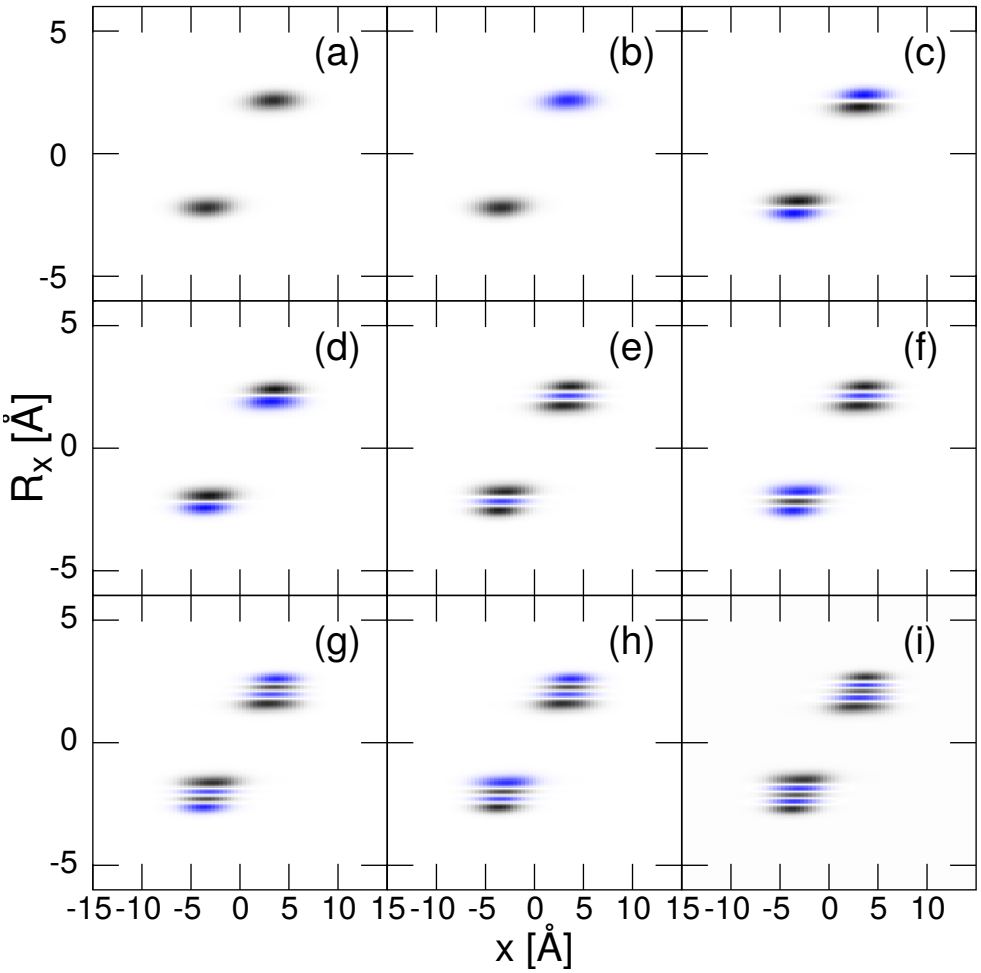

Figure 4-7: **Exact Eigenfunctions $|\psi_{nm}(x, R_x)\rangle$ for the Double Minimum Region (I)**. The black color shows positive values, and the blue color shows negative values of the wave function. Quantum numbers for the eigenfunctions are assigned in table 4.2.

For higher quantum numbers m, the extend of the wave function $|\psi_{0,m}(x, R_x)\rangle$ is diagonal in coordinate space. This is in accordance with the development of the adiabatic electronic ground state function $|\phi_0(x; R_x)\rangle$, thus, it is in accordance with the product ansatz eq. (4.11).

4.2.1.4 (II) - Above the Double Minimum Barrier

In fig. 4-8, the eigenfunctions in the energetic region of the transition from the double well to the region energetically above the barrier are depicted.

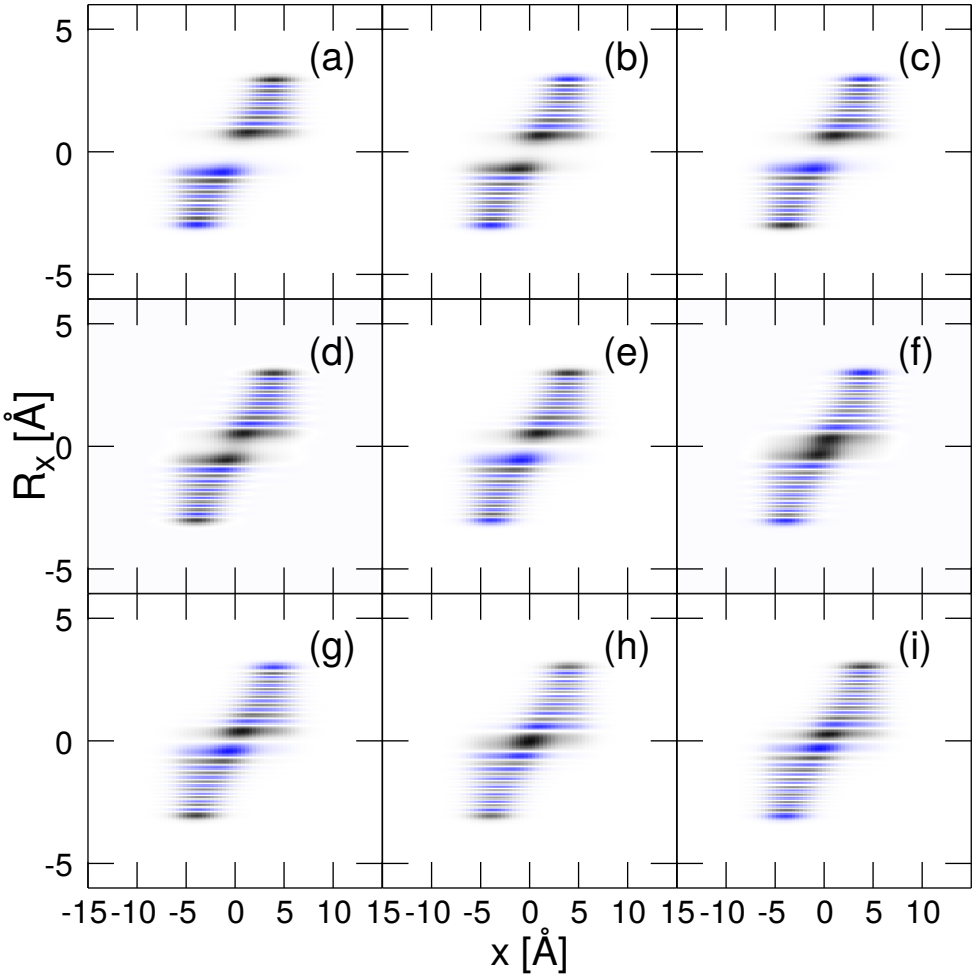

Figure 4-8: **Exact Eigenfunctions for the Energetic Region (II)**. The black color shows positive values, and the blue color shows negative values of the wave function. Quantum numbers for the eigenfunctions are assigned in table 4.3.

Table 4.3 includes the corresponding quantum number with $m = 29$ highlighted, as this corresponds to the exact eigenfunction, which is the first to be spread all over both minima of the potential (see fig. 4-3 left panel), connecting both minima.

Table 4.3: **Nuclear Quantum Numbers for Exact Eigenfunctions.**

panel:	(a)	(b)	(c)	(d)	(e)	(f)	(g)	(h)	(i)
m:	22	23	24	25	26	27	28	29	30
$E_{0m}[eV]$:	2.374	2.374	2.427	2.427	2.471	2.477	2.507	2.526	2.552

Reaching from $m = 22$ to $m = 28$, the twin peaks of the lower eigenfunctions are evolving towards each other and finally are connected to each other in case of $m = 29$. From this quantum number onwards, the eigenfunctions of the electronic ground state are spread over both minima.

4.2.1.5 Energetic Region (III)

As E_{0m} approaches the energetic region of the adiabatic potential $u_{11}(R_x)$ around 3.70 eV, one expects an influence on the eigenfunctions.

This can be seen by the eigenfunction $|\psi_{1,0}(x, R_x)\rangle$ in fig. 4-9 (b), which has an additional nodal structure along the x-coordinate and an eigenenergy of 3.708 eV. Simultaneously, the nodal structure of this eigenfunction in the R_x-coordinate repeats from the very first time with $m = 0$. Then, $|\psi_{1,0}(x, R_x)\rangle$ is the vibrational ground state of the first excited electronic state. From now on, the high-level excited vibrational states lie within the same energy range as the further excited vibrational states of the first excited electronic state. This can be seen by looking at the panels (e) to (i) in fig. 4-9.

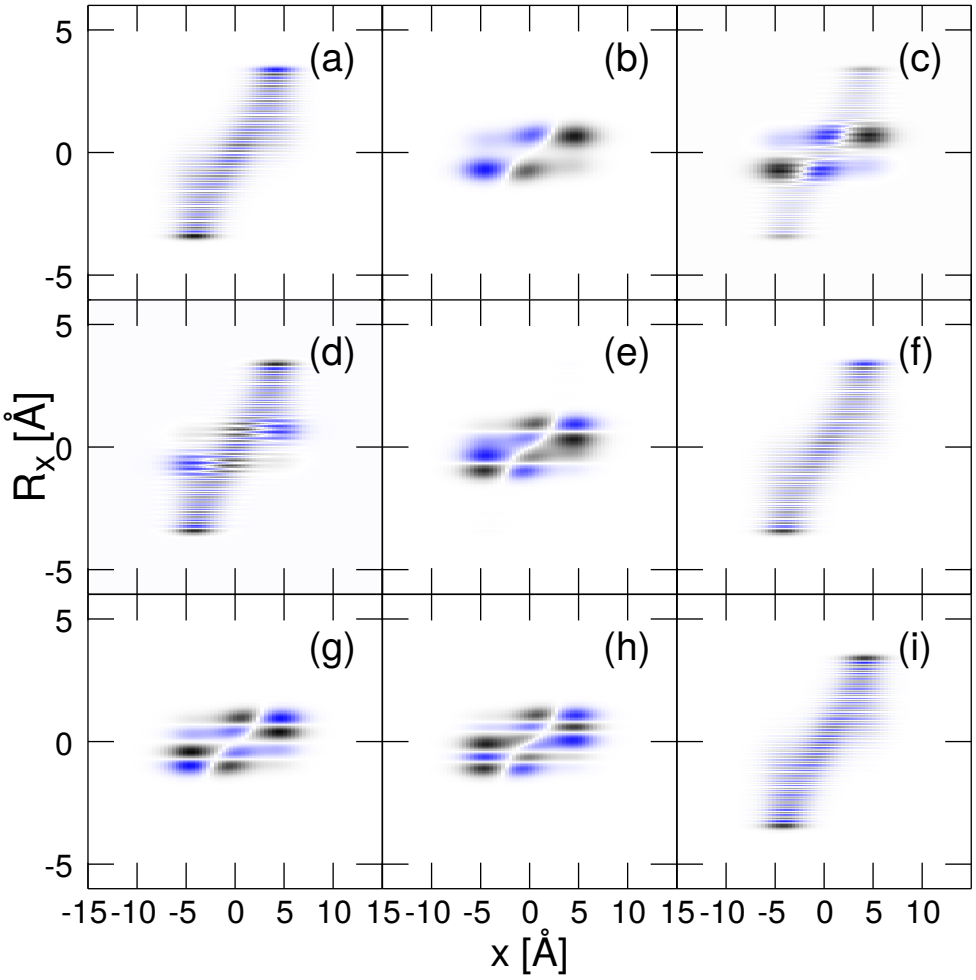

Figure 4-9: **Exact Eigenfunctions for First Excited Adiabatic Electronic Eigenstate in Region (III)**. The black color shows positive values, and the blue color shows negative values of the wave function. Quantum numbers for the eigenfunctions are assigned in table 4.4.

The assigned quantum numbers to the eigenfunctions in fig. 4-9 can be drawn from table 4.4

Table 4.4: **Nuclear Quantum Numbers for Exact Eigenfunctions.**

panel:	(a)	(b)	(c)	(d)	(e)	(f)	(g)	(h)	(i)
n:	0	1	mix	mix	1	0	1	1	0
m:	60	0	–	–	2	62	3	4	63
$E_{nm}[eV]$:	3.708	3.709	3.709	3.754	3.757	3.761	3.795	3.806	3.817

A special case is presented in panel (c) and (d) table 4.4. Both panels depict a superposition of eigenfunctions, which have clearly different electronic and vibrational character. This is due to non-adiabatic coupling elements, which are weak in this case study but still apparent in some manner. As a result quantum numbers can not be assigned in this case.

4.2.2 Strong Coupling

4.2.2.1 Adiabatic Electronic Eigenfunctions in the Strong Coupling Case

To realize the situation of a strong coupling case, the shielding parameter is set to $R_c = 2.5$ Å, which is larger than in the weak coupling case, where a value of $R_c = 1.5$ Å was used. This results in a decrease of the Coulomb interaction between the electron and the mobile proton. For consistency, all the other parameters are kept as in the weak coupling case, see table 4.1.

The first two adiabatic electronic eigenfunctions $|\phi_n(x; R_x)\rangle$ with $n = 0, 1$ are shown in fig. 4-10. There a schematic separation of the wave function into four areas (α),(β),(γ) and (δ) in coordinate space is made which serves to identify the different characteristic of the adiabtic wave function, see below.

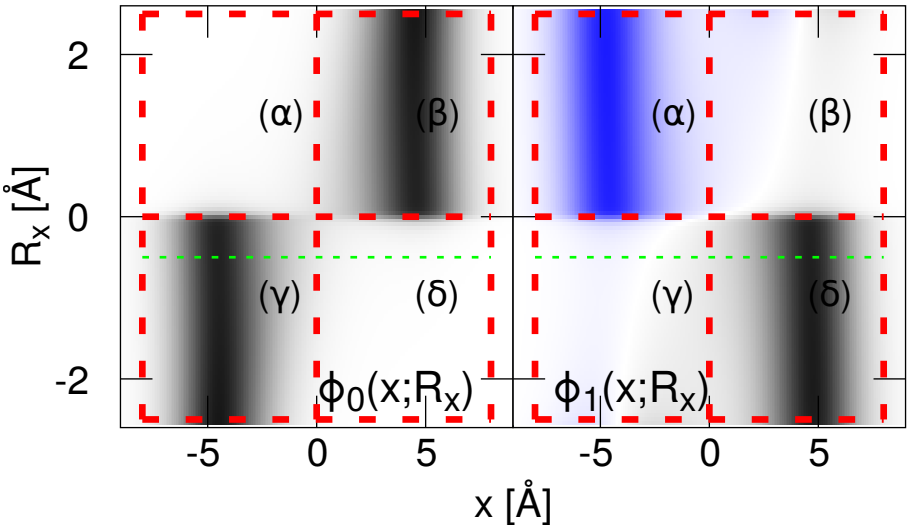

Figure 4-10: **Adiabatic Electronic Eigenfunctions of the Strong Coupling Case**. The left panel corresponds to the adiabatic electronic ground state, and the right panel is the adiabatic electronic first excited state. The black color shows positive values, and the blue color shows negative values of the wave function.

The first two adiabatic electronic eigenfunctions exhibit a structure different from the ones in the weak coupling case. Here, the adiabatic electronic ground state $|\phi_0(x;R_x)\rangle$ exhibits an abrupt change along the R_x-coordinate at its value of $R_x = 0.0$ Å. The same is seen in the adiabatic first excited state. This indicates that the two adiabatic electronic eigenfunctions are strongly coupled.

In the adiabatic ground state wave function, regarding the x-coordinate, this change separates the eigenfunction into two parts. One being unchanged upon variation of R_x in the region (β), in which the center of the electronic wave function is located at approximately $x = +5.0$ Å; the other part is unchanged in the region (γ), where the center of the electronic wave function is located at approximately $x = -5.0$ Å.

A similar separation is found in the first excited adiabatic electronic eigenfunction $|\phi_1(x;R_x)\rangle$ depicted in fig. 4-10, right panel. There are again two parts being separated by an abrupt change in the wave function. Region (δ), in which the center

of the electronic wave function is located at approximately $x = +5.0$ Å, and region (α), where the center of the electronic wave function is located at approximately $x = -5.0$ Å, but with a negative amplitude.

Regarding the adiabatic excited state $|\phi_1(x; R_x)\rangle$ region (α) is just the extension of the region (γ) in the adiabatic ground state $|\phi_0(x; R_x)\rangle$. The same can be said about the region (β) and (δ) in both eigenfunctions. This is an indication for another state representation in which the shape of the electronic eigenfunction is constant.

In what follows only the two lowest adiabatic electronic eigenstates $|\phi_n(x; R_x)\rangle$ are regarded, with $n = 0, 1$. The potential curves $u_{00}(R_x)$ and $u_{11}(R_x)$ are given in fig. 4-11. The vanishing energetic difference between $u_{00}(R_x)$ and $u_{11}(R_x)$ also indicates that the two adiabatic electronic eigenfunctions are strongly coupled with each other, see eq. (4.5).

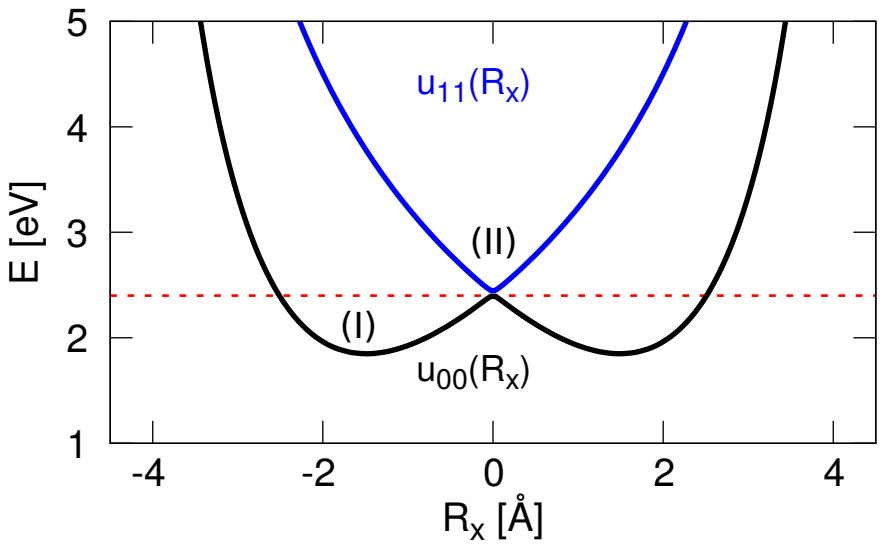

Figure 4-11: **Adiabatic Potentials - Strong Coupling Case**. The black curve represents the electronic ground state, and the blue curve represents the electronic excited state. (I) and (II) mark the energetic regions where the progression of the nuclear component of the exact eigenfunctions changes.

The two potentials exhibit an avoided crossing at $R_x = 0.0$ Å. Confirming eq. (4.5),

additionally the numerically calculated NACTs for the coupled case are depicted in fig. 4-12. Taking large values, they are localized at the origin of the coordinate system with $R_x = 0.0$ Å in an especially narrow interval around the avoided crossing.

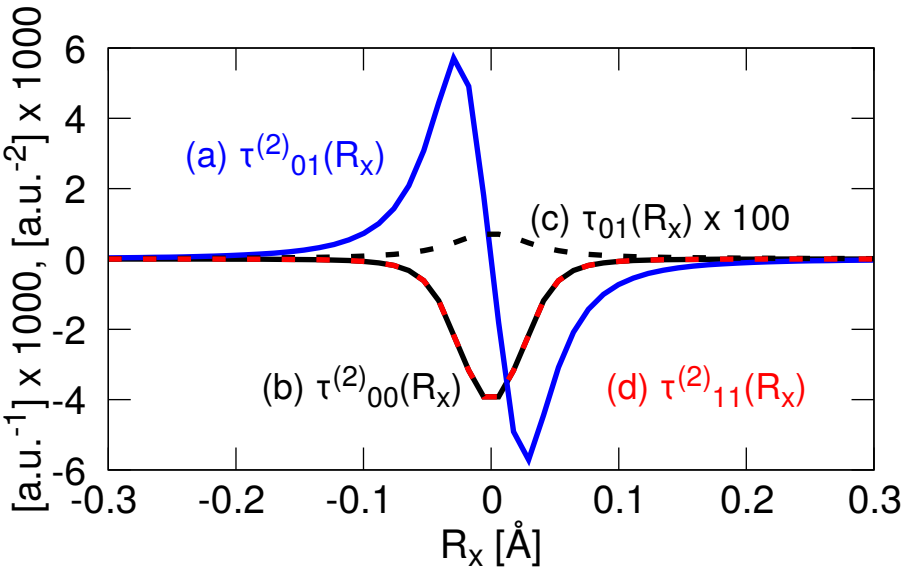

Figure 4-12: **Non-Adiabatic Coupling Elements (NACTs) - Strong Coupling Case**. The NACTs assume high values in the coupling region. Note that curve (c) is multiplied by a factor of 100.

4.2.2.2 Eigenfunctions in the Strong Coupling Case

4.2.2.3 (I) - Double Well Region

As the non-adiabatic coupling elements are localized at the vicinity of the origin, the exact eigenfunctions are expected to have no mixed electronic character when they are separated from this region. The coupling is localized to the interval $R_x = [-0.2; 0.2]$ Å, see fig. 4-12. As can be seen in fig. 4-13, the eigenfunctions raising in the double minimum region of the potential for low eigenenergy values resemble the ones of the double minimum potential in the weak coupling case. Therefore, the same product ansatz as for the weak coupling case is applied, see eq. (4.11). In table 4.5, the quantum numbers for the vibrational progression

are listed to the corresponding eigenfunctions $|\psi_{0,m}(x, R_x)\rangle$ in fig. 4-13 within the double minimum region (I).

Table 4.5: **Nuclear Quantum Numbers for Exact Eigenfunctions.**

panel:	(a)	(b)	(c)	(d)	(e)	(f)	(g)	(h)	(i)
m:	0	1	2	3	4	5	6	7	8
$E_{0m}[eV]$:	1.877	1.877	1.932	1.932	1.987	1.987	2.042	2.042	2.097

Regarding the eigenfunctions in fig. 4-13, the extension of the eigenfunctions for raising m values is vertical in x-direction. This is in contrast to the double minimum region of the weak coupling case in section 4.2.1.3. There, the extension was diagonal in the R_x-x plane.

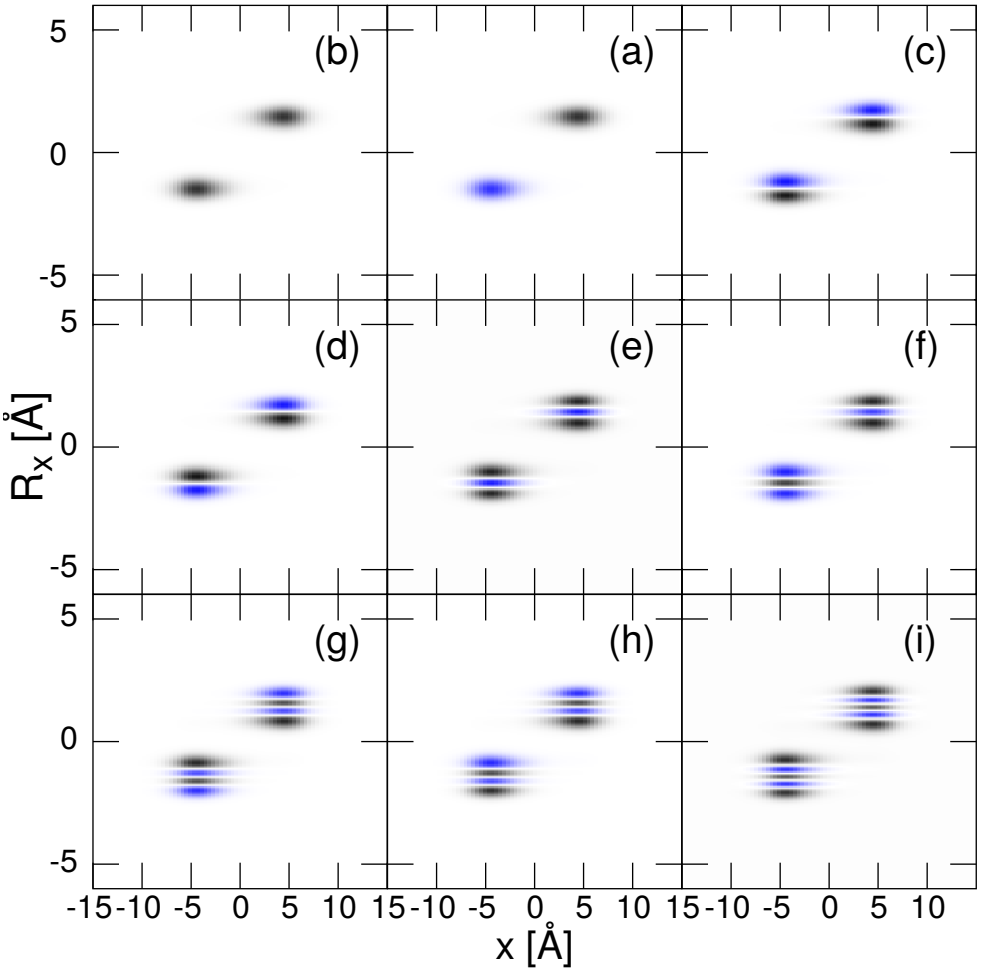

Figure 4-13: **Exact Eigenfunctions for the Double Minimum Region (I)**. The black color shows positive values, and the blue color shows negative values of the wave function. Quantum numbers for the eigenfunctions are assigned in table 4.5.

4.2.2.4 (II) - Coupling Region

In the coupling region $R_x = [-0.2; 0.2]$ Å, the adiabatic electronic ground state $|\phi_0(x; R_x)\rangle$ and the electronic excited state $|\phi_1(x; R_x)\rangle$ are coupled. As a result, eigenfunctions which are a composition of the two mentioned adiabatic eigenfunctions with a nuclear vibrational progression $|\xi_k(R_x)\rangle$ and $|\xi_l(R_x)\rangle$ are present.

$$|\psi_{nm}(x, R_x)\rangle = N\left[c_0 \cdot |\phi_0(x; R_x)\rangle|\xi_k(R_x)\rangle + c_1 \cdot |\phi_1(x; R_x)\rangle|\xi_l(R_x)\rangle\right]. \quad (4.12)$$

Here, c_0 and c_1 are coefficients and N is a normalization constant. This mixture of two adiabatic electronic states is assigned as mix for the quantum number n in $|\psi_{nm}(x, R_x)\rangle$ in table 4.6. m is the vibrational quantum number continued from lower eigenfunctions.

Table 4.6: **Nuclear Quantum Numbers for Exact Eigenfunctions.**

panel:	(a)	(b)	(c)	(d)	(e)	(f)	(g)	(h)	(i)
n:	mix	mix	mix	mix	mix	mix	mix	mix	mix
m:	72	73	74	75	76	77	78	79	80
$E_{nm}[eV]$:	3.782	3.833	3.838	3.889	3.893	3.945	3.948	4.002	4.003

The eigenfunctions, see fig. 4-14, show at $x = -5.0$ Å a spreading of the wave function over the interval $R_x = [-4.5; 2.0]$ Å. The same can be seen in the right branch at $x = +5.0$ Å, with a spreading over the interval $R_x = [-2.0; +4.5]$ Å. This indicates that an alternative description of the eigenfunctions is possible, where a linear combination of R_x-independent electronic eigenfunctions $|\tilde{\phi}_0(x)\rangle$ and $|\tilde{\phi}_1(x)\rangle$ is used for representation. These two electronic functions describe the left and the right branch of the exact eigenfunctions centered at $x \approx -5.0$ Å and $x \approx +5.0$ Å.

$$|\psi_{nm}(x, R_x)\rangle = N \left[c_{0p} |\tilde{\phi}_0(x)\rangle \cdot |\chi_p(R_x)\rangle + c_{1q} |\tilde{\phi}_1(x)\rangle \cdot |\chi_q(R_x)\rangle \right]. \tag{4.13}$$

$|\chi_p(R_x)\rangle$ and $|\chi_q(R_x)\rangle$ correspond to the vibrational progression on the electronic eigenfunctions, where $q, p \in \mathbb{N}$ are vibrational quantum numbers. As eq. (4.13) is a linear combination with coefficients, c_{0p} and c_{1q} are assigned as weightening coefficients. In the next section this ansatz of constant electronic eigenfunctions is used for a diabatization.

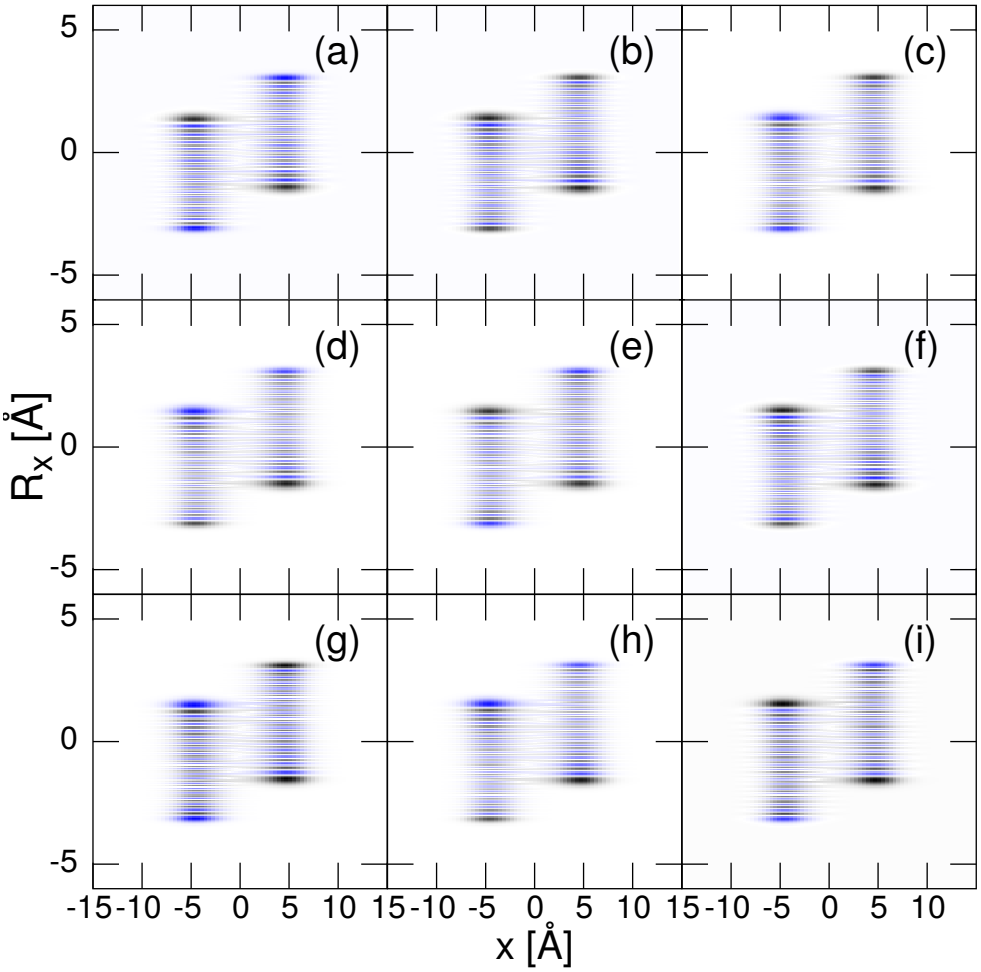

Figure 4-14: **Exact Eigenfunctions for the Coupling Region (II)**. The black color shows positive values, and the blue color shows negative values of the wave function. Quantum numbers for the eigenfunctions are assigned in table 4.6.

Concluding Remarks

Based on former work, it is shown that the weak and strong coupling case of the Shin-Metiu model exhibit strong differences concerning non-adiabatic coupling elements, adiabatic potentials and adiabatic electronic eigenfunctions. In particular the difference among the exact eigenfunctions of the weak and strong coupling situation is illustrated.

In the weak coupling case, the eigenfunction can be represented within an adiabatic product ansatz. In contrast to the strong coupling situation, where a strong

coupling between the adiabatic electronic eigenstates is present, this leads to eigenfunctions which are a linear combination of different adiabatic states with a vibrational progression. Furthermore, first indications for an alternative representation containing electronic eigenfunctions with constant electronic character are seen. In what follows a diabatization is carried out in the strong coupling case in order to justify the alternative state representation.

4.3 Diabatization Applied to the Strong Coupling Case

In what follows, diabatic electronic eigenfunctions are constructed from the adiabatic electronic eigenfunctions. The expansion of the total wave function in terms of the diabatic basis leads to a nuclear dynamics in the diabatic framework, which is compared to the dynamics obtained from a full-dimensional propagation.

4.3.1 Definition of the Diabatic Basis Set

Again, the electronic Schrödinger equation for the adiabatic electronic eigenfunctions $|\phi_n(x; R_x)\rangle$ is regarded, with $n = 0, 1$:

$$\hat{H}_{el}(x; R_x)|\phi_n(x; R_x)\rangle = u_{nn}(R_x)|\phi_n(x; R_x)\rangle. \tag{4.14}$$

The ground state $|\phi_0(x; R_x)\rangle$ and the first excited state $|\phi_1(x; R_x)\rangle$ are displayed in fig. 4-10. These two states are regarded solely as an electronic two-level system, where the two adiabatic states are coupled to each other. As the adiabatic description forms a two-state system, a two-state representation in the diabatic representation is needed. Here, the indications of a R_x-independent electronic eigenfunction basis set is used.

Therefore, two electronic eigenfunctions are chosen in the following way:

$$|\tilde{\phi}_0(x)\rangle = |\tilde{\phi}_0(x; \underline{R_x})\rangle = |\phi_0(x; R_x = -0.5 \text{ Å})\rangle \tag{4.15}$$

and

$$|\tilde{\phi}_1(x)\rangle = |\tilde{\phi}_1(x; \underline{R_x})\rangle = |\phi_1(x; R_x = -0.5 \text{ Å})\rangle. \tag{4.16}$$

These two functions are by definition orthogonal to each other:

$$0 = \langle\tilde{\phi}_0(x)\,|\,\tilde{\phi}_1(x)\rangle_x. \tag{4.17}$$

The choice of a diabatic basis set is arbitrary in phase and distance R_x. This

includes orthogonality and completeness of the basis set. The two diabatic wave functions $|\tilde{\phi}_n(x)\rangle$, with $n = 0, 1$, can be seen in fig. 4-15.

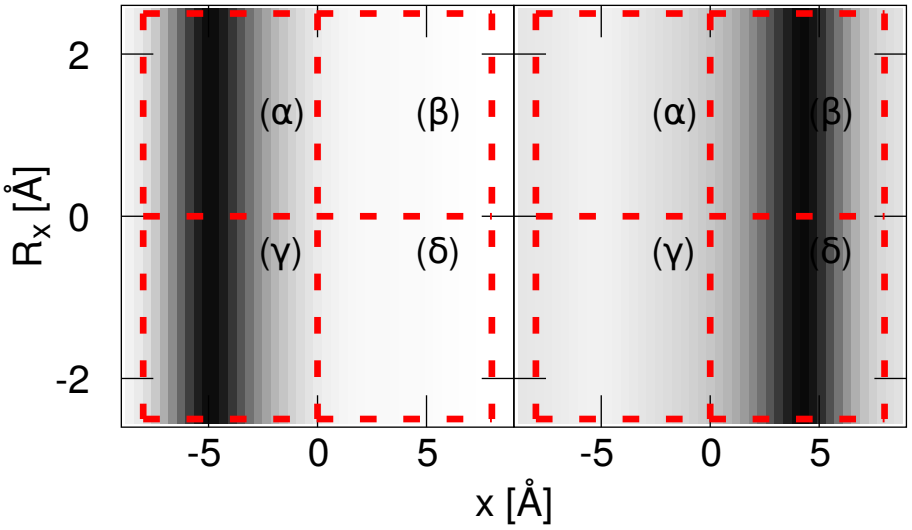

Figure 4-15: **Diabatic Electronic Eigenfunctions**. The left panel corresponds to the diabatic electronic state $|\tilde{\phi}_0(x)\rangle$, and the right panel shows the diabatic electronic state $|\tilde{\phi}_1(x)\rangle$.

The adiabatic wave functions in fig. 4-10 look like a geometry dependent superposition of the diabatic eigenfunctions in fig. 4-15. This is an indication for a mixing or rotation involved within the transformation from diabatic to adiabatic eigenfunctions. In section 2.4.2.2, it has already been seen that, under certain conditions, a transformation from the diabatic to the adiabatic framework and vice versa is possible.

4.3.2 Diabatic-to-Adiabatic Transformation

Two transformations connecting the diabatic and adiabatic representation are specified in what follows.

One is the projection of the diabatic basis set onto the adiabatic basis set, and the other one is obtained via the non-adiabatic coupling elements.

4.3.2.1 Transformation as a Projection of the Diabatic Basis Set onto the Adiabatic Basis Set

The following transformation ansatz is chosen, where the geometry of the diabatic basis set is indicated by $\underline{R_x}$:

$$
\begin{aligned}
|\phi_n(x;R_x)\rangle &= \underbrace{\sum_m |\tilde{\phi}_m(x;\underline{R_x})\rangle\langle\,\tilde{\phi}_m(x;\underline{R_x})|}_{\mathbb{1}}\,\phi_n(x;R_x)\rangle_x \\
&= \sum_m \underbrace{\langle\tilde{\phi}_m(x;\underline{R_x})\,|\,\phi_n(x;R_x)\rangle_x}_{(a^{-1})_{nm}(R_x;\underline{R_x})}\,|\tilde{\phi}_m(x;\underline{R_x})\rangle \\
|\phi_n(x;R_x)\rangle &= \sum_m (a^{-1})_{nm}(R_x;\underline{R_x})\;|\tilde{\phi}_m(x;\underline{R_x})\rangle. \qquad (4.18)
\end{aligned}
$$

The transformation matrix is obtained by the projection of the diabatic basis set onto the adiabatic basis set. Only a certain geometry $\underline{R_x}$ for the diabatic basis set has to be chosen, but as the wave function behaves stationary for the R_x-coordinate in the interval $[-2.2; 2.2]$ Å, it is possible to choose any fixed geometry $\underline{R_x}$ in this interval, see fig. 4-16.

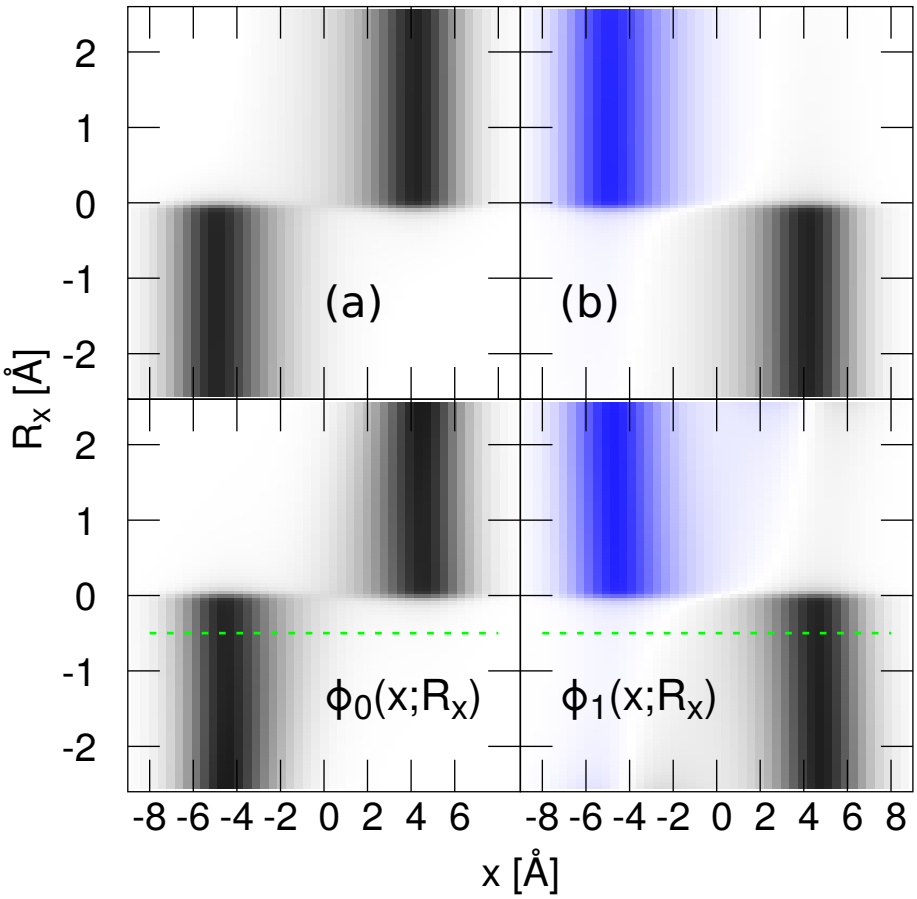

Figure 4-16: **Adiabatic Electronic Eigenfunctions and Their Reconstruction by a Diabatic Basis Set**. The lower panels correspond to the adiabatic electronic ground state and to the first excited state. The black color shows positive values, and the blue color shows negative values of the wave function. The adiabatic eigenfunctions constructed via eq. (4.18) can be seen in the upper panels (a) and (b), respectively.

Then, the transformation matrix coefficients $(a^{-1})_{nm}(R_x; \underline{R_x})$ read as the transformation from the diabatic basis set at a fixed geometry $\underline{R_x}$, to the adiabatic basis set at the geometry R_x, so this is a dynamical transformation, which is specific for every R_x-coordinate position and, under certain conditions, path-dependent. A fixed geometry is chosen at $\underline{R_x} = -0.5$ Å, and the adiabatic basis set is constructed from the diabatic basis set. This is illustrated in fig. 4-16, which compares the numerically calculated adiabatic wave functions (lower panels) to the ones ob-

tained by the basis set expansion of eq. (4.18). The transformation is only valid in the interval $R_x = [-2.2; 2.2]$ Å, because outside this interval, the second excited state gets involved. This situation is not addressed.

4.3.2.2 Transformation Using Non-Adiabatic Coupling Elements

Another approach to obtain the transformation matrix for the basis set transition involves the non-adiabatic coupling elements, see also section 2.4.2.2. These elements can be seen in fig. 4-12. The non-adiabatic coupling element $\tau_{01}(R_x)$ is of largest interest. The elements $\tau_{nm}(R_x)$ δ_{nm} are zero.

It has been seen in section 2.4.2.2, that for a successful transformation, the curl condition must be fulfilled:

$$0 = \vec{\nabla}_{\vec{R}} \times \vec{\tau}_{ki}(R_x), \tag{4.19}$$

which in the one-dimensional model system is trivially fulfilled. Then, one looks for a solution for the following equation for a two-state system, with $k, i, n = 0, 1$, consisting of the two lowest adiabatic states:

$$\sum_i \nabla_{R_x} \delta_{ki} (A^{-1})_{in}(R_x) + \tau_{ki}(R_x)(A^{-1})_{in}(R_x) = 0. \tag{4.20}$$

In section 2.4.2.2, the solution has been derived, and this leads to a geometry-dependent rotation martrix:

$$(A^{-1})(R_x; \underline{R_x}) = \begin{pmatrix} \cos(\varphi(R_x; \underline{R_x})) & -\sin(\varphi(R_x; \underline{R_x})) \\ \sin(\varphi(R_x; \underline{R_x})) & \cos(\varphi(R_x; \underline{R_x})) \end{pmatrix} (A^{-1})(\underline{R_x}; \underline{R_x}), \tag{4.21}$$

where the rotation angle is given by the line integral:

$$\varphi(R_x; \underline{R_x}) = -\int_{\underline{R_x}}^{R_x} \tau_{01}(\tilde{R}_x)\ \partial \tilde{R}_x, \tag{4.22}$$

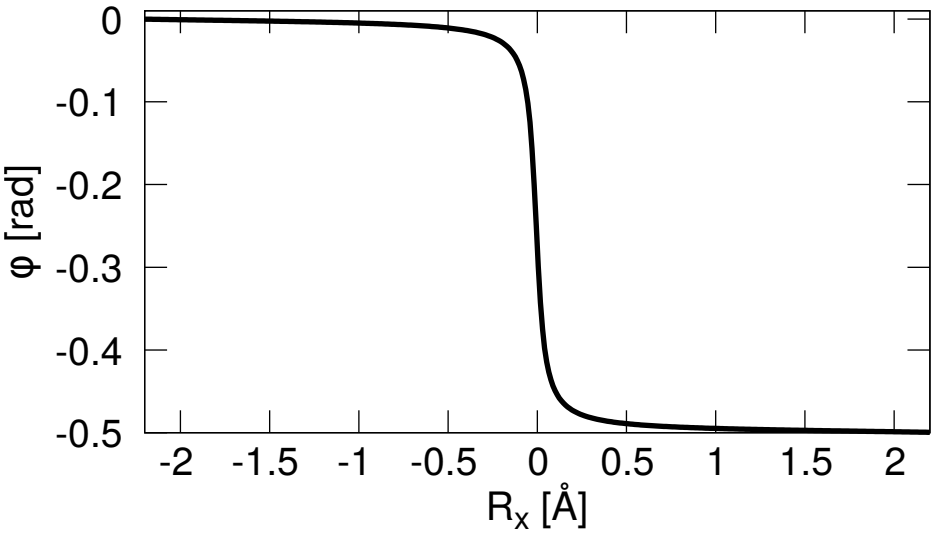

Figure 4-17: **Geometric Phase associated with the Diabatic-to-Adiabatic Transformation**. In the beginning a vanishing of the mixing angle is recognized. Reaching the coupling region, the angle is increased and finally reaches the full value of $-\frac{\pi}{2}$.

which is just the geometric phase associated with the transformation. Integrating $\tau_{01}(R_x)$ in fig. 4-12 over the only possible path from $R_x = -2.2$ Å $R_x = 2.2$ Å to in R_x-direction yields $-\frac{\pi}{2}$, see fig. 4-17.

Remembering that the diabatic basis is defined at $R_x = -0.5$ Å from the adiabatic eigenfunctions, the transformation starts with a vanishing mixing angle value for this position. The value is then decreasing for the distances $R_x > -0.5$ Å and increasing for the distances $R_x < -0.5$ Å, see fig. 4-18.

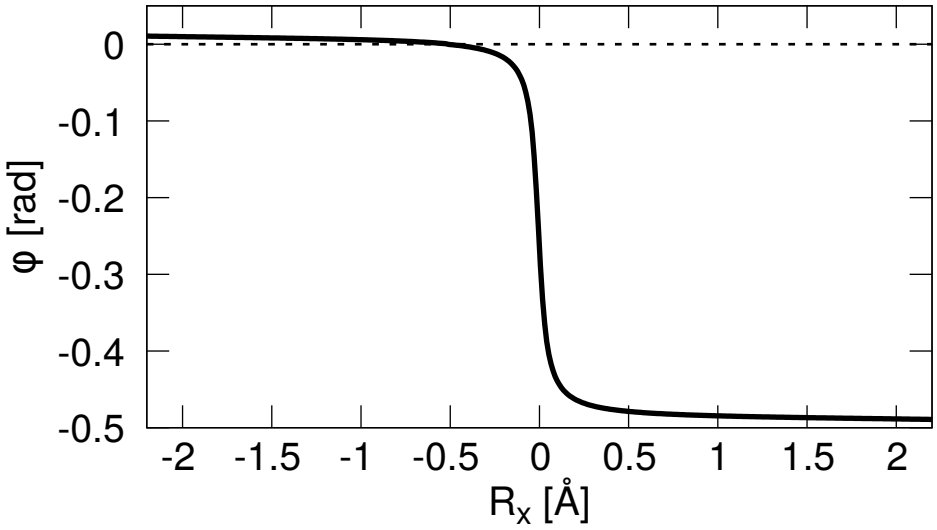

Figure 4-18: **Mixing Angle for the Diabatic-to-Adiabatic Transformation**. At the position $R_x = -0.5$ Å, a vanishing mixing angle is recognized. Up to distanced right of $R_x = -0.5$ Å, the angle is decreasing and reaches nearly the value of $-\frac{\pi}{2}$. For distances left of $R_x = -0.5$ Å, the angle is increasing.

According to this mixing angle, the adiabatic eigenfunctions can be construced from the diabatic basis via the associated rotation matrix. Beyond the coupling region in R_x-direction the sign and x position of the wave function changes. Therefore, the adiabatic eigenfunction $|\phi_1(x; R_x)\rangle$, which is a mixture of two diabatic states, being fully changed in the coupling region at $R_x = 0.0$ Å is obtained, see fig. 4-19.

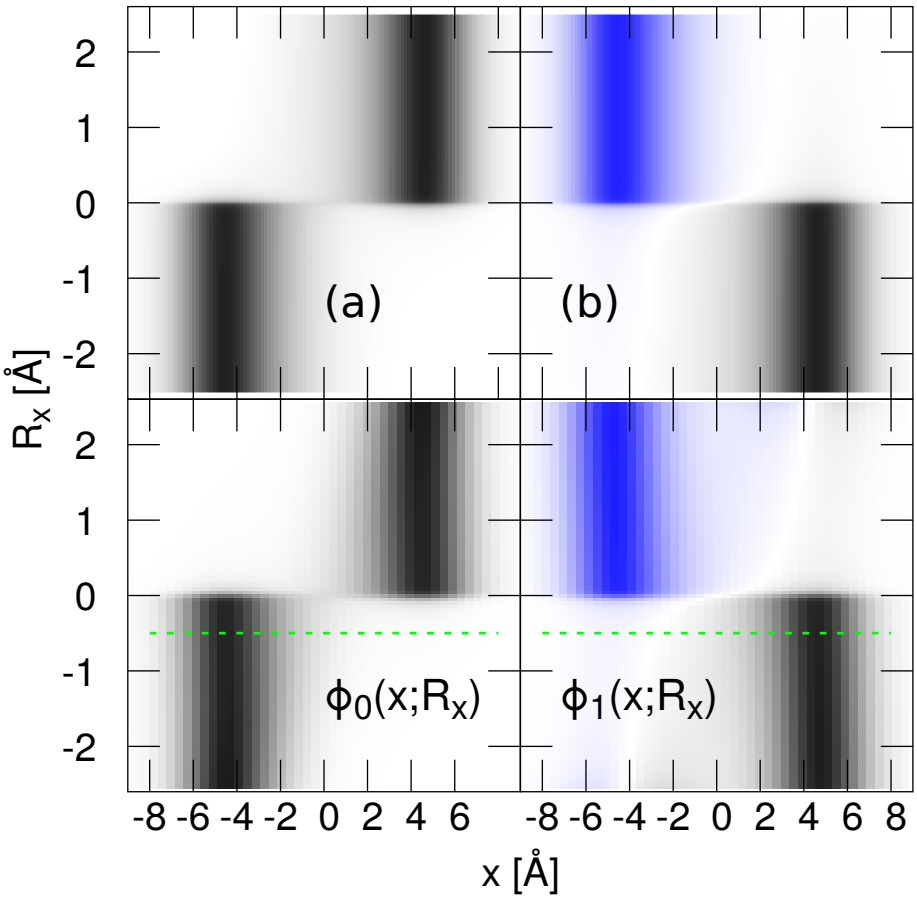

Figure 4-19: **Reconstruction of the Adiabatic Electronic Eigenfunctions by the Diabatic Basis Set and the Rotation Matrix**. Same as fig. 4-16. The adiabatic eigenfunctions constructed via the rotation matrix eq. (4.21) can be seen in the upper panels (a) and (b), respectively.

4.3.2.3 Diabatic Potentials and Diabatic Coupling Elements

Next, the adiabatic eigenenergies $u_{nn}(R_x)$ are regarded, and the diabatic eigenenergies $\tilde{u}_{nn}(R_x;\underline{R_x})$ are obtained by the transformation matrix $a^{-1}(R_x;\underline{R_x})$ from the diabatic to the adiabatic representation. The inverse transformation matrix can be formulated [95], and the diabatic potential matrix can be calculated.

The adiabatic eigenenergies $u_{nn}(R_x)$, obtained via the ITP, are given in fig. 4-20 as solid curves. There, the black curve is the adiabatic ground state, and the blue

curve represents the adiabatic first excited state energy. The avoided crossing between the ground state and the excited state can be seen clearly.

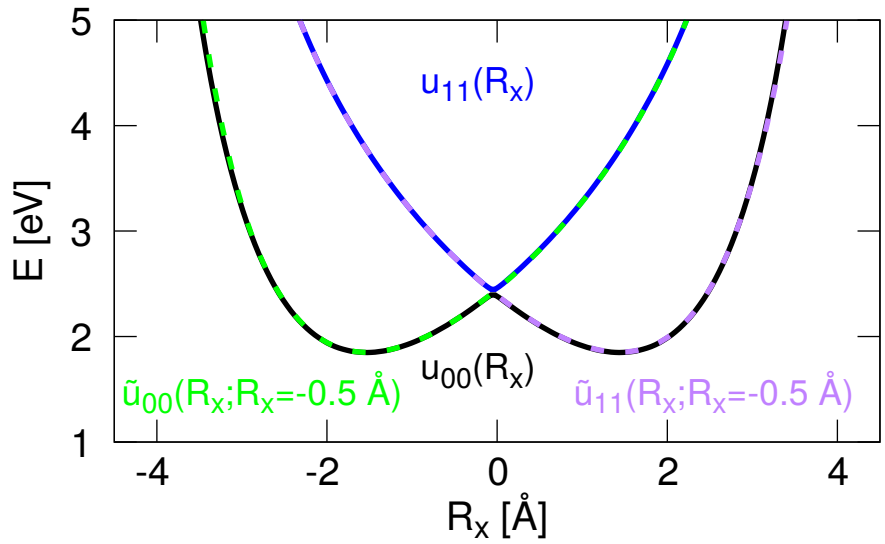

Figure 4-20: **Adiabatic and Diabatic Potentials**. The diabatic potentials are obtained via the adiabatic-to-diabatic transformation.

The diabatic potentials are obtained via :

$$\sum_m (a^{-1})_{km}(R_x;\underline{R_x})a_{mn}(R_x;\underline{R_x}) = \delta_{kn}, \tag{4.23}$$

which is just a property of orthogonal matrices. Then, the transformation from diabatic to adiabatic potentials can be written as [39]:

$$\begin{aligned}
u_{nm}(R_x) &= \sum_{k,o}(a^{-1})_{nk}(R_x;\underline{R_x})a_{ko}(R_x;\underline{R_x})u_{om}(R_x) \\
\sum_m u_{nm}(R_x)(a^{-1})_{mi}(R_x;\underline{R_x}) &= \sum_{k,o,m}(a^{-1})_{nk}(R_x;\underline{R_x})a_{ko}(R_x;\underline{R_x})u_{om}(R_x)(a^{-1})_{mi}(R_x;\underline{R_x}) \\
\sum_k \delta_{kp}\tilde{u}_{ki}(R_x;\underline{R_x}) &= \sum_{m,n} a_{pn}(R_x;\underline{R_x})u_{nm}(R_x)(a^{-1})_{mi}(R_x;\underline{R_x}) \\
\tilde{u}_{pi}(R_x;\underline{R_x}) &= \sum_{m,n} a_{pn}(R_x;\underline{R_x})u_{nm}(R_x)(a^{-1})_{mi}(R_x;\underline{R_x})
\end{aligned} \tag{4.24}$$

This yields the diabatic potentials $\tilde{u}_{00}(R_x;\underline{R_x})$ and $\tilde{u}_{11}(R_x;\underline{R_x})$ in fig. 4-20. The diabatic potential coupling $\tilde{u}_{10}(R_x;\underline{R_x})$ and $\tilde{u}_{01}(R_x;\underline{R_x})$ are obtained, too, and depicted in fig. 4-21.

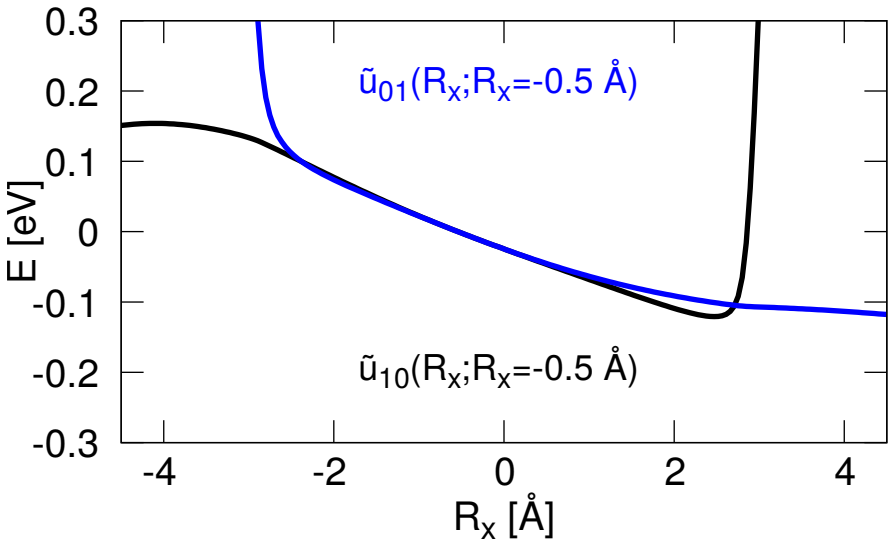

Figure 4-21: **Diabatic Coupling Potentials**. The diabatic coupling potentials are obtained numerically from the adiabatic-to-diabatic transformation.

The two coupling potentials are only parallel to each other where the diabatic representation is valid. The coupling in the valid interval is linear and not constant, as this is sometimes assumed in theory, when two diabatic states are constructed to couple with each other [96, 97]. At the origin, the coupling takes up small values which is in accordance with the appearance of the avoided crossing. It is again seen, as expected, that the diabatic approximation is only valid for the interval $R_x = [-2.2; 2.2]$ Å.

4.3.2.4 Comparison of the Exact Dynamics and the Diabatic Dynamics

Finally, the exact dynamic of a nuclear wave packet can be reproduced using the diabatic representation. The following coupled equations of motion for the diabatic representation have to be solved:

$$i\frac{\partial}{\partial t}|\tilde{\chi}_k(R_x,t)\rangle = \sum_i \left\{ -\frac{\vec{\nabla}^2_{R_x}}{2M}\delta_{ki} + \tilde{u}_{ki}(R_x;\underline{R_x}) \right\} |\tilde{\chi}_i(R_x,t)\rangle. \tag{4.25}$$

Parallel, the time-dependent Schrödinger equation is solved:

$$i\hbar\ \frac{\partial}{\partial t}|\psi(x,R_x,t)\rangle = \hat{H}(x,R_x)\ |\psi(x,R_x,t)\rangle. \tag{4.26}$$

In the following, a comparison between the projected adiabatic nuclear density $\rho^a_k(R_x,t) = |\chi_k(R_x,t)|^2 = |\langle\phi_k(x;R_x)\,|\,\psi(x,R_x,t)\rangle_x|^2$ of the exact calculation and the density $\rho^d_k(R_x,t) = |\tilde{\chi}_k(R_x;\underline{R_x},t)|^2$ of the calculation in the diabatic representation is made.

For the exact propagation, a Gaussian wave-packet is chosen to be in the adiabatic first excited state with a nuclear displacement:

$$|\psi_{init}(x,R_x,t_0)\rangle = N|\phi_1(x;R_x)\rangle \cdot e^{-\beta(R_x-R_{eq})^2}, \tag{4.27}$$

with $\beta = 7.14\ \frac{1}{\text{Å}^2}$, $R_{eq} = -1.86$ Å and N as normalization constant. In the diabatic representation, the nuclear wave function is the Gaussian wave-packet with the identical nuclear displacement in the first diabatic state $|\tilde{\phi}_1(x;\underline{R_x})\rangle$.

$$|\tilde{\chi}_{1,init}(R_x;\underline{R_x},t_0)\rangle = Ne^{-\beta(R_x-R_{eq})^2}. \tag{4.28}$$

The results of the two calculations are displayed in fig. 4-22. Regarding the exact calculation, the wave packet starts in the adiabatic first excited state and approaches the origin of the coordinate system, where the coupling region begins. After the wave packet has arrived at the coupling region, a complete non-adiabatic transition to the ground state takes place. This happens again vice versa as the wave packet re-enters the coupling region after approximately $t = 55$ fs.

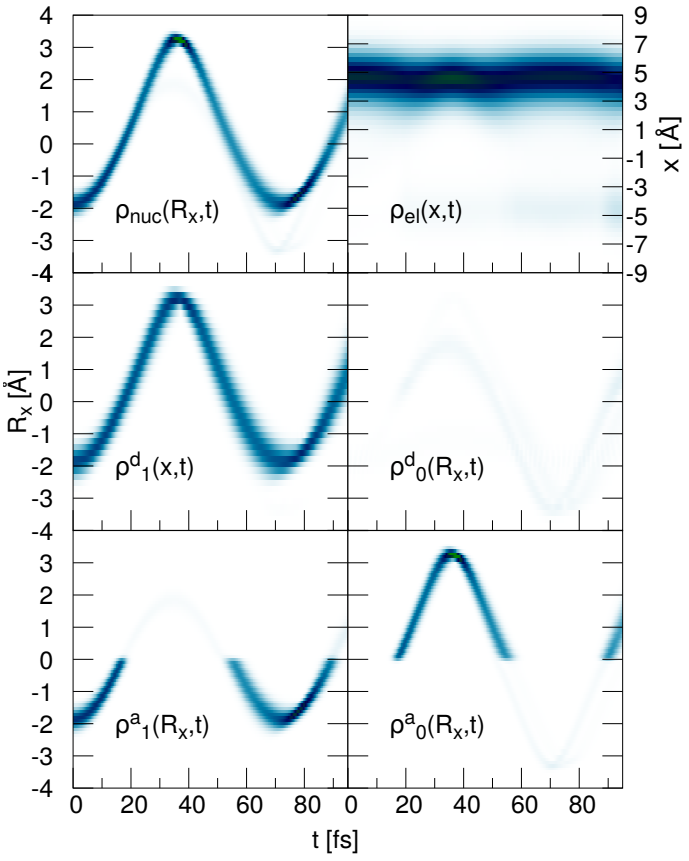

Figure 4-22: **Comparison of Wave-Packet Dynamics in the Diabatic Representation to the Exact Propagation.** In the upper panels, the nuclear density (left) and the electron density (right) is plotted from the numerically exact propagation. It is seen that the electron density does not follow the nuclear density. In the middle panels, the diabatic nuclear densities are seen for the first diabatic state (left) and the second diabatic state (right). The projected adiabatic nuclear densities from the exact calculation are shown in the lower panels. Here, the dynamics is mapped in both adiabatic states.

Regarding now the middle panels in fig. 4-22, one can see $\rho_k^d(R_x, t)$ in the reduced propagation scheme. Here, it becomes clear that the dynamics of the wave packet takes only place in one diabatic state. There is no transition between the diabatic states. The reduced dynamic in the diabatic representation fits very well with

the exact calculation. It should be noted that the dynamics is well reproduced although the propagation is partially done outside of the interval $R_x = [-2.2; 2.2]$ Å.

Concluding Remarks

Comparing the diabatization from an earlier work [91], which was applied by fitted diabatic potentials and an assumed constant coupling between the two fitted diabatic potentials, the approach followed here relies on the transformation from the adiabatic to the diabatic basis. The diabatic eigenfunctions are defined as the adiabatic eigenfunctions at a certain geometry. Therefore, orthonormality is guaranteed.

From this point, the diabatic basis set can be checked to reproduce the adiabatic eigenfunctions in good agreement. With the eigenfunctions in the two representations at hand, one can define the transformation matrix and can finally obtain the diabatic potentials. The coupling potentials are linear in shape and very small at the coupling region. Finally, it can be shown that the exact dynamics of a wave packet can be reproduced in good agreement within the diabatic representation.

4.4 Spectroscopy of the Shin-Metiu Model

In what follows, the spectroscopy of the Shin-Metiu model is addressed by regarding the linear absorption spectra first. This study has already been performed in previous works [66, 91], but is revisited here in more detail, as the linear absorption spectra are important to understand the two-dimensional spectroscopy. The simulation parameters in table 4.7 are used throughout the analysis.

Table 4.7: **Model Parameters.**

symbol:	description:	value
$[R_{x_{min}}; R_{x_{max}}]$	range in R_x-space	[-6;6]Å
$[x_{min}; x_{max}]$	range in x-space	[-50;50]Å
N_R	grid points in R_x-direction (p^+)	256
N_x	grid points in x-direction (e^-)	256
m_p	proton mass	1836.15 a.u.
$\Delta\tau$	time-step ITP	0.5 a.u.
Δt	time-step propagation	2.0 a.u.
R_f	shielding: e^- and p^+_{fixed}	1.5 Å

4.4.1 Linear Absorption Spectra

First, the description of the laser pulses acting upon the model system is addressed. As already mentioned in section 2.7.2, light-matter interactions are described via a semi-classical approach, meaning the use of classical electric transversal waves. In the model system, only resonant transitions are regarded. In these cases, the system takes energy out of the electric field via an absorptive process and decreases its internal energy via a stimulated emission [62].

As was argued in section 2.7.2, the dipole approximation is applied and, therefore, the coordinate dependence of the electric field description is omitted. In the simulation, the direction of the electric field is adjusted parallel to the axis of the model system. The direction of the laser pulse is omitted and, therefore, the electric field is written without the vector notation.

The electric field is of the form, with $m = 1$,:

$$E(t) = \sum_{n=1}^{m} E_n(t - t_n) = \sum_{n=1}^{m} E_n^{(+)}(t - t_n) + E_n^{(-)}(t - t_n), \tag{4.29}$$

with the components correspondent to the absorptive process $E_n^{(+)}$ and stimulated emission $E_n^{(-)}$ in $|\psi(x, R_x, t)\rangle$:

$$E_n^{(\pm)}(t) = \epsilon e^{\mp i\omega_n(t-t_n)} e^{-\alpha(t-t_n)^2}. \tag{4.30}$$

The spectrum is defined as Fourier transform of the model system's emitted electric field $E_{sig.}(\tilde{t}')$ during the acquisition time, after the light-matter interaction has taken place [69]. To be more precise, the acquisition time, denoted as t', is the detection time span starting after the last light-matter interaction has acted upon the system and having a finite length after which the detection process is terminated. This length basically determines the resolution of the spectrum in $E_{t'}$

$$S(E_{t'}) = \frac{1}{\sqrt{2\pi}} \int_{t'} d\tilde{t}' E_{sig.}(\tilde{t}')\ e^{+iE_{t'}\tilde{t}'}. \tag{4.31}$$

The last expression is further constrained as the light-matter interaction is simulated via time-dependent perturbation theory, and as one is only interested in the peak position and their relative height to each other, all proportionality factors are omitted within the time-dependent perturbation theory.
The emitted electric field is proportional to the polarization function $P_{sig.}(\tilde{t}')$ and rotated by 90^o in phase [62, 69, 98]. Then, eq. (4.31) is rewritten as:

$$S(E_{t'}) = i \int_{t'} d\tilde{t}' P_{sig.}(\tilde{t}')\ e^{+iE_{t'}\tilde{t}'}. \tag{4.32}$$

To calculate the spectrum, the first-order polarization has to be evaluated, see section 2.7.2. Then, for the first-order polarization expression for $P_{sig.}(t) = P^{(1)}(t)$,

one obtains[1] [62]:

$$
\begin{aligned}
P^{(1)}(t) &= i\int_0^\infty dt_1\{J(t_1) - J^*(t_1)\}E_1(t-t_1) \\
&= 2\int_0^\infty dt_1 \mathfrak{Im}\{J(t_1)E_1^{(+)}(t-t_1)\} \\
&= \mathfrak{Im}\left\{\int_0^\infty dt_1 J(t_1)E_1^{(+)}(t-t_1)\right\},
\end{aligned}
\tag{4.33}
$$

where the factor 2 is droped, and the component of the response function $J(t_1)$ is given as:

$$
J(t_1) = \langle\hat{\mu}(x,R_x)\,|\,\rho(x,R_x,t_0)\,|\,\hat{\mu}(x,R_x,t_1)\rangle_{x,R_x}. \tag{4.34}
$$

The completeness relation $\sum_\beta|\psi_\beta(x,R_x)\rangle\langle\,\psi_\beta(x,R_x)| = \mathbb{1}$ is inserted for the system's propagator $\hat{U}(t_p,t_q)$, and the interaction picture of the dipole moment operator is transferred to the Schrödinger picture.

$$
\hat{U}(t_p) = \sum_e |\psi_e(x,R_x)\rangle e^{-iE_e t_p}\langle\psi_e(x,R_x)|. \tag{4.35}
$$

So, the polarization function is written as:

$$
\begin{aligned}
P^{(1)}(t) = \mathfrak{Im}\Bigg\{\int_0^\infty dt_1 \langle\psi_{E_0}(x,R_x,t_0)|\hat{U}^*(t_1)\hat{\mu}(x,R_x)\hat{U}(t_1)\,\times \\
\hat{\mu}(x,R_x)|\psi_{E_0}(x,R_x,t_0)\rangle_{x,R_x} \quad E_1^{(+)}(t-t_1)\Bigg\}.
\end{aligned}
\tag{4.36}
$$

The system is in the ground state with energy E_{E_0} at $t = t_0$. Introducing the new time-variable $t_1' = t - t_1$ yields:

[1] The system is assumed to be initially in the ground state, so there is no stimulated emission out of the ground state.

$$P^{(1)}(t) = \mathfrak{Im}\left\{\sum_e \langle\psi_{E_0}(x,R_x,t_0)\,|\,\hat{\mu}(x,R_x)\,|\,\psi_e(x,R_x)\rangle_{x,R_x}\times \right.$$
$$\langle\psi_e(x,R_x)\,|\,\hat{\mu}(x,R_x)\,|\,\psi_{E_0}(x,R_x,t_0)\rangle_{x,R_x}\times$$
$$\left. e^{+i(E_{E_0}-E_e)t}\int_{-\infty}^{t} dt_1' e^{-i(E_{E_0}-E_e)(t_1')}\ E_1^{(+)}(t_1')\right\}. \tag{4.37}$$

The time variable $t = t'$ is redefined as the acquisition time for the spectrum. Then one gets:

$$P^{(1)}(t') = \sin\left[(E_{E_0}-E_e)t'\right]\times$$
$$\mathfrak{Im}\left\{\sum_e \langle\psi_{E_0}(x,R_x,t_0)\,|\,\hat{\mu}(x,R_x)\,|\,\psi_e(x,R_x)\rangle_{x,R_x}\times \right.$$
$$\langle\psi_e(x,R_x)\,|\,\hat{\mu}(x,R_x)\,|\,\psi_{E_0}(x,R_x,t_0)\rangle_{x,R_x}\times$$
$$\left.\int_{-\infty}^{\infty} dt_1' e^{-i(E_{E_0}-E_e)(t_1')}\ E_1^{(+)}(t_1')\right\}. \tag{4.38}$$

The upper boundary for the integral was extended to infinity, as finite short light pulses are used. One can unify all transition dipole moments into the scalar factors $N_{E_0,e}$ and unify the integral expression into the factor $g_{E_0,e,E_1^{(+)}}$:

$$P^{(1)}(t') = \sin\left[(E_{E_0}-E_e)t'\right]\sum_e N_{E_0,e}\ g_{E_0,e,E_1^{(+)}}. \tag{4.39}$$

Inserting the expression above into eq. (4.32) yields for the spectral function $|S(E_{t'})|$:

$$|S(E_{t'})| = \left|\sum_e N_{E_0,e}\ g_{E_0,e,E_1^{(+)}}\ \int_{t'} d\tilde{t}'\ e^{+iE_{t'}\tilde{t}'}\ \sin\left[(E_{E_0}-E_e)\tilde{t}'\right]\right|. \tag{4.40}$$

Dropping the factor of $\frac{1}{2}$, one finally obtains:

$$|S(E_{t'})| = \left| \sum_{e} N_{E_0,e}\ g_{E_0,e,E_1^{(+)}}\ \ \{\delta[E_{t'} - (E_{E_0} - E_e)] + \delta\left[E_{t'} - (E_e - E_{E_0})\right]\} \right|. \tag{4.41}$$

The signal then contains the appearing coherences prompted by the light-matter interaction, which will yield information about energetic spacings within the model system via peaks, where the height of these peaks are mediated by certain factors $N_{E_0,e}$ and laser pulse properties $g_{E_0,e,E_1^{(+)}}$. In the simulation of a linear absorption spectrum, an interaction hits the system, namely a short Gaussian laser pulse with direction, $\pm k_1$. These are the reddish arrows depicted in fig. 4-23. After this interaction, the system is set in the coherences $|E_0\rangle\langle e|$ and $|e\rangle\langle E_0|$. These coherences are then detected during the acquisition time t'. Afterwards, not concerned in the simulation, but common practice in this notation, at some point the system relaxes to population states, indicated by the final wavy arrow $-k_s$ [62]. Note that, as a matter of formalism, here the direction is always drawn to the left side of the diagram.

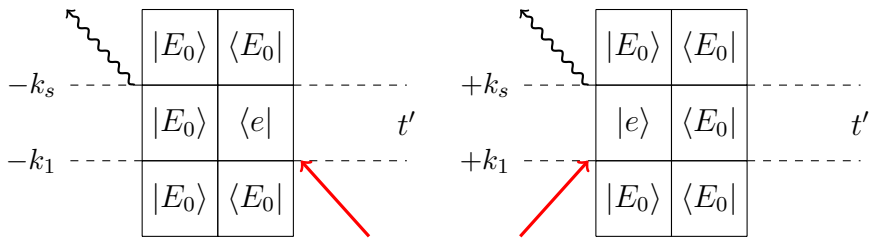

Figure 4-23: **Double-Sided Feynman Diagram for a Linear Absorption Spectrum.**

The pulse direction was already constrained to $-k_1$, because the signal direction $k_s = -k_1 + k_2 + k_3$ is used for the two-dimensional spectrum later on. Therefore, the left double-sided Feynman diagram in fig. 4-23 is regarded. Then, the linear absorption spectrum is expected to contain the energy differences between the laser excited states $|\psi_e(x, R_x)\rangle$ and the ground state $|\psi_{E_0}(x, R_x)\rangle$.

In the following, the linear absorption spectrum is calculated via the polarization within the numerical time-dependent perturbation theory. This is done by the expression for the left Feynman diagram.

$$P^{(1,ex)}(t) = \langle \psi^{(1,ex)}(x, R_x, +k_1, t) \,|\, \hat{\mu}(x, R_x) \,|\, \psi^{(0,ex)}(x, R_x, t) \rangle_{x,R_x}. \tag{4.42}$$

Here, the index ex stands for the numerically exact propagation in full-dimensional coordinate space. For the calculation of $|\psi^{(1,ex)}(x, R_x, -k_1, t)\rangle$, the following numerical ansatz is used:

$$\begin{aligned} |\psi^{(1,ex)}(-k_1, x, R_x, t + \Delta t)\rangle =& \hat{U}(\Delta t)|\psi^{(1,ex)}(-k_1, x, R_x, t)\rangle \\ & - i\Delta t \left(\hat{\mu}(x, R_x) E_1^{(+)}(t + \Delta t)\right) |\psi^{(0,ex)}(x, R_x, t + \Delta t)\rangle. \end{aligned} \tag{4.43}$$

Then, the obtained expression for eq. (4.42) is calculated for the acquisition time t' and is then Fourier transformed along t'.

4.4.1.1 Weak Coupling

For this simulation, parameters are used for the model system which due to consistency are only slightly varied compared to the previous section, where the eigenfunctions were discussed. These parameters as well as the parameters characterizing the Gaussian laser pulse are found in table 4.8.

Table 4.8: **Model Parameters for the Linear Absorption Spectrum.**

symbol:	description:	weak coupling	strong coupling
t'	aquisition time	4.65 ps	4.65 ps
E_{off}	offset energy	11.58 eV	10.01 eV
R_c	shielding: e^- and p^+	1.5 Å	2.5 Å
α	Gaussian broadening	$1.0 \cdot 10^{-4}$ $\frac{1}{\text{fs}^2}$	$1.0 \cdot 10^{-4}$ $\frac{1}{\text{fs}^2}$
ω_1	excitation energy	2.9 eV	1.9 eV

The excitation energy is chosen as the energetic difference between the adiabatic first excited state and the ground state minimum, see fig. 4-5. Regarding the linear absorption spectrum in fig. 4-24, the laser pulse with the central frequency of 2.9 eV resonantly excites the first electronic adiabatic state.

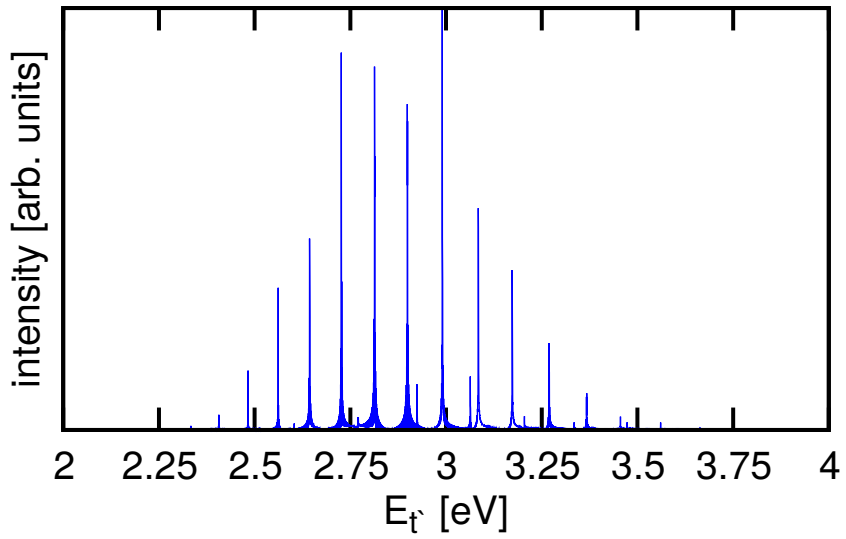

Figure 4-24: **Linear Absorption Spectrum of the Weak Coupling Case.** Shown is the absolute signal.

According to eq. (4.41), the spectrum is expected to show peaks at energy differences between the laser excited states $|\psi_e(x, R_x)\rangle$ and the ground state $|\psi_{E_0}(x, R_x)\rangle$. As ground state, $|\psi_{n,m}(x, R_x)\rangle$ is used, with $n = m = 0$. This eigenfunction is displayed in fig. 4-7 panel (a). The spectral peaks and corresponding energetic differences are assigned in table 4.9 together with fig. 4-25.

Table 4.9: **Assignment of Spectral Peaks.**

peak:		1	2	3	4	5	6	7	8
e	n:	1	1	1	1	1	2	1	1
	m:	8	10	12	14	16	1	18	20
$E_{nm} - E_0$	[eV]:	2.264	2.332	2.405	2.483	2.561	2.602	2.644	2.726
fig. 4-26		(a)	(b)	(c)	(d)	(e)	(f)	(g)	(h)

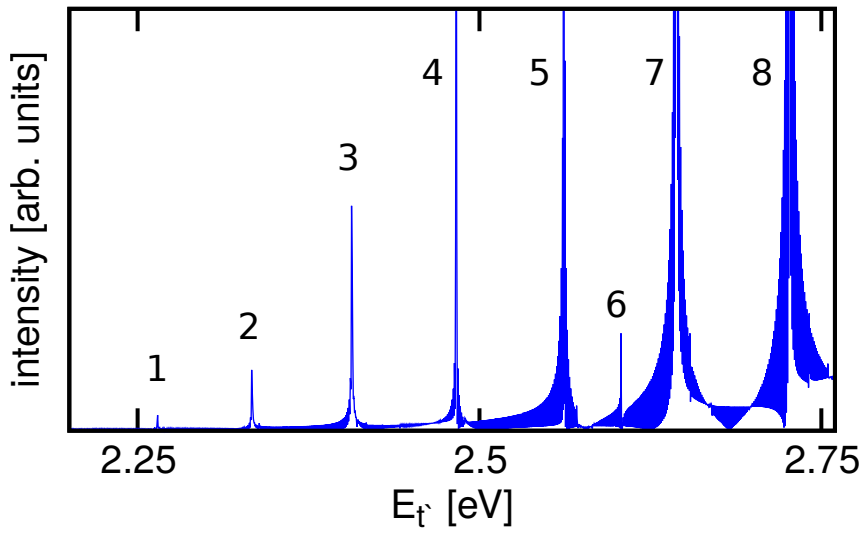

Figure 4-25: **Excerpt of the Linear Absorption Spectrum of the Weak Coupling Case.** Shown is the absolute signal. The spectrum is given for an energetic interval $E_{t'} = [2.2; 2.76]$ eV and shows the first 8 peaks. The intensity is cut. The wiggling structure on top of the peaks are artifacts from the numerical Fourier transform.

From table 4.9, it emerges that only gerade vibrational states of the first electronic state are excited. This is in perfect agreement with the previous chapter, where the adiabatic product ansatz was elucidated as a proper state representation for the eigenfunctions of the weak coupling case. Then, the propensity rule according to the transition dipole moments in $N_{E_0,e}$ are given as the transitions from the symmetric initial ground state $|\psi_{E_0}(x, R_x)\rangle$ to the target excited states $|\psi_e(x, R_x)\rangle$:

$$
\begin{aligned}
&\langle \psi_e(x,R_x) \,|\, \hat{\mu}(x,R_x) \,|\, \psi_{E_0}(x,R_x) \rangle_{x,R_x} \\
&= \langle \chi_{1,m}(R_x) | \langle \phi_1(x;R_x) \,|\, \hat{\mu}(x,R_x) \,|\, \phi_0(x;R_x) \rangle_x | \chi_{0,0}(R_x) \rangle_{R_x} \\
&= \langle \chi_{1,m}(R_x) \,|\, R_x \langle \phi_1(x;R_x) \,|\, \phi_0(x;R_x) \rangle_x \,|\, \chi_{0,0}(R_x) \rangle_{R_x} \\
&\quad - \langle \chi_{1,m}(R_x) \,|\, \langle \phi_1(x;R_x) \,|\, x \,|\, \phi_0(x;R_x) \rangle_x \,|\, \chi_{0,0}(R_x) \rangle_{R_x} \\
&= \underbrace{- \langle \chi_{1,m}(R_x) \,|\, \underbrace{\langle \phi_1(x;R_x) \,|\, x \,|\, \phi_0(x;R_x) \rangle_x}_{\neq 0 \;\forall R_x} \,|\, \chi_{0,0}(R_x) \rangle_{R_x}}_{\neq 0,\ for\ m{=}gerade}
\end{aligned}
\tag{4.44}
$$

This can be directly seen by regarding the eigenfunctions of the target states in fig. 4-26. The panels are matched with the corresponding peaks mentioned in table 4.9. A closer look reveals that the target wave functions are antisymmetric in x-direction and symmetric in R_x-direction.

There is also one exception in fig. 4-26 panel (f), namely the excitation to the second excited adiabtic state $|\psi_{n,m}(x,R_x)\rangle$ with $n=2, m=1$. There, the eigenfunction is symmetric in x-direction and antisymmetric in R_x-direction. According to the propensity rule:

$$
\begin{aligned}
&\langle \psi_e(x,R_x) \,|\, \hat{\mu}(x,R_x) \,|\, \psi_{E_0}(x,R_x) \rangle_{x,R_x} \\
&= \langle \chi_{2,1}(R_x) \,|\, R_x \underbrace{\langle \phi_2(x;R_x) \,|\, \phi_0(x;R_x) \rangle_x}_{=0} \,|\, \chi_{0,0}(R_x) \rangle_{R_x},
\end{aligned}
\tag{4.45}
$$

this transition is not allowed. Remembering the weak non-adiabatic coupling and the resulting eigenfunction with slightly mixed electronic character in fig. 4-9, this is the evidence for another spectral band below the transitions to the first excited state. It was also confirmed in previous studies [91] that there are two excitation bands.

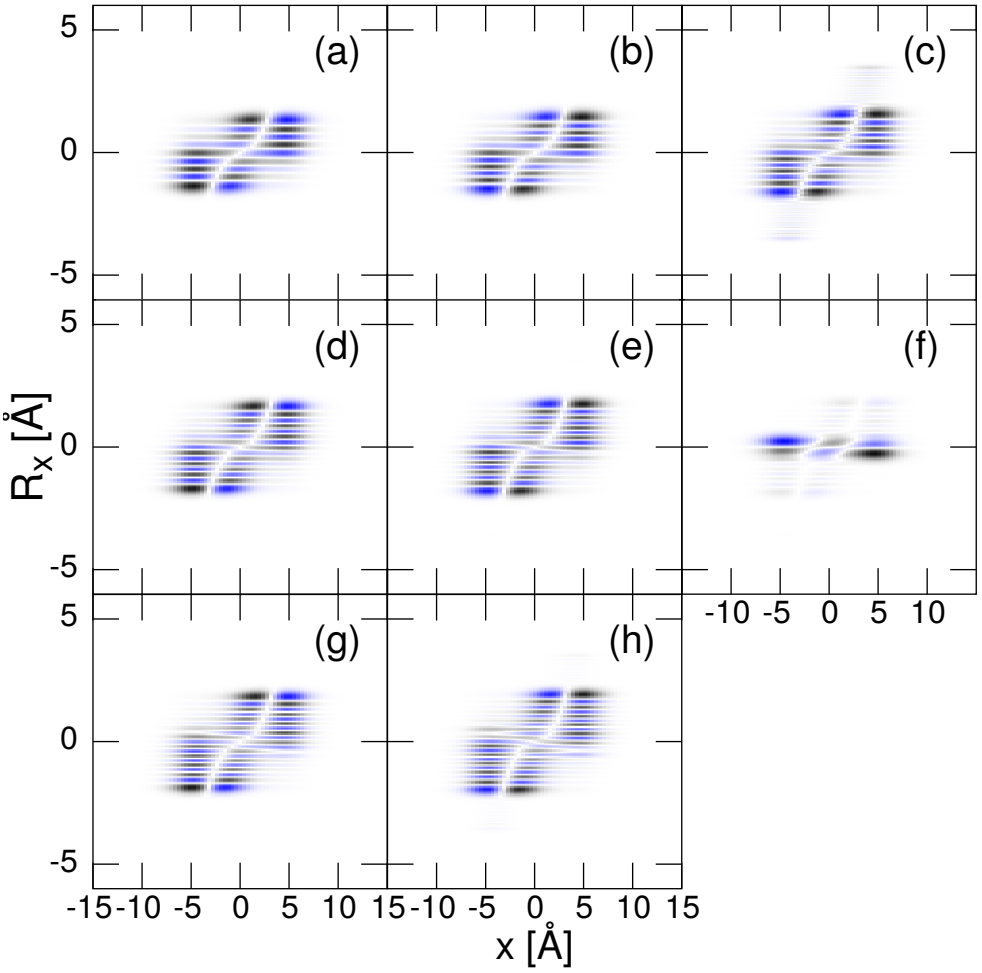

Figure 4-26: **Eigenfunctions Corresponding to the Spectroscopic Transitions of the Weak Coupling Case**. The black color shows positive values, and the blue color shows negative values of the wave function. Quantum numbers for the eigenfunctions are assigned in table 4.9.

4.4.1.2 Strong Coupling

Regarding the spectrum displayed in fig. 4-27, an excitation in the interval $E_{t'} = [2.4; 3.1]$ eV is mainly seen. This is unexpected since the laser pulse has an excitation energy of 1.9 eV.

The peak progression to higher energies and the transitions to the second adiabatic excited state have been already identified [91], and for the relatively small peak progression around 1.9 eV, it was confirmed that those correspond to the

transitions to mixed states, which are composed of the adiabatic ground state as well as the adiabatic first excited state due to strong non-adiabatic coupling.

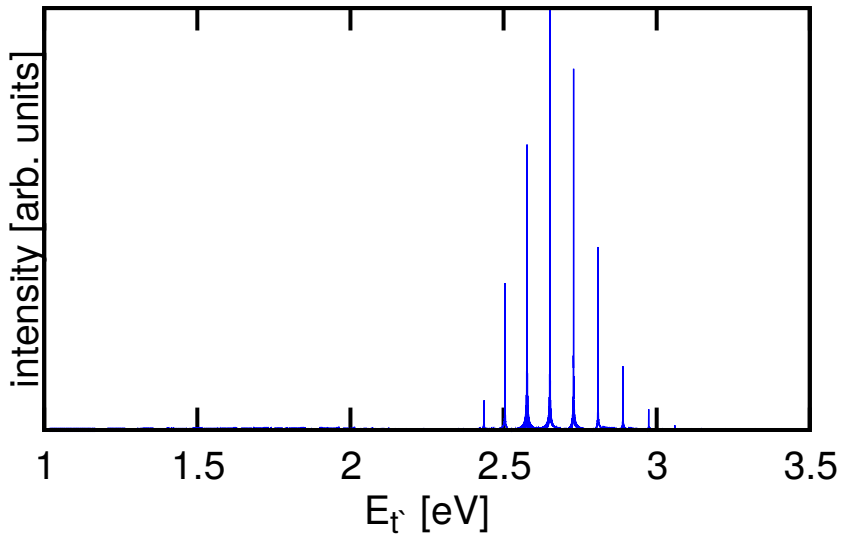

Figure 4-27: **Linear Absorption Spectrum of the Strong Coupling Situation.** Shown is the absolute signal.

A reproduction of the peak structure by simulating the absorption spectrum within the diabatic framework was tried in previous studies. This had some agreement and could partially reproduce the structure of the exact spectrum [91].

The study is continued with the transitions both to the mixed states as well as to the second excited state. Like in the weak coupling case, symmetry characteristics of the eigenfunctions are regarded.

In fig. 4-28, two major characteristic

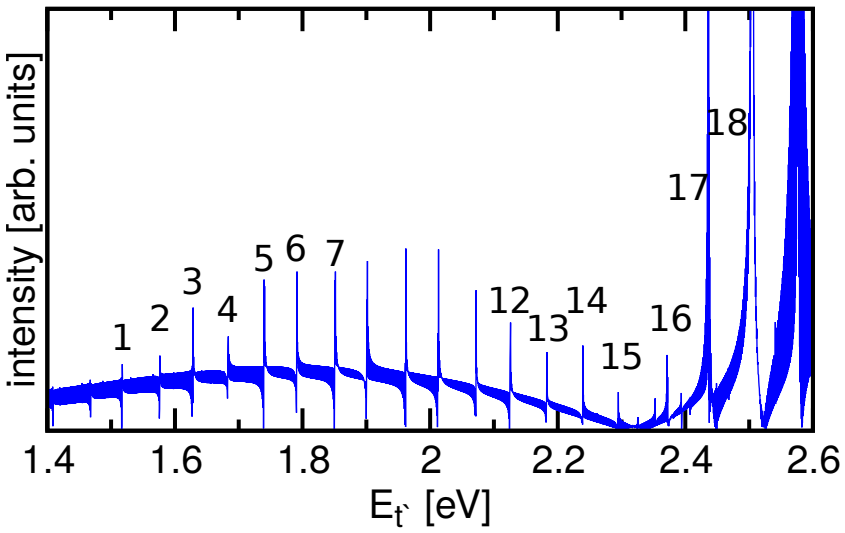

Figure 4-28: **Absorption Spectrum of the Strong Coupling Situation.** Shown is the absolute signal. The spectrum is given for a energetic interval $E_{t'} = [1.0; 3.5]$ eV and shows the spectrum cut in intensity. A closer look reveals also transitions to energetic levels around 1.8 eV.

regions are seen in the peaks' progression. The first one is seen in the interval $[1.4; 2.3]$ eV, which is the region around the laser excitation. Here, an analysis of the excited eigenstates reveals and confirmes that the laser excited states have a mixed electronic character which is composed of both the electronic adiabatic ground state and the first excited state $n = mix$, see fig. 4-10. These first peaks are listed in table 4.10. A closer study of the target eigenfunctions, see fig. 4-29, reveals that these transitions exhibit a certain propensity rule.

Table 4.10: **Assignment of Spectral Peaks.**

peak:	1	2	3	4	5	6	7
n:	mix	mix	mix	mix	mix	mix	mix
m:	56	59	60	62	65	66	69
$E_{nm} - E_0$[eV]:	1.517	1.577	1.628	1.683	1.742	1.790	1.853
fig. 4-29:	(a)	(b)	(c)	(d)	(e)	(f)	(g)

This propensity rule can be seen in regarding the corresponding target eigenfunc-

tions, where one has only contributions of eigenfunctions symmetric in one of the directions x or R_x, but antisymmetric in the other direction. Those target eigenfunctions which are not laser excited have only gerade or ungerade symmetry in both directions.

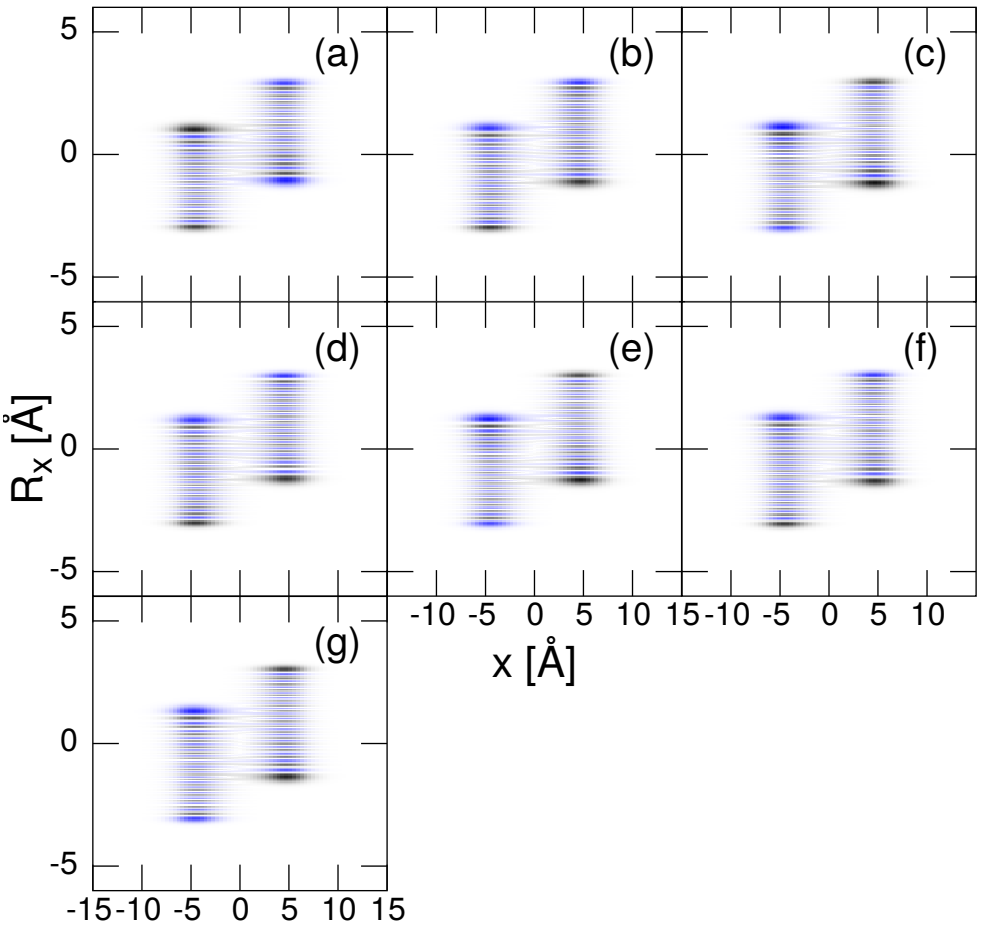

Figure 4-29: **Eigenfunctions Corresponding to Final States for the Spectral Transitions of the Strong Coupling Case**. The black color shows positive values, and the blue color shows negative values of the wave function. Quantum numbers for the eigenfunctions are assigned in table 4.10.

Continuing the study, some conclusions are drawn on the second characteristic peak progression in fig. 4-28 in the interval $[2.3; 2.6]$ eV. In table 4.11, peaks of the transition region are listed from $[2.1; 2.6]$ eV.

The peaks are decreasing in intensity regarding the mixed characteristic $n = mix$,

but are strongly increasing for the next characteristic with the $n = 2$ peaks, representing the transition to the second excited adiabatic state.

Table 4.11: **Assignment of Spectral Peaks.**

peak:	12	13	14	15	16	17	18
n:	mix	mix	mix	mix	2	2	mix
m:	78	81	83	84	1	3	91
$E_{nm} - E_0$[eV]:	2.126	2.184	2.239	2.295	2.372	2.437	2.504
fig. 4-31:	(a)	(b)	(c)	(d)	(e)	(f)	(g)

This, can again be understood in regarding the target eigenfunctions of the laser excitation, see fig. 4-31 and table 4.11.

Here, also the propensity rule holds for the transition to the second excited state, as this state is compared to the ground state energetically well separated, and leads to the formulation of an adiabatic product ansatz, just like in the case of the weak coupling case. Now the second excited adiabatic state is antisymmetric in x-direction (not shown):

$$\begin{aligned}
&\langle \psi_e(x,R_x) \,|\, \hat{\mu}(x,R_x) \,|\, \psi_{E_0}(x,R_x)\rangle_{x,R_x} \\
&= \langle \chi_{2,m}(R_x) | \langle \phi_2(x;R_x) \,|\, \hat{\mu}(x,R_x) \,|\, \phi_0(x;R_x)\rangle_x | \chi_{0,0}(R_x)\rangle_{R_x} \\
&= \underbrace{\langle \chi_{2,m}(R_x) \,|\, \underbrace{\langle \phi_2(x;R_x) \,|\, x \,|\, \phi_0(x;R_x)\rangle_x}_{\neq 0,\ ungerade} \,|\, \chi_{0,0}(R_x)\rangle_{R_x}}_{\neq 0,\ for\ m=ungerade}
\end{aligned} \tag{4.46}$$

As can be seen in fig. 4-30, the term $\langle \phi_2(x;R_x) \,|\, x \,|\, \phi_0(x;R_x)\rangle_x$ is an antisymmetric function with respect to the R_x coordinate.

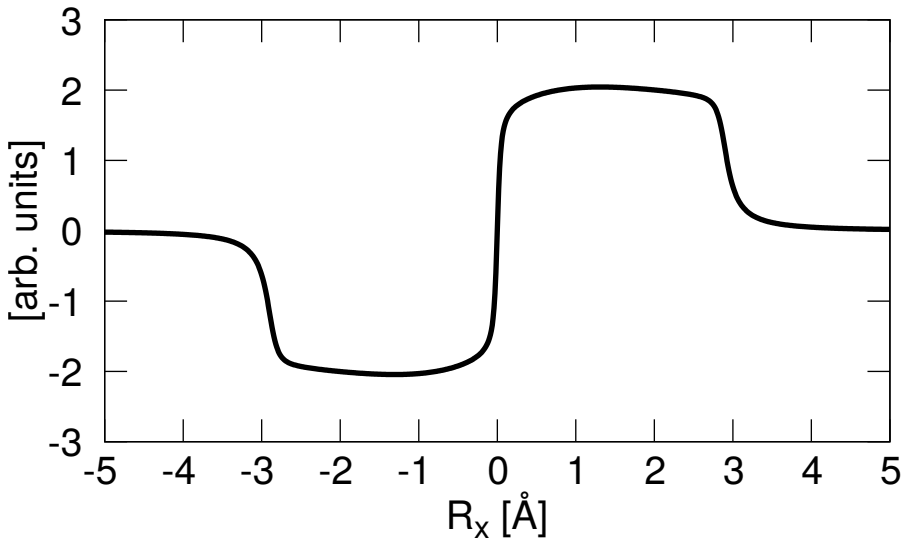

Figure 4-30: **Evaluation of $\langle \phi_2(x; R_x) \,|\, x \,|\, \phi_0(x; R_x) \rangle_x$ for the Strong Coupling Case.** The integral expression is antisymmetric with respect to the R_x coordinate.

Then, the propensity rule states, that only ungerade vibrational states in the second adiabatic excited state can be laser excited.

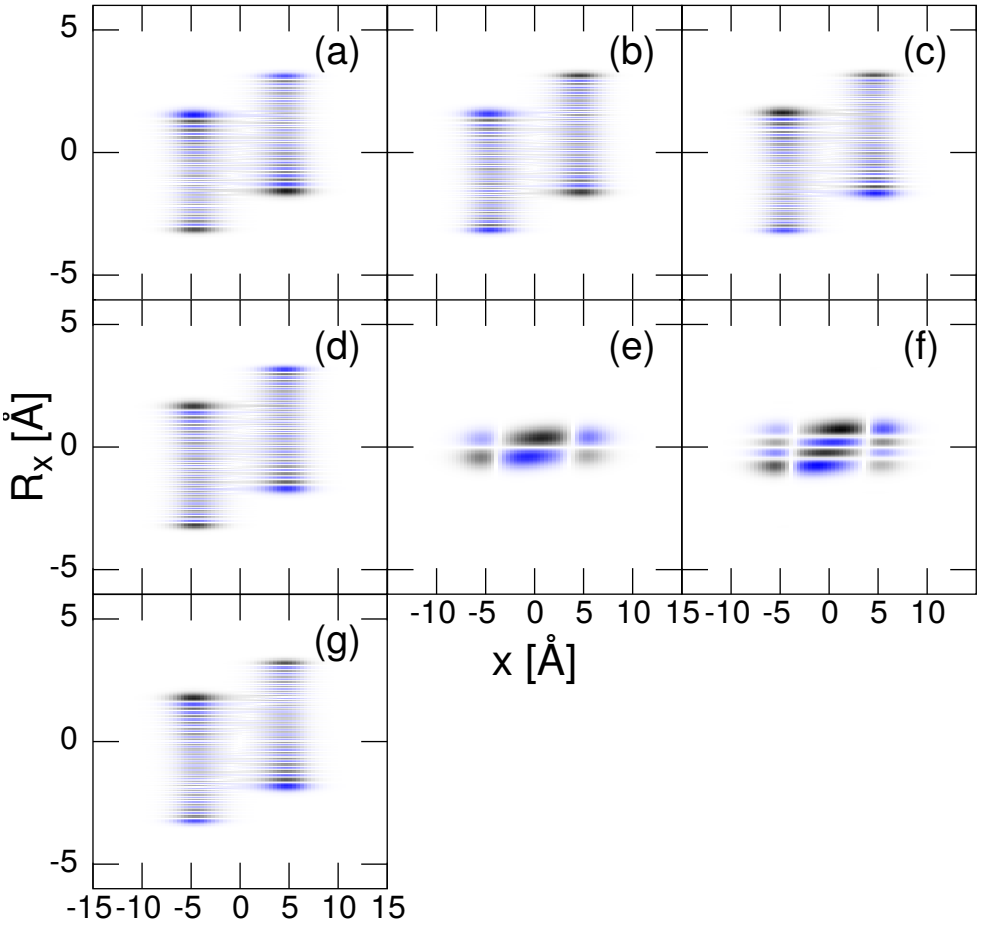

Figure 4-31: **Exact Eigenfunctions Corresponding to Final Transition States for the Absorption Spectrum of the Strong Coupling Case**. The black color shows positive values, and the blue color shows negative values of the wave function. Quantum numbers for the eigenfunctions are assigned in table 4.11.

Concluding Remarks

The linear spectroscopy for two different coupling situations was studied. In the case where the Born-Oppenheimer approximation is valid, a well defined peak progression with an overall Gaussian envelope was seen. As has already been studied [91], such spectroscopic results can also be achieved in a reduced or adiabatic representation within the Born-Oppenheimer approximation as well as in a diabatic approach.

The findings of the last section put the study one step further in the interpretation of two-dimensional spectra of the weak coupling case, as now the transitions and their intensity, prompted by a single laser-pulse, are known from the linear spectra. By keeping the same laser pulse parameters as well as the direction for the first pulse $-k_1$ for the two-dimensional laser setup, arguing about multiple transitions and their reflection in the two-dimensional spectrum is possible.
On the other hand, a more complex structure of the strong coupling case in a linear spectrum is seen, and it was found that some peaks are referred to transitions in electronically coupled states.

4.4.2 Two-Dimensional Spectra

The three-photon echo arises from the interaction of three laser pulses described by eq. (4.29), with m=3, with the system. The direction of the incoming laser pulses and of the outgoing signal is determined by the wave vector $k_s = -k_1 + k_2 + k_3$. The temporal arrangement of the laser pulses is depicted in fig. 4-32.

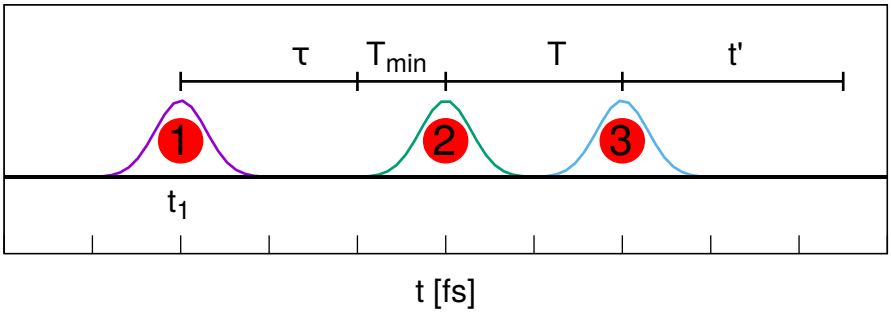

Figure 4-32: **Pulse Sequence for the Photon-Echo Experiment**. The first pulse starts the experiment, the second is delayed by τ with respect to the first pulse. After a population time T [98] and the fixed waiting time T_{min}, the third pulse generates the polarization. The correspondent signal is detected as a function of t'.

The simulation starts with the arrival of the first laser pulse at t_1. After a delay time τ, the second laser pulse acts upon the system. After the second pulse, there is a waiting time T_{min} which guarantees the pulses not to overlap [65]. Between

this waiting time and the third pulse, the time span is referred to as the population time T. Finally, the detection or acquisition time t' is set after the last laser pulse has interacted with the system. The polarization is detected as a function of the acquisition time and for different delay times τ. A double Fourier transform with respect to t' and τ finally yields a two-dimensional spectrum [62, 67, 69, 99]:

$$|S(E_{t'}, E_\tau, T)| = \left| \int_\tau \int_{t'} d\tilde{t}' d\tilde{\tau} P_{sig.}(\tilde{t}', \tilde{\tau}, T)\ e^{+iE_{t'}\tilde{t}'} e^{-iE_\tau \tilde{\tau}} \right|. \tag{4.47}$$

Here, the polarization function of third order determined within time-dependent perturbation theory (section 2.7.2) enters. It reads [62]:

$$\begin{aligned} P^{(3)}(t) = i^3 \int_0^\infty dt_3 \int_0^\infty dt_2 \int_0^\infty dt_1\ & E_1(t - t_3 - t_2 - t_1) \times \\ & E_2(t - t_3 - t_2) E_3(t - t_3) \times \\ & \sum_{a=1}^{4} \left[R_a(t_1, t_2, t_3) - R_a^*(t_1, t_2, t_3) \right]. \end{aligned} \tag{4.48}$$

As an initial condition, the system is constrained to the ground state $|\psi_{E_0}(x, R_x, t_0)\rangle$. As a result, the contributions to the polarization in which a stimulated emission is prompted by the first laser pulse can be omitted. Furthermore, excited state absorption contributions are neglected because only two state Born-Oppenheimer results are compared to the numerically exact calculations [23]. Neglecting the above mentioned contributions, the expression for the polarization reads:

$$
\begin{aligned}
P^{(3)}(t) =& \mathfrak{Im}\left\{\int_0^\infty dt_3 \int_0^\infty dt_2 \int_0^\infty dt_1 \; E_1^{(+)}(t-t_3-t_2-t_1)\times \right. \\
& E_2^{(-)}(t-t_3-t_2)E_3^{(+)}(t-t_3)R_1(t_1,t_2,t_3) \\
& + E_1^{(+)}(t-t_3-t_2-t_1)E_2^{(+)}(t-t_3-t_2)\times \\
& \left. E_3^{(-)}(t-t_3)R_2(t_1,t_2,t_3) \quad \right\}, \qquad (4.49)
\end{aligned}
$$

with the response function $R_1(t_1,t_2,t_3)$ [62]:

$$
\begin{aligned}
& R_1(t_1,t_2,t_3) = \\
& \langle \hat{\mu}(x,R_x) \,|\, \hat{\mu}(x,R_x,t_1)\hat{\mu}(x,R_x,t_1+t_2+t_3)\hat{\mu}(x,R_x,t_1+t_2) \,|\, \rho(x,R_x,t_0)\rangle_{x,R_x}. \qquad (4.50)
\end{aligned}
$$

This response demonstrates two interactions on the *ket*-element of the density matrix at times t_1 and t_1+t_2, corresponding to the first and the second laser pulse. The third light-matter interaction takes place at $t_1+t_2+t_3$ and acts upon the *bra*-element of the density matrix. A slightly different expression is $R_2(t_1,t_2,t_3)$:

$$
\begin{aligned}
& R_2(t_1,t_2,t_3) = \\
& \langle \hat{\mu}(x,R_x) \,|\, \hat{\mu}(x,R_x,t_1+t_2)\hat{\mu}(x,R_x,t_1+t_2+t_3)\hat{\mu}(x,R_x,t_1) \,|\, \rho(x,R_x,t_0)\rangle_{x,R_x}. \qquad (4.51)
\end{aligned}
$$

In what follows, the expression for the third-order polarization is derived with the two contributions to the response function above mentioned. First, a change in time variables is made accordingly to:

$$t_3' = t - t_3, \tag{4.52}$$

$$t_2' = t - t_3 - t_2, \tag{4.53}$$

$$t_1' = t - t_3 - t_2 - t_1. \tag{4.54}$$

Then, similar to the previous section, the following expression for the third-order polarization within the Hilbert space description of eigenstates $\alpha, \alpha', \alpha''$ and the initial state E_0 is obtained [65]:

$$\begin{aligned} P^{(3)}(t) =& \mathfrak{Im}\Bigg\{ \int_{-\infty}^{t} dt_3' \int_{-\infty}^{t_3'} dt_2' \int_{-\infty}^{t_2'} dt_1' \langle \psi_{E_0}(x,R_x)|\hat{U}^*(t_1'-t_0)\times \\ & \hat{\mu}(x,R_x)E_1^{(+)*}(t_1')\hat{U}^*(t_2'-t_1')\hat{\mu}(x,R_x)E_2^{(-)*}(t_2')\times \\ & \hat{U}^*(t-t_2')\hat{\mu}(x,R_x)\hat{U}(t-t_3')\hat{\mu}(x,R_x)E_3^{(+)}(t_3')\times \\ & \hat{U}(t_3'-t_0)|\psi_{E_0}(x,R_x)\rangle_{x,R_x} + \langle \psi_{E_0}(x,R_x)|\hat{U}^*(t_1'-t_0)\times \\ & \hat{\mu}(x,R_x)E_1^{(+)*}(t_1')\hat{U}^*(t_3'-t_1')\hat{\mu}(x,R_x)E_3^{(-)*}(t_3')\times \\ & \hat{U}^*(t-t_3')\hat{\mu}(x,R_x)\hat{U}(t-t_2')\hat{\mu}(x,R_x)E_2^{(+)}(t_2')\times \\ & \hat{U}(t_2'-t_0)|\psi_{E_0}(x,R_x)\rangle_{x,R_x} \quad \Bigg\}. \end{aligned} \tag{4.55}$$

The expression for the system's propagator in the basis state representation is plugged in [69, 100, 101]:

$$\hat{U}(t_p) = \sum_{\beta} |\psi_\beta(x,R_x)\rangle e^{-iE_\beta t_p} \langle \psi_\beta(x,R_x)|. \tag{4.56}$$

Furthermore, the delay time τ of the second laser pulse as well as the population time T [98] is introduced, extending the time span between the second and third pulse. Then, the laser fields become:

$$E_1(t_1') \rightarrow E_1(t_1') \tag{4.57}$$

$$E_2(t_2') \rightarrow E_2(t_2' - \tau - T_{min}) \tag{4.58}$$

$$E_3(t_3') \rightarrow E_3(t_3' - \tau - T - T_{min}) \tag{4.59}$$

Putting all together, one is left with an expression for the third-order polarization, containing time-independent factors $N_{E_0,\alpha,\alpha',\alpha''}$, which are dipole moment matrix elements. The polarization expression also contains the two time-dependent contributions $b^x_{E_0,\alpha,\alpha',\alpha''}(t,\tau,T,T_{min})$ and $b^y_{E_0,\alpha,\alpha',\alpha''}(t,\tau,T,T_{min})$, which will be regarded later.

$$\begin{aligned} P^{(3)}(\tau,T,t) =& \mathfrak{Im}\left\{ \sum_{\alpha,\alpha',\alpha''} N_{E_0,\alpha,\alpha',\alpha''} \times \right. \\ & \left. \left\{ b^x_{E_0,\alpha,\alpha',\alpha''}(t,\tau,T,T_{min}) + \; b^y_{E_0,\alpha,\alpha',\alpha''}(t,\tau,T,T_{min}) \right\} \right\}, \end{aligned} \tag{4.60}$$

Here, the $N_{E_0,\alpha,\alpha',\alpha''}$ are explicitely given by:

$$\begin{aligned} N_{E_0,\alpha,\alpha',\alpha''} =& \langle \psi_{E_0}(x,R_x) \,|\, \hat{\mu}(x,R_x) \,|\, \psi_{\alpha''}(x,R_x) \rangle_{x,R_x} \times \\ & \langle \psi_{\alpha''}(x,R_x) \,|\, \hat{\mu}(x,R_x) \,|\, \psi_{\alpha'}(x,R_x) \rangle_{x,R_x} \times \\ & \langle \psi_{\alpha'}(x,R_x) \,|\, \hat{\mu}(x,R_x) \,|\, \psi_{\alpha}(x,R_x) \rangle_{x,R_x} \times \\ & \langle \psi_{\alpha}(x,R_x) \,|\, \hat{\mu}(x,R_x) \,|\, \psi_{E_0}(x,R_x) \rangle_{x,R_x}. \end{aligned} \tag{4.61}$$

$b^x_{E_0,\alpha,\alpha',\alpha''}(t,\tau,T,T_{min})$ and $b^y_{E_0,\alpha,\alpha',\alpha''}(t,\tau,T,T_{min})$ are influenced by the electric fields and by the time evolution of eigenstates, and are defined as:

$$
\begin{aligned}
b^{x}_{E_0,\alpha,\alpha',\alpha''}(t,\tau,T,T_{min}) = \int_{-\infty}^{t} dt_3' \int_{-\infty}^{t_3'} dt_2' \int_{-\infty}^{t_2'} dt_1' \times \\
& e^{-\alpha\left[(t_3'-\tau-T-T_{min})^2+(t_2'-\tau-T_{min})^2+(t_1')^2\right]} \times \\
& e^{-i\omega_3\ (t_3'-\tau-T-T_{min})}\ e^{-i\omega_2(t_2'-\tau)}\ e^{i\omega_1 t_1'} \times \\
& e^{i(E_\alpha-E_{E_0})t_3'}\ e^{i(E_{\alpha''}-E_{\alpha'})t_2'}\ e^{i(E_{E_0}-E_{\alpha''})t_1'}\ e^{i(E_{\alpha'}-E_\alpha)t},
\end{aligned}
\tag{4.62}
$$

and

$$
\begin{aligned}
b^{y}_{E_0,\alpha,\alpha',\alpha''}(t,\tau,T,T_{min}) = \int_{-\infty}^{t} dt_3' \int_{-\infty}^{t_3'} dt_2' \int_{-\infty}^{t_2'} dt_1' \times \\
& e^{-\alpha\left[(t_3'-\tau-T-T_{min})^2+(t_2'-\tau-T_{min})^2+(t_1')^2\right]} \times \\
& e^{-i\omega_3(t_3'-\tau-T-T_{min})}\ e^{-i\omega_2(t_2'-\tau)}\ e^{i\omega_1 t_1'} \times \\
& e^{i(E_{\alpha''}-E_{\alpha'})t_3'}\ e^{i(E_\alpha-E_{E_0})t_2'}\ e^{i(E_{E_0}-E_{\alpha''})t_1'}\ e^{i(E_{\alpha'}-E_\alpha)t}.
\end{aligned}
\tag{4.63}
$$

Finally, introducing the new time variables:

$$
\begin{aligned}
t' &= t-\tau-T-T_{min}, \\
\tilde{t}_1 &= t_1', \\
\tilde{t}_2 &= t_2'-\tau-T_{min} \quad \text{and} \\
\tilde{t}_3 &= t_3'-\tau-T-T_{min},
\end{aligned}
\tag{4.64}
$$

eq. (4.60) can be rearranged in time and, therefore, the time-dependent contributions are transformed to $b'^{,x}_{E_0,\alpha,\alpha',\alpha''}(t',\tau,T,T_{min})$ and $b'^{,y}_{E_0,\alpha,\alpha',\alpha''}(t',\tau,T,T_{min})$. Because the laser pulses are finite, the boundaries for the integrals over t_1', t_2' and t_3' can be extended to infinity:

$$
\begin{aligned}
b'^{,x}_{E_0,\alpha,\alpha',\alpha''}(t',\tau,T,T_{min}) = &\int_{-\infty}^{\infty} d\tilde{t}_3 \int_{-\infty}^{\infty} d\tilde{t}_2 \int_{-\infty}^{\infty} d\tilde{t}_1 \times \\
&e^{-\alpha\left[(\tilde{t}_3)^2+(\tilde{t}_2)^2+(\tilde{t}_1)^2\right]}\ e^{-i\omega_3\tilde{t}_3}\ e^{-i\omega_2\tilde{t}_2}\ e^{i\omega_1\tilde{t}_1} \times \\
&e^{i(E_\alpha - E_{E_0})\tilde{t}_3}\ e^{i(E_{\alpha''}-E_{\alpha'})\tilde{t}_2}\ e^{i(E_{E_0}-E_{\alpha''})\tilde{t}_1} \times \\
&e^{-i(E_{E_0}-E_{\alpha''})\tau}\ e^{-i(E_{E_0}-E_{\alpha'})T}\ e^{-i(E_\alpha - E_{\alpha'})t'} \times \\
&e^{-i(E_{E_0}-E_{\alpha''})T_{min}}.
\end{aligned}
\tag{4.65}
$$

$$
\begin{aligned}
b'^{,y}_{E_0,\alpha,\alpha',\alpha''}(t',\tau,T,T_{min}) = &\int_{-\infty}^{\infty} d\tilde{t}_3 \int_{-\infty}^{\infty} d\tilde{t}_2 \int_{-\infty}^{\infty} d\tilde{t}_1 \times \\
&e^{-\alpha\left[(\tilde{t}_3)^2+(\tilde{t}_2)^2+(\tilde{t}_1)^2\right]}\ e^{-i\omega_3\tilde{t}_3}\ e^{-i\omega_2\tilde{t}_2}\ e^{i\omega_1\tilde{t}_1} \times \\
&e^{i(E_{\alpha''}-E_{\alpha'})\tilde{t}_3}\ e^{i(E_\alpha - E_i)\tilde{t}_2}\ e^{i(E_{E_0}-E_{\alpha''})\tilde{t}_1} \times \\
&e^{-i(E_{E_0}-E_{\alpha''})\tau}\ e^{-i(E_\alpha - E_{\alpha''})T}\ e^{-i(E_\alpha - E_{\alpha'})t'} \times \\
&e^{-i(E_{E_0}-E_{\alpha''})T_{min}}.
\end{aligned}
\tag{4.66}
$$

Finally, one can simplify eq. (4.60) to:

$$
\begin{aligned}
P^{(3)}(\tau,T,t',T_{min}) = &\mathfrak{Im}\left\{ \sum_{\alpha,\alpha',\alpha''} N_{E_0,\alpha,\alpha',\alpha''} \left\{ \tilde{b}^x_{E_0,\alpha,\alpha',\alpha''}\ e^{-i(E_{E_0}-E_{\alpha'})T} \right.\right. \\
&\left. + \tilde{b}^y_{E_0,\alpha,\alpha',\alpha''} e^{-i(E_\alpha - E_{\alpha''})T} \right\} \times \\
&\left.\left. e^{-i(E_{E_0}-E_{\alpha''})\tau} e^{-i(E_\alpha - E_{\alpha'})t'} e^{-i(E_{E_0}-E_{\alpha''})T_{min}} \right\}.
\end{aligned}
\tag{4.67}
$$

where $\tilde{b}^x_{E_0,\alpha,\alpha',\alpha''}$ belongs to the right-hand double-sided Feynman diagram in fig. 4-33 and is defined as:

$$\tilde{b}^{x}_{E_0,\alpha,\alpha',\alpha''} = \int_{-\infty}^{\infty} d\tilde{t}_3 \int_{-\infty}^{\infty} d\tilde{t}_2 \int_{-\infty}^{\infty} d\tilde{t}_1 \times \\ e^{-\alpha\left[(\tilde{t}_3)^2+(\tilde{t}_2)^2+(\tilde{t}_1)^2\right]}\ e^{-i\omega_3\tilde{t}_3}\ e^{-i\omega_2\tilde{t}_2}\ e^{i\omega_1\tilde{t}_1} \times \\ e^{i(E_\alpha - E_{E_0})\tilde{t}_3}\ e^{i(E_{\alpha''} - E_{\alpha'})\tilde{t}_2}\ e^{i(E_{E_0} - E_{\alpha''})\tilde{t}_1}, \tag{4.68}$$

and $\tilde{b}^{y}_{E_0,\alpha,\alpha',\alpha''}$ belongs to the left-hand double-sided Feynman diagram in fig. 4-33 and is defined as:

$$\tilde{b}^{y}_{E_0,\alpha,\alpha',\alpha''} = \int_{-\infty}^{\infty} d\tilde{t}_3 \int_{-\infty}^{\infty} d\tilde{t}_2 \int_{-\infty}^{\infty} d\tilde{t}_1 \times \\ e^{-\alpha\left[(\tilde{t}_3)^2+(\tilde{t}_2)^2+(\tilde{t}_1)^2\right]}\ e^{-i\omega_3\tilde{t}_3}\ e^{-i\omega_2\tilde{t}_2}\ e^{i\omega_1\tilde{t}_1} \times \\ e^{i(E_{\alpha''} - E_{\alpha'})\tilde{t}_3}\ e^{i(E_\alpha - E_{E_0})\tilde{t}_2}\ e^{i(E_{E_0} - E_{\alpha''})\tilde{t}_1}. \tag{4.69}$$

Out of the polarization, a two-dimensional spectrum is obtained by a double Fourier transform in τ and t'.

$$|S(E_{t'}, E_\tau, T, T_{min})| = \left| \int_\tau d\tilde{\tau} \int_{t'} d\tilde{t}' e^{i(E_{t'}\tilde{t}' - E_\tau\tilde{\tau})} \mathfrak{Im}\left\{ P^{(3)}(\tilde{\tau}, T, \tilde{t}', T_{min}) \right\} \right|. \tag{4.70}$$

Strictly regarding the two only contributions, where the light-matter interaction prompts an absorptive process in $-k_1$ direction, one is left with the expression for the modulus of the two-dimensional spectrum:

$$|S(E_{t'}, E_\tau, T, T_{min})| = \Bigg| \sum_{\alpha,\alpha',\alpha''} N_{E_0,\alpha,\alpha',\alpha''}\ e^{-i(E_{E_0}-E_{\alpha''})T_{min}} \times \Big\{ \tilde{b}^x_{E_0,\alpha,\alpha',\alpha''} e^{-i(E_{E_0}-E_{\alpha'})T} + \tilde{b}^y_{E_0,\alpha,\alpha',\alpha''} e^{-i(E_\alpha - E_{\alpha''})T} \Big\} \times \delta(E_\tau - [E_{\alpha''} - E_{E_0}])\delta(E_{t'} - [E_\alpha - E_{\alpha'}]) \Bigg| . \tag{4.71}$$

With the direction and the temporal order of the pulses, the following contributions, which are displayed in a double-sided Feynman diagram [62], are given:

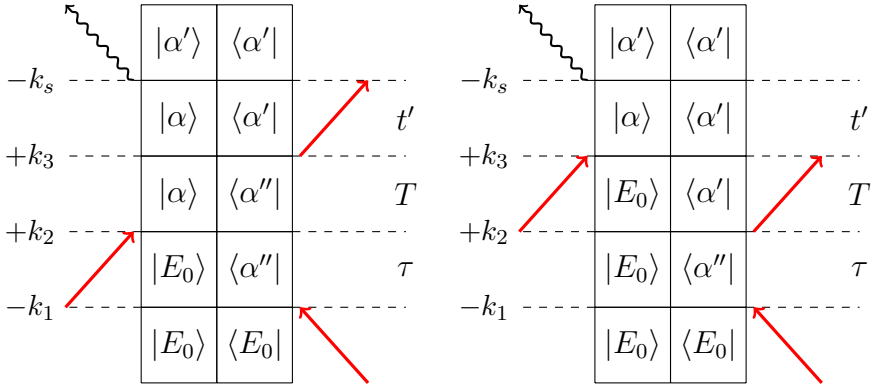

Figure 4-33: **Double-Sided Feynman Diagram Illustrating Two Contributions to the Two-Dimensional Spectrum**. Depicted are the two contributions to the spectral signal left due to eq. (4.71).

The parameters used in the simulation are summarized in table 4.12.

Table 4.12: **Parameters for the Calculation of the Two-Dimensional Spectra.**

symbol:	description:	weak coupling	strong coupling
τ	delay time	325.6 fs	325.6 fs
T_{min}	waiting time	9.3 fs	9.3 fs
T	population time	0.0 fs	0.0 fs
t'	aquisition time	325.6 fs	325.6 fs
E_{off}	offset energy	11.58 eV	10.01 eV
R_c	shielding: e^- and p^+	1.5 Å	2.5 Å
α	Gaussian broadening	$1.0 \cdot 10^{-4}$ $\frac{1}{\text{fs}^2}$	$1.0 \cdot 10^{-4}$ $\frac{1}{\text{fs}^2}$
$\omega_1 = \omega_2 = \omega_3$	excitation energy	2.9 eV	1.9 eV

4.4.2.1 Weak Coupling

For the third-order polarization, the following two contributions for the simulation are needed:

$$\begin{aligned} P^{(3,ex)}(-k_1,+k_2,+k_3,t) = \\ \langle\psi_1^{(2,ex)}(+k_2,-k_1,x,R_x,t)\,|\,\hat{\mu}(x,R_x)\,|\,\psi^{(1,ex)}(+k_3,x,R_x,t)\rangle_{x,R_x} \\ +\langle\psi_1^{(2,ex)}(+k_3,-k_1,x,R_x,t)\,|\,\hat{\mu}(x,R_x)\,|\,\psi^{(1,ex)}(+k_2,x,R_x,t)\rangle_{x,R_x}. \end{aligned} \tag{4.72}$$

These two contributions are obtained from eq. (4.67).
The third-order polarization is calculated exemplarily for $\langle\psi_1^{(2,ex)}(+k_2,-k_1,x,R_x,t)|$ in eq. (4.72) via:

$$\begin{aligned} \langle\psi^{(1,ex)}(-k_1,x,R_x,t+\Delta t)| =& \hat{U}^*(\Delta t)\langle\psi^{(1,ex)}(-k_1,x,R_x,t)| \\ &+ i\Delta t\left(\hat{\mu}(x,R_x)E_1^+(t+\Delta t)\right)\langle\psi_{E_0}^{(0,ex)}(x,R_x,t+\Delta t)|, \end{aligned} \tag{4.73}$$

then, for the second order, the perturbative propagation of the wave function is:

$$\langle\psi^{(2,ex)}(+k_2-k_1,x,R_x,t+\Delta t)| = \hat{U}^*(\Delta t)\langle\psi^{(2,ex)}(+k_2-k_1,x,R_x,t)| + i\Delta t\left(\hat{\mu}(x,R_x)E_2^-(t+\Delta t)\right)\langle\psi^{(1,ex)}(-k_1,x,R_x,t+\Delta t)|. \quad (4.74)$$

And finally, the term $|\psi^{(1,ex)}(+k_3,x,R_x,t)\rangle$:

$$|\psi^{(1,ex)}(+k_3,x,R_x,t+\Delta t)\rangle = \hat{U}(\Delta t)|\psi^{(1,ex)}(+k_3,x,R_x,t)\rangle - i\Delta t\left(\hat{\mu}(x,R_x)E_3^-(t+\Delta t)\right)|\psi_{E_0}^{(0,ex)}(x,R_x,t+\Delta t)\rangle, \quad (4.75)$$

where the exact propagation of the wave function is used. Applying the Born-Oppenheimer approximation, the perturbative calculation can be analogously specified, with $n,p=1,2$ and $m=0$, as:

$$\langle\chi_n^{(1,BO)}(k_1,R_x,t+\Delta t)| = \hat{U}_n^*(R_x,\Delta t)\langle\chi_n^{(1,BO)}(k_1,R_x,t)| + i\Delta t\left(\hat{\mu}_{n0}(R_x)E_1^+(t+\Delta t)\right)\langle\chi_0^{(0,BO)}(R_x,t+\Delta t)|, \quad (4.76)$$

$$\langle\chi_m^{(2,BO)}(-k_2+k_1,R_x,t+\Delta t)| = \hat{U}_m^*(R_x,\Delta t)\langle\chi_m^{(2,BO)}(-k_2+k_1,R_x,t)| + i\Delta t\left(\hat{\mu}_{mn}(R_x)E_2^-(t+\Delta t)\right)\langle\chi_n^{(1,BO)}(k_1,R_x,t+\Delta t)| \quad (4.77)$$

and

$$|\chi_p^{(1,BO)}(+k_3, R_x, t+\Delta t)\rangle = \hat{U}_p(R_x, \Delta t)|\chi_p^{(1,BO)}(+k_3, R_x, t)\rangle - i\Delta t\left(\hat{\mu}_{p0}(R_x)E_3^-(t+\Delta t)\right)|\chi_0^{(0,BO)}(R_x, t+\Delta t)\rangle, \tag{4.78}$$

with:

$$\hat{U}_n(R_x, \Delta t) = e^{-i\left(-\frac{1}{2M}\nabla_{R_x}^2 + u_{nn}(\vec{R}_x)\right)\Delta t}. \tag{4.79}$$

Combining the Born-Oppenheimer treatment with the knowledge obtained from the linear absorption spectrum for the weak coupling case, one expects peaks along the diagonal with a vibrational progression because the electronic ground state and the excited state are almost decoupled from each other.

This is indeed the case, both for the exact propagation scheme and for the propagation within the Born-Oppenheimer approximation, as can be seen in fig. 4-34. The absolute value of the two-dimensional spectrum for the exact calculation (left hand panel) matches perfectly with the spectrum calculated in the approximated picture.

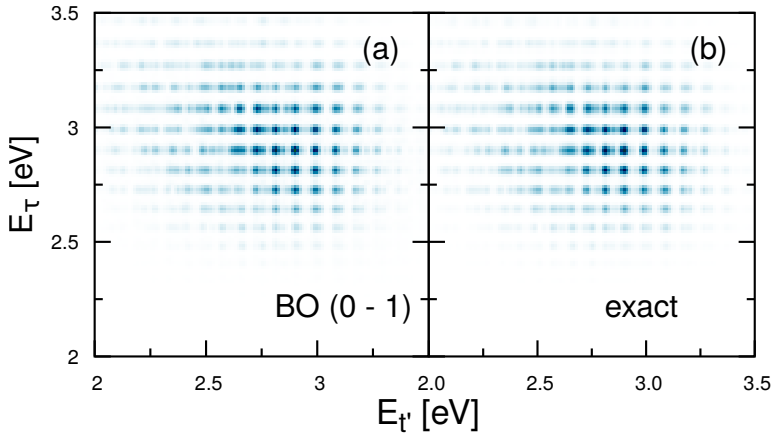

Figure 4-34: **Two-Dimensional Spectrum of the Weak Coupling Case**. The peaks are given as absolute of the signal in arbitrary units. Panel (a) shows the spectrum obtained within the adiabatic treatment. Panel (b) shows the spectrum obtained from the exact propagation scheme.

The two-dimensional spectrum exhibits, as expected, peaks along the diagonal at approximately $E_{t'} = E_\tau = 2.9$ eV. Comparing this to the eigenenergies obtained in section 4.2.1 and to the vertical excitation in fig. 4-25, it is in very good agreement. This can be characterized as the transition from the ground state to the adiabatic first electronic excited state. This fact now helps to characterize the peaks along the $E_{t'}$ axis, which is a more complex task regarding eq. (4.80), eq. (4.71) and corresponding double-sided Feynman diagrams. According to this, a huge variety of combinations of energy differences $E_{\alpha'} - E_\alpha$ is possible to reflect the peaks appearing along the $E_{t'}$ axis. This is due to the fact that these peaks are the result of three laser pulses acting upon the system, each with a strong energetic broadening [23].

$$E_\tau = (E_{\alpha''} - E_{E_0}) \text{ and } E_{t'} = (E_{\alpha'} - E_\alpha). \tag{4.80}$$

Remembering that the two-dimensional spectrum can be reproduced by the adiabatic calculation, puts some constrains to the interpretation of the transitions during the detection time t'. The decoupled adiabatic states and the laser pulse

settings allow transitions between the vibrational states within the adiabatic electronic ground state $|\psi_{0,\nu}(x, R_x)\rangle$ and the adiabatic electronic first excited state $|\psi_{1,\nu'}(x, R_x)\rangle$. Then, the quantum numbers can be chosen according to the electronic and nuclear degree of freedom and yield as peak structure:

$$E_\tau = (E_{1,\nu''} - E_{0,0}) \text{ and } E_{t'} = (E_{0,\nu} - E_{1,\nu'}). \tag{4.81}$$

In the signal, these transitions are not too difficult to interpret and are derived from transitions within the vibrational energy levels in the adiabatic ground state and first electronic excited state. The peaks appearing at smaller $E_{t'}$ arise because $E_{0,\nu} > E_{0,0}$ for $\nu \neq 0$. Then $|E_{0,\nu} - E_{1,\nu'}| < |E_{1,\nu''} - E_{0,0}|$. A double-sided Feynman diagram shows the possible transitions:

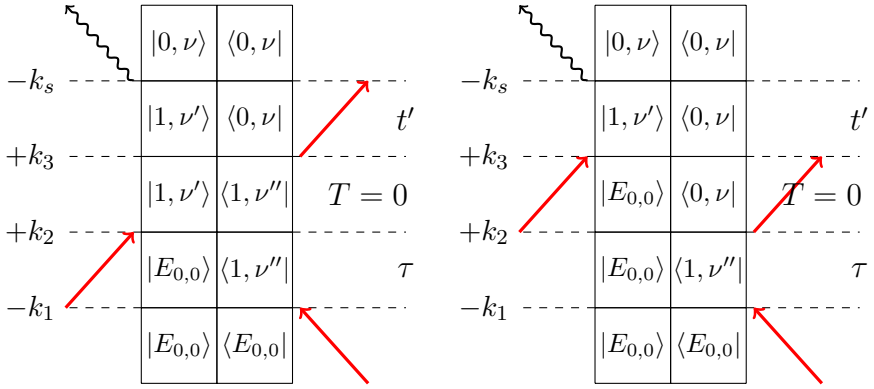

Figure 4-35: **Double-Sided Feynman Diagram for the Two-Dimensional Spectrum of the Weak Coupling Case**. Depicted are the two contributions left due to the selection rules put on the simualtion, but with further restrictions on vibrational ν, ν', ν'' and electronic states $0, 1$ involved during the experiment.

4.4.2.2 Strong Coupling

Next, the two-dimensional spectrum of the strong coupling case with $R_c = 2.5$ Å is studied. The spectrum is calculated with a photon energy of 1.9 eV for all pulses. It displays a rather complicated structure. As can be seen in fig. 4-36, a diagonal component in the peak structure at about $E_\tau = E_{t'} = 2.6$ eV is visible. Regarding the absorption spectrum fig. 4-27, this corresponds to transitions in the

second excited state. Additionally, in fig. 4-36 panel (a) shows the transition to the first excited state, calculated in the adiabatic representation within the Born-Oppenheimer approximation. Also here, a diagonal peak at $E_\tau = E_{t'} = 2.6$ eV can be matched to the transition in the exact calculated spectrum in region (β) in panel (c).

The spectrum also exhibits peaks in the region (δ) of $E_\tau = E_{t'} = 1.9$ eV which correspond to the $|\psi_{E_0}(x, R_x)\rangle$ and $|\psi_{mix}(x, R_x)\rangle$ transition, see fig. 4-29, but these are rather small as can be confirmed by the absorption spectra from section 4.4.1.2. These peaks, however, are of high interest, because they are influenced by non-adiabatic coupling. In the case of calculating the transition between $|\psi_{E_0}(x, R_x)\rangle$ and $|\psi_{mix}(x, R_x)\rangle$ in the adiabatic framework, or Born-Oppenheimer framework, fig. 4-36 panel (b) shows that this spectrum is in bad agreement with the exact calculated one, panel (c). This is because the coupling is neglected in this calculation, and it has already been seen that the coupling is essential for the structure of the eigenfunctions in section 4.4.1.1 and in the calculation of absorption spectra [91].

This confirms that these peaks can not be matched to certain electronic or vibrational transitions, because they are electronically coupled and exhibit a non-trivial structure [23].

Though, an interpretation of the two-dimensional exact spectrum of the strong coupling situation is possible. Starting with the yet uncharacterized region (α) in the interval $E_\tau = [2.25; 3.0]$ eV and approximately $E_{t'} = [0.75; 2.3]$ eV, this region derives from high energetic coherences during the coherence time τ [99]. They are prompted after the first laser pulse has excited the model system. This energetic difference must correspond to the second excited state transitions, regarding the energy of 2.7 eV along the E_τ-axis. The small energy components in $E_{t'}$-direction are then prompted by coherences between the mixed states and the second excited state. There, energetic spacings of at least 0.5 eV and higher are present. These transitions correspond to the off-diagonal region in the two-dimensional spectrum.

Also noteworthy are transitions defining the second off-diagonal region in the interval between the $E_\tau = [1.5; 2.3]$ eV and $E_{t'} = [2.3; 3.0]$ eV. These peaks are mainly formed by transitions to the states with mixed electronic characteristic prompted by the first laser pulse. After this, during the acquisition time, coherences between the second excited state and the ground state are seen, as this is the only energetic difference high enough in energy to match the values of $E_{t'} = 1.9$ eV.

Regarding the two-dimensional spectrum of the strong coupling case, one is still left with the question whether the two-dimensional spectrum can reveal the mixing character of the adiabatic ground state and adiabatic first excited state. This indeed can not be distinguished by this numerical experiment. The only fact seen is the appearance of states coupled via the light-matter interaction and exhibit a defined energetic window, in which transitions are allowed.

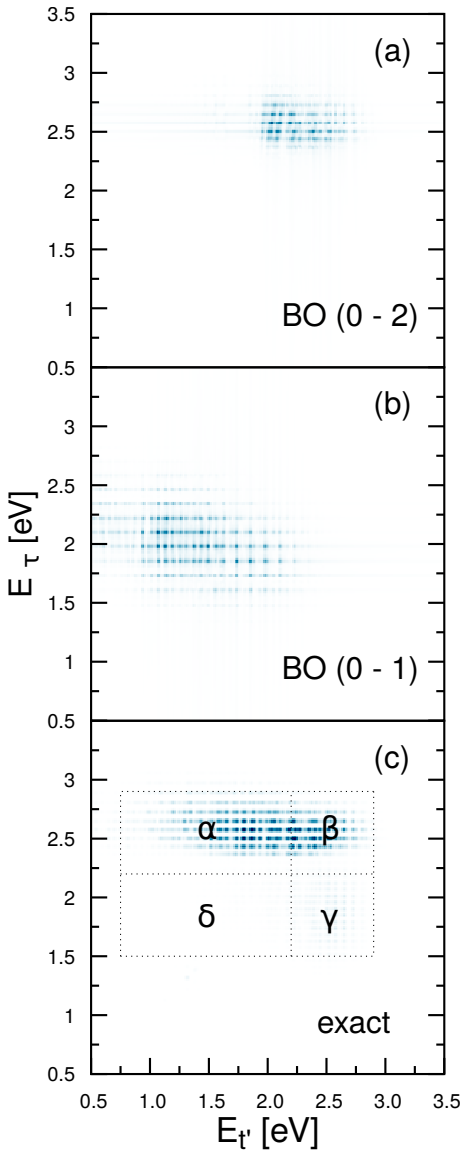

Figure 4-36: **Two-Dimensional Spectrum of the Strong Coupling Case**. The peaks are given as the absolute signal in arbitrary values. Panel (a) shows the spectrum within the adiabatic treatment of ground state and second excited adiabatic state. The validity of the Born-Oppenheimer approximation is assumed. Panel (b) shows the spectrum within the adiabatic treatment of ground state and first excited adiabatic state. Panel (c) contains the spectrum obtained from the exact propagation.

4.4.3 Distinction between Vibrational and Electronic Coherences

In the last section the polarization function was regarded as a function of the delay-time τ and the acquisition time t'. This gave the information about the coherences appearing between the first and the second pulse and after the third pulse, respectively. The population time T was set to $T = 0$ fs. A variation of the population time implies coherences and, therefore, oscillations in the intensity of the two-dimensional spectrum. These oscillations are often matched to electronic, vibrational and vibronic coherences within the model system [102–106].

This section is dedicated to the distinction of the characteristics of such oscillations. The numerical experiments for the weak coupling and strong coupling case are repeated, but in contrast, the delay time τ and the detection time t' are fixed to a value of $\tau = 0$ fs and $t' = 9.3$ fs, respectively. Only the population time T is varied in the interval $T = [0.0, 232.6]$ fs. The polarization is proportional to the terms given in eq. (4.82) [23]:

$$P^{(3,ex)}(t', \tau, T) \sim e^{i(E_{\alpha'} - E_{\alpha})t'} \; e^{i(E_{\alpha''} - E_{E_0})\tau} \left\{ e^{i(E_{\alpha'} - E_{E_0})T} + e^{i(E_{\alpha''} - E_{E_0})T} \right\}. \tag{4.82}$$

In the case of the weak coupling situation, the numerically exact spectrum can be reproduced within the Born-Oppenheimer treatment. As a result, peaks can be matched to the quantum numbers α, α' and α'' appearing in eq. (4.82) to product states of an electronic and vibrational component [23]:

$$\begin{aligned} P^{(3,BO)}(t', \tau, T) \sim \; & e^{i(E_{0,v} - E_{1,v})t'} \; e^{i(E_{1,v''} - E_{0,0})\tau} \times \\ & \left\{ e^{i(E_{0,v} - E_{0,0})T} + e^{i(E_{1,v''} - E_{1,v'})T} \right\}, \end{aligned} \tag{4.83}$$

where the appearing coherences during the population time T are of vibrational character in the electronically excited state and of the ground state, respectively.

These are inter-electronic vibrational coherences. A comparison to the exactly calculated spectrum obtained by:

$$S(E_T) = \frac{1}{\sqrt{2\pi}} \int_T d\tilde{T} P^{(3,ex)}(t', \tau, \tilde{T})\ e^{+iE_T\tilde{T}} \tag{4.84}$$

and the spectrum obtained within the Born-Oppenheimer treatment using $P^{(3,BO)}(t', \tau, T)$ shows a good agreement and proves the statement.

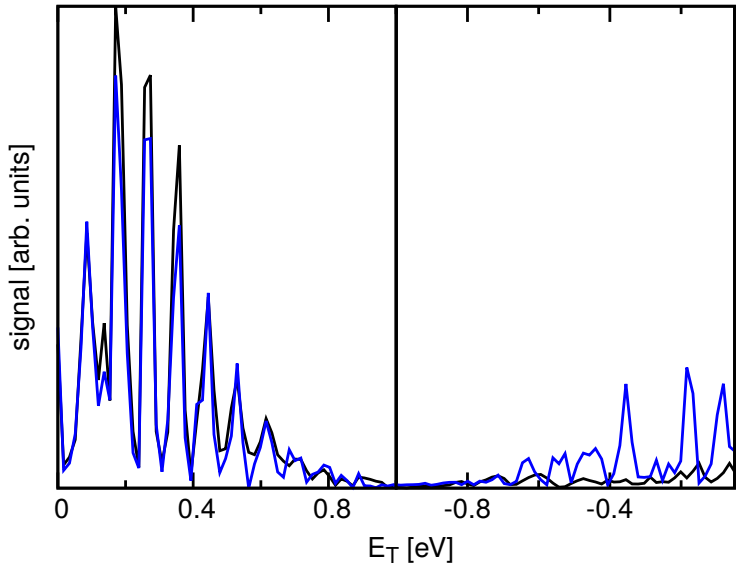

Figure 4-37: **Abolute Spectrum Showing Coherences during the Population Time T within the Weak Coupling Case**. The black curve represents the spectrum, simulated within the adiabatic framework and the assumption of the Born-Oppenheimer approximation. The blue curve shows the spectrum within the exact propagation scheme.

In fig. 4-37, both positive and negative energy differences appear as can be checked by eq. (4.83). On the other hand, in the strong coupling case it is not possible to distinguish between vibrational and electronic coherences because of the non-adiabatic coupling between the adiabatic ground state and the adiabatic first excited state. Therefore, coherences are of strongly mixed vibronic character in the spectrum fig. 4-38. The blue line shows the exact calculation and neither the

black nor the red line, obtained from the Born-Oppenheimer treatment incorporating the first and second excited state, respectively, can reproduce the exact spectrum [23].

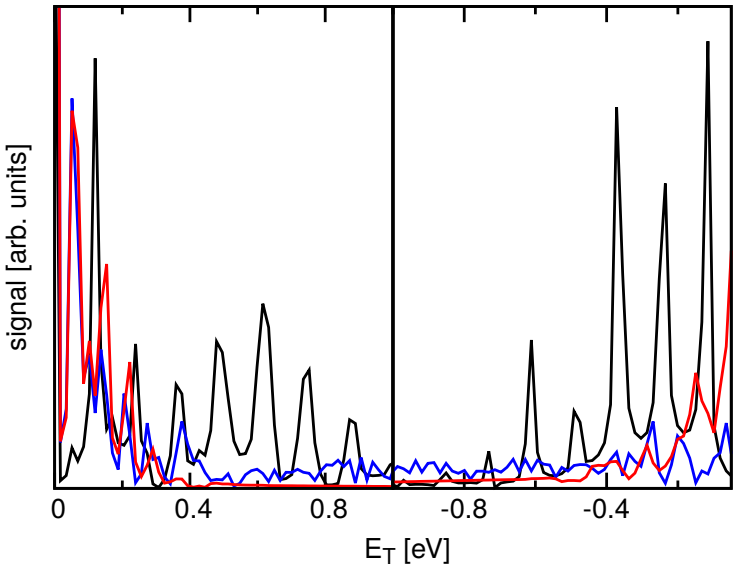

Figure 4-38: **Abolute Spectrum Showing Coherences during Population Time T within the Strong Coupling Case**. The black and red curve represent the spectrum, simulated within the adiabatic framework between the ground state and the first and second excited state, respectively. The blue curve shows the spectrum within the exact propagation scheme.

Concluding Remarks

The results show that only in case of an adiabatic dynamic within the validity of the Born-Oppenheimer approximation, the distinction of vibrational from other characteristic oscillations is possible within a two-level system, where the three photon-experiment prompts only transitions within the two weakly coupled adiabatic states. In case of non-adiabatic coupling, which can not be neglected, a distinction between vibrational and electronic coherences is not possible. The properties of eigenfunctions being of mixed electronic character strictly leads then to the apperance of vibronic coherences.

4.4.4 Degenerated Four-Wave Mixing

Next, the time-resolved four-wave mixing (FWM) signal of the model is calculated. The impact of non-adiabatic coupling on the FWM signal of the weak coupling and strong coupling case is studied again and the previous study is continued. With the FWM signal, one is able to look at ground state and excited state wave-packet dynamics [107–113].

The laser setup consists of four equal pulses. The first and the second pulse act simultaneously, while the third pulse is delayed by a time τ with both positive and negative values to the previous two pulses. Last but not least, a fourth pulse serves as to record the third-order signal in a homodyne detection scheme [72]. To calculate such signals only three pulses are needed, though, given in eq. (4.85); then the setup is arranged like in fig. 4-39.

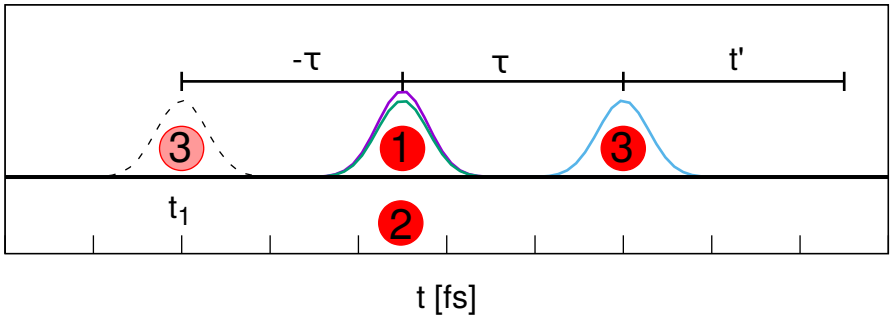

Figure 4-39: **Pulse Sequence for a FWM Signal Experiment**. The scheme shows the first pulse and the second pulse to interact simultaneously, and the third pulse being delayed with both negative delay times and positive delay times with respect to the first two pulses.

$$E(t) = \sum_{n=1}^{3} \left(E_n^{(+)}(t - t_n) + E_n^{(-)}(t - t_n) \right). \tag{4.85}$$

The components are given as :

$$E_n^{(\pm)}(t - t_n) = \frac{1}{2} e^{-\alpha(t-t_n)^2} \cdot e^{\mp i\omega_n(t-t_n)}. \tag{4.86}$$

This time, the signal in direction $k_s = k_1 - k_2 + k_3$ is detected. The polarization is numerically calculated according to eq. (4.87), where only a single contribution is regarded [113, 114].

$$P^{(3,ex)}(t,\tau) = \langle \psi^{(0,ex)}(x, R_x, t) \,|\, \hat{\mu}(x, R_x) \,|\, \psi^{(3,ex)}(k_3 - k_2 + k_1, x, R_x, t) \rangle_{x,R_x}. \tag{4.87}$$

In case of a Born-Oppenheimer treatment, one can be more specific and use transitions between adiabatic states. So, the third-order polarization is written as:

$$P^{(3,BO)}(t,\tau) = \langle \chi_1^{(0,BO)}(R_x, t) \,|\, \hat{\mu}_{1n}(R_x) \,|\, \chi_n^{(3,BO)}(k_3 - k_2 + k_1, R_x, t) \rangle_{x,R_x}. \tag{4.88}$$

The third-order polarization is numerically obtained via time-dependent perturbation theory, see section 3.5.

$$\begin{aligned} |\psi^{(1,ex)}(k_1, x, R_x, t + \Delta t)\rangle =& \hat{U}(\Delta t) |\psi^{(1,ex)}(k_1, x, R_x, t)\rangle \\ & - i\Delta t \left(\hat{\mu}(x, R_x) E_1^+(t + \Delta t)\right) |\psi^{(0,ex)}(x, R_x, t + \Delta t)\rangle, \end{aligned} \tag{4.89}$$

$$\begin{aligned} |\psi^{(2,ex)}(-k_2 + k_1, x, R_x, t + \Delta t)\rangle &= \hat{U}(\Delta t) |\psi^{(2,ex)}(-k_2 + k_1, x, R_x, t)\rangle \\ - i\Delta t \left(\hat{\mu}(x, R_x) E_2^-(t + \Delta t)\right) &|\psi^{(1,ex)}(k_1, x, R_x, t + \Delta t)\rangle \end{aligned} \tag{4.90}$$

and

$$|\psi^{(3,ex)}(k_3 - k_2 + k_1, x, R_x, t + \Delta t)\rangle = \hat{U}(\Delta t)|\psi^{(3,ex)}(k_3 - k_2 + k_1, x, R_x, t)\rangle$$
$$- i\Delta t \left(\hat{\mu}(x, R_x)E_3^+(t + \Delta t)\right) |\psi^{(2,ex)}(k_2 + k_1, x, R_x, t + \Delta t)\rangle. \quad (4.91)$$

In the Born-Oppenheimer treatment, the perturbation can be specified, with $n, p = 1, 2$ and $m = 0$, as:

$$|\chi_n^{(1,BO)}(k_1, R_x, t + \Delta t)\rangle = \hat{U}_n(\Delta t)|\chi_n^{(1,BO)}(k_1, R_x, t)\rangle$$
$$- i\Delta t \left(\hat{\mu}_{n0}(R_x)E_1^+(t + \Delta t)\right) |\chi_0^{(0,BO)}(R_x, t + \Delta t)\rangle, \quad (4.92)$$

$$|\chi_m^{(2,BO)}(-k_2 + k_1, R_x, t + \Delta t)\rangle = \hat{U}_m(\Delta t)|\chi_m^{(2,BO)}(-k_2 + k_1, R_x, t)\rangle$$
$$- i\Delta t \left(\hat{\mu}_{mn}(R_x)E_2^-(t + \Delta t)\right) |\chi_n^{(1,BO)}(k_1, R_x, t + \Delta t)\rangle \quad (4.93)$$

and

$$|\chi_p^{(3,BO)}(k_3 - k_2 + k_1, R_x, t + \Delta t)\rangle = \hat{U}_p(\Delta t)|\chi_p^{(3,BO)}(k_3 - k_2 + k_1, R_x, t)\rangle$$
$$- i\Delta t \left(\hat{\mu}_{pm}(R_x)E_3^+(t + \Delta t)\right) |\chi_m^{(2,BO)}(k_2 + k_1, R_x, t + \Delta t)\rangle. \quad (4.94)$$

According to the homodyne detection [72], the absolute square of the polarization is integrated over a time-span of $T_p = 23.4$ fs.

$$S^{(s)}(\tau) = \int_{-T_p}^{T_p} dt |P^{(3,s)}(t, \tau)|^2 \quad (4.95)$$

For the calculation, the parameters in table 4.13 are given for both cases:

Table 4.13: **Model Parameters for the Calculation of the Degenerate Four-Wave Mixing Signal.**

symbol:	description:	weak coupling	strong coupling
$\pm\tau$	delay time	186.0 fs	186.0 fs
E_{off}	offset energy	11.58 eV	10.01 eV
R_c	shielding: e^- and p^+	1.5 Å	2.5 Å
α	Gaussian broadening	$1.0 \cdot 10^{-4}$ $\frac{1}{\text{fs}^2}$	$1.0 \cdot 10^{-4}$ $\frac{1}{\text{fs}^2}$
ω	excitation energy	2.9 eV	1.9 eV

4.4.4.1 Weak Coupling

First, the weak coupling case is regarded. Pulses of a bandwidth of 2.8 fs and a central frequency of 2.9 eV are used. These pulse parameters justify the use of the impulsive limit [72]. Within this limit, the third-order polarization for positive delay-times τ is given as [113]:

$$\begin{aligned} P^{(3,BO)}(t,\tau) = - e^{iE_{0,0}t} \sum_{m_0,m_1} & \langle \psi_0^{(0)}(R_x, t=0) \,|\, \hat{\mu}_{01}(R_x) \,|\, \varphi_{1,m_1}(R_x) \rangle_{R_x} \times \\ & \langle \varphi_{1,m_1}(R_x) \,|\, \hat{\mu}_{10}(R_x) \,|\, \varphi_{0,m_0}(R_x) \rangle_{R_x} \times \\ & \langle \varphi_{0,m_0}(R_x) \,|\, \hat{\mu}_{01}(R_x) \hat{\mu}_{10}(R_x) \,|\, \psi_0^{(0)}(R_x, t=0) \rangle_{R_x} \times \\ & e^{-iE_{1,m_1}t} e^{i(E_{1,m_1} - E_{0,m_0})\tau}, \end{aligned} \tag{4.96}$$

where $|\psi_0^{(0)}(R_x, t=0)\rangle$ is the lowest vibrational eigenfunction in the adiabatic ground state with energy $E_{0,0}$. The vibrational eigenstates of the adiabatic ground state are denoted as m_0 and the vibratinal states of the adiabatic first excited state are denoted as m_1. Then $|\varphi_{1,m_1}(R_x)\rangle$ denotes a vibrational eigenfunction in the adiabatic first excited state.

The signal can be obtained by integrating over T_p:

$$S^{(BO)}(\tau) = \sum_{m_0,m_1} \sum_{m_0',m_1'} c(m_0, m_1, m_0', m_1') e^{i(E_{1,m_1} - E_{1,m_1'})\tau} \times$$
$$e^{i(E_{0,m_0} - E_{0,m_0'})\tau} \int_{-T_p}^{T_p} dt e^{i(E_{1,m_1} - E_{1,m_1'})t}. \tag{4.97}$$

For a long time-span of T_p, the integral becomes a δ-function and the whole expression for the signal can be reduced to:

$$S_+^{(BO)}(\tau) \approx \sum_{m_0,m_1} \sum_{m_0',m_1'} c(m_0, m_1, m_0', m_1') e^{i(E_{0,m_0} - E_{0,m_0'})\tau}. \tag{4.98}$$

For negative delay times τ, the polarization is calculated as:

$$\begin{aligned} P^{(3,BO)}(t,\tau) = - e^{iE_{0,0}t} \sum_{m_1,m_1'} & \langle \psi_0^{(0)}(R_x, t=0) \,|\, \hat{\mu}_{01}(R_x) \,|\, \varphi_{1,m_1}(R_x) \rangle_{R_x} \times \\ & \langle \varphi_{1,m_1}(R_x) \,|\, \hat{\mu}_{10}(R_x) \hat{\mu}_{01}(R_x) \,|\, \varphi_{1,m_1'}(R_x) \rangle_{R_x} \times \\ & \langle \varphi_{1,m_1'}(R_x) \,|\, \hat{\mu}_{10}(R_x) \,|\, \psi_0^{(0)}(R_x, t=0) \rangle_{R_x} \times \\ & e^{-iE_{1,m_1}t} e^{i(E_{1,m_1} - E_{1,m_1'})\tau}, \end{aligned} \tag{4.99}$$

then the signal reduces to

$$S_-^{(BO)}(\tau) \approx \sum_{m_1} \sum_{m_1'} b(m_1, m_1') e^{i(E_{1,m_1} - E_{1,m_1'})\tau}. \tag{4.100}$$

The previous signal was derived for the Born-Oppenheimer treatment and it is shown that the signal is modulated by the oscillations as a function of the delay-time τ. In the following, the derivation of the signal function is given for the exact case:

$$S_{+}^{(BO)}(\tau) \approx \sum_{\alpha,\alpha'} \sum_{\beta} c(\alpha, \alpha', \beta) e^{i(E_\alpha - E_{\alpha'})\tau}. \tag{4.101}$$

for positive τ. And for negative τ values, it becomes:

$$S_{-}^{(BO)}(\tau) \approx \sum_{\beta,\beta'} b(\beta, \beta') e^{i(E_\beta - E_{\beta'})\tau}. \tag{4.102}$$

The oscillating signal of the weak coupling case can be seen in fig. 4-40. Looking at eq. (4.98), for positive delay times τ, the oscillations appear as vibrational energy differences in the ground state. According to eq. (4.100), oscillations are seen as vibrational energy differences in the first excited state for negative τ.

The energetic difference in the ground state between gerade states is $\Delta E_1 = 0.074$ eV, and in the first excited state the difference is $\Delta E_2 = 0.086$ eV (see section 4.2.1). This is in very good agreement with the obtained signal, which oscillates with a period of $T_{1,vib} = \frac{2\pi}{\Delta E_1} = 55$ fs and $T_{2,vib} = \frac{2\pi}{\Delta E_2} = 47$ fs.

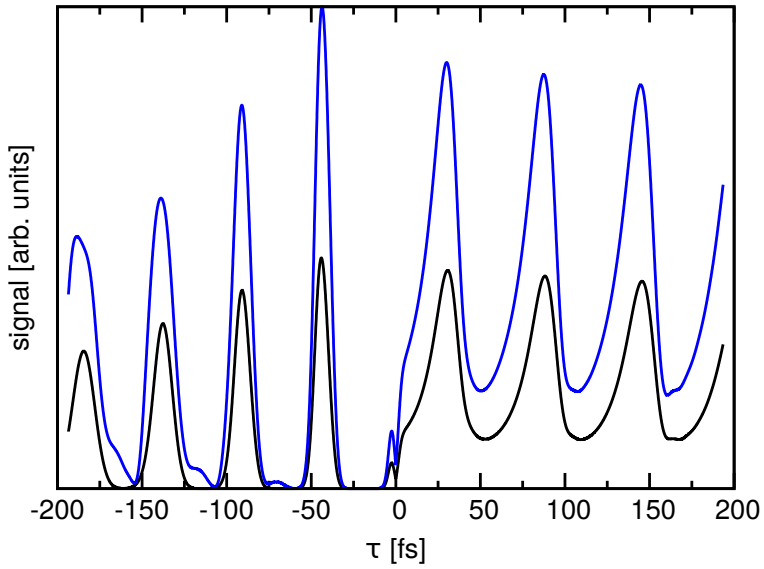

Figure 4-40: **FWM Signal for the Weak Coupling Case.** The black curve represents the signal within the exact treatment and the blue curve the signal within the Born-Oppenheimer treatment.

The exact calculated signal and the one within the Born-Oppenheimer treatment are in good agreement and underline the validity of the Born-Oppenheimer approximation. This, furthermore, reveals that the arbitrary energy differences which could appear in an exact calculation can be matched to vibrational energy differences within the electronic ground state and electronic excited state, respectively [113].

4.4.4.2 Strong Coupling

Next, the strong coupling case with $R_c = 2.5$ Å is regarded. The exact calculated signal is shown in fig. 4-41. For negative delay-times τ, there are only small amplitudes. On the other hand for positive τ, there are oscillations of approximately 75 fs periodically. These oscillactions are on top of a large offset signal background. Now, a comparison of the Born-Oppenheimer treatment with the adiabatic ground state and the first excited adiabatic state results in a mismatch. Obviously, this demonstrates that the Born-Oppenheimer treatment is not valid.

Comparing on the other hand the Born-Oppenheimer treatment including the ground state and the second excited state with the exact signal, one can see that at least for positive delay-times τ, the signal has the same oscillation period. Also, there appears a large background signal at positive τ values. At this point, it can be said that the incorporation of the second excited state is able to reproduce the exact signal, as the second excited state and the ground state are also well separated energetically, which means that here the Born-Oppenheimer treatment should be valid, as has already been seen in the weak coupling case.
Nevertheless, the first excited state, as a matter of coupling, is not able to reproduce any signal characteristics.

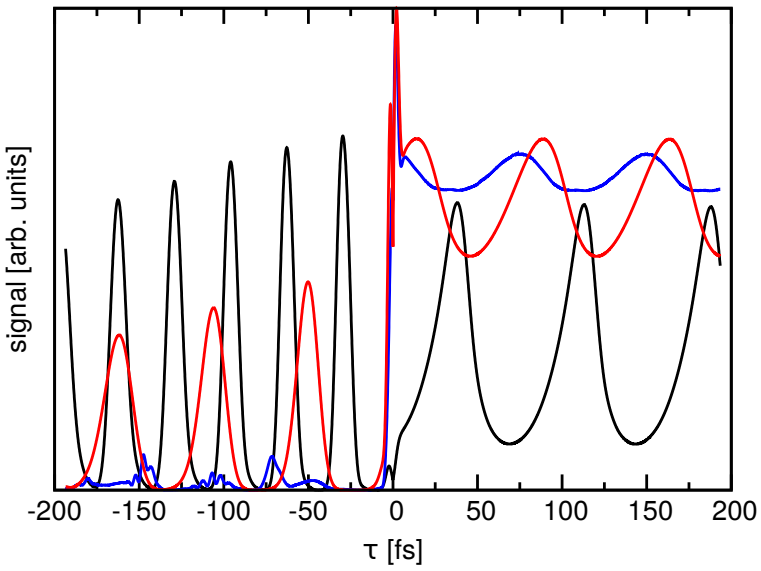

Figure 4-41: **FWM Signal for the Strong Coupling Case.** The blue curve represents the signal obtained within the exact treatment. The reddish curve and the black curve represent the signal within the Born-Oppenheimer treatment between the ground state and the second adiabatic state and the second adiabatic state, respectively.

As it has been revealed that the second excited state plays an important role in the light-matter-interaction process [115], longer pulses are chosen with $\alpha = 1.6 \cdot 10^{-5} \frac{1}{\mathrm{fs}^2}$ in order to surpress the second excited state. The results of this numerical experiment can be seen in fig. 4-42, where the excited state beating

has been seen in the Born-Oppenheimer treatment of ground state and second excited adiabatic state is surpressed. Nevertheless, in the ground state vibrational beatings are again resolved.

Also, the Born-Oppenheimer treatment with the ground state and the first excited state fails [113].

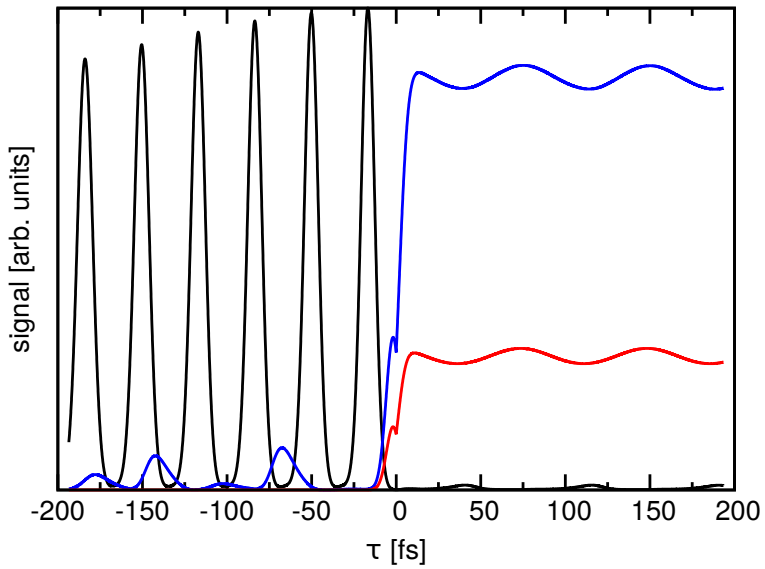

Figure 4-42: **FWM Signal for the Weak Coupling Case with Longer Laser Pulses.** Same as fig. 4-41.

Concluding Remarks

It has been seen that the characteristics obtained from two-dimensional spectra are in good agreement with those extracted from the FWM signals. Also, one saw that as long as the Born-Oppenheimer approximation is valid, the beating in the signal can be matched to vibrational energy differences in either the ground state or in one of the excited states, respectively. For the strong coupling case, this is not possible.

4.5 Quantum versus Classical Dynamics

As was mentioned earlier, there is a relation between quantum dynamics and classical dynamics, and it is common to treat nuclear dynamics classically employing the potential energy surface in a fixed electronic state. This approach has a long history [116, 117] and modern MD calculations rest on classical mechanics [19]. To describe coupled electron-nuclear motion, one is forced to modify the classical description by, for example, surface hopping procedures which allow the classical trajectories to switch between different potentials [18, 118].

In the following, the question of how non-adiabatic coupling is visible in the electron-nuclear coupled quantum-dynamics of a wave packet is investigated, which will address the possibility to describe this coupled dynamics via a complete classical treatment on the potential, defined by all interactions between the protons and the electron.

4.5.1 Quantum Dynamical Case Study on Three Different Coupling Cases

In order to separate the dynamical properties, three different coupling cases are regarded, and thus, the one-dimensional Shin-Metiu model is again employed with the following parameters, see table 4.14.

Table 4.14: **Simulation Parameters.**

symbol:	description:	value
$[R_{x_{min}} : R_{x_{max}}]$	range in R_x-space	[-6:6]Å
$[x_{min} : x_{max}]$	range in x-space	[-10:10]Å
N_R	grid points in R_x-direction (p^+)	256
N_x	grid points in x-direction (e^-)	256
m_p	proton mass	1836.15 a.u.
$\delta\tau$	time-step ITP	1.0 a.u.
δt	time-step	0.5 a.u.
R_f	shielding e^- and p^+_{fixed}	1.5 Å

Besides the constant parameters in table 4.14, R_c is varied from low values, eg.

high electron-nuclear interaction, to high values, meaning low particle interaction, and the three cases of different interaction strength can be classified as weak, intermediate and strong coupling, respectively.

Table 4.15: **Shielding Parameters.**

scenario:	R_c
weak coupling	1.0 Å
intermediate coupling	2.0 Å
strong coupling	2.5 Å

Solving the electronic Schrödinger equation, the adiabatic potentials are obtained, and they are depicted in the left panels in fig. 4-43.

The initial conditions for the time-dependent Schrödinger equation are chosen such that the dynamics takes place only in the lowest two adiabatic electronic states. These states are obtained via eq. (4.4). The initial wave packet is:

$$|\psi_{init}(x, R_x)\rangle = N|\phi_0(x; R_x)\rangle \cdot e^{-\beta(R_x - R_{eq})^2}, \tag{4.103}$$

with the given parameters in table 4.16.

Table 4.16: **Initial Conditions for Quantum Wave-Packet Dynamics.**

scenario:	R_{eq}	β
weak coupling	3.5 Å	7.14 $\frac{1}{\text{Å}^2}$
intermediate coupling	3.0 Å	7.14 $\frac{1}{\text{Å}^2}$
strong coupling	2.5 Å	7.14 $\frac{1}{\text{Å}^2}$

Thus, the wave packet starts in the electronic ground state. The population dynamics are shown in fig. 4-43 right-hand, for each case.

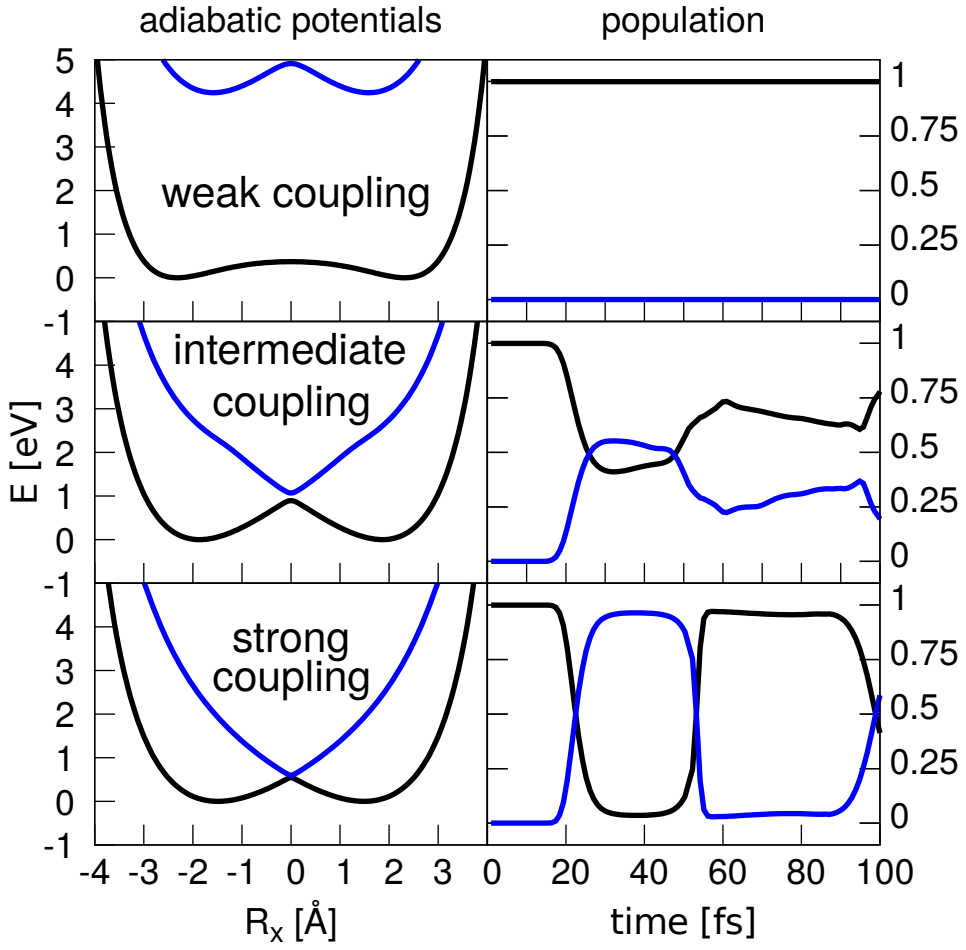

Figure 4-43: **Adiabatic Potentials and Population Dynamics**. The left panels show the adiabatic potentials with shifted energy minimum for the three different coupling cases. The right panels show the population dynamics of a wave packet being initially in the electronic ground state.

In the weak coupling case, no population transfer between the adiabatic ground state and the adiabatic excited state is seen, as expected [66, 91]. An almost complete electronic transition takes place in the strong coupling case. Finally, the intermediate coupling results in about 50 % transfer during each passing of the coupling region.

4.5.2 Comparison of Quantum and Classical Dynamics

In the following, the dynamics of classical trajectories propagated in the potential $V(x, R_x)$ are compared to the quantum-dynamical calculation [24]. Both the integrated densities $\varrho_{el}(R_x, t)$ from the quantum-dynamical calculation and $\rho_{el}(R_x, t)$, obtained from the trajectory study, are regarded.

For the classical trajectories, the initial wave function is chosen to define the initial conditions. The trajectories are sampled from the quantum-mechanical phase-space function:

$$\rho(x, R_x, p_x, P_{R_x}, t) = |\psi(x, R_x, t_0)|^2 |\psi(p_x, P_{R_x}, t_0)|^2, \tag{4.104}$$

yielding the distribution function [18, 59, 119]:

$$W\left(x_i(t_0), R_{x,j}(t_0), p_{x,i'}(t_0), P_{R_x,j'}(t_0)\right) = |\psi(x_i, R_{x,j}, t_0)|^2 |\psi(p_{x,i'}, P_{R_x,j'}, t_0)|^2, \tag{4.105}$$

Finally, the classical density is given as:

$$\begin{aligned}\rho(x, R_x, p_x, P_{R_x}, t) =& \frac{1}{N} \sum_{i,j,i',j'} W(x_i(t), R_{x,j}(t), p_{x,i'}(t), P_{R_x,j'}(t)) \times \\ & \delta(x - x_i(t)) \delta(R_x - R_{x,j}(t)) \times \\ & \delta(p_x - p_{x,i'}(t)) \delta(P_{R_x} - P_{R_x,j'}(t)).\end{aligned} \tag{4.106}$$

For the electron density, one obtains:

$$\begin{aligned}\rho_{el}(x, t) =& \frac{1}{N} \sum_{i,j,i',j'} W(x_i(t), R_{x,j}(t), p_{x,i'}(t), P_{R_x,j'}(t)) \times \\ & \delta(x - x_i(t))\end{aligned} \tag{4.107}$$

and

$$\rho_{nuc}(R_x,t) = \frac{1}{N}\sum_{i,j,i',j'} W(x_i(t),R_{x,j}(t),p_{x,i'}(t),P_{R_x,j'}(t))\times \delta(R_x - R_{x,j}(t)) \tag{4.108}$$

for the nuclear density, respectively [120].

4.5.3 Integrated Densities

4.5.3.1 Weak Coupling

First, the weak coupling case is regarded. As the Born-Oppenheimer approximation is valid in this case, one expects the electron density to follow the nuclear density [91]. In fig. 4-44, left panels, the quantum-dynamical calculated densities $\varrho_{el}(R_x,t)$ and $\varrho_{nuc}(x,t)$ can be seen, which exhibit the same time-evolution. Starting at -4.0 Å, the density proceeds with constant velocity across the adiabatic potential until it is reflected after approximately 45 fs from a nuclear position of $+4.0$ Å, and a complete period is finished within 80 fs.
Regarding the right panels of fig. 4-44, $\rho_{el}(R_x,t)$, obtained from the classical trajectories, shows a very good agreement within the first 45 fs, which is just the first half period.

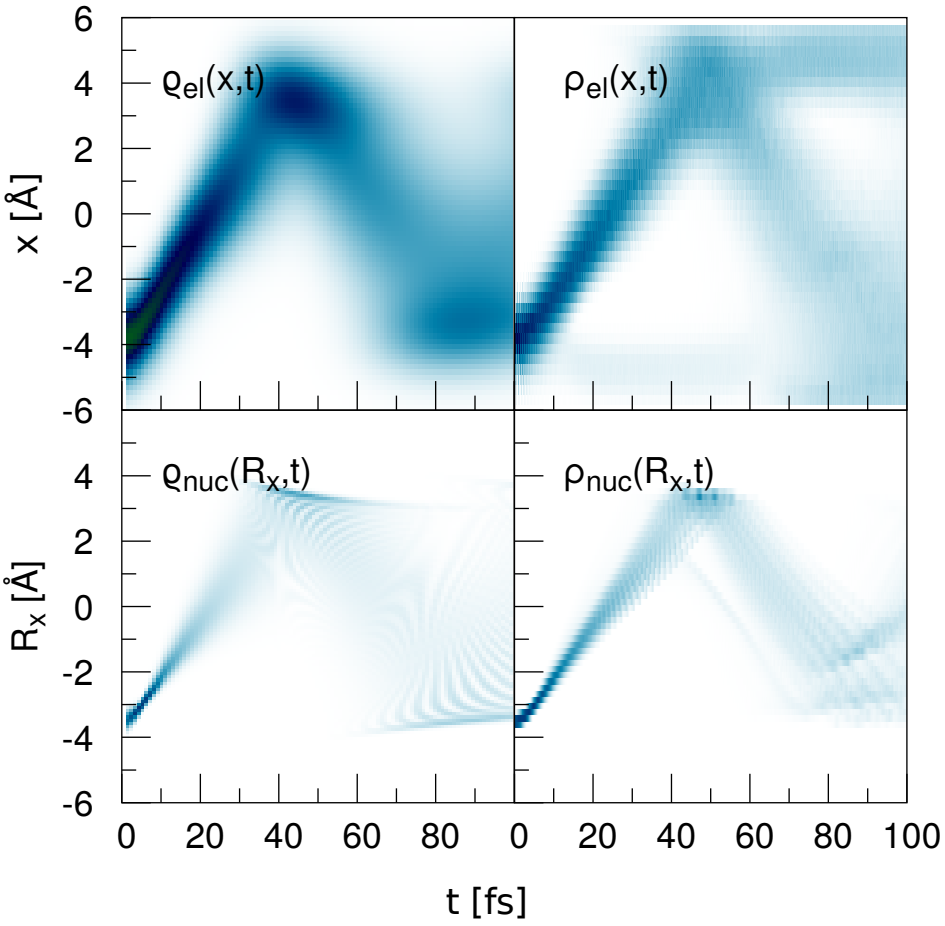

Figure 4-44: **Density Dynamics in the Weak Coupling Case.** The left panels correspond to the quantum-dynamical calculation and show the electron density to follow the nuclear density. In comparison, the right panels show the correspondent classical calculation.

A difference between the quantum-dynamical and classical calculation can be seen, comparing $\rho_{el}(R_x, t)$ and $\varrho_{el}(R_x, t)$. The classical trajectories remain at the fixed proton position +4.0 Å after a passage of the wave packet. This behavior is more characteristic for the dynamics in the strong coupling situation, which is regarded in the following.

4.5.3.2 Strong Coupling

In the strong coupling case, the quantum-dynamical propagation should exhibit major differences compared to the weak coupling case one. This can indeed be seen in fig. 4-45, left panels. The electron density does not follow the nuclear density $\varrho_{nuc}(R_x, t)$. $\varrho_{el}(x, t)$ remains at the left fixed proton position around -4.0 Å, while the movable proton takes up the motion similar to the one which was seen within the diabatic potentials in fig. 4-20 and the corresponding dynamics in fig. 4-22.

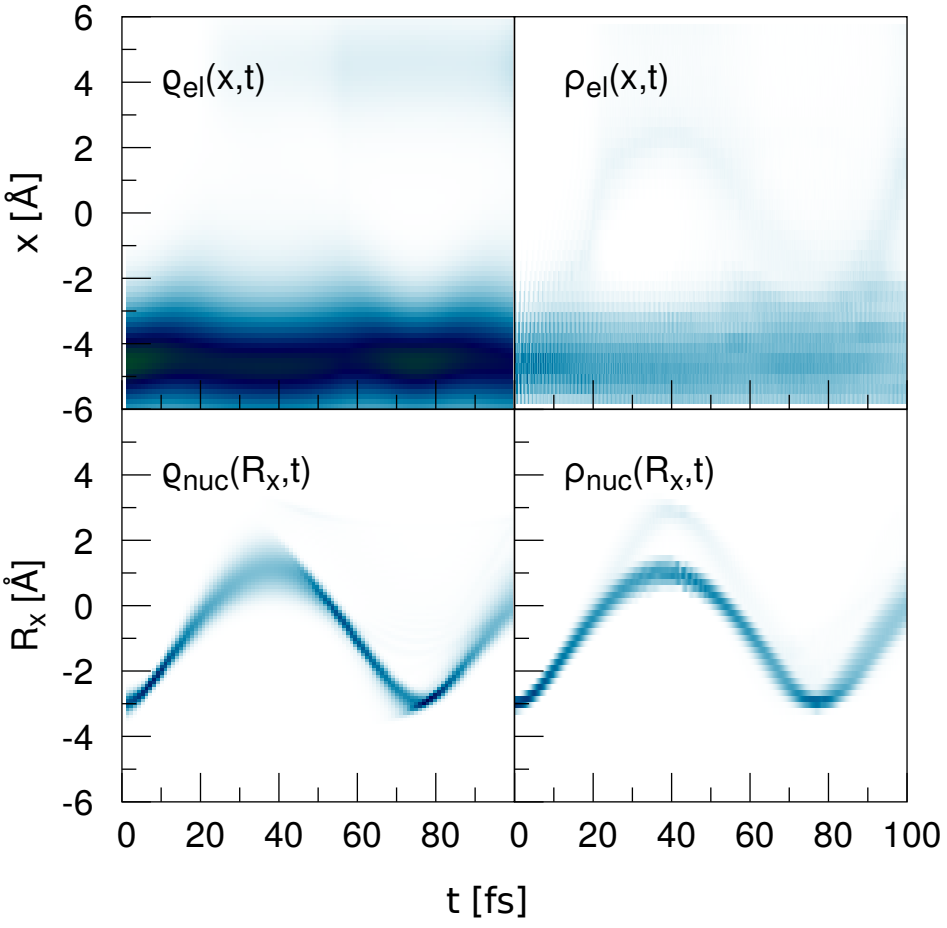

Figure 4-45: **Density Dynamics in the Strong Coupling Case.** Same as fig. 4-44.

The nuclear density evolves, compared to the uncoupled case, independently of

the electron density. The densities obtained from the classical trajectories are in very good agreement with the quantum densities.

4.5.3.3 Intermediate Coupling

For the intermediate case, a superposition of both diabatic and adiabatic dynamics is expected. This is indeed the case as is seen in fig. 4-46, left panels. The nuclear density $\varrho_{nuc}(R_x, t)$ exhibits two branches. These can be distinguished in regarding the different turning points. The adiabatic branch is the one reaching to the other side of the potential at +4.0 Å, and the diabatic one returns earlier, as has already been seen in the uncorrelated motion at +1.0 Å.

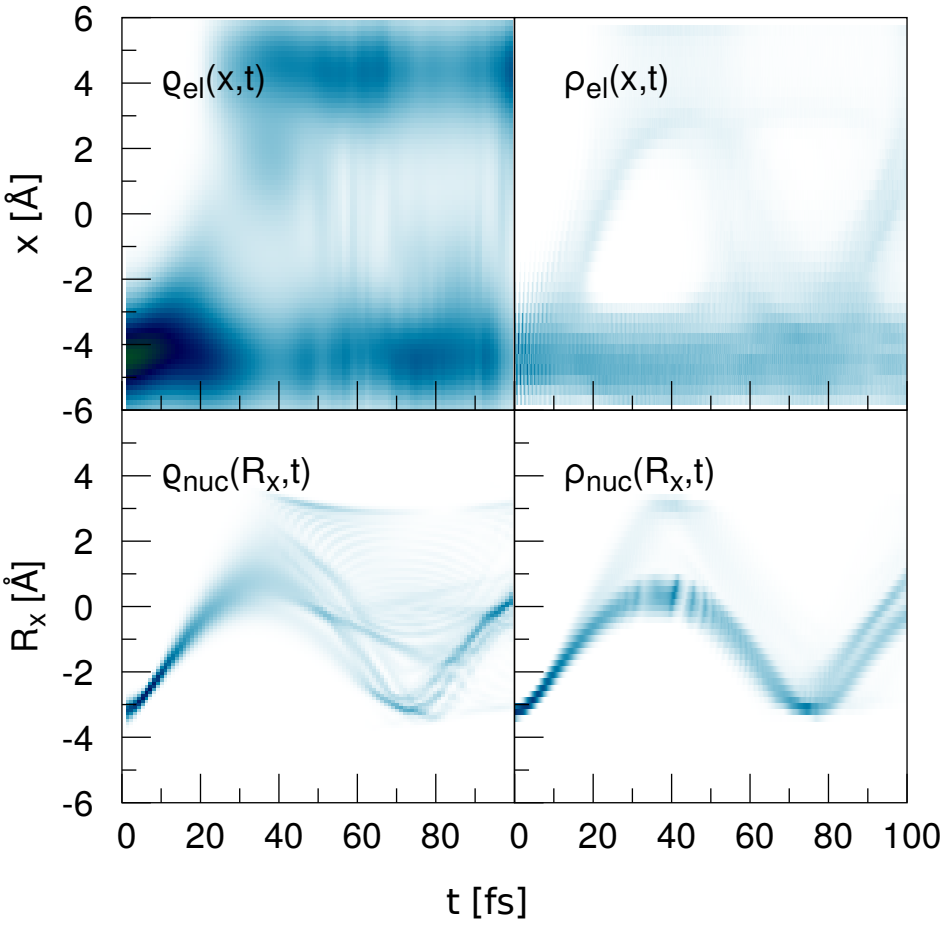

Figure 4-46: **Density Dynamics in the Intermediate Coupling Case.** Same as in fig. 4-44.

Also, the electron density exhibits both characteristics. As for the diabatic motion, the density remains at the fixed protons. For the adiabatic motion, which can be associated with the density moving along with the proton.

Regarding the classical trajectories (right panels), it can also be seen that the superposition of a diabatic and adiabatic motion is present. Qualitatively, there are also two points of return which help to distinguish the two different motions from each other. The point of return for the diabatic motion is +3.0 Å, whereas the point of return for the adiabatic motion is +0.5 Å.

The electron density shows a superposition with most of the amount of density

remaining at the fixed right ion (+5.0 Å) and some of the density located in the middle between the fixed protons.

4.5.4 Densities in Nuclear and Electronic Coordinate Space

The wave-packet dynamics given by $\varrho(R_x, x, t)$ for the quantum-mechanical calculation and $\rho(R_x, x, t)$ for the classical propagation are now compared in the weak, strong and intermediate coupling case. The main interest is on the time-interval, where the wave packet passes the coupling region for the first time.

4.5.4.1 Weak Coupling

The quantum-mechanical density $\varrho(R_x, x, t)$ for the times of 17, 22, 27 and 31 fs is shown in fig. 4-47. As expected, the motion of $\varrho(R_x, x, t)$ is diagonal in coordiante space. This is in accordance with an adiabatic motion because the electronic wave function adapts to the nuclear position. The classical density $\rho(R_x, x, t)$ evolves along the path of steepest descend, which is the elongated minimum accounting for the diagonal motion. It tracks the motion of the quantum-mechanical wave-packet [24].

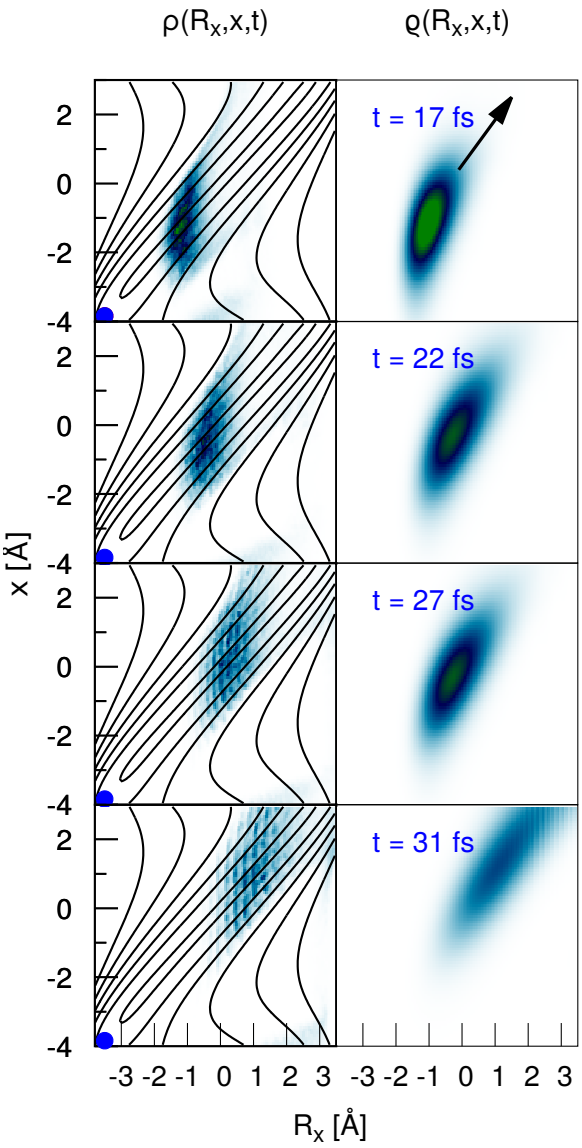

Figure 4-47: **Density Dynamics in the Weak Coupling Case.** The left panels show the density obtained from the classical treatment. The black lines correspond to the potential $V(x, R_x)$ starting at a value of 0.0 eV and increasing in 0.1 eV steps. The right panels show the correspondent densities obtained from the quantum calculation. The blue dot marks the initial position of the wave packet.

4.5.4.2 Strong Coupling

This time, only a motion in the nuclear coordiante R_x is seen. In contrast to the weak coupling case, the electron remains at the position of the fixed proton position at $R_x = -5.0$ Å. Interestingly, the wave packet does not change in shape while passing the coupling region at $R_x = 0.0$ Å.

Regarding now the left hand panels of fig. 4-48, one can see that the classical trajectories also follow the trend of the quantum-dynamical calculation. The motion of the classical trajectories exhibit the determined path along the steepest descend. As long as this minimum just evolves along the R_x-coordinate, this is in good agreement. Small deviations come from the anharmonicity of the potential along the trajectorial motion which can be seen by the contours in fig. 4-48 [24].

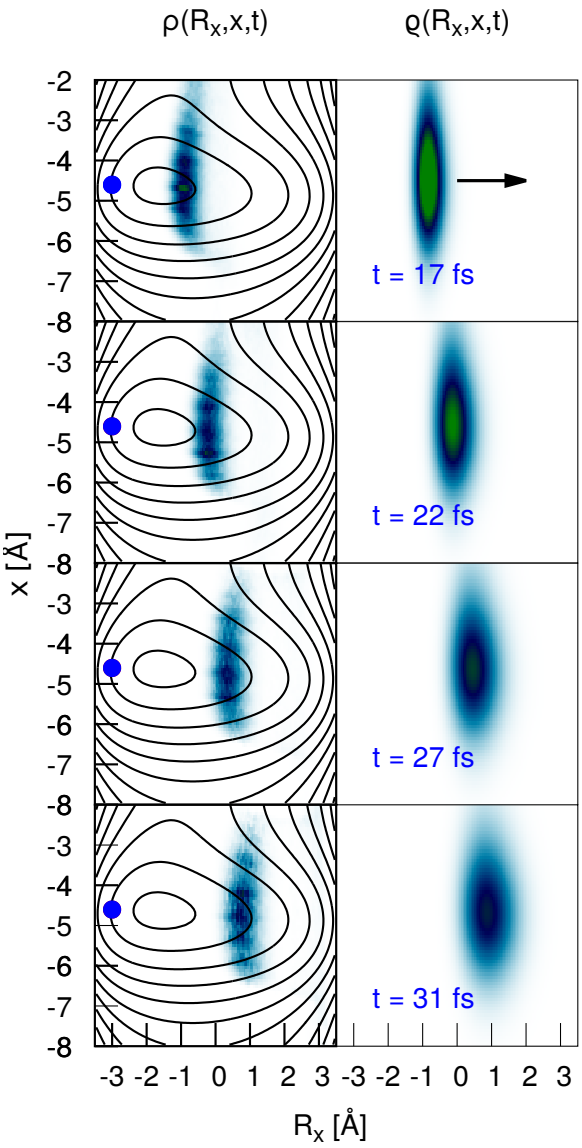

Figure 4-48: **Density Dynamics in the Strong Coupling Case.** Same as fig. 4-47.

4.5.4.3 Intermediate Coupling

The dynamics in the intermediate coupling case is regarded in fig. 4-49. As has already been confirmed, this case is a superposition of adiabatic and diabatic motion, and this is also seen in the time-evolution of $\varrho(R_x, x, t)$ in fig. 4-48, right hand panels. A splitting of the density into two parts is observed as the wave

packet crosses the coupling region. Compared to the weak coupling case, where a diagonal motion in coordiante space was seen, the part of the wave packet moving diagonal can be matched to the adiabatic motion, whereas the other part, moving horizontally, can be matched to the diabatic motion in the strong coupling case [24].

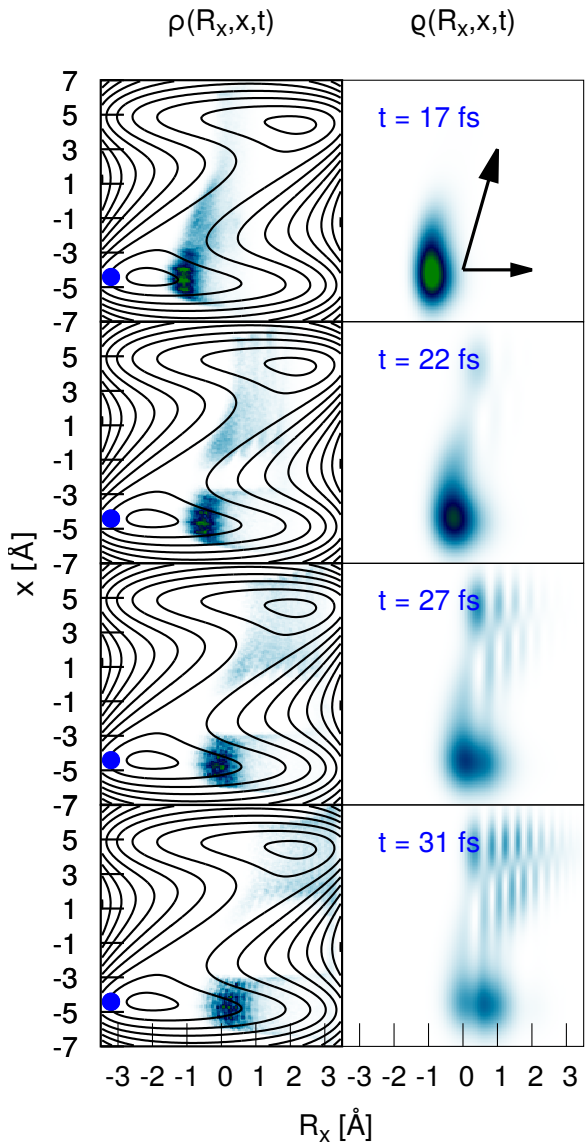

Figure 4-49: **Density Dynamics in the Intermediate Coupling Case.** Same as fig. 4-47.

Regarding the classical density $\rho(R_x, x, t)$ in fig. 4-49 left hand panels, one recognizes that the characteristics of adiabatic motion and diabatic motion are present after the wave packet crosses the coupling region, but there also appear differences to the quantum densities. Of course, the interferences, seen for $\varrho(R_x, x, t = 37\ fs)$, can not be reproduced by classical trajectories. Furthermore, the ratio of diabatically and adiabatically moving density is not the same as in the quantum calculation. There is much more percentage trapped in the diabatic motion than in the classical calculation. Regarding the contours of the potential in fig. 4-49, the anharmonicity prompts deviations between the classical and the quantum motion [24].

Concluding Remarks

In case of weak coupling it is seen that the classical and the quantum dynamics are quite similar. The description of the nuclear dynamics takes place in a single adiabatic electronic state which is decoupled from other adiabatic states, because the Born-Oppenheimer approximation is valid. In this case, the classical motion can be matched with the motion in this adiabatic state potential.

In case of strong non-adiabatic coupling, the classical and quantum-mechanical calculation are also in very good agreement. The complete population transfer in the adiabatic picture can be referred, according to section 4.3, to a diabatic motion within one diabatic state. As a result, the classical motion takes place in a single diabatic potential.

The intermediate case shows both for the quantum and for the classical density a splitting of the wave packet passing the coupling region. It thus represents a superposition of a purely adiabatic motion and diabatic motion.

4.6 Electron Flux

Within the weak coupling case ($R_c = 1.5$ Å) the electron flux obtained from a full-dimensional calculation is compared with the electron flux within the adiabatic approximation. The electron flux is defined as [121–124]:

$$j(x,t) = \int dR_x \; \mathfrak{Im}\left(\psi^*(x,R_x,t)\frac{\partial}{\partial x}\psi(x,R_x,t)\right). \tag{4.109}$$

$|\psi(x,R_x,t)\rangle$ is determined via eq. (2.6). The continuity equation relates the flux to the time-derivative of the density [33] as:

$$\frac{\partial \varrho(x,t)}{\partial t} = -\frac{\partial j(x,t)}{\partial x}. \tag{4.110}$$

Rewriting eq. (4.109) using the adiabatic product and assuming the Born-Oppenheimer approximation so that the dynamics takes place only in the electronic ground state (see section 4.2.1), the electron flux can be written as:

$$j^{BO}(x,t) = \int dR_x \; |\chi(R_x,t)|^2 \; \mathfrak{Im}\left(\phi_0^*(x;R_x)\frac{\partial}{\partial x}\phi_0(x;R_x)\right) \tag{4.111}$$

Because $|\phi_0(x;R_x)\rangle$ is real, the flux becomes zero within the usual definition. However, the electron flux within the Born-Oppenheimer treatment does not necessarily vanish if one employs the continuity equation eq. (4.110). Within the adiabatic representation, the density can be written in the following form:

$$\varrho^{BO}(x,t) = \int dR_x \; |\chi(R_x,t)|^2 |\phi_0(x;R_x)|^2, \tag{4.112}$$

Using eq. (4.110), the electron flux within the Born-Oppenheimer approximation

can be rewritten as follows [121, 124, 125]:

$$j^{BO}(x,t) = -\int_{-\infty}^{x} dx' \; \frac{\partial \varrho^{BO}(x',t)}{\partial t} \tag{4.113}$$

$$= -\int_{-\infty}^{\infty} dR_x \frac{\partial \varrho_N^{BO}(R_x,t)}{\partial t} f(x;R_x), \tag{4.114}$$

with

$$f(x;R_x) = \int_{-\infty}^{x} dx' \; |\phi_0(x';R_x)|^2 \tag{4.115}$$

and

$$\varrho_N^{BO}(R_x,t) = |\chi(R_x,t)|^2. \tag{4.116}$$

Using now the equivalent of eq. (4.110) for the nuclear flux:

$$\frac{\partial \varrho_N^{BO}(R_x,t)}{\partial t} = -\frac{\partial j_N^{BO}(R_x,t)}{\partial R_x}, \tag{4.117}$$

one finds, by partial integration,

$$j^{BO}(x,t) = -\int_{-\infty}^{\infty} dR_x \; j_N^{BO}(R_x,t) \; w(x;R_x), \tag{4.118}$$

where the window function is defined as:

$$w(x;R_x) = \frac{\partial f(x;R_x)}{\partial R_x}. \tag{4.119}$$

Equation (4.118) directly connects the electron flux with the nuclear flux within the Born-Oppenheimer approximation.

In what follows a calculation of the electron flux in the electronic ground state is carried out both in the full-dimensional coordinate space (eq. (4.109)) and within the Born-Oppenheimer approximation (eq. (4.118)).

As initial wave packet for the full-dimensional calculation $|\psi(x, R_x, t = 0)\rangle$ is defined as:

$$|\psi(x, R_x, t = 0)\rangle = N e^{-\beta(R_x - R_{eq})^2} |\phi_0(x; R_x)\rangle, \tag{4.120}$$

with $\beta = -7.14\ \frac{1}{\text{Å}^2}$ and $R_{eq} = -3.6$ Å. N is a normalization constant. Within the adiabatic treatment the same initial wave packet is chosen. Figure 4-50 shows in the upper panels the nuclear flux obtained from the full-dimensional calculation (right) and from the Born-Oppenheimer treatment (left). As expected, they are in very good agreement and show the wave packet to move back and forth within the electronic ground state. In the middle panels, the time-derivative of the electron density is seen to follow the nuclear density. This also applies to the electron flux which is displayed in the lower panels. Here, results from the Born-Oppenheimer treatment are also in good agreement with the full-dimensional calculation. It is seen that the electron flux is positive as the wave packet propagates with positive momentum from the initial position to larger distances. The electron flux changes to negative values as the wave packet returns to the initial position after 60 fs.

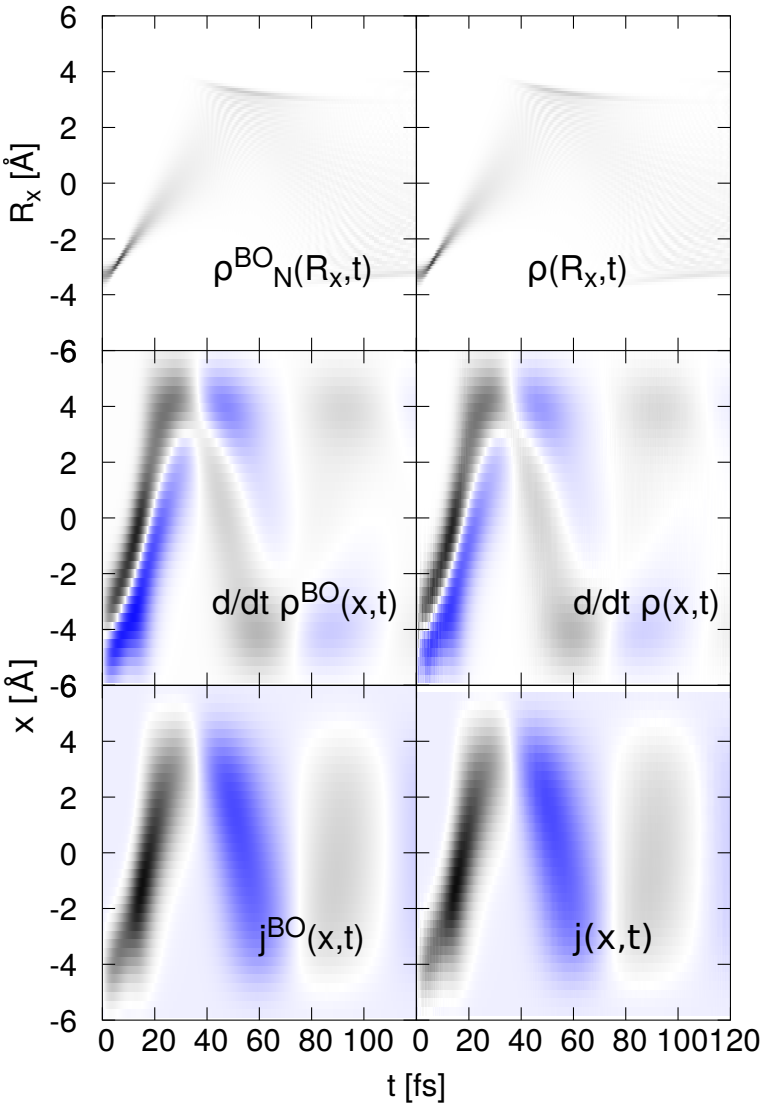

Figure 4-50: **Comparison of the Born-Oppenheimer and the Full-Dimensional Calculation.** The upper panels display the nuclear density. The middle panels compare the time-derivative of the electron density and the lower panels compare the electron flux. The black color shows positive values, and the blue color shows negative values of the quantities.

In what follows, eq. (4.118) is used to derive a reflection principle [119, 126–130]. The function $w(x; R_x)$ is displayed in fig. 4-51. The maximum of this window function occurs at the nuclear position:

$$\langle R_x \rangle(x) = \frac{\int dR_x \ |w(x; R_x)| \ R_x}{\int dR_x \ |w(x; R_x)|}, \tag{4.121}$$

and one replaces the window function by:

$$w(x; R_x) = w(x; \langle R_x \rangle(x)) \delta(R - \langle R_x \rangle(x)). \tag{4.122}$$

Then eq. (4.118) becomes:

$$j^{map}(x,t) = j_N^{BO}(\langle R_x \rangle(x), t) \ w(x; \langle R_x \rangle(x)), \tag{4.123}$$

and describes a flux-flux reflection-principle which is illustrated in fig. 4-51. The nuclear flux (upper left panel) is mapped onto the electron flux (lower right panel). The mapped electron flux can then be compared to the electron flux (lower left panel) for the full-dimensional calculation. It is seen that $j^{map}(x,t)$ gives the right trend, but also there appear deviations due to the δ-function approximation [25].

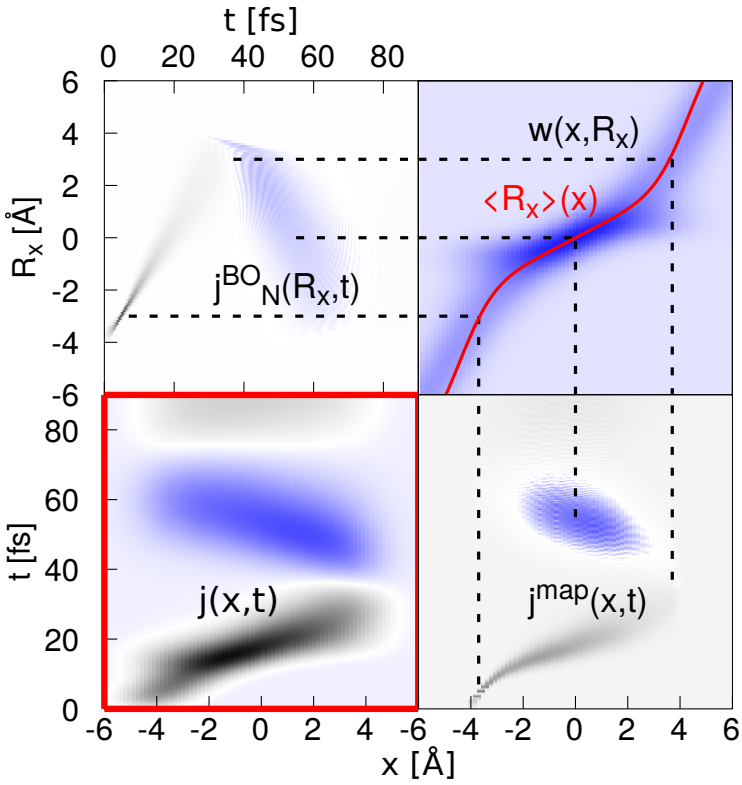

Figure 4-51: **Flux-Flux Reflection-Principle.** The mapped electron flux in the lower right panel is compared to the numerically exact electron flux (lower left panel). The mapped electron flux is obtained by a mapping of the nuclear flux via the window function $w(x; R_x)$, which is seen in the upper right panel in combination with $\langle R_x \rangle(x)$.

Concluding Remarks

The results show that within the one-dimensional model, a calculation of the electron flux within the Born-Oppenheimer treatment is possible. The electron flux can be shown to reflect the nuclear flux. This flux-flux reflection-principle uses a window function which is related to the adiabatic ground state function. It yields a direct relation between the two particle fluxes. However, extensions to more complex dynamics provide a challange [25].

Chapter 5

Adiabatic Dynamics and Non-Adiabatic Dynamics in the Two-dimensional Shin-Metiu Model

In the previous chapter the nuclear hamiltonian for the one-dimensional Shin-Metiu model was constructed in the adiabatic and in the diabatic representation, and the transformation between the two representations was discussed. Furthermore, the nuclear dynamics on the adiabatic and diabatic potentials has been compared.

In this chapter, a more advanced case, where an additional degree of freedom for the electron and the nucleus is present, is studied. Here, conical intersections [131–135] (CoIns) of the adiabatic potential surfaces are present, which present a more general situation as the case of avoided crossings between the adiabatic potential curves in the one-dimensional system.

Since CoIns play a mayor role in quantum dynamics, the study on this extended model system is of large interest. Recently, the diabatic dynamics through a CoIn

and an adiabatic dynamics around a CoIn was studied [136, 137] using a similar model system. It was shown that the diabatic dynamics of a Gaussian wave-packet through a CoIn is accompained by an electron density that remains almost stationary during this process. This again is an indication of the existence of a proper diabatic representation, and therefore, in what follows a diabatization is carried out as well as a diabatic wave-packet dynamics.

On the other hand, the adiabatic wave-packet dynamics around a CoIn was investigated. It was shown that the rotational motion of the electron density is correlated to the rotational motion of the nuclear density. Based on this work, in the following study, the circling around a CoIn is further investigated. This includes the study of the geometric phase [138, 139] connected to the surrounding of a CoIn. Furthermore, the long-time behavior of the diabatic and adiabatic motion is studied [26].

5.1 The Two-Dimensional Shin-Metiu Model

The Shin-Metiu model has been extended to two dimensions by Gross and coworkers [140]. Here, their model is modified in a way that a single CoIn appears with the consequence that the system can be mapped on a linear Jahn-Teller hamiltonian. The hamiltonian is given for the electron coordinates $\vec{r} = (x, y)$ and the proton coordinates $\vec{R} = (R_x, R_y)$ as:

$$\begin{aligned}\hat{H}(\vec{R},\vec{r}) =& \frac{\hat{\vec{p}}_{\vec{r}}^{\,2}}{2} + \frac{\hat{\vec{p}}_{\vec{R}}^{\,2}}{2M} - \frac{1}{\sqrt{a+|\vec{r}-\vec{R}|^2}} - \frac{1}{\sqrt{a+|\vec{r}-\vec{R}_1|^2}} \\ & - \frac{1}{\sqrt{a+|\vec{r}-\vec{R}_2|^2}} + \frac{1}{\sqrt{b+|\vec{R}_1-\vec{R}_2|^2}} \\ & + \frac{1}{\sqrt{b+|\vec{R}-\vec{R}_1|^2}} + \frac{1}{\sqrt{b+|\vec{R}-\vec{R}_2|^2}} \\ & + \left(\frac{\vec{R}}{R_0}\right)^4 . \end{aligned} \tag{5.1}$$

The coordinate system is shifted to the position of the mobile proton being in the D_{3h} symmetry configuration. A confining potential $\left(\frac{\vec{R}}{R_0}\right)^4$ centered at this position, where the CoIn exists, is added.

As depicted in fig. 5-1, both the electron and one proton move in a plane. Two other protons are fixed in the same plane at positions $\vec{R}_1 = (-L, -L\sqrt{3})$ a.u. and $\vec{R}_2 = (L, -L\sqrt{3})$ a.u., respectively, with $L = 2\frac{\sqrt{3}}{5}$ a.u.. The shielding parameters a and b for the electron-nuclear and nuclear-nuclear interaction, respectively, are taken as: $a = 0.5$ a.u. and $b = 10.0$ a.u. and $R_0 = 1.5$ a.u. is the parameter of the strength of the confining potential [26].

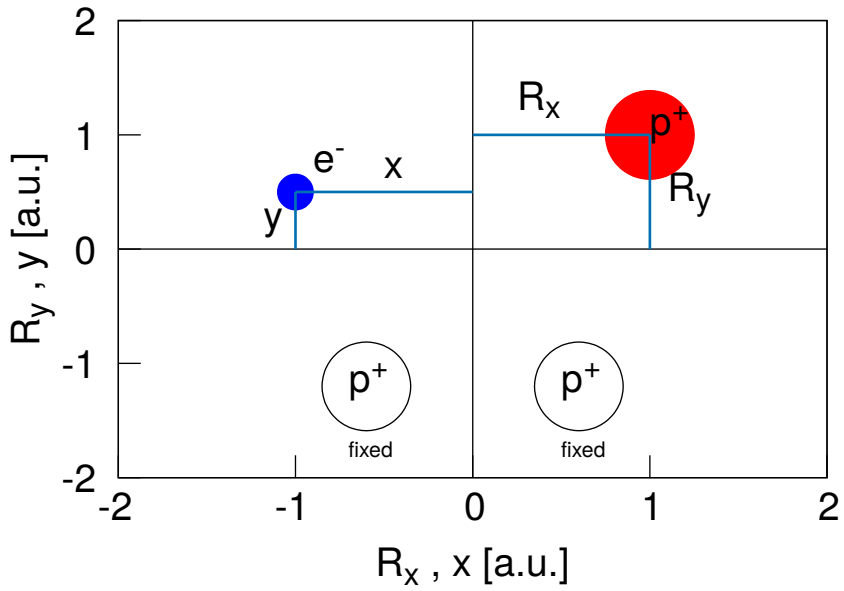

Figure 5-1: **Two-Dimensional Shin-Metiu Model.** The configuration model consists of two fixed protons (p^+) at $(-L, -L\sqrt{3})$ a.u. and $(L, -L\sqrt{3})$ a.u., respectively. Along with the mobile electron e^- with coordinate x, y and the mobile proton p^+ with coordinate R_x and R_y, this model has four internal degrees of freedom.

For the following study, the parameters in table 5.1 are used.

Table 5.1: **Parameters Employed for the Calculations.**

symbol:	description:	value
$[R_{x_{min}}; R_{x_{max}}]$	range in R_x-space	[-1.5;1.5] a.u.
$[R_{y_{min}}; R_{y_{max}}]$	range in R_y-space	[-1.5;1.5] a.u.
$[x_{min}; x_{max}]$	range in x-space	[-12;12] a.u.
$[y_{min}; y_{max}]$	range in y-space	[-12;12] a.u.
N_{R_x}	grid points in R_x-direction (p^+)	51
N_{R_y}	grid points in R_y-direction (p^+)	51
N_x	grid points in x-direction (e^-)	81
N_y	grid points in y-direction (e^-)	81
$\delta\tau$	time-step ITP	0.1 a.u.
dt	time-step	0.1 a.u.

5.2 Adiabatic Representation and Diabatic Representation of the Two-Dimensional Shin-Metiu Model

5.2.1 Adiabatic Representation

The adiabatic eigenfunctions are obtained by solving the electronic Schrödinger equation.

$$\left(\hat{H}_{el}(x, y; R_x, R_y) - u_{nn}(R_x, R_y)\right) |\phi_n(x, y; R_x, R_y)\rangle = 0. \tag{5.2}$$

The correspondent eigenvalues $u_{nn}(R_x, R_y)$ are the adiabatic potential surfaces. Similar to the one-dimensional Shin-Metiu model, the adiabatic eigenfunctions are obtained as real-valued functions with arbitrary sign. In order to get a continuous wave function description, the adiabatic eigenfunctions are adjusted in phase to each other for each adjacent proton position. To illustrate the adiabatic eigenfunctions, they are represented by the vector field [140]:

$$\vec{\nu}_n(R_x, R_y) = \begin{pmatrix} \langle \phi_n(x, y; R_x, R_y) \,|\, x \,|\, \phi_n(x, y; R_x, R_y) \rangle_{x,y} \\ \langle \phi_n(x, y; R_x, R_y) \,|\, y \,|\, \phi_n(x, y; R_x, R_y) \rangle_{x,y} \end{pmatrix}, \tag{5.3}$$

with $n = 1, 2$.

In fig. 5-2, panel (a) with $n = 2$ and (c) with $n = 1$, $\vec{\nu}_n(R_x, R_y)$ is given for the first and the second adiabatic state. The orientation of $|\phi_n(x, y; R_x, R_y)\rangle$ was aligned to the initial configuration of $|\phi_n(x, y; R_x = -1.5\ a.u., R_y = -1.5\ a.u.)\rangle$ in the way that the scalar product of two spatially adjacent $\vec{\nu}_n(R_x, R_y)$ is positive. Another possible orientation is seen in panel (b) with $n = 2$ and (d) with $n = 1$, where the initial configuration of $|\phi_n(x, y; R_x = -1.5\ a.u., R_y = 1.5\ a.u.)\rangle$ was used.

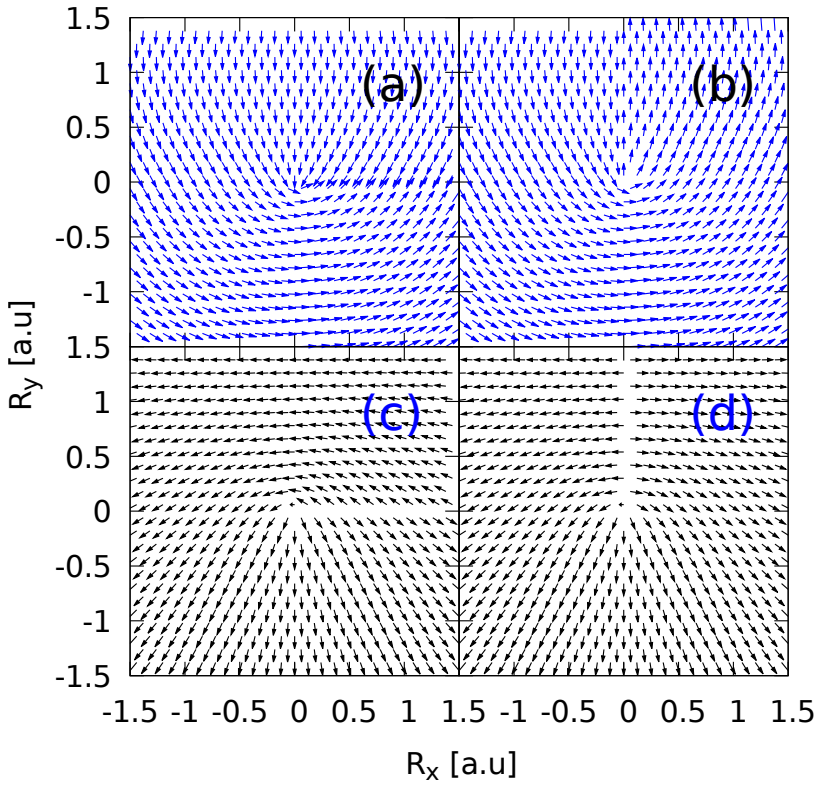

Figure 5-2: **Vector Fields of the Adiabatic Eigenfunctions.** The orientation of the adiabatic eigenfunctions according to the vector-field definition of $\vec{\nu}_n(R_x, R_y)$ is shown. It is seen that there appears a discontinuity within the allignment.

It is seen that the orientation of the eigenfunctions change dramatically at the origin. This indicates the existence of kinetic non-adiabtic coupling elements. The change of the adiabatic eigenfunctions is strongest in the vicinity of the CoIn, indicating that the non-adiabatic coupling elements in this region are large. The components of the NACT $\vec{\tau}_{12}(R_x, R_y)$ are seen in fig. 5-3.

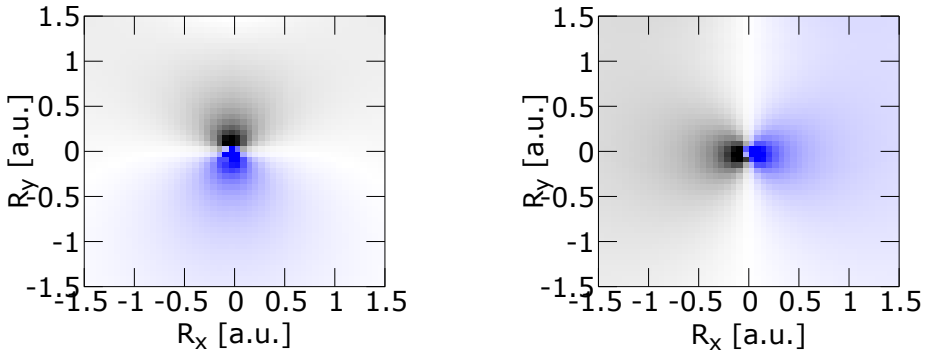

Figure 5-3: **Components of the Non-Adiabatic Coupling Element.** The left panel shows the R_x-component of the NACT $\vec{\tau}_{12}(R_x, R_y)$, and the right panel shows the R_y-component. The blue color shows negative values, and the black color shows positive values.

In fig. 5-4, panel (a), the adiabatic electronic eigenfunctions $|\phi_2(x, y; R_x, R_y)\rangle$ for the geometry at ($R_x = 0.0$, $R_y = 0.4$) a.u. are displayed. It is seen that the eigenfunction has a nodal structure with a node parallel to the R_x-axis. Furthermore, it has two slopes in R_y-direction with opposite sign. The shape of this eigenfunction is, in what follows, denoted as p_y-like. Arguing in the same manner, $|\phi_1(x, y; R_x, R_y)\rangle$, depicted in panel (b), is denoted as p_x-like.

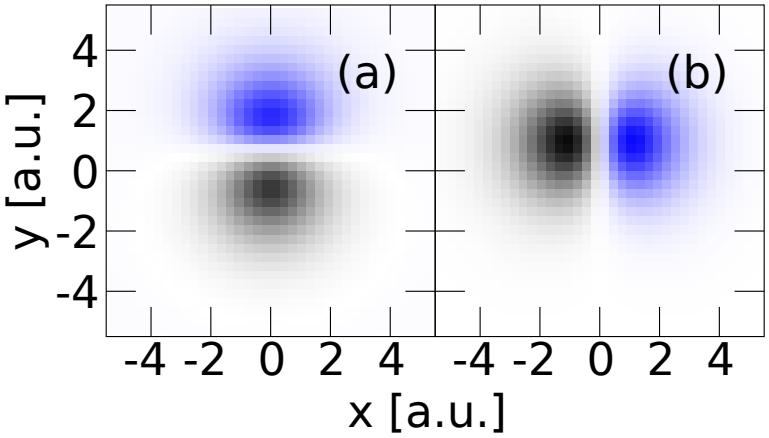

Figure 5-4: **Adiabatic Eigenfunctions.** In panel (a), the adiabatic eigenfunction $|\phi_2(x, y, R_x, R_y)\rangle$, and in panel (b) $|\phi_1(x, y; R_x, R_y)\rangle$ for the fixed nuclear position at $R_x = 0.0\ a.u., R_y = 0.4\ a.u.$ is depicted. The black color shows positive values, and the blue color shows negative values of the wave function.

The adiabatic potential surfaces of the first and second adiabatic electronic state are depicted in fig. 5-5, where a conical intersection is seen at the origin of the coordinate system, as expected. This degeneracy can be explained by the use of a character table. Although the model system is restricted to a plane, the use of a character table is valid, if the symmetry operations and irreducible representations are projected on the system's plane.

As the proton skeleton is assumed to have D_{3h} symmetry at the location of ($R_x = 0.0$, $R_y = 0.0$), table 5.2 can be used.

Table 5.2: **Excerpt of the Character Table of the D_{3h} Symmetry Point Group** [141].

D_{3h}	E	$2C_3$	$3C_2'$	σ_h	$2S_3$	$3\sigma_v$	translation
e'	2	-1	0	2	-1	0	$(x, y); (R_x, R_y)$ [1]

In the D_{3h} character table, the coordinates for translation x and y belong to the e' irreducible representation, which is degenerated. The p_x- and p_y-like adiabatic eigenfunctions belong to this irreducible representation.

[1] (R_x, R_y) are the coordinates of the mobile proton.

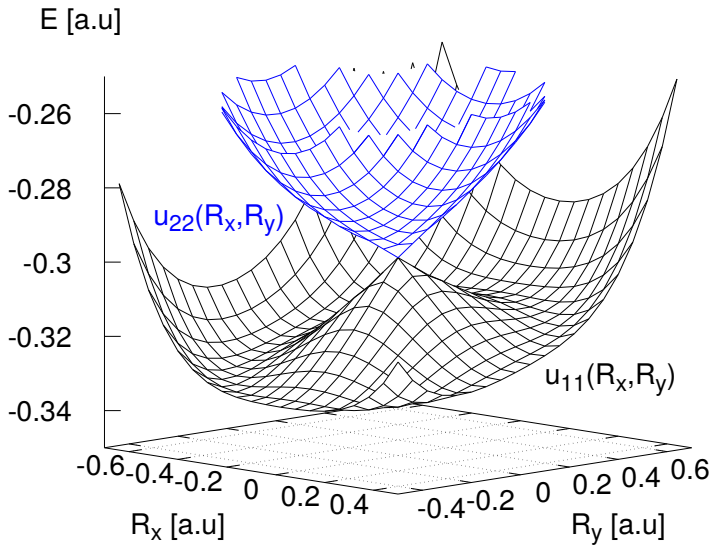

Figure 5-5: **Adiabatic Potentials of the Two-Dimensional Shin-Metiu Model**. The black surface shows $u_{11}(R_x, R_y)$ of the first excited state $|\phi_1(x, y; R_x, R_y)\rangle$ and the blue surface shows $u_{22}(R_x, R_y)$ of the second excited state $|\phi_2(x, y; R_x, R_y)\rangle$. The CoIn appears at the origin of the nuclear coordinate system. There, the two adiabatic electronic states are degenerated. It should be noted that the ground state and the third excited state are energetically well separated by 0.44 $a.u.$ and 0.81 $a.u.$, respectively, from the regarded two states.

A nuclear displacement from this geometry leaves the adiabatic surfaces with an energetic separation. Regarding the symmetry breaking along the R_y-coordinate first, the point group of the proton skeleton is assumed to have C_{2v}, which is a subgroup of D_{3h}. The character table of C_{2v} is given in table 5.3.

Table 5.3: **Excerpt of the Character Table of the C_{2v} Symmetry Point Group** [141].

C_{2v}	E	$2C_2(y)$	$\sigma(xy)$	$\sigma(yz)$	translation
a_1	1	1	1	1	$y; R_y$
b_1	1	-1	-1	1	$x; R_x$

The adiabatic eigenfunctions differ in their symmetry. The lower state $|\phi_1(x, y, R_x, R_y)\rangle$ has in the interval $R_y = [-1.5; 0.0[$ a.u. and $R_x = 0.0$ a.u. a_1 symmetry. $|\phi_2(x, y, R_x, R_y)\rangle$ has b_1 symmetry within the same interval. On the opposite side of the CoIn, these properties are just interchanged.

A symmetry breaking $R_x \neq 0$ is not connected to the C_{2v} symmetry group. Although, regarding fig. 5-2, it is seen that the adiabatic eigenfunctions can also be represented by a linear combination of the a_1 and b_1 irreducible representations of the C_{2v} symmetry group, which can be followed in fig. 5-2, where the vector fields represent these linear combinations by vectors which are not parallel to the coordinate axis.

The adiabatic electronic eigenfunctions depend parametrically on the nuclear coordinates. They build a complete basis set $\{|\phi_n(x, y; R_x, R_y)\rangle\}$, and the total wave function $|\Psi(x, y, R_x, R_y)\rangle$ can be expanded as:

$$\begin{aligned} |\Psi(x, y, R_x, R_y, t)\rangle &= \sum_n |\phi_n(x, y; R_x, R_y)\rangle \underbrace{\langle \phi_n(x, y; R_x, R_y) \,|\, \Psi(x, y, R_x, R_y, t)\rangle_{x,y}}_{|\chi_n(R_x, R_y, t)\rangle} \\ &= \sum_n |\phi_n(x, y; R_x, R_y)\rangle |\chi_n(R_x, R_y, t)\rangle. \end{aligned} \tag{5.4}$$

5.2.2 Diabatic Representation

5.2.2.1 Definition of the Diabatic Basis Set

For the definition of diabatic states, one solves the electronic Schrödinger equation at a fixed position $(\underline{R_x}, \underline{R_y})$:

$$\left(\hat{H}_{el}(x,y;\underline{R_x},\underline{R_y}) - \tilde{u}_{nn}(\underline{R_x},\underline{R_y};\underline{R_x},\underline{R_y})\right)|\tilde{\phi}_n(x,y;\underline{R_x},\underline{R_y})\rangle = 0. \tag{5.5}$$

As a diabatic basis, the following two wave functions are chosen:

$$|\tilde{\phi}_1(x,y)\rangle = |\phi_1(x,y;R_x = 0.0\ a.u., R_y = 0.4\ a.u.)\rangle, \tag{5.6}$$

$$|\tilde{\phi}_2(x,y)\rangle = |\phi_2(x,y;R_x = 0.0\ a.u., R_y = 0.4\ a.u.)\rangle. \tag{5.7}$$

The two determined diabatic eigenfunctions $|\tilde{\phi}_1(x,y)\rangle$ and $|\tilde{\phi}_2(x,y)\rangle$ are depicted in fig. 5-6. These two eigenfunctions build the diabatic basis for the description of a wave function within the adiabatic first and second excited electronic states $|\phi_1(x,y;R_x,R_y)\rangle$ and $|\phi_2(x,y;R_x,R_y)\rangle$.

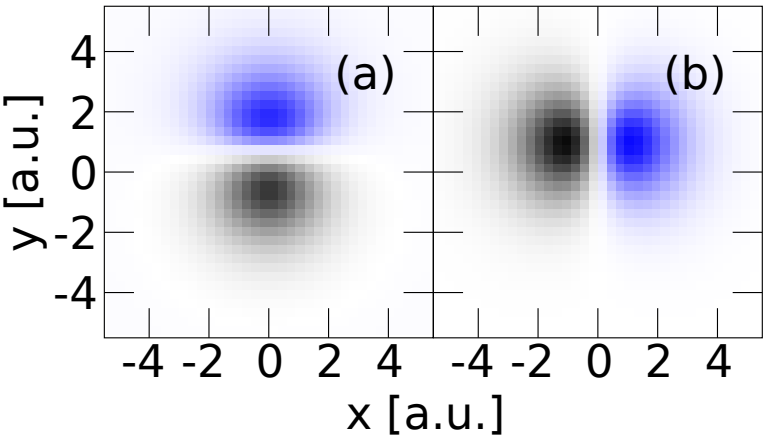

Figure 5-6: **Diabatic Eigenfunction Basis Set**. In panel (a), the diabatic eigenfunction $|\tilde{\phi}_2(x,y)\rangle$, and in panel (b) $|\tilde{\phi}_1(x,y)\rangle$ for the fixed nuclear position at $\underline{R_x} = 0.0\ a.u., \underline{R_y} = 0.4\ a.u.$ is depicted. The black color shows positive values, and the blue color shows negative values of the wave function.

The diabatic expansion then reads:

$$|\Psi(x,y,R_x,R_y,t)\rangle = \sum_{n=1}^{2} |\tilde{\phi}_n(x,y)\rangle \underbrace{\langle \tilde{\phi}_n(x,y) \,|\, \Psi(x,y,R_x,R_y,t)\rangle_{x,y}}_{|\tilde{\chi}_n(R_x,R_y,t)\rangle}$$
$$= \sum_{n=1}^{2} |\tilde{\phi}_n(x,y)\rangle |\tilde{\chi}_n(R_x,R_y,t)\rangle. \tag{5.8}$$

5.2.2.2 Transformation from the Diabatic Representation to the Adiabatic Representation

To establish the transformation between the diabatic representation and adiabatic representation, one writes:

$$|\phi_n(x,y;R_x,R_y)\rangle = \sum_{m=1}^{2} |\tilde{\phi}_m(x,y;\underline{R_x},\underline{R_y})\rangle \langle \tilde{\phi}_m(x,y;\underline{R_x},\underline{R_y}) \,|\, \phi_n(x,y;R_x,R_y)\rangle_{x,y}$$
$$= \sum_{m=1}^{2} (a^{-1})_{nm}(R_x,R_y;\underline{R_x},\underline{R_y}) |\tilde{\phi}_m(x,y;\underline{R_x},\underline{R_y})\rangle. \tag{5.9}$$

Then $a(R_x,R_y;\underline{R_x},\underline{R_y})$ is the inverse of $a^{-1}(R_x,R_y;\underline{R_x},\underline{R_y})$, so:

$$|\tilde{\phi}_n(x,y;\underline{R_x},\underline{R_y})\rangle = \sum_{m=1}^{2} a_{nm}(R_x,R_y;\underline{R_x},\underline{R_y}) |\phi_m(x,y;R_x,R_y)\rangle, \tag{5.10}$$

with this transformation, the following relations are given:

$$\sum_m a_{km}(R_x,R_y;\underline{R_x},\underline{R_y})\ (a^{-1})_{mn}(R_x,R_y;\underline{R_x},\underline{R_y}) = \delta_{kn}, \tag{5.11}$$

$$\sum_m (a^{-1})_{km}(R_x,R_y;\underline{R_x},\underline{R_y})\ a_{mn}(R_x,R_y;\underline{R_x},\underline{R_y}) = \delta_{kn}. \tag{5.12}$$

To clarify the question if the NACTs deliver an analytic solution for the transformation matrix, one follows another ansatz which was also used in the previous chapters. This ansatz is employed via the non-adiabatic coupling elements between

the first adiabatic and second adiabatic electronic eigenstate.

Following the previous chapter, one has to find a solution for:

$$\sum_{i=1}^{2} \vec{\nabla}_{\vec{R}} \delta_{ki} (A^{-1})_{in}(R_x, R_y) + \vec{\tau}_{ki}(R_x, R_y)(A^{-1})_{in}(R_x, R_y) = 0. \tag{5.13}$$

In order to obtain a solution for eq. (5.13), the curl condition must be fulfilled:

$$0 = \frac{\partial}{\partial R_x}(\tau_{12}(R_x, R_y))_{R_y} - \frac{\partial}{\partial R_y}(\tau_{12}(R_x, R_y))_{R_x}. \tag{5.14}$$

This can also be evaluated numerically, and the result can be seen in fig. 5-7.

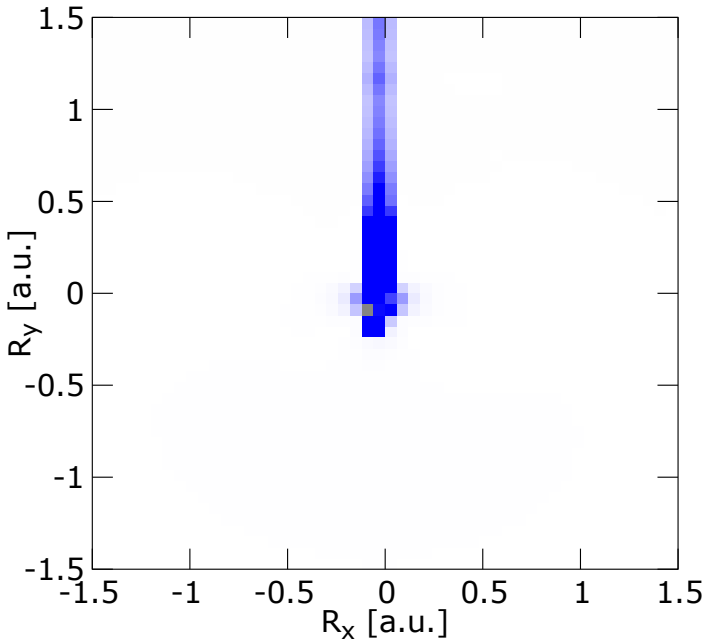

Figure 5-7: **The Curl of $\tau_{12}(R_x, R_y)$.** It can be seen that the curl condition is valid for the white area, where the value of the curl is zero. This holds neither for the location of the CoIn, nor for the discontinuity. It should be noted that the discontinuity can be shifted, and finally the curl condition is valid for all points within the numerical range, except of the location of the CoIn.

The curl equation is fulfilled for the white area.

Equation (5.13) is solved according to earlier sections:

$$A^{-1}(R_x, R_y; \underline{R_x}, \underline{R_y}) = \begin{pmatrix} \cos(\varphi(R_x, R_y)) & -\sin(\varphi(R_x, R_y)) \\ \sin(\varphi(R_x, R_y)) & \cos(\varphi(R_x, R_y)) \end{pmatrix} \cdot A^{-1}(\underline{R_x}, \underline{R_y}; \underline{R_x}, \underline{R_y}), \tag{5.15}$$

where the rotation angle is given by the path integral:

$$\varphi(R_x, R_y; \underline{R_x}, \underline{R_y}) = \int_{\underline{R_x}, \underline{R_y}}^{R_x, R_y} \begin{pmatrix} (\tau_{12}(R_x, R_y))_{\tilde{R}_x} \\ (\tau_{12}(R_x, R_y))_{\tilde{R}_y} \end{pmatrix}^T \cdot \begin{pmatrix} \partial \tilde{R}_x \\ \partial \tilde{R}_y \end{pmatrix}. \tag{5.16}$$

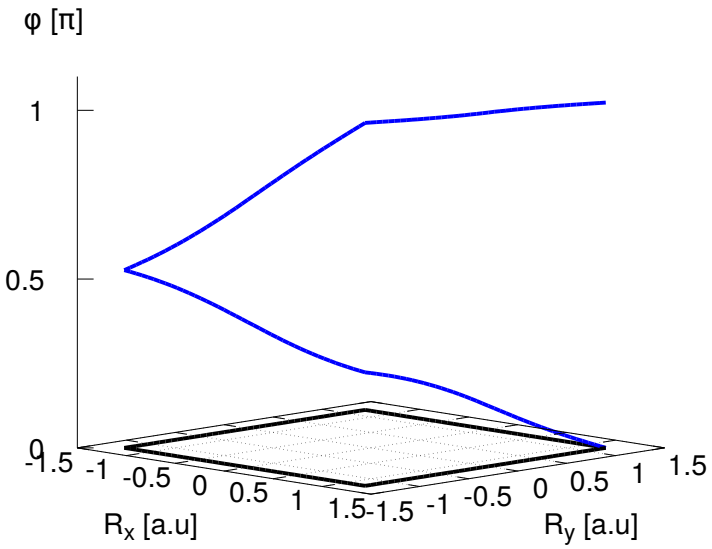

Figure 5-8: **Mixing Angle along a Closed Random Path around the CoIn.** The black line depicts the path around the CoIn, and the blue line is the phase gathered upon the line integration along this path.

The mixing angle is path-dependent. The transformation starts at the initial geometry defining the diabatic basis set. There, the function $|\phi_1(x,y;R_x,R_y)\rangle$ has p_x-shape and $|\phi_2(x,y;R_x,R_y)\rangle$ has p_y-shape. As the adiabatic eigenfunctions are identical to the diabatic ones in this location, the transformation matrix reads with a vanishing mixing angle:

$$A^{-1}(R_x = 0.0\ a.u., R_y = 0.4\ a.u.; \underline{R_x}, \underline{R_y}) = \begin{pmatrix} 1 & 0 \\ 0 & 1 \end{pmatrix} A^{-1}(\underline{R_x}, \underline{R_y}; \underline{R_x}, \underline{R_y}). \tag{5.17}$$

After a half circle around the CoIn, following this path in fig. 5-2, the adiabatic wave functions are reversed in shape with respect to the initial starting point. Then, $|\phi_1(x,y;R_x,R_y)\rangle$ has p_y-shape, and $|\phi_n(x,y;R_x,R_y)\rangle$ has p_x-shape. This is in agreement with the mixing angle of $\frac{\pi}{2}$, gathered around a half cycle. Then, the transformation matrix is given by:

$$A^{-1}(R_x = 0.0\ a.u., R_y = -0.4\ a.u.; \underline{R_x}, \underline{R_y}) = \begin{pmatrix} 0 & -1 \\ 1 & 0 \end{pmatrix} A^{-1}(\underline{R_x}, \underline{R_y}; \underline{R_x}, \underline{R_y}) \tag{5.18}$$

and upon a full clockwise circle around the CoIn, the mixing angle amounts to π and the transformation matrix is:

$$A^{-1}(R_x = 0.0\ a.u., R_y = 0.4\ a.u.; \underline{R_x}, \underline{R_y}) = \begin{pmatrix} -1 & 0 \\ 0 & -1 \end{pmatrix} A^{-1}(\underline{R_x}, \underline{R_y}; \underline{R_x}, \underline{R_y}), \tag{5.19}$$

which is again in perfect agreement with fig. 5-2. The transformation from adia-

batic potentials to diabatic potentials is given by:

$$\sum_{n,m} a_{kn}(R_x, R_y; \underline{R_x}, \underline{R_y}) u_{nm}(R_x, R_y)(a^{-1})_{mi}(R_x, R_y; \underline{R_x}, \underline{R_y}) = \tilde{u}_{ki}(R_x, R_y; \underline{R_x}, \underline{R_y}). \tag{5.20}$$

the diabatic potentials are given as: $\tilde{u}_{nm}(R_x, R_y; \underline{R_x}, \underline{R_y})\delta_{nm}$, and the off-diagonal coupling elements as: $\tilde{u}_{nm}(R_x, R_y; \underline{R_x}, \underline{R_y})$, with $n \neq m$.

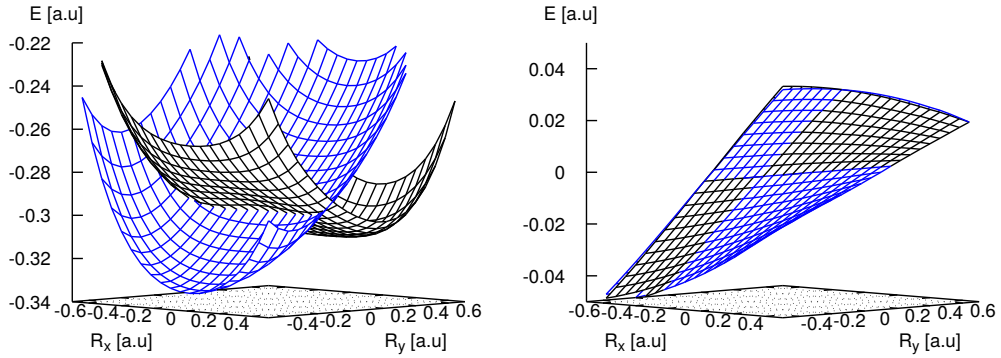

Figure 5-9: **Diabatic Potentials**. In the left panel, the diabatic diagonal potentials $\tilde{u}_{nn}\left(R_x, R_y; \underline{R_x}, \underline{R_y}\right)$, with $n = 1, 2$, and for a fixed nuclear geometry of $\underline{R_x} = 0.0\ a.u., \underline{R_y} = 0.4\ a.u.$ are depicted. In the right panel the off-diagonal coupling potentials $\tilde{u}_{12}\left(R_x, R_y; \underline{R_x}, \underline{R_y}\right)$ and $\tilde{u}_{21}\left(R_x, R_y; \underline{R_x}, \underline{R_y}\right)$ are shown.

The nuclear time-depenedent Schrödinger equation in the diabatic basis is written as:

$$\begin{aligned}\sum_{i=1}^{2} \left\{ -\frac{\vec{\nabla}^2_{\vec{R}}}{2M}\delta_{ki} + \tilde{u}_{ki}\left(R_x, R_y; \underline{R_x}, \underline{R_y}\right) \right\} |\tilde{\chi}_i(R_x, R_y; \underline{R_x}, \underline{R_y}; t)\rangle \\ = i\frac{\partial}{\partial t}|\tilde{\chi}_k(R_x, R_y; \underline{R_x}, \underline{R_y}; t)\rangle.\end{aligned} \tag{5.21}$$

The hamiltonian can be written in matrix from:

$$
\begin{aligned}
\hat{H}(R_x, R_y) &= \hat{T}_N(R_x, R_y) + \hat{V}(R_x, R_y; \underline{R_x}, \underline{R_y}) \\
&= \begin{pmatrix} -\frac{1}{2M}\left(\frac{\partial^2}{\partial R_x^2} + \frac{\partial^2}{\partial R_y^2}\right) & 0 \\ 0 & -\frac{1}{2M}\left(\frac{\partial^2}{\partial R_x^2} + \frac{\partial^2}{\partial R_y^2}\right) \end{pmatrix} \\
&\quad + \begin{pmatrix} \tilde{u}_{11}\left(R_x, R_y; \underline{R_x}, \underline{R_y}\right) & \tilde{u}_{12}\left(R_x, R_y; \underline{R_x}, \underline{R_y}\right) \\ \tilde{u}_{21}\left(R_x, R_y; \underline{R_x}, \underline{R_y}\right) & \tilde{u}_{22}\left(R_x, R_y; \underline{R_x}, \underline{R_y}\right) \end{pmatrix}. \qquad (5.22)
\end{aligned}
$$

If the diabatic approximation is valid, a diabatic propagation in comparison to the exact propagation should reproduce the results of the numerically exact propagation.

It should be noticed that the diabatic potentials in fig. 5-9 are in very good agreement with a linear hamiltonian of Jahn-Teller form [94], which reads as:

$$
\hat{V}_{JT}(R_x, R_y) = \begin{pmatrix} \frac{\omega_1}{2}(R_x^2 + R_y^2) & 0 \\ 0 & \frac{\omega_2}{2}(R_x^2 + R_y^2) \end{pmatrix} + \kappa \begin{pmatrix} R_y & R_x \\ R_x & -R_y \end{pmatrix}. \qquad (5.23)
$$

One has two concentric two-dimensional harmonic oscillators $\frac{\omega_n}{2}(R_x^2 + R_y^2)$ with coordinates R_x, R_y and frequencies ω_n. These two harmonic oscillators are then separated in energy by the diagonal elements κR_y and $-\kappa R_y$. The off-diagonal elements in the Jahn-Teller hamiltonian are chosen linear with κR_x. Regarding the off-diagonal elements of the numerically determined diabatic coupling potential in fig. 5-9, one sees clearly the linearity in these potential along the R_x-coordinate. Along the R_y-coordinate, this coupling potential stays more or less constant which confirms the characteristic of the off-diagonal elements within the linear Jahn-Teller hamiltonian.

Furthermore, the diagonal elements of the diabatic potential matrix resemble harmonic potentials displaced in R_y. This is nothing else than two harmonic concentric oscillators modulated by a negative linear term and a positive linear term

in R_y-direction. This is also in perfect agreement with the potential form of the linear Jahn-Teller hamiltonian, where one has $\frac{\omega_1}{2}(R_x^2+R_y^2)+\kappa R_y$ for the first state potential, and $\frac{\omega_2}{2}(R_x^2+R_y^2)-\kappa R_y$ for the other potential, which corresponds to $\tilde{u}_{11}\left(R_x,R_y;\underline{R_x},\underline{R_y}\right)$ and $\tilde{u}_{22}\left(R_x,R_y;\underline{R_x},\underline{R_y}\right)$, respectively.

5.3 Exact Wave-Packet Dynamics in Comparison to the Dynamics in the Adiabatic Representation and Diabatic Representation

In what follows the adiabatic as well as the diabatic representation are used to characterize the wave-packet dynamics through, around and circuitting the CoIn. These representations are compared to the numerically exact propagation.

5.3.1 Nuclear Wave-Packet Dynamic Through a Conical Intersection

As was already reported [136, 137], a nuclear wave-packet motion directly through a CoIn is under certain circumstances a process where the electronic character stays almost constant. This holds for a dynamics where, upon passage of the CoIn, a large population transfer between the involved adiabatic states is observed passing a CoIn. A comparable situation with a motion through a CoIn as in former studies [137] is regarded. But this process is further investigated by a diabatization which replicates the dynamics in the reduced diabatic picture with a remarkable resemblance compared to the fully coupled electron-nuclear propagation.

5.3.1.1 Full-Dimensional Dynamics

First, the numerically exact coupled electron-nuclear propagation is discussed. The wave packet is obtained by solving eq. (2.6). In order to visualize the starting point of the nuclear wave-packet motion, it is marked on the adiabatic potential surface $u_{22}\left(R_x,R_y\right)$ at $(R_{x_0}=0.0\ a.u.,R_{y_0}=0.4\ a.u.)$ in fig. 5-10.

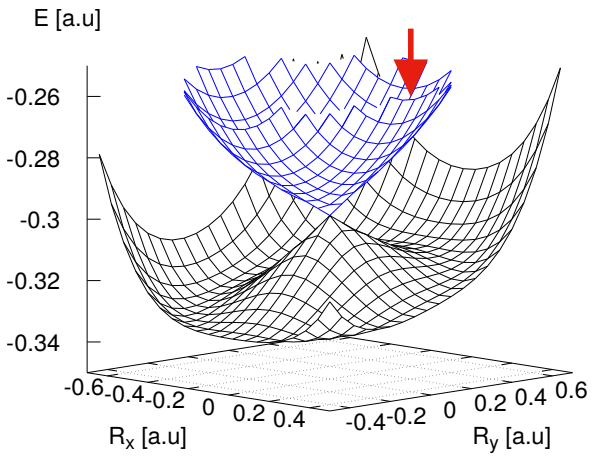

Figure 5-10: **Starting Point of the Wave Packet in the Adiabatic Representation.** Shown are the adiabatic potentials $u_{11}(R_x, R_y)$ and $u_{22}(R_x, R_y)$ of the first and the second excited state. The red arrow marks the position of the wave packet at the second adiabatic potential energy surface, which refers to the starting point of the simulation.

The initial wave function in full-dimensional coordinate space is given as the product of a Gaussian nuclear wave-packet and the second adiabatic excited electronic eigenstate:

$$|\Psi(x, y, R_x, R_y, t = 0)\rangle = N \cdot e^{-\beta(R_x - R_{x0})^2} e^{-\beta(R_y - R_{y0})^2} \cdot |\phi_2(x, y; R_x, R_y)\rangle, \quad (5.24)$$

with $\beta = 10.0\ \frac{1}{a.u.}$, and $R_{x_0} = 0.0\ a.u.$, and $R_{y_0} = 0.4\ a.u.$. N is a normalization constant. The parameters for the wave-packet propagation are summarized in table 5.1. The dynamics is characterized by the nuclear and electron densities $\rho_{nuc}(R_x, R_y, t)$ and $\rho_{el}(x, y, t)$, defined as:

$$\rho_{nuc}(R_x, R_y, t) = \langle \Psi(x, y, R_x, R_y, t) \,|\, \Psi(x, y, R_x, R_y, t) \rangle_{x,y} \tag{5.25}$$

and

$$\rho_{el}(x, y, t) = \langle \Psi(x, y, R_x, R_y, t) \,|\, \Psi(x, y, R_x, R_y, t) \rangle_{R_x,R_y}. \tag{5.26}$$

Regarding the nuclear wave-packet dynamics in the picture of adiabatic potential surfaces, see fig. 5-10, it is seen that the Gaussian wave-packet evolves towards the CoIn and finally passes it. This is due to the gradient of the potential surface $u_{22}\,(R_x, R_y)$ towards the location of the CoIn.

The temporal evolution of the nuclear density $\rho_{nuc}(R_x, R_y, t)$ is displayed in fig. 5-11. The density is depicted for times ranging from 1 to 4 fs.

Shown before [136], the nuclear wave packet stays rather compact and Gaussian like while passing the CoIn the location of which is marked by the black point in the origin of the nuclear coordinate space. Also shown is the potential $V(x, y, R_{x,t}, R_{y,t})$, where ($R_{x,t}$,$R_{y,t}$) is the temporal mean position of the nuclear density. This represents the interaction potential, a classical electron would be exposed to. During this motion, the electron density does not change significantly. Rather, it remains almost stationary [26, 136, 137].

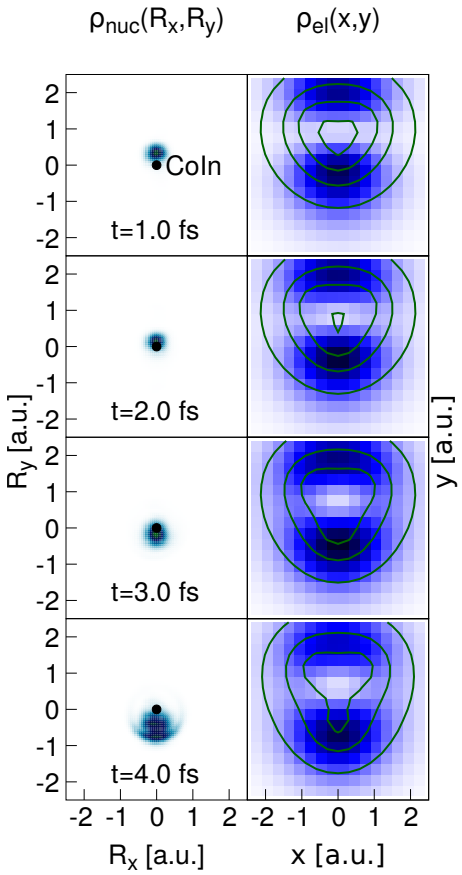

Figure 5-11: **Densities for the Wave-Packet Motion through the CoIn.** The left panels show the nuclear density, and the right panels the electron density. The contour lines represent the interaction potential $V(x, y, R_{x,t}, R_{y,t})$. They start with the value of -0.5 a.u. (outer line) and decrease in steps of 0.5 a.u..

To be more precise the electronic component of the wave packet starts in the p_y-like electronic state and keeps its initial character. In other words, it conserves its symmetry along with the wave-packet dynamics. Starting with a_1 symmetry, it becomes then the degenerate e' representation in D_{3h} symmetry during the time, when the wave packet is located at the position of the CoIn and after passing the CoIn the symmetry stays a_1-like.

This is in accordance with a diabatic motion. The population transfer can additionally be seen in the population dynamics depicted in fig. 5-12. The transition starts at approximately 2 fs, and upon the first crossing of the CoIn, about 80 percent of the population is transferred. Further crossings turn out to be less

efficient as the transition rate goes down [26].

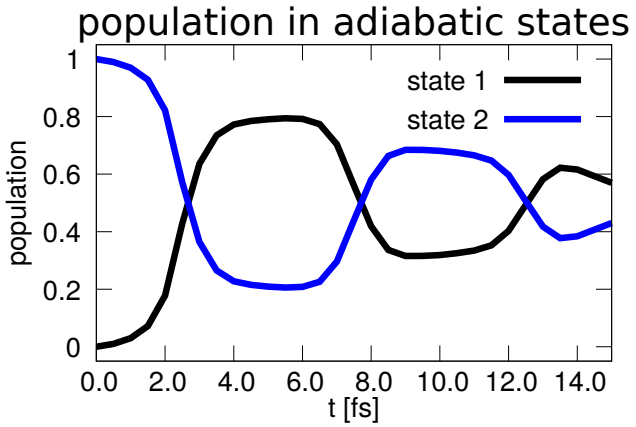

Figure 5-12: **Population Dynamics for the Wave-Packet Motion Through the CoIn.** Shown is the population dynamics in the two adiabatic states, as indicated. A large population transfer takes place at the first passage of the CoIn after 2 fs.

5.3.1.1.1 Full-Dimensional Dynamics Regarded in the Adiabatic Representation. Concentrating on the first adiabatic state transition of the wave packet in the time-interval $[0.0; 4.0]$ fs, one can calculate the adiabatic densities:

$$\rho_n^a(R_x, R_y, t) = \langle \phi_n(x, y; R_x, R_y) \,|\, \Psi(x, y, R_x, R_y, t) \rangle_{x,y}, \tag{5.27}$$

with $n = 1, 2$.

These densities are compared to the total nuclear density $\rho_{nuc}(R_x, R_y, t)$ in fig. 5-13. It is clearly seen that the initially populated component vanishes and, simultaneously, the other component appears at the location of the CoIn. Remarkably, the transition at the location of the CoIn is large and spatially localized, where slight deviations from the position of the CoIn show almost no transferred density. It is seen that the total density does not exhibit such dramatic changes while passing the CoIn.

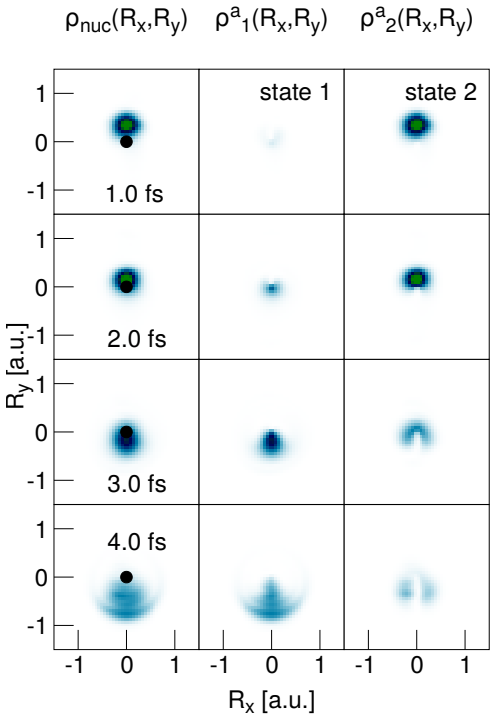

Figure 5-13: **Density Dynamics Projected on the Adiabatic States.** The left panels show the nuclear density. The middle and the right panels show the adiabatic densities. It is seen that the density changes from the second to the first adiabatic state while passing the CoIn.

5.3.1.1.2 Full-Dimensional Dynamical Approach Regarded in the Diabatic Representation. The diabatic representation is used and the fully coupled electron-nuclear dynamics is projected on the diabatic representation. Therefore, using the ansatz already introduced in the second part of this chapter, one obtains the diabatic potential surfaces $\tilde{u}_{11}\left(R_x, R_y; \underline{R_x}, \underline{R_y}\right)$ and $\tilde{u}_{22}\left(R_x, R_y; \underline{R_x}, \underline{R_y}\right)$ in fig. 5-14. The nuclear wave packet starts at the same nuclear coordinates as in the previous propagation with the same initial nuclear wave function, but now one just projects the nuclear density on the two diabatic states $|\tilde{\phi}_{n=1,2}(x, y; \underline{R_x}, \underline{R_y})\rangle$.

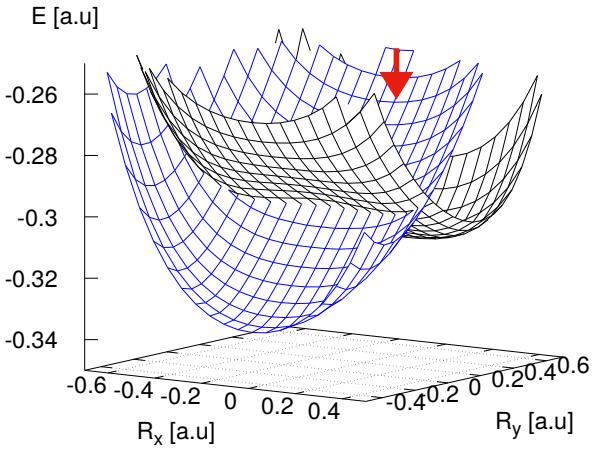

Figure 5-14: **Starting Point of the Wave Packet in the Diabatic Representation.** The black surface represents $\tilde{u}_{11}\left(R_x, R_y; \underline{R_x}, \underline{R_y}\right)$ and the blue surface represents $\tilde{u}_{22}\left(R_x, R_y; \underline{R_x}, \underline{R_y}\right)$ of the first and the second diabatic state, respectively. The arrow marks the position of the initial wave packet.

The nuclear wave packet is expected to follow the negative gradient of the diabatic potential surface $\tilde{u}_{22}\left(R_x, R_y; \underline{R_x}, \underline{R_y}\right)$. The dynamics clearly takes place mainly in the second diabatic state $|\tilde{\phi}_2(x, y; \underline{R_x}, \underline{R_y})\rangle$, as is documented by the diabatic state populations shown in fig. 5-15.

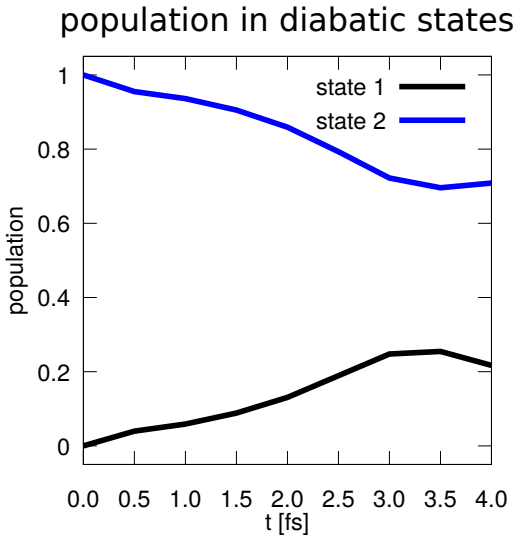

Figure 5-15: **Population Dynamics Projected on the Diabatic States.** Shown is the population dynamics in the two diabatic states. It is seen that most of the population stays in the second diabatic state.

The dynamics can also be illustrated by the diabatic densities:

$$\rho_n^d(R_x, R_y, t) = \langle \tilde{\phi}_n(x, y; \underline{R_x}, \underline{R_y}) \,|\, \Psi(x, y, R_x, R_y, t) \rangle_{x,y}, \tag{5.28}$$

with $n = 1, 2$.

They are depicted in fig. 5-16. The nuclear density stays mostly in the second diabatic state $|\tilde{\phi}_2(x, y; \underline{R_x}, \underline{R_y})\rangle$. One can claim that the electron stays stationary or constant while the nuclear wave packet is passing the CoIn, as this diabatic state is uniform in character and has a_1 symmetry.

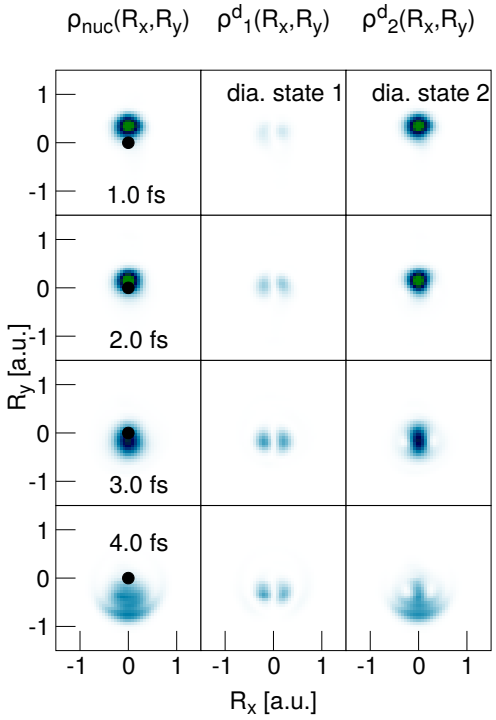

Figure 5-16: **Density Dynamics Projected on the Diabatic States.** The left panels show the nuclear density. The middle and right panels show the diabatic densities. It is seen that the density remains mostly in the second diabatic state during the dynamics.

5.3.1.2 Diabatic State Dynamics

The nuclear dynamics is obtained from the solution of the time-dependent Schrödinger equation eq. (5.21). As initial condition, the following wave functions are chosen:

$$|\tilde{\chi}_2(R_x, R_y; \underline{R_x}, \underline{R_y}, t = 0)\rangle = N \cdot e^{-\beta(R_x - R_{x_0})^2} e^{-\beta(R_y - R_{y_0})^2}, \tag{5.29}$$

and

$$|\tilde{\chi}_1(R_x, R_y; \underline{R_x}, \underline{R_y}, t = 0)\rangle = 0.0. \tag{5.30}$$

The numerical parameters are the same as used before. The result of the diabatic propagation is seen in fig. 5-17, where the nuclear densities are depicted for the two diabatic states (middle and right panel), and also the total densities are defined

as:

$$\varrho^d_{tot}(R_x, R_y, t) = \varrho^d_1(R_x, R_y, t) + \varrho^d_2(R_x, R_y, t), \tag{5.31}$$

where

$$\varrho^d_n(R_x, R_y, t) = \langle \tilde{\chi}_n(R_x, R_y; \underline{R_x}, \underline{R_y}, t) \,|\, \tilde{\chi}_n(R_x, R_y; \underline{R_x}, \underline{R_y}, t) \rangle, \tag{5.32}$$

with $n = 1, 2$. As one can see, the dynamics is in very good agreement with the result obtained from the coupled dynamics, see fig. 5-16.

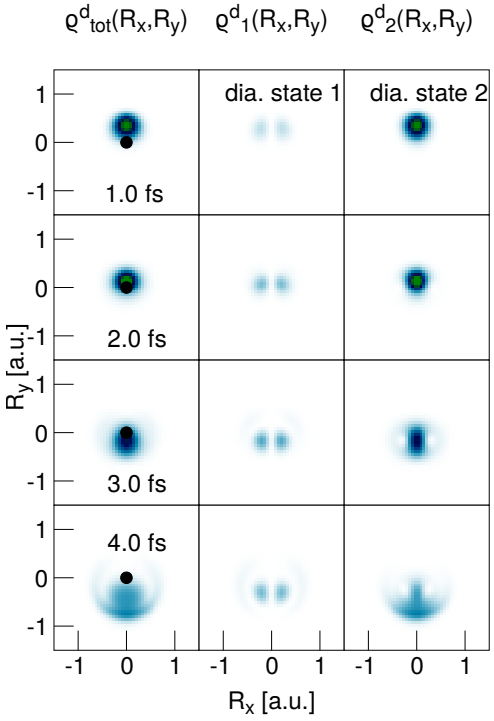

Figure 5-17: **Density Dynamics in the Diabatic State Representation.** The left panels show the total nuclear density. The middle and the right panels show the diabatic densities. It is seen that the density remains mostly in the second diabatic state during the dynamics and that it is in very good agreement with the numerically exact propagation fig. 5-16.

5.3.1.3 Long-Time Behavior of a Wave Packet Passing the Conical Intersection

Regarding the long-time behavior of the case where a nuclear wave packet crosses the CoIn multiple times, one can verify the process to remain diabatic. This is seen in fig. 5-18, where the nuclear wave packet stays compact while passing the CoIn at least three times after 12 fs, see fig. 5-12. This indicates that the electronic character should also be constant as it is observed for the short-time behavior crossing the CoIn once. Regarding the right panels in fig. 5-18, this can be verified as the electron density remains mostly in a p_y-like shape, i.e. the symmetry of the initial electronic wave function symmetry [26].

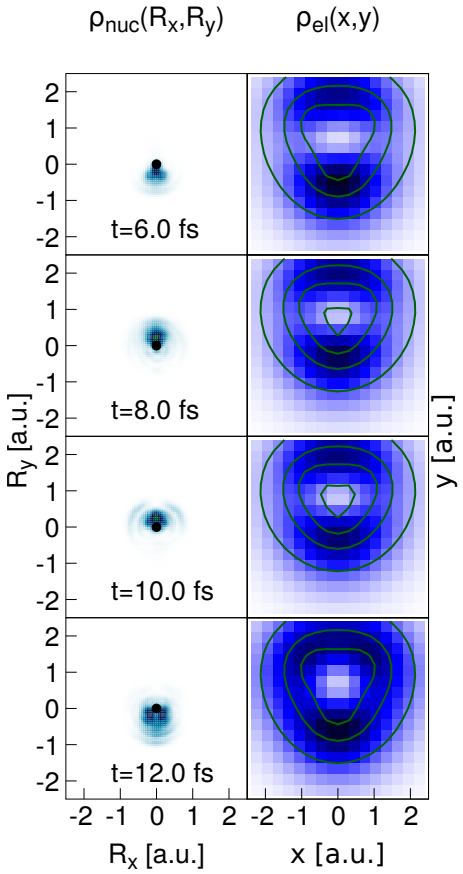

Figure 5-18: **Densities for the Wave-Packet Motion through the CoIn for Longer Times.** Same as in fig. 5-11, but for times up to 12 fs.

5.3.1.4 Changing Nuclear-Electron Interaction

As observed in fig. 5-12, about 80 percent of the population was transferred, while the nuclear wave packet passed the CoIn for the first time. In this case, the shielding parameter for the electron-proton interaction is set to a value of $a = 0.5$ a.u.. In what follows, the population transfer for weaker and stronger shielding between the electron and the mobile proton are regarded. As with different shielding parameters the topology changes, the initial conditions are slightly adapted and are comparable to the already known situation of a wave packet crossing the CoIn. The initial conditions are only changed to a $R_{y_0} = 0.7\ a.u.$ displacement.
Regarding fig. 5-20, it is observed that neither for stronger shielding nor for weaker shielding the population transfer significantly changes. Although the topology changes for different shielding, see fig. 5-19, the topology keeps exhibiting the CoIn. It was seen earlier that the location of the CoIn marks the point on the adiabatic surfaces where the population transfer is very efficient. This is in contrast to the case of the one-dimensional model, where an avoided crossing is present. There the energy gap between the two non-crossing potentials can be toggled by variing the shielding. As seen in section 4.5.1, this has an influence on the population transfer between the involved adiabatic states.

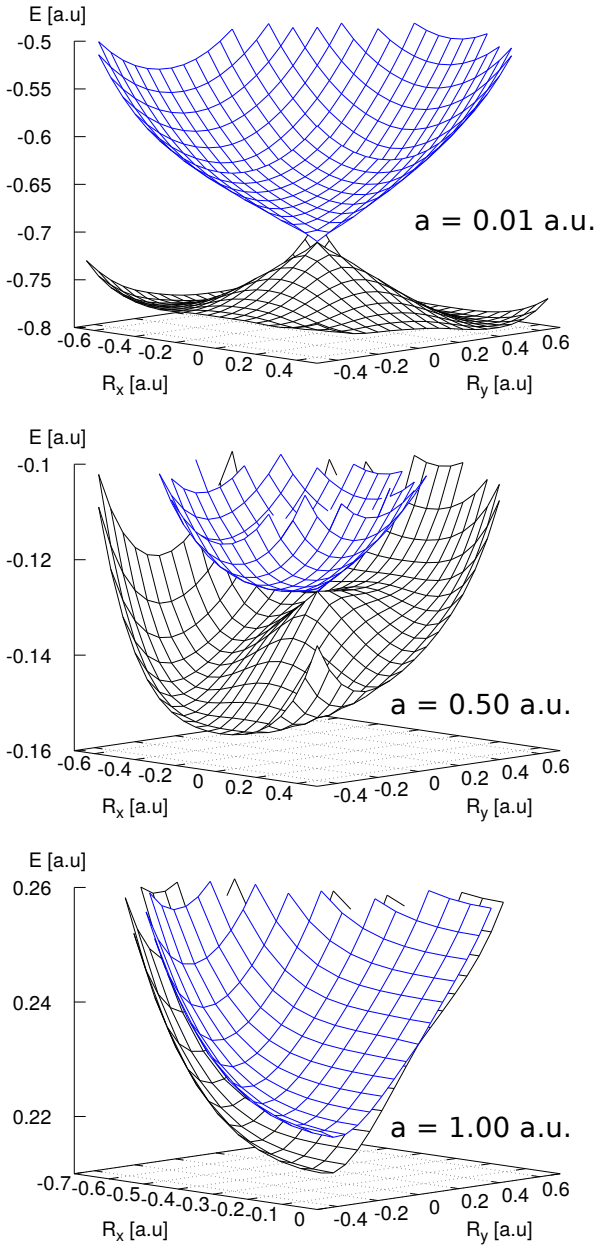

Figure 5-19: **Potential Energy Surfaces for Weaker and Stronger Electron-Proton Interaction.** The blue surface represents the potential energy surface of the second adiabatic state, and the black surface represents the potential energy surface of the first adiabatic state, respectively.

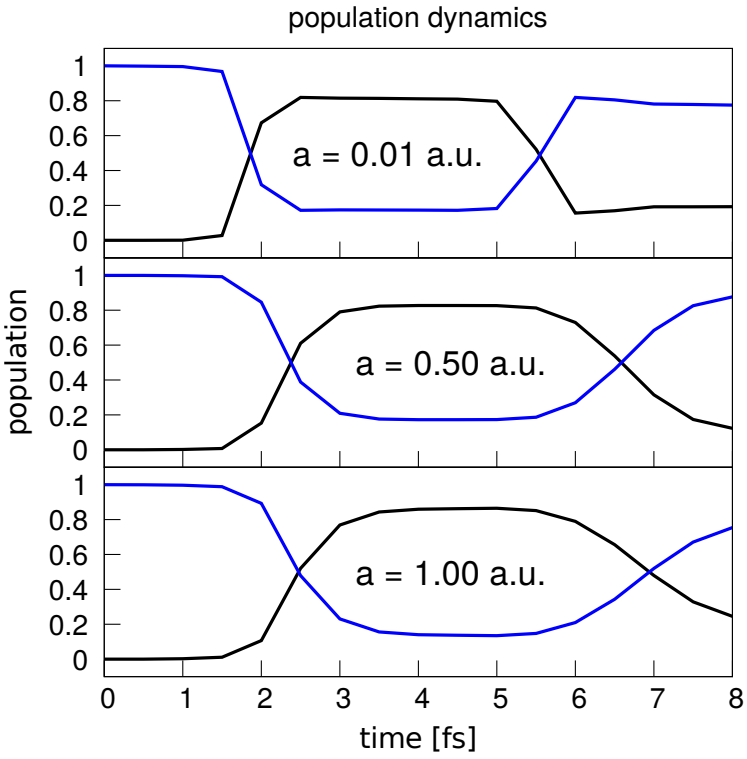

Figure 5-20: **Population Dynamics for Weaker and Stronger Electron-Proton Interaction.** The blue curve represents the population of the second adiabatic state, and the black curve represents the population of the first adiabatic state, respectively. Neither for stronger interaction (upper panel), nor for the weaker (lower panel) the population transfer changes significantly.

5.3.1.5 Wave-Packet Dynamics Through the CoIn from a Different Angle

To complete the study, a case is chosen where the initial condition leads to a crossing of the CoIn at a different angle. The initial wave packet is given by eq. (5.24), with $R_x = 0.4$ a.u. and $R_y = 0.0$ a.u..

The densities for the proton $\rho_{nuc}(R_x, R_y, t)$ and the electron $\rho_{el}(x, y, t)$ can be followed in fig. 5-21 for the time interval in which the wave packet passes the CoIn. Again, it can be seen that the nuclear wave packet stays compact in shape while passing the CoIn. Parallel, the density for the electron stays stationary in shape indicating a constant electronic character.

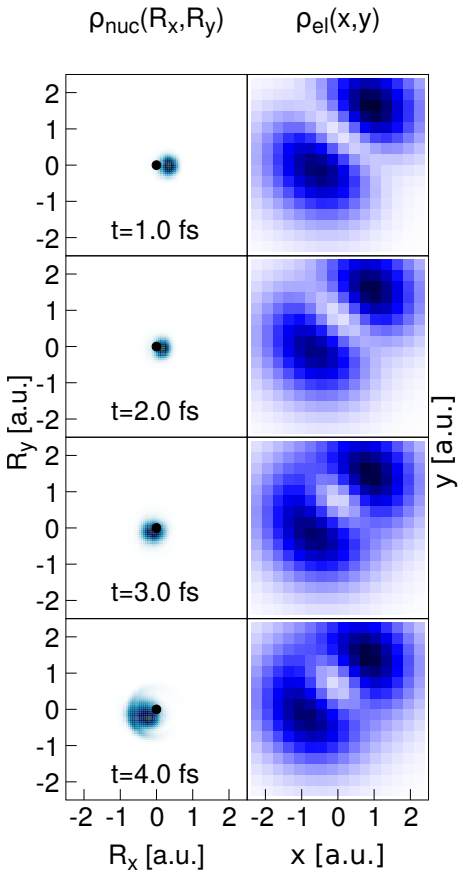

Figure 5-21: **Densities for the Wave-Packet Motion through the CoIn from a Different Angle.** The left panels show the nuclear density, and the right panels show the electron density for times up to 4 fs.

As a result, a diabatic representation can be chosen in order to follow this diabatic process. Therefore, the following states are chosen as diabatic basis states:

$$|\tilde{\phi}_1(x,y)\rangle = |\phi_1(x,y;R_x = 0.4\ a.u., R_y = 0.0\ a.u.)\rangle, \tag{5.33}$$

$$|\tilde{\phi}_2(x,y)\rangle = |\phi_2(x,y;R_x = 0.4\ a.u., R_y = 0.0\ a.u.)\rangle. \tag{5.34}$$

These functions are depicted in fig. 5-22.

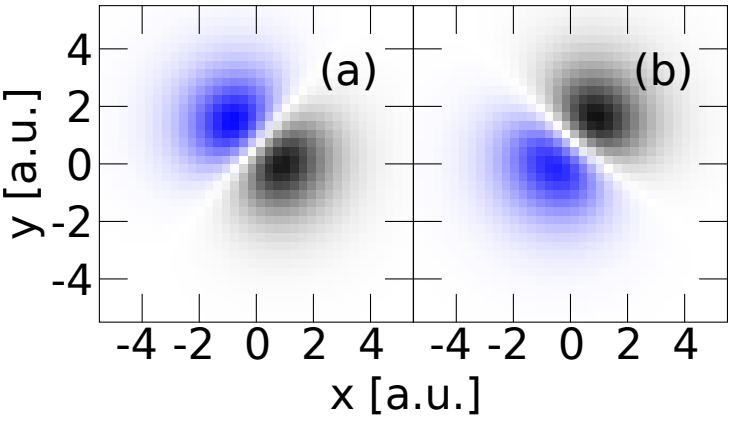

Figure 5-22: **Diabatic Basis States.** In panel (a), the adiabatic eigenfunction $|\phi_1(x,y,R_x,R_y)\rangle$ for a fixed nuclear geometry of $R_x = 0.4\ a.u., R_y = 0.0\ a.u.$ is depicted. In panel (b), $|\phi_2(x,y,R_x,R_y)\rangle$ for the fixed nuclear position at $R_x = 0.4\ a.u., R_y = 0.0\ a.u.$ is depicted. The black color shows positive and the blue color negative values of the wave function.

In this diabatic basis, a wave-packet dynamics can be clearly seen, which mostly takes place in the second diabatic state. This is also confirmed in the population dynamics of the diabatic states in fig. 5-23. There, about 70 percent of the population stays in the first diabatic state. This states that the crossing from a different angle is also a diabatic motion.

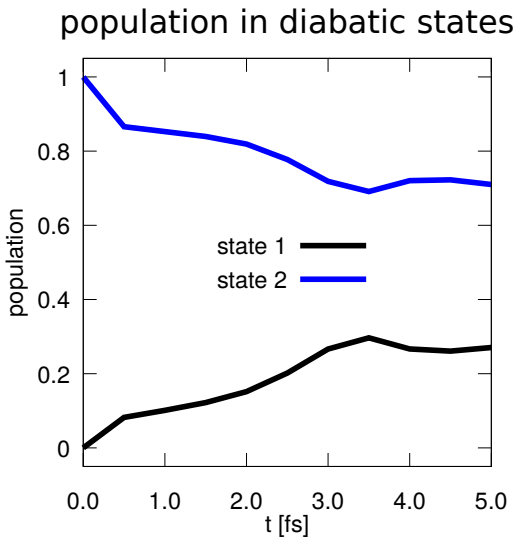

Figure 5-23: **Population Dynamics in the Diabatic Electronic States.** Shown is the diabatic population dynamics for the nuclear wave-packet motion through the CoIn from a different angle.

A projection of the full-dimensional propagation on the diabatic representation is shown in fig. 5-24 and confirmes that most of the nuclear wave packet stays in the second diabatic state.

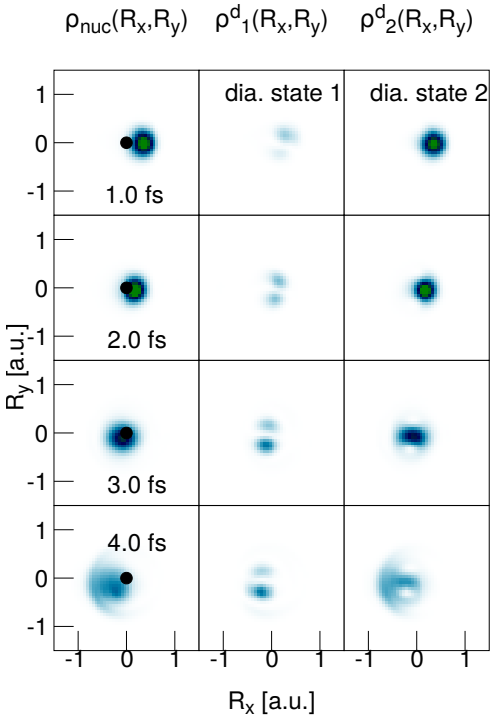

Figure 5-24: **Density Dynamics in the Diabatic State Representation.** The left panels show the nuclear density for the nuclear wave-packet motion through the CoIn from a different angle. The middle and the right panels show the projected diabatic nuclear density for corresponding times for the first and the second diabatic state. It is seen that most of the density stays in the second diabatic state.

5.3.1.6 Diabatization for the Wave-Packet Dynamics Through the CoIn from a Different Angle

In what follows, a diabatization is carried out in order to underline the findings from above. The system is represented in the diabatic representation where the diabatic potentials and potential coupling elements take an already known form, see fig. 5-25.

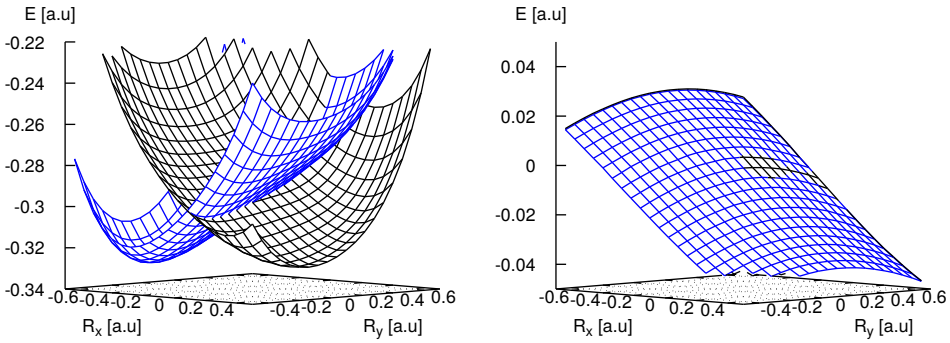

Figure 5-25: **Diabatic Potentials for the Different Diabatic Basis.** In the left panel, $\tilde{u}_{11}\left(R_x, R_y; \underline{R_x}, \underline{R_y}\right)$ is shown as black surface and $\tilde{u}_{22}\left(R_x, R_y; \underline{R_x}, \underline{R_y}\right)$ is shown as blue surface. The diabatic coupling potentials $\tilde{u}_{12}\left(R_x, R_y; \underline{R_x}, \underline{R_y}\right)$, $\tilde{u}_{21}\left(R_x, R_y; \underline{R_x}, \underline{R_y}\right)$ are depicted in the right panel. These potentials are obtained a diabatic basis at the fixed nuclear geometry of $\underline{R_x} = 0.4\ a.u., \underline{R_y} = 0.0\ a.u.$

.

As an initial condition, the nuclear wave packet is chosen to be in the second diabatic state according to eq. (5.29) and eq. (5.30). The parameters are kept with the full dimensional propagation for consistency.

This results in a dynamics in the diabatic representation shown in fig. 5-26. As expected, they are in very good agreement with the nuclear dynamics obtained from the full-dimensional propagation.

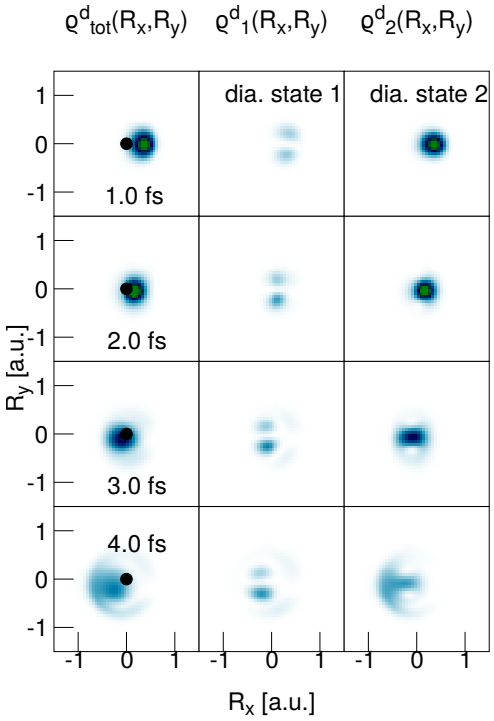

Figure 5-26: **Density Dynamics in the Diabatic State Representation for the Nuclear Wave-Packet Motion Through a CoIn from a Different Angle.** Left, the total nuclear density is shown. In the middle and the right panels, the diabatic nuclear densities of the first and second diabatic state are shown. The nuclear wave-packet dynamics is in very good agreement with the full-dimensional approach fig. 5-24.

5.3.2 Nuclear Wave-Packet Dynamics Around a Conical Intersection

Another interesting case is the surrounding of a CoIn by a wave packet. This has also been studied [142] using a Jahn-Teller model hamiltonian with linear coupling elements, which exhibits a 'Mexican-hat'-like structure of the adiabatic potentials. This was seen already in section 5.2.2.2. A similar propagation around a CoIn can also be realized here using the 2D model system which also exhibits a 'Mexican-hat'-like energetical topology of the potential energy surfaces and a small decline from positive to negative R_y values. But additionally, in this model system the total wave function is propagated, and as far as the reduction of the system to the diabatic picture resembles the linear Jahn-Teller hamiltonian, these two dynam-

ical approaches can be compared to each other. Most important, the electronic wave-packet dynamics can be studied. This is of great advantage, because phase sensitive processes like the gathering of a geometric phase by a wave function surrounding a CoIn are maybe observable in the full dimensional dynamics.

5.3.2.1 Full-Dimensional Dynamical Approach in Comparison to the Adiabatic and Diabatic Dynamical Approaches

First, the electron-nuclear coupled propagation is regarded. The initial wave function is defined as in eq. (5.24), but with $|\phi_1(x, y; R_x, R_y)\rangle$ as initial electronic state.

The center of the inital wave function is marked by an arrow in fig. 5-27. It starts at a saddle point and, upon bifurcating into two parts, evolves along the valley around the CoIn, see fig. 5-29, left panels. Within 10 fs, the surrounding is complete and the electronic character has changed from p_x-like to p_y-like [26]. The dynamics proceeds adiabatic as can be taken from fig. 5-28 and fig. 5-28.

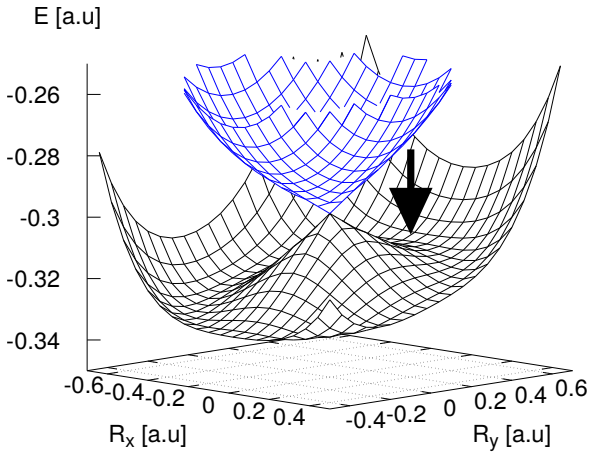

Figure 5-27: **Initial Condition for a Wave Packet to Surround the CoIn.** Shown are the adiabatic potentials $u_{11}\,(R_x, R_y)$ and $u_{22}\,(R_x, R_y)$. The black arrow marks the position of the nuclear wave packet in the adiabatic representation.

It should be noted that before the surrounding is complete, the nuclear density of the full-dimensional approach and the reduced adiabatic approach within the Born-Oppenheimer approximation (obtained from eq. (2.45)) are identical. This changes as the left and the right branch of the density join at negative values of the R_y-axis. The full-dimensional approach exhibits a destructive interference, whereas the Born-Oppenheimer treatment shows a constructive interference. This is due to the geometric phase connected to the surrounding of the CoIn [26].

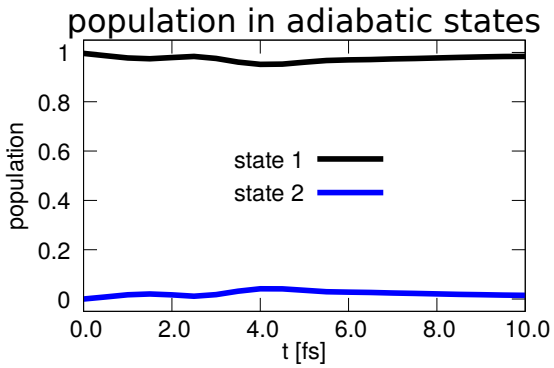

Figure 5-28: **Population Dynamics for a Wave Packet Surrounding the CoIn.** The population stays almost constant in the lower adiabatic state.

As a result, in the exact propagation, the phase difference between the left and right branch has at the point of joining the value of π, which leads to a destructive interference.

On the contrary, in the Born-Oppenheimer treatment the phase connected to both branches is the same resulting in a constructive interference. The destructive interference in the exact propagation can also by explained using symmetry reasons. The initial wave function has a nodal structure along the R_x-axis as the Gaussian nuclear wave packet is symmetric and the electronic eigenfunction is antisymmetric in this direction. Now at 10 fs, the nuclear wave packet has moved to the opposite side of the coordinate system as well as the CoIn. There, the electronic wave function is symmetric in R_x-direction and as a consequence of symmetry conservation, the nuclear wave packet has to be antisymmetric in the point where both branches join [26].

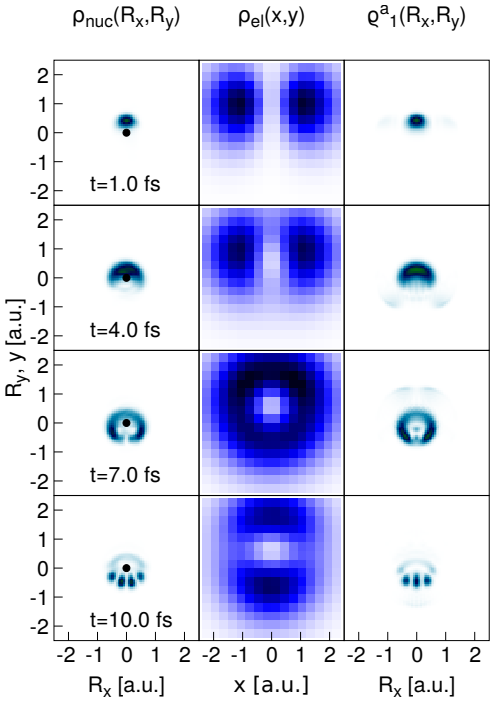

Figure 5-29: **Comparison of Numerically Exact Propagation and Born-Oppenheimer Treatment.** The left panels show the nuclear density and the middle panels show the corresponding electron density obtained from the exact calculation. The right panels show the nuclear density within the Born-Oppenheimer treatment. It is seen that the outcome of the Born-Oppenheimer treatment is different in phase.

Additionally, one can reproduce the dynamics in the diabatic framework. The result can be seen in fig. 5-30, where the geometric phase effect is present because the potential coupling elements are incorporated. The outcome is also in good agreement with the full coupled propagation. These results imply that the conditions for the diabatization must be well fulfilled.

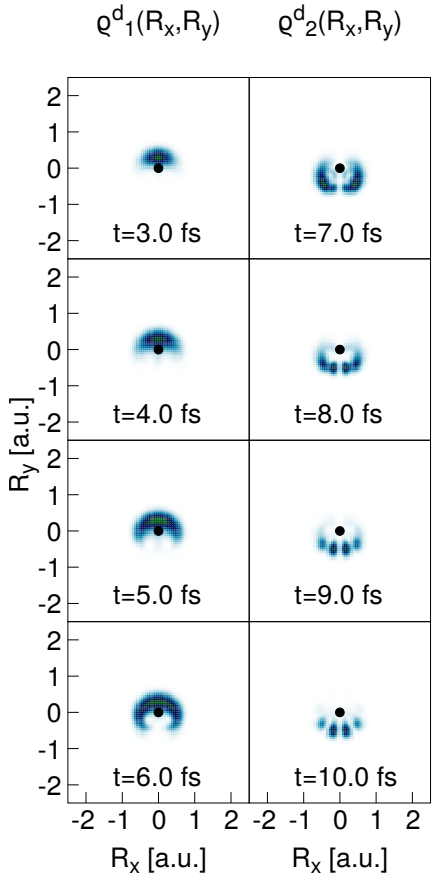

Figure 5-30: **Nuclear Density Dynamics within the Diabatic Representation.** The diabatic nuclear density resembles the numerically exact nuclear density dynamics in fig. 5-29 and reproduces the correct phase of the wave function.

5.3.3 Circuitting of a CoIn by a Nuclear Wave Packet

As a last case the circuitting of a nuclear wave packet around a CoIn is regarded. This is an adiabatic motion, but it is regarded here to study the geometric phase effect with the help of an autocorrelation function.

5.3.3.1 Full-Dimensional Dynamical Approach

In this case the initial wave function is similar to the previous section and given with an additional momentum:

$$|\Psi(x,y,R_x,R_y,t=0)\rangle = N\cdot e^{-\beta(R_x-R_{x0})^2}e^{-\beta(R_y-R_{y0})^2}e^{-iP_{R_x}R_x}\cdot|\phi_1(x,y;R_x,R_y)\rangle. \tag{5.35}$$

The initial momentum is set to $P_{R_x} = 14.84$ a.u., where $R_{x_0} = 0.0$ a.u. and $R_{y_0} = 0.6$ a.u.. The resulting dynamics is depicted in fig. 5-31.

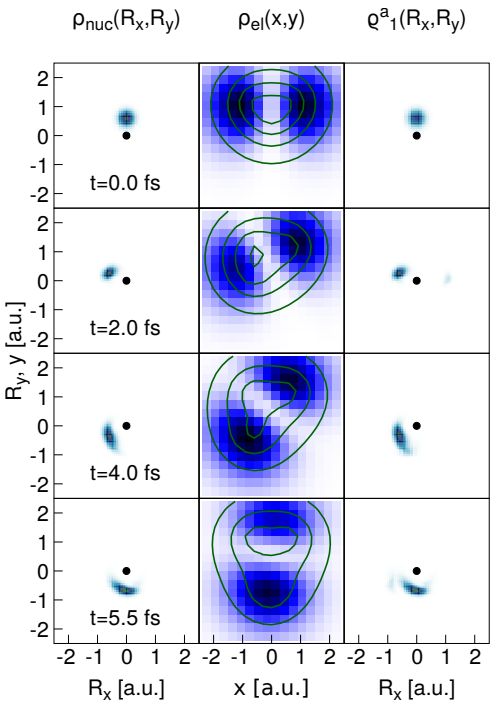

Figure 5-31: **Nuclear Wave Packet Circuitting the CoIn.** The left panels show the nuclear density from the numerically exact propagation. The middle panels show the corresponding electron density. The contour lines represent $V(x,y,R_{x,t},R_{y,t})$. The outer line starts with a value of -0.5 a.u. and decreases in steps of 0.5 a.u.. The right panels show the nuclear density in the Born-Oppenheimer treatment. They are in excellent agreement with the exact treatment.

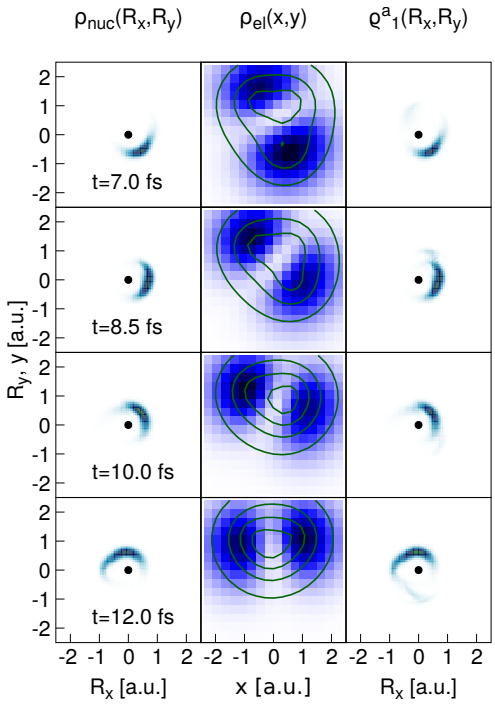

Figure 5-32: **Nuclear Wave Packet Circuitting the CoIn.** Same as fig. 5-31, but for longer times.

Starting with the nuclear density of the exact propagation, the initial momentum pushes the nuclear wave packet into a circular counterclockwise motion around the CoIn. The population dynamics in the adiabatic representation (not shown) exhibits no significant state transition which proves this motion to be adiabatic. Following the nuclear density up to 5.5 fs, the nuclear wave packet makes a half cycle around the CoIn. Regarding the corresponding electron density, this results in a rotation of the electronic wave function from p_x- to p_y-like shape. The circular motion is complete at about 12 fs (fig. 5-32). Then, the corresponding electron density is again p_x-like. But the electronic wave function is now inverted and the associated phase can be connected to the geometric phase [26].

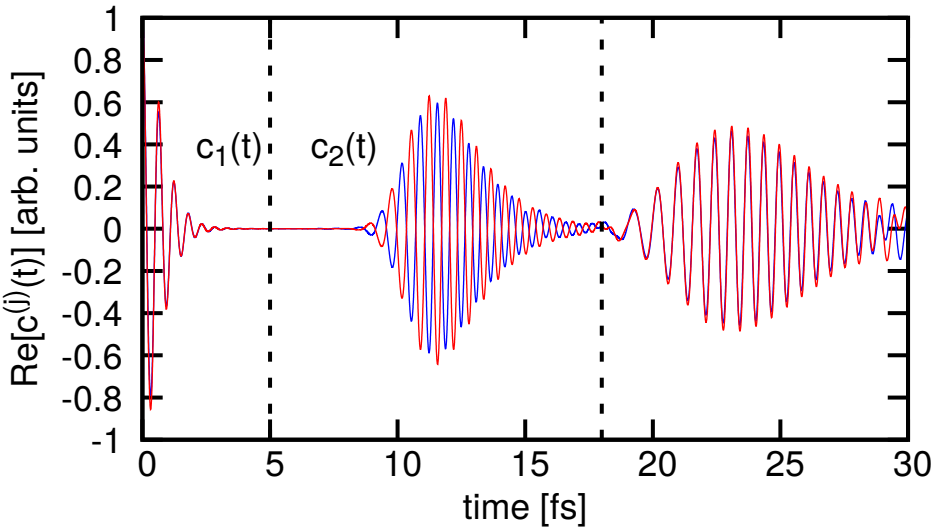

Figure 5-33: **Autocorrelation Functions.** Shown are the autocorrelation functions from the numerically exact treatment (blue) and the Born-Oppenheimer treatment (red). In the beginning, the autocorrelation functions are identical but differ after 9 fs by π in phase. The time interval corresponds to a full cycle of the CoIn by the wave packet. After a second cycle around 17 fs, the functions are in phase again.

This phase can not be seen in the nuclear densities which appear nearly identical in the exact propagation and the Born-Oppenheimer treatment. But it can be visualized using autocorrelation functions obtained from the exactly propagated wave function and the Born-Oppenheimer approximation. They are defined as

$$c^{(ex)}(t) = \langle \Psi(x, y, R_x, R_y, t = 0) \,|\, \Psi(x, y, R_x, R_y, t) \rangle \tag{5.36}$$

and

$$c^{(ad)}(t) = \langle \chi_1(R_x, R_y, t = 0) \,|\, \chi_1(R_x, R_y, t) \rangle, \tag{5.37}$$

where we use the same initial nuclear wave packet for the propagation. The real

parts of the autocorrelation functions are plotted in fig. 5-33. There, both functions are oscillating in phase at the beginning of the simulation. At the time when the wave packet is located on the opposite side of the CoIn, the autocorrelation function vanishes. After a full circle and a recurrence time of 12 fs, the autocorrelation functions are found to be out of phase by π. Following the temporal behavior up to 24 fs, which is twice the recurrence time, the functions are in phase again [26].

From the autocorrelation functions $c^{(j)}(t)$ $(j = ex, ad)$, spectra can be obtained according to [119, 143, 144]:

$$\sigma^{(j)}(E) = \int dt\ e^{iEt} c^{(j)}(t). \tag{5.38}$$

It is sufficient to investigate the autocorrelation functions until 19 fs. They can be decomposed in two parts $(n = 1, 2)$ which is approximately written as [26, 119]:

$$c_n^{(j)}(t) = a_n \left(e^{-\alpha_n (t-T_n)^2} + e^{-\alpha_n (t+T_n)^2} \right) e^{-i\beta_n t}, \tag{5.39}$$

where a_n, α_n, β_n are parameters, $T_1 = 0$ and $T_2 \sim 12$ fs. Figure 5-33 shows that $c_1^{(ex)} = c_1^{(ad)}$ and $c_2^{(ex)} = -c_2^{(ad)}$. This results in a spectrum which can be approximately written as:

$$\sigma^{(ex)}(E) = \sigma_1(E) + \sigma_2(E), \tag{5.40}$$

$$\sigma^{(ad)}(E) = \sigma_1(E) + \sigma_2(E), \tag{5.41}$$

with

$$\sigma_n(E) = a_n e^{-(E-\beta_n)^2/(4\alpha_n)} \cos\left[(E-\beta_n)T_n\right]. \tag{5.42}$$

In the expression for $\sigma_n(E)$, the Gaussian envelop is modulated by an oscillating term which corresponds to the findings form the numerically obtained spectra [26].

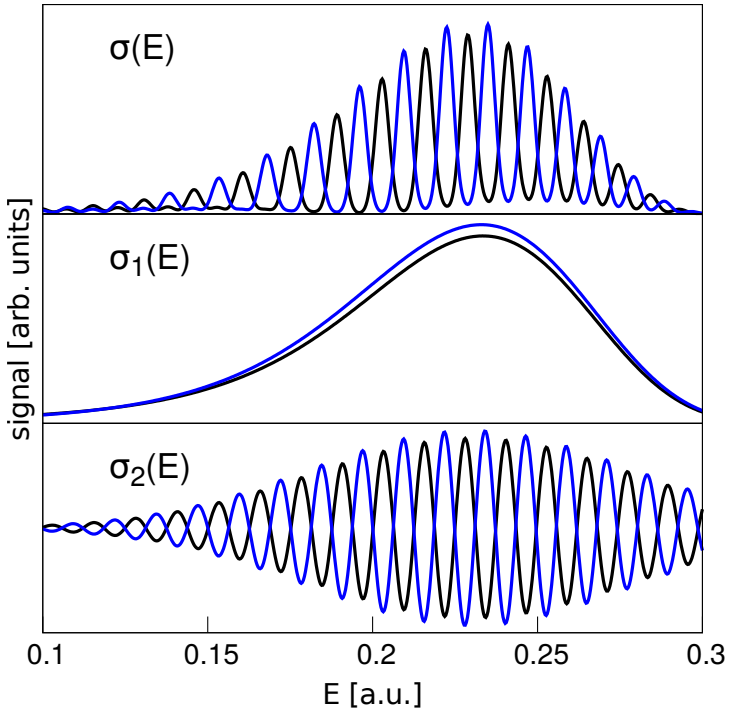

Figure 5-34: **Spectra Derived from Autocorrelation Functions.** In the upper panel the spectra of the numerically exact treatment (black) and the Born-Oppenheimer treatment (blue) are compared. The middle panel shows (same color code) the background spectrum, and the lower panel shows the oscillating part of the spectrum.

The spectrum is composed of two parts. $\sigma_1(E)$ is a Gaussian background and is identical for both spectra. The other part $\sigma_2(E)$ is an oscillating function with a Gaussian envelope. According to eq. (5.40) and eq. (5.41), the oscillating part is added or substracted, which results in a spectra where the positions of the maxima of exact treatment lie between the positions of the maxima of the

Born-Oppenheimer treatment. This can be seen in fig. 5-34, where the numerically obtained spectra are reproduced by addition of the background terms and oscillating terms [26].

Chapter 6

Summary

In the context of quantum mechanical calculations, the properties of non-adiabatic coupling in a small system, the Shin-Metiu model, is investigated. The transition from adiabatic to non-adiabatic dynamics is elucidated in modifying the electron-nuclear interaction. This allows the comparison of weakly correlated electron-nuclear motion with the case where the strong correlations determine the dynamics. There, the eigenfunctions are analyzed and the impact of non-adiabatic coupling is characterized. It is shown that in the weak coupling regime, the eigenfunctions are well represented within the adiabatic product ansatz, where the adiabatic electronic eigenfunctions are decoupled from each other and separated in their electronic character. On the contrary, in the strong coupling regime, the adiabatic electronic eigenfunctions and corresponding vibrational eigenfunctions are strongly coupled, and a diabatic basis set turns out to be an equivalent but a more intuitive representation in the description of eigenfunctions.

With these findings, a diabatization is carried out, and the nuclear dynamics obtained from a numerically exact quantum dynamical wave-packet propagation is compared to the corresponding propagation in the diabatic representation. The dynamics are in very good agreement and show that the diabatization ansatz is suitable for uncorrelated electron-nuclear motion and classifies the wave-packet dynamics in the strong coupling regime as a diabtic motion.

The studies of the one-dimensional model are extended to include spectroscopical transitions being present in two-dimensional and degenerate four-wave mixing (FWM) spectroscopy. Linear spectroscopy is used as a precursor for the non-linear spectroscopic methods. Here, the findings are in agreement with previous studies. Two-dimensional spectra probing the coupled electron-nuclear motion are calculated. A comparison of the weak and the strong coupling regime reveals that, in the weak coupling case, the spectra are reproducable in the Born-Oppenheimer treatment. The conclusion states that parts of the spectrum which can not be reproduced within the Born-Oppenheimer treatment result from mixed states due to strong non-adiabatic coupling.

Being able to tune the model between the weak and strong coupling regime, the question of the signatures of vibrational and electronic coherences in two-dimensional spectra could be addressed. Therefore, the spectra are analyzed as a function of the population time. In the case of the weak coupling, this study reveals that the occuring coherences are of vibrational character. On the contrary, it is shown that due to the mixed state character in the strong coupling regime case, the coherences are of vibronic character so that it is not possible to distinguish between a pure vibrational or electronic character.

As another method, degenerate four-wave mixing is applied, which is able to monitor the ground state and excited state dynamics by changing the pulse sequence. Here, both for negative and positive delay times, the two coupling cases are addressed and it is studied when the separation between ground and excited-state dynamics breaks down within the adiabatic representation.

Furthermore, the quantum and classical time-evolution of the coupled motion in the complete electron-nuclear phase space is compared for the two coupling cases. In the weakly coupled case, it is shown that the short-time behavior of the classical calculation is in good agreement with quantum dynamics. This also applies in the strongly coupled situation. It is shown that the dynamics in the strong coupling regime takes place mostly in a single diabatic state, as can be expected

from the investigation of the diabatization ansatz. This states that the classical trajectory motion is very similar to the diabatic quantum motion. As a result, a classical treatment in the complete phase space of electron and nuclear degrees of freedom reproduces the quantum dynamics, where strong non-adiabatic coupling is present.

Finally, the numerically exact electron flux within the weak coupling case is compared to the Born-Oppenheimer treatment. Within the usual definition the electron flux vanishes in the Born-Oppenheimer approximation. The approach of calculating the electron flux directly from the continuity equation results in a non-zero flux and a flux-flux reflection-principle which maps the electron flux onto the nuclear flux and vice versa.

In the last part of the thesis, the one-dimensional model is extended to two dimensions. The system then possesses potential energy surfaces which exhibit a typical 'Mexican hat'-like structure and a CoIn in the adiabatic representation. Thus, it is possible to map properties of the system onto a vibronic coupling (Jahn-Teller) hamiltonian.

Exact wave-packet propagations as well as nuclear wave-packet dynamics in the adiabatic and diabatic representation are performed. It is shown that the crossing of a wave packet through a CoIn carries the characteristics of a diabatic motion and is a highly efficient process. The nuclear dynamics is well reproduced in the diabatic representation. Furthermore, the motion around the CoIn can be characterized as an adiabatic motion with changing electronic character.

Here, a geometric phase appears, which is traced back to the rotational motion of the electronic wave function. The influence of the geometric phase on time-correlation functions as well as the corresponding spectra derived from them, is analyzed. Furthermore, the geometric phase is explicitly calculated as a mixing angle for the transformation between the diabatic representation and the adiabatic representation.

To summarize, the here presented model calculations, although they are restricted

to only two particles, reveal many fundamental aspects of correlated electron-nuclear dynamics.

Chapter 7

Zusammenfassung

Im Rahmen quantenmechanischer Rechnungen werden die Eigenschaften nicht-adiabatischer Kopplungen in einem kleinen Modellsystem, dem Shin-Metiu Modell, untersucht. Die Fallunterscheidung zwischen adiabatischen und nicht-adiabatischen Prozessen wird durch eine Parameterisierung der Elektronen-Kernwechselwirkung realisiert. Dies ermöglicht den Vergleich zwischen korrelierter und unkorrelierter Elektronen-Kernbewegung. Innerhalb dieser zwei Extrema werden die Eigenfunktionen betrachtet und der Einfluss nicht-adiabtischer Kopplungen auf diese analysiert. Es wird gezeigt, dass im Fall einer schwachen Kopplung die Eigenfunktionen als adiabatisches Produkt dargestellt werden können, soweit die adiabatischen elektronischen Eigenfunktionen voneinander entkoppelt sind und unterschiedlichen elektronischen Charakter besitzen. Auf der anderen Seite sind die adiabatischen elektronischen Eigenfunktionen und die Vibrationseigenfunktionen im Bereich einer starken Kopplung miteinander gekoppelt, und es zeigt sich, dass die Eigenfunktionen in der diabatischen Darstellung eine zur adiabatischen äquivalente, aber intuitivere Beschreibung darstellen.

Anhand dieser Ergebnisse wird eine Diabatisierung und ein Vergleich zwischen exakter Elektronen-Kernpropagation und der Propagation im diabatischen Bild durchgeführt. Dieser Vergleich ist in sehr guter Übereinstimmung und zeigt, dass der Ansatz der Diabatisierung für unkorrelierte Elektronen-Kernbewegungen hin-

reichend ist und gleichzeitig klassifiziert er die Wellepacketdynamik im Bereich starker Kopplungen als diabatisch.

Die theoretischen Untersuchungen des eindimensionalen Modells werden auf spektroskopische Übergänge erweitert, welche lineare und nichtlineare System-Feld Wechselwirkungen beinhalten. Ein Vergleich zwischen zweidimensionalen Spektren bezüglich schwach und stark gekoppelter Elektronen-Kern Dynamik zeigt, dass im Fall schwacher Kopplungen, die Spektren durch analoge Rechnungen im Rahmen der Born-Oppenheimer Näherung reproduzierbar sind.

Es zeigt sich, dass diejenigen Teile des Spektrums, welche auf gleiche Weise nicht reproduzierbar sind, elektronisch gemischten Zuständen, aufgrund starker nichtadiabtischer Kopplungen, zuzuordnen sind. Die Möglichkeit, das System zwischen schwacher und starker Kopplung zu variieren, erlaubt es Vibrationskohärenzen und elektronischen Kohärenzen in zweidimensionalen Spektren zu analysieren. Dazu werden die zweidimensionalen Spektren als Funktion der Populationszeit betrachtet. Es ergibt sich, dass im Fall schwacher Kopplungen die Kohärenzen während der Populationszeit Vibrationskohärenzen zugeordnet werden können. Im Gegensatz dazu ergeben sich im Bereich starker Kopplungen, aufgrund des gemischten elektronischen Charakters der Zustände, Kohärenzen vibronischer Art.

Als weitere Methode wird die Degenerierte-Vier-Wellen-Mischen Spektroskopie (FWM) untersucht. Diese ist in der Lage Grundzustandsdynamiken und Dynamiken im angeregten Zustand separat zu verfolgen. Sowohl für negative als auch für positive Verzögerungszeiten werden die zwei verschiedenen Kopplungsszenarien untersucht und der Zusammenbruch dieser Methode bezüglich der nicht möglichen Trennung der Grundzustandsdynamik und Dynamik im angeregten Zustand innerhalb der adiabatischen Beschreibung betrachtet.

Als weiterer Aspekt, wird die quantenmechanische und klassische Zeitentwicklung der gekoppelten Elektronen-Kernbewegung im vollständigen Phasenraum für verschiedene Kopplungsstärken verglichen. Im Fall schwacher Kopplung stimmt im Kurzzeitverhalten die klassische Berechung mit der quantenmechanischen gut

überein. Dies kann auch im Fall starker Kopplungen gezeigt werden, was die weitere Schlussfolgerung zulässt, dass die Dynamik im Bereich starker Kopplungen hauptsächlich in einem diabatischen Zustand stattfindet. Das zeigt, dass die klassische Bewegung sehr ähnlich zu der diabatischen quantenmechanischen Bewegung verläuft. Als Konsequenz reproduziert eine klassische Bewegung im vollständigen Phasenraum eine quantenmechanische, bei der nicht-adiabatische Kopplungen stark involviert sind.

Als letzte Betrachtung des eindimensionalen Shin-Metiu Modells, wird der Elektronenfluss im schwach gekoppelten Fall untersucht und der numerisch exakt berechnete Fluss mit dem in der Born-Oppenheimer Näherung verglichen. Innerhalb der üblichen Definition verschwindet der Elektronenfluss im Rahmen der Born-Oppenheimer Näherung. Durch die Verwendung der Kontinuitätsgleichung für den Elektronenfluss ergibt sich jedoch ein nicht-verschwindender Elektronenfluss. Weiter wurde ein Reflektionsprinzip hergeleitet, welches den Elektronenfluss auf den Kernfluss abbildet und umgekehrt.

Zum Abschluss der Untersuchungen des eindimensionalen Shin-Metiu Modells wird das System auf zwei Dimensionen erweitert. Dabei zeigt sich, dass die adiabatischen Potentialflächen des Modells eine typische 'Mexican-hat' Topologie aufweist. Daraus ergibt sich, dass es möglich ist das System auf einen vibronischen (Jahn-Teller) Hamiltonian zurückzuführen. Im Zuge dessen wird das zweidimensionale System hinsichtlich der exakten Elektronen-Kerndynamik, sowie der Dynamik in den adiabatischen und diabatischen Anschauungen betrachtet. Die durchgeführten Rechnungen zeigen, dass das Passieren eines Wellenpaketes durch eine Konische Durchschneidung als eine diabatische Dynamik klassifiziert werden kann, wobei ein effizienter adiabatischer Populationstransfer stattfindet. Dieser Prozess kann sehr gut im diabatischen Bild reproduziert werden. Des Weiteren wird eine Wellenpaketdynamik um eine Konische Durchschneidung herum betrachtet und als adiabatische Dynamik klassifiziert. Der interessante Aspekt der geometrischen Phase, die mit dem Umrunden einer Konischen Durchschneidung assoziiert ist,

wird mit der Rotation der elektronischen Wellenfunktion verknüpft. Zusätzlich wird hier das Auftreten der geometrische Phase in Autokorrelationsfunktionen und den daraus abgeleiteten Spektren charakterisiert. Die geometrische Phase wird zusätzlich als Mischungswinkel der Transformation zwischen dem diabatischen und adiabatischen Bild explizit berechnet. Zusammenfassend zeigen die Rechnugen an den verwendeten Modellsystemen viele fundamentale Aspekte der korrelierten Elektronen-Kerndynamik, obwohl sie auf lediglich zwei Partikel begrenzt sind.

Appendix A

In what follows eq. (2.30) is derived from eq. (2.29) according to [39].

$$
\begin{aligned}
&\underbrace{-\frac{1}{2M}\sum_{k,n} A_{ok}(\vec{R};\underline{\vec{R}})\Big[\vec{\nabla}_{\vec{R}}\delta_{kn}+\vec{\tau}_{kn}(\vec{R})\Big]^2\sum_m (A^{-1})_{nm}(\vec{R};\underline{\vec{R}})A_{mn}(\vec{R};\underline{\vec{R}})|\chi_n(\vec{R})\rangle}_{C(\vec{R};\underline{\vec{R}})}\\
&+\sum_{k,n} A_{ok}(\vec{R};\underline{\vec{R}})\Big(u_{kn}(\vec{R})\delta_{kn}-E\Big)\sum_m (A^{-1})_{nm}(\vec{R};\underline{\vec{R}})A_{mn}(\vec{R};\underline{\vec{R}})|\chi_n(\vec{R})\rangle=0.
\end{aligned}
\tag{A.1}
$$

First, $C(\vec{R};\underline{\vec{R}})$ is defined as part of the above expression which is rewritten in the following separately:

$$
\begin{aligned}
&C(\vec{R};\underline{\vec{R}})\\
&=\sum_{k,n,s} A_{ok}(\vec{R};\underline{\vec{R}})\Big[\vec{\nabla}_{\vec{R}}\delta_{ks}+\vec{\tau}_{ks}(\vec{R})\Big]\Big[\vec{\nabla}_{\vec{R}}\delta_{sn}+\vec{\tau}_{sn}(\vec{R})\Big]\sum_m (A^{-1})_{nm}(\vec{R};\underline{\vec{R}})|\tilde{\chi}_m(\vec{R};\underline{\vec{R}})\rangle\\
&=\sum_{k,n,s} A_{ok}(\vec{R};\underline{\vec{R}})\Big[\vec{\nabla}_{\vec{R}}\vec{\nabla}_{\vec{R}}\delta_{ks}\delta_{sn}+\vec{\nabla}_{\vec{R}}\delta_{ks}\vec{\tau}_{sn}(\vec{R})+\vec{\tau}_{ks}(\vec{R})\vec{\nabla}_{\vec{R}}\delta_{sn}+\vec{\tau}_{ks}(\vec{R})\vec{\tau}_{sn}(\vec{R})\Big]\times\\
&\sum_m (A^{-1})_{nm}(\vec{R};\underline{\vec{R}})|\tilde{\chi}_m(\vec{R};\underline{\vec{R}})\rangle.
\end{aligned}
\tag{A.2}
$$

Then one ends up with four terms within the square brackets. To these four terms, different colors are attatched in the following:

$$
\begin{aligned}
& C(\vec{R};\underline{\vec{R}}) \\
= & \sum_{k,n,m,s} A_{ok}(\vec{R};\underline{\vec{R}})\vec{\nabla}_{\vec{R}}\left(\vec{\nabla}_{\vec{R}}\delta_{ks}\delta_{sn}(A^{-1})_{nm}(\vec{R};\underline{\vec{R}})|\tilde{\chi}_m(\vec{R};\underline{\vec{R}})\rangle\right) \\
& + A_{ok}(\vec{R};\underline{\vec{R}})\vec{\nabla}_{\vec{R}}\delta_{ks}\left(\vec{\tau}_{sn}(\vec{R})(A^{-1})_{nm}(\vec{R};\underline{\vec{R}})|\tilde{\chi}_m(\vec{R};\underline{\vec{R}})\rangle\right) \\
& + A_{ok}(\vec{R};\underline{\vec{R}})\vec{\tau}_{ks}(\vec{R})\left(\vec{\nabla}_{\vec{R}}\delta_{sn}(A^{-1})_{nm}(\vec{R};\underline{\vec{R}})|\tilde{\chi}_m(\vec{R};\underline{\vec{R}})\rangle\right) \\
& + A_{ok}(\vec{R};\underline{\vec{R}})\vec{\tau}_{ks}(\vec{R})\vec{\tau}_{sn}(\vec{R})(A^{-1})_{nm}(\vec{R};\underline{\vec{R}})|\tilde{\chi}_m(\vec{R};\underline{\vec{R}})\rangle. \qquad \text{(A.3)}
\end{aligned}
$$

Furthermore, the orange term can be further expanded, so there are in total ten terms:

$$
\begin{aligned}
& C(\vec{R};\underline{\vec{R}}) \\
= & \sum_{k,n,m,s} A_{ok}(\vec{R};\underline{\vec{R}})\left(\vec{\nabla}_{\vec{R}}\vec{\nabla}_{\vec{R}}(A^{-1})_{km}(\vec{R};\underline{\vec{R}})\right)|\tilde{\chi}_m(\vec{R};\underline{\vec{R}})\rangle \\
& + A_{ok}(\vec{R};\underline{\vec{R}})\left(\vec{\nabla}_{\vec{R}}(A^{-1})_{km}(\vec{R};\underline{\vec{R}})\right)\left(\vec{\nabla}_{\vec{R}}|\tilde{\chi}_m(\vec{R};\underline{\vec{R}})\rangle\right) \\
& + A_{ok}(\vec{R};\underline{\vec{R}})\left(\vec{\nabla}_{\vec{R}}(A^{-1})_{km}(\vec{R};\underline{\vec{R}})\right)\left(\vec{\nabla}_{\vec{R}}|\tilde{\chi}_m(\vec{R};\underline{\vec{R}})\rangle\right) \\
& + A_{ok}(\vec{R};\underline{\vec{R}})(A^{-1})_{km}(\vec{R};\underline{\vec{R}})\left(\vec{\nabla}_{\vec{R}}\vec{\nabla}_{\vec{R}}|\tilde{\chi}_m(\vec{R};\underline{\vec{R}})\rangle\right) \\
& + A_{ok}(\vec{R};\underline{\vec{R}})\left(\vec{\nabla}_{\vec{R}}\vec{\tau}_{kn}(\vec{R})\right)(A^{-1})_{nm}(\vec{R};\underline{\vec{R}})|\tilde{\chi}_m(\vec{R};\underline{\vec{R}})\rangle \\
& + A_{ok}(\vec{R};\underline{\vec{R}})\vec{\tau}_{sn}(\vec{R})\left(\vec{\nabla}_{\vec{R}}\delta_{ks}(A^{-1})_{nm}(\vec{R};\underline{\vec{R}})\right)|\tilde{\chi}_m(\vec{R};\underline{\vec{R}})\rangle \\
& + A_{ok}(\vec{R};\underline{\vec{R}})\vec{\tau}_{sn}(\vec{R})(A^{-1})_{nm}(\vec{R};\underline{\vec{R}})\left(\vec{\nabla}_{\vec{R}}\delta_{ks}|\tilde{\chi}_m(\vec{R};\underline{\vec{R}})\rangle\right) \\
& + A_{ok}(\vec{R};\underline{\vec{R}})\vec{\tau}_{ks}(\vec{R})\left(\vec{\nabla}_{\vec{R}}\delta_{sn}(A^{-1})_{nm}(\vec{R};\underline{\vec{R}})\right)|\tilde{\chi}_m(\vec{R};\underline{\vec{R}})\rangle \\
& + A_{ok}(\vec{R};\underline{\vec{R}})\vec{\tau}_{ks}(\vec{R})(A^{-1})_{nm}(\vec{R};\underline{\vec{R}})\left(\vec{\nabla}_{\vec{R}}\delta_{sn}|\tilde{\chi}_m(\vec{R};\underline{\vec{R}})\rangle\right) \\
& + A_{ok}(\vec{R};\underline{\vec{R}})\vec{\tau}_{ks}(\vec{R})\vec{\tau}_{sn}(\vec{R})(A^{-1})_{nm}(\vec{R};\underline{\vec{R}})|\tilde{\chi}_m(\vec{R};\underline{\vec{R}})\rangle. \qquad \text{(A.4)}
\end{aligned}
$$

Equation (A.4) can be rewritten as:

$$
\begin{aligned}
&C(\vec{R};\underline{\vec{R}}) \\
&= \sum_{k,n,m,s} A_{ok}(\vec{R};\underline{\vec{R}})(A^{-1})_{km}(\vec{R};\underline{\vec{R}}) \left(\vec{\nabla}_{\vec{R}}\vec{\nabla}_{\vec{R}}|\tilde{\chi}_m(\vec{R})\rangle\right) \\
&+ \Big[2A_{ok}(\vec{R};\underline{\vec{R}}) \left(\vec{\nabla}_{\vec{R}}(A^{-1})_{km}(\vec{R};\underline{\vec{R}})\right) + A_{ok}(\vec{R};\underline{\vec{R}})\vec{\tau}_{kn}(\vec{R})(A^{-1})_{nm}(\vec{R};\underline{\vec{R}}) \\
&+A_{ok}(\vec{R};\underline{\vec{R}})\vec{\tau}_{kn}(\vec{R})(A^{-1})_{nm}(\vec{R};\underline{\vec{R}})\Big] \left(\vec{\nabla}_{\vec{R}}|\tilde{\chi}_m(\vec{R};\underline{\vec{R}})\rangle\right) \\
&+ \Big[A_{ok}(\vec{R};\underline{\vec{R}}) \left(\vec{\nabla}_{\vec{R}}\vec{\nabla}_{\vec{R}}(A^{-1})_{km}(\vec{R};\underline{\vec{R}})\right) \\
&+ A_{ok}(\vec{R};\underline{\vec{R}}) \left(\vec{\nabla}_{\vec{R}}\vec{\tau}_{kn}(\vec{R})\right)(A^{-1})_{nm}(\vec{R};\underline{\vec{R}}) \\
&+ A_{ok}(\vec{R};\underline{\vec{R}})\vec{\tau}_{kn}(\vec{R}) \left(\vec{\nabla}_{\vec{R}}(A^{-1})_{nm}(\vec{R};\underline{\vec{R}})\right) \\
&+ A_{ok}(\vec{R};\underline{\vec{R}})\vec{\tau}_{kn}(\vec{R}) \left(\vec{\nabla}_{\vec{R}}(A^{-1})_{nm}(\vec{R};\underline{\vec{R}})\right) \\
&+A_{ok}(\vec{R};\underline{\vec{R}})\vec{\tau}_{ks}(\vec{R})\vec{\tau}_{sn}(\vec{R})(A^{-1})_{nm}(\vec{R};\underline{\vec{R}})\Big] |\tilde{\chi}_m(\vec{R};\underline{\vec{R}})\rangle. \qquad \text{(A.5)}
\end{aligned}
$$

This can be summarized to:

$$
\begin{aligned}
&C(\vec{R};\underline{\vec{R}}) \\
&= \sum_{k,n,m,s} A_{ok}(\vec{R};\underline{\vec{R}})(A^{-1})_{km}(\vec{R};\underline{\vec{R}}) \left(\vec{\nabla}_{\vec{R}}\vec{\nabla}_{\vec{R}}|\tilde{\chi}_m(\vec{R})\rangle\right) \\
&+ \Big[2A_{ok}(\vec{R};\underline{\vec{R}}) \left(\vec{\nabla}_{\vec{R}}(A^{-1})_{km}(\vec{R};\underline{\vec{R}})\right) + A_{ok}(\vec{R};\underline{\vec{R}})\vec{\tau}_{kn}(\vec{R})(A^{-1})_{nm}(\vec{R};\underline{\vec{R}}) \\
&+A_{ok}(\vec{R};\underline{\vec{R}})\vec{\tau}_{kn}(\vec{R})(A^{-1})_{nm}(\vec{R};\underline{\vec{R}})\Big] \left(\vec{\nabla}_{\vec{R}}|\tilde{\chi}_m(\vec{R};\underline{\vec{R}})\rangle\right) \\
&+ A_{ok}(\vec{R};\underline{\vec{R}})\times \\
&\Big[\left(\vec{\nabla}_{\vec{R}}\delta_{ks} + \vec{\tau}_{ks}\right) \left(\vec{\nabla}_{\vec{R}}\delta_{sn}(A^{-1})_{nm}(\vec{R};\underline{\vec{R}}) + \vec{\tau}_{sn}(\vec{R})(A^{-1})_{nm}(\vec{R};\underline{\vec{R}})\right)\Big] \times \\
&|\tilde{\chi}_m(\vec{R};\underline{\vec{R}})\rangle. \qquad \text{(A.6)}
\end{aligned}
$$

Combining the above expression with eq. (A.1) yields eq. (A.7) which corresponds to eq. (2.30).

$$
\begin{aligned}
&-\frac{1}{2M}\vec{\nabla}^2_{\vec{R}}|\tilde{\chi}_o(\vec{R};\underline{\vec{R}})\rangle+\\
&2\sum_{k,m,n}\left[A_{ok}(\vec{R};\underline{\vec{R}})\underbrace{\left(\vec{\nabla}_{\vec{R}}\delta_{kn}(A^{-1})_{nm}(\vec{R};\underline{\vec{R}})+\vec{\tau}_{kn}(A^{-1})_{nm}(\vec{R};\underline{\vec{R}})\right)}_{=0}\right]\vec{\nabla}_{\vec{R}}|\tilde{\chi}_m(\vec{R};\underline{\vec{R}})\rangle\\
&+\sum_{k,m,n,s}A_{ok}(\vec{R};\underline{\vec{R}})\times\\
&\left[\left(\vec{\nabla}_{\vec{R}}\delta_{ks}+\vec{\tau}_{ks}(\vec{R})\right)\underbrace{\left(\vec{\nabla}_{\vec{R}}\delta_{sn}(A^{-1})_{nm}(\vec{R};\underline{\vec{R}})+\vec{\tau}_{sn}(A^{-1})_{nm}(\vec{R};\underline{\vec{R}})\right)}_{=0}\right]\times\\
&|\tilde{\chi}_m(\vec{R};\underline{\vec{R}})\rangle+\sum_m\left(\tilde{u}_{om}(\vec{R};\underline{\vec{R}})-E\right)|\tilde{\chi}_m(\vec{R};\underline{\vec{R}})\rangle=0. \qquad \text{(A.7)}
\end{aligned}
$$

Bibliography

[1] C. Brüning and V. Engel. *On the time-dependent calculation of angular averaged vibronic absorption spectra with an application to molecular aggregates. Chem. Phys.*, 482:64–68, 2016.

[2] A. Schubert, V. Settels, L. Wanlan, F. Würthner, C. Meier, R. F. Fink, S. Schindlbeck, S. Lochbrunner, and V. Engels, B. Engel. *Ultrafast Exciton Self-Trapping upon Geometry Deformation in Perylene-Based Molecular Aggregates. J. Phys. Chem. Lett.*, 4:792–796, 2013.

[3] M. Son, B. Fimmel, V. Dehm, F. Würthner, and D. Kim. *Folding-Induced Modulation of Excited-State Dynamics in an Oligophenylene-Ethynylene-Tethered Spiral Perylene Bisimide Aggregate. ChemPhysChem*, 16:1757–1767, 2015.

[4] J. Sung, P. Kim, B. Fimmel, F. Würthner, and D. Kim. *Direct Observation of Ultrafast Coherent Exciton Dynamics in Helical pi-Stacks of Self-Assembled Perylene Bisimides. Nat. Commun.*, 6:8656, 2015.

[5] C. Brückner, C. Walter, and B. Engels. *Theoretical investigation of the interactions between the pi-systems of molecular organic semiconductors and an analysis of the contributions of repulsion and electrostatics. Int. J. Quant. Chem.*, 15:1138–1152, 2016.

[6] B. Engels and V. Engel. *The dimer-approach to characterize opto-electronic properties of exciton trapping and diffusion in organic semiconductor aggregates and crystals . Phys. Chem. Chem. Phys.*, 19:12604, 2017.

[7] B. Geffroy, le R. Philippe, and P. Christophe. *Organic light-emitting diode (OLED) technology: materials, devices and display technologies . Polym. Int.*, 55:572–582, 2006.

[8] G. Horowitz. *Organic field-effect transistors. Adv. Mater.*, 10:365–377, 1998.

[9] V. Settels, A. Schubert, M. Tafipolski, W. Liu, V. Stehr, A. K. Topczak, J. Pflaum, and C. Deibel. *Identification of Ultrafast Relaxation Processes As a Major Reason for Inefficient Exciton Diffusion in Perylene-Based Organic Semiconductors. J. Am. Chem. Soc.*, 136:9327, 2014.

[10] D. Bellinger, J. Pflaum, C. Brüning, V. Engel, and B. Engels. *The electronic character of PTCDA thin films in comparison to other perylene-based organic*

semi-conductors: ab initio-, TD-DFT and semi-empirical computations of the opto-electronic properties of large aggregates. Phys. Chem. Chem. Phys., 19:2434, 2017.

[11] C. Brüning, J. Wehner, J. Hausner, M. Wenzel, and V. Engel. *Exciton dynamics in perturbed vibronic molecular aggregates. Struct. Dyn.*, 3:043201, 2016.

[12] P.-A. Plötz, P. Polyutov, S. D. Ivanov, F. Fennel, S. Wolter, T. Niehaus, Z. Xie, S. Lochbrunner, F. Würthner, and O. Kühn. *Biphasic Aggregation of a Perylene Bisimide Dye Identified by Exciton-Vibrational Spectra. Struct. Dyn.*, 3:043201, 2016.

[13] R. K. Preston and J. C. Tully. *Effect of Surface Crossing in Chemical Reactions: The H_3^+. J. Chem. Phys.*, 54:4297, 1971.

[14] P. Hamm and G. Stock. *Vibrational Conical Intersections as a Mechanism of Ultrafast Vibrational Relaxation. Phys. Rev. Lett.*, 109:173201, 2012.

[15] W. Domcke and D. R. Yarkony. *Role of Conical Intersections in Molecular Spectroscopy and Photoinduced Chemical Dynamics. Annu. Rev. Phys. Chem.*, 65:325, 2012.

[16] K. Blum. *Density Matrix Theory and Applications.* Springer, Berlin, 3 edition, 2012.

[17] U. Weiss. *Quantum Dissipative Systems.* World Scientific, Singapore, 2 edition, 1993.

[18] V. Bonačić-Koutecký and R. Mitric. *Theoretical Exploration of Ultrafast Dynamics in Atomic Clusters: Analysis and Control. Chem. Rev.*, 105:11–65, 2005.

[19] G. Stock and M. Thoss. *Classical Description of Nonadiabatic Quantum Dynamics. Adv. Chem. Phys.*, 131:243, 2005.

[20] M. Ben-Nun, J. Quenneville, and T. J. Martínez. *Ab Initio Multiple Spawning: Photochemistry from First Principles Quantum Molecular Dynamics. J. Phys. Chem. A*, 104:5161, 2000.

[21] S. Shin and M. Metiu. *Nonadiabatic effects on the charge transfer rate constant: a numerical study of a simple model system. J. Chem. Phys.*, 102:9285, 1995.

[22] S. Shin and M. Metiu. *Multiple Time Scale Quantum Wave Packet Propagation: Electron-Nuclear Dynamics. J. Phys. Chem.*, 100:7867, 1996.

[23] J. Albert, M. Falge, S. Gomez, I. R. Sola, H. Hildenbrand, and V. Engel. *Vibrational and vibronic coherences in the two dimensional spectroscopy of coupled electron-nuclear motion. J. Chem. Phys.*, 143:041102/1–041102/4, 2015.

[24] J. Albert, D. Kaiser, and V. Engel. *Adiabatic and non-adiabatic electron-nuclear motion: Quantum and classical dynamics. J. Chem. Phys.*, 145:171103/1–171103/4, 2016.

[25] J. Albert, K. Hader, and V. Engel. *On the calculation of time-dependent electron flux within the Born-Oppenheimer approximation: a flux-flux reflection-principle. J. Chem. Phys., (under review)*, 2018.

[26] J. Albert, K. Hader, and V. Engel. *Coupled electron-nuclear quantum dynamics through and around a conical intersection. J. Chem. Phys.*, 147:064302/1–064302/8, 2017.

[27] David Tannor. *Introduction to Quantum Mechanics - A Time-dependent Perspective*. University Science Books, Sausalito, California, 1 edition, 2007.

[28] E. B. Manoukian. *Quantum Theory: A Wide Spectrum*. Springer, 1 edition, 2005.

[29] E. Schrödinger. *Quantisierung als Eigenwertproblem I. Ann. Phys.*, 79:361–376, 1926.

[30] E. Schrödinger. *Quantisierung als Eigenwertproblem II. Ann. Phys.*, 79:361–376, 1926.

[31] E. Schrödinger. *Quantisierung als Eigenwertproblem II. Ann. Phys.*, 79:361–376, 1926.

[32] E. Schrödinger. *Quantisierung als Eigenwertproblem IV. Ann. Phys.*, 79:361–376, 1926.

[33] Eugen Merzbacher. *Quantum Mechanics*. John Wiley & Sons, Inc, Hoboken, New Jersey, 3 edition, 1998.

[34] L. Debnath and D. Bhatta. *Integral transforms and their applications*. Chapmann & Hall/CRC, Taylor & Francis Group, Boca Raton, 2 edition, 2007.

[35] C. Cohen-Tannoudji. *Quantum mechanics*. Dover Publications, Inc., Mineola, New York, 1 edition, 1977.

[36] L. Debnath. *Nonlinear Partial Differential Equations for Scientists and Engineers*. Springer New York, New York, 3 edition, 2012.

[37] P.A.M. Dirac. *The Principles of Quantum Mechanics*. Oxford University Press, Oxford, New York, 1 edition, 1930.

[38] R. Kosloff and H. Tal-Ezer. *A direct relaxation method for calculating eigenfunctions and eigenvalues of the schrödinger equation on a grid. Chem. Phys. Lett.*, 127:223–230, 1986.

[39] M. Baer. *Beyond Born-Oppenheimer: electronic nonadiabatic coupling terms and conical intersections*. John Wiley & Sons, Inc., Hoboken, New Jersey, 1 edition, 2006.

[40] A. Szabo and N.S. Ostlund. *Modern Quantum Chemistry: Introduction to Advanced Electronic Structure Theory*. Dover Books on Chemistry. Dover Publications, London, 1989.

[41] N. P. Blake and H. Metiu. The short-time dynamics of a small quantum system embedded in a medium: the absorption lineshape. In L. Wöste J. Manz, editor, *Femtosecond Chemistry*, pages 533–562. Verlag Chemie, Weinheim, 1995.

[42] M. Sprik and M. L. Klein. *Optimization of a distributed Gaussian basis set using simulated annealing: application to adiabatic dynamics of the solvated electron. J. Chem. Phys.*, 89:1592, 1988.

[43] M. Born and J. R. Oppenheimer. *Ann. Phys.*, 84:457, 1927.

[44] M. Born and K. Hunag. *Dynamical Theory of Crystal Lattices*. Oxford at the Clarendon Press, Great Clarendon Street,Oxford, 1 edition, 1998.

[45] M. Baer. *Adiabatic and diabatic representations for atom-molecule collisions. treatment of the collinear arrangement. Chem. Phys. Lett.*, 35:112, 1975.

[46] M. Baer. *Introduction to the theory of electronic non-adiabatic coupling terms in molecular systems. Phys. Rep.*, 358:75, 2002.

[47] W. D. Hobey and A. D. McLachlan. *Dynamical Jahn-Teller effect in hydrocarbon radicals. J. Chem. Phys.*, 33:1695, 1960.

[48] ed. M. Baer. *Theory of Chemical Reaction Dynamics*. Springer Science + Business Media, Inc 2005, New York, 1 edition, 1985.

[49] H. C. Longuet-Higgins. *Adv. Spectrosc.*, 2:429, 1961.

[50] F. T. Smith. *Phys. Rev*, 179:111, 1969.

[51] T. Pacher, L. S. Cederbaum, and H. Köppel. *Adiabatic and quasidiabatic states in a gauge theoretical framework. Adv. Chem. Phys.*, 84:293, 1993.

[52] W. Moffitt and A. D. Liehr. *Phys. Rev.*, 106:1195, 1956.

[53] A. D. McLachlan. *The wave functions of electronically degenerate states. Molec. Phys.*, 4:417, 1961.

[54] W. Lichten. *Molecular wavefunctions and inelastic atomic collisions. Phys. Rev.*, 164:131, 1967.

[55] W. Lichten. *Resonant charge exchange in atomic collisions. Phys. Rev.*, 121:229, 1963.

[56] C. J. Ballhausen and A. E. Hansen. *Ann. Rev. Phys. Chem.*, 23:15, 1972.

[57] W. B. Case. *Wigner functions and Weyl transforms for pedestrians. Am. J. Phys.*, 76:937–946, 2008.

[58] E. J. Heller. *Quantum corrections to classical photodissociation models. J. Chem. Phys.*, 68:2066–2075, 1978.

[59] W. P. Schleich. *Quantum Optics in Phase Space.* WILEY-VCH Verlag Berlin GmbH, D-13086 Berlin, 1 edition, 2001.

[60] W. Nolting. *Grundkurs Theoretische Mechanik 2: Analytische Mechanik.* Springer Spektrum, 9 edition, 2014.

[61] M. Cho. *Two-Dimensional Optical Spectroscopy.* CRC, Taylor & Francis Group, Boca Raton, London, New York, 2009.

[62] S. Mukamel. *Principles of Nonlinear Optical Spectroscopy.* Oxford University Press, Inc, New York, New York, 1995.

[63] U. Fano. *Phys. Rev.*, 131:259, 1963.

[64] F. Schwabl. *Quantenmechanik (QM I) - Eine Einführung.* Springer Berlin Heidelberg New York, Berlin, 7 edition, 2007.

[65] A. Schubert. *Kohärente und dissipative Wellenpaketdynamik und zeitaufgelöste Spektroskopie: Von zweiatomigen Molekülen zu molekularen Aggregaten.* Dissertation, Julius-Maximilians Universität Würzburg, Department of Chemistry, 2012.

[66] M. Falge. *Dynamik gekoppelter Elektron-Kern-Systeme in Laserfeldern.* Dissertation, Julius-Maximilians Universität Würzburg, Department of Chemistry, 2012.

[67] M. Cho. *Coherent Two-Dimensional Optical Spectroscopy. Chem. Rev.*, 108(4):1331–1418, 2008.

[68] S. Mukamel. *Multidimensional Femtosecond Correlation Spectroscopies of Electronic and Vibrational Excitations. Annu. Rev. Phys. Chem.*, 51:691–729, 2000.

[69] D. Jonas. *Two-Dimensional Femtosecond Spectroscopy. Annu. Rev. Phys. Chem.*, 54:425–463, 2003.

[70] F. Ehlotzky. *Quantenmechanik und ihre Anwendungen.* Springer New York, New York, 2005.

[71] W. H. Louisell. *Quantum Statistical Properties of Radiation.* Wiley, New York, 1973.

[72] W. Domcke and G. Stock. *Theory of Ultrafast Nonadiabatic Excited-State Processes and their Spectroscopic Detection in Real Time. Adv. Chem. Phys.*, 100:1, 1997.

[73] L. Onsager and S. Machlup. *Fluctuations and irreversible processes. Phys. Rev.*, 91:1505, 1953.

[74] P. N. Butcher. *Nonlinear Optical Phenomena.* Ohio State University Enegenieering Publications, Columbus, 1 edition, 1965.

[75] J. A. Armstrong, N. Bloembergen, J. Ducuing, and P. S. Pershan. *Interactions between light waves in a nonlinear dielectric. Phys. rev*, 127:1918, 1962.

[76] S. Doinach and E. H. Sondheimer. *Green's Functions for Solid State Physicists.* W. A. Benjamin, Inc., London, 1 edition, 1974.

[77] E. N. Economou. *Green's Functions in Quantum Physics.* Springer-Verlag, Berlin, 2 edition, 1983.

[78] M. L. Goldberger and R. M. Watson. *Collision Theory.* Wiley, New York, 1964.

[79] S. Mukamel. *Collisional broadening of spectral line shapes in two-photon and multiphoton processes. Phys. Reports*, 93:1, 1982.

[80] S. Mukamel and R. F. Loring. *Nonlinear response function for time-domain and frequency-domain four-wave mixing. J. Opt. Soc. Am. B*, 3:595, 1986.

[81] S. Mukamel. *Femtosecond optical spectroscopy: a direct look at elementary chemical events. Annu. Rev. Phys. Chem.*, 41:647, 1990.

[82] R. Kosloff. Quantum molecular dynamics on grids. In J. Z. Zhang R. E. Wyatt, editor, *Dynamics of Molecules and Chemical Reactions*, pages 185–230. Marcel Dekker Inc, New York, 1996.

[83] R. Kosloff. *Propagation Methods for Quantum Molecular Dynamics. Annu. Rev. Phys. Chem.*, 45:145–178, 1994.

[84] J. A. Jr. Fleck, J. R. Morris, and M. D. Feit. *Time-Dependent Propagation of High Energy Laser Beams through the Atmosphere. Appl. Phys.*, 10:129–160, 1976.

[85] M. D. Feit, J. A. Jr. Fleck, and Steiger A. *Solution of the Schrödinger-Equation by a Spectral Method. J. Comput. Phys.*, 47(3):412, 1982.

[86] M. Frigo and S. Johnson. *The Design and Implementation of FFTW3. Proc. IEEE*, 93:216, 2005.

[87] K. Renziehausen, P. Marquetand, and V. Engel. *On the divergence of time-dependent perturbation theory applied to laser-induced molecular transitions. J. Phys. B.*, 42:195402, 2009.

[88] V. Engel. *Excitation of molecules with ultrashort laser pulses: exact time-dependent quantum calculation. Comput. Phys. Commun.*, 63:228, 1991.

[89] L. Verlet. *Computer "Experiments" on Classical Fluids. I. Thermodynamical Properties of Lennard-Jones Molecules. Phys. Rev.*, 159:98–103, 1967.

[90] M. P. Allen and D. J. Tildesley. *Computer Simulation of Liquids*. Oxford University Press, New York, 1 edition, 1987.

[91] M. Erdmann. *Coupled Electron and Nuclear Dynamics in Model Systems*. Dissertation, Julius-Maximilians Universität Würzburg, Department of Chemistry, 2004.

[92] M. Falge, V. Engel, and S. Gräfe. *Time-resolved photoelectron spectroscopy of coupled electron-nuclear motion. J. Chem. Phys.*, 134:184307, 2011.

[93] M. Falge, V. Engel, and S. Gräfe. *Fingerprints of Adiabatic versus Diabatic Vibronic Dynamics in the Asymmetry of Photoelectron Momentum Distribution. J. Phys. Chem. Lett.*, 3:2617, 2012.

[94] G. A. Worth and L. S. Cederbaum. *Beyond Born-Oppenheimer: Molecular Dynamics Through a Conical Intersection. Annu. Rev. Phys. Chem.*, 55:127–158, 2004.

[95] E. Anderson, Z. Bai, C. Bischof, S. Blackford, J. Demmel, J. Dongarra, J. Du Croz, A. Greenbaum, S. Hammarling, A. McKenny, and D. Sorensen. *LAPACK Users' Guide*. Society for Industrial and Applied Mathematics, Philadelphia, 3 edition, 1999.

[96] B. Lasorne, M.-C. Bacchus-Montabonel, N. Vaeck, and M. Desouter-Lecomte. *Nonadiabatic interactions in wave packet dynamics of the bromoacetyl chloride photodissociation. J. Chem. Phys.*, 120:1271–1278, 2004.

[97] L. Pichl, H. Nakamura, and J. Horáček. *Complete reflection in two-state crossing and noncrossing potential systems. J. Chem. Phys.*, 113:906–918, 2000.

[98] T. Brixner, T. Manačal, I. V. Stiopkin, and G. R. Fleming. *Phase-stabilized two-dimensional electronic spectroscopy. J. Chem. Phys.*, 121:4221–4236, 2004.

[99] P. Kjellberg, B. Brüggemann, and T. Pullerits. *Two-dimensional electronic spectroscopy of an excitonically coupled dimer. Phys. Rev. B*, 74:024303, 2006.

[100] A. Schubert and V. Engel. *Two-dimensional vibronic spectroscopy of coherent wave-packet motion. J. Chem. Phys.*, 134:104304/1, 2011.

[101] D. Egorova. *Oscillations in two-dimensional photon-echo signals of excitonic and vibronic systems: Stick-spectrum analysis and its computational verification. J. Chem. Phys.*, 140:034314/1, 2014.

[102] M. B. Plenio, J. Almeida, and S. F. Huelga. *Origin of long-lived oscillations in 2D-spectra of a quantum vibronic model: Electronic versus vibrational coherence. J. Chem. Phys.*, 139:235102, 2013.

[103] D. Egorova, M. F. Gelin, and W. Domcke. *Analysis of cross peaks in two-dimensional electronic photon-echo spectroscopy for simple models with vibrations and dissipation. J. Chem. Phys.*, 126:074314/1–074314/11, 2001.

[104] J. Yuen-Zhou, J. J. Krich, and A. Aspuru-Guzik. *A witness for coherent electronic vs vibronic-only oscillations in ultrafast spectroscopy. J. Chem. Phys.*, 136:234501/1–234501/11, 2012.

[105] T. Vivek, W. K. Peters, and D. M. Jonas. *Electronic resonance with anticorrelated pigment vibrations drives photosynthetic energy transfer outside the adiabatic framework. PNAS*, 110:1203–1208, 2013.

[106] K. A. Fransted and G. S. Engel. *Probing vibrational dynamics of PM650 with two-dimensional electronic spectroscopy. Chem. Phys.*, 403:59–67, 2012.

[107] M. Schmitt, G. Knopp, A. Materny, and W. Kiefer. *Femtosecond time-resolved coherent anti-Stokes Raman scattering for the simultaneous study of ultrafast ground and excited state dynamics: iodine vapor. Chem. Phys. Lett.*, 270:9–15, 1997.

[108] M. Schmitt, G. Knopp, A. Materny, and W. Kiefer. *Femtosecond time-resolved four-wave mixing spectroscopy in iodine vapor. Chem. Phys. Lett.*, 280:339–347, 1997.

[109] M. Schmitt, G. Knopp, A. Materny, and W. Kiefer. *The Application of Femtosecond Time-Resolved Coherent Anti-Stokes Raman Scattering for the Investigation of Ground and Excited State Molecular Dynamics of Molecules in the Gas Phase. J. Phys. Chem.*, 102:4059–4065, 1998.

[110] A. Materny, T. Chen, M. Schmitt, T. Seibert, A. Vierheilig, V. Engel, and W. Kiefer. *Wave packet dynamics in different electronic states investigated by femtosecond time-resolved four-wave-mixing spectroscopy. Appl. Phys. B.*, 71:299–317, 2000.

[111] B. I. Grimberg, V. V. Lozovoy, M. Dantus, and S. Mukamel. *Ultrafast Nonlinear Spectroscopic Techniques in the Gas Phase and Their Density Matrix Representation. J. Phys. Chem. A.*, 106:697–718, 2002.

[112] T. Lang, H.-M. Frey, P. Beaud, and M. Motzkus. *High resolution femtosecond coherent anti-Stokes Raman scattering: determination of rotational constants, molecular anharmonicity, collisional line shifts, and temperature. J. Chem. Phys.*, 115:5418–5426, 2001.

[113] J. Albert and V. Engel. *Femtosecond time-resolved four-wave mixing spectroscopy of coupled electron-nuclear motion. Asian Journal of Physics*, 25:in press, 2016.

[114] S. Meyer, M. Schmitt, A. Materny, W. Kiefer, and V. Engel. *A theoretical analysis of the time-resolved femtosecond CARS spectrum of I_2. Chem. Phys. Lett.*, 281:332–336, 1997.

[115] M. Erdmann and V. Engel. *Combined electronic and nuclear dynamics in a simple model system. II. Spectroscopic transitions. J. Chem. Phys.*, 120:158–164, 2004.

[116] W. L. Hase. Classical trajectory studies of unimolecular dynamics. In U. Landman, editor, *Aspects of the Kinetics and Dynamics of Surface Reactions*, pages 109–136. American Institute of Physics, New York, 1980.

[117] N. F. Mott and A. S. W. Massey. *Theory of Atomic Collisions.* Oxford University Press, New York, New York, 3 edition, 1965.

[118] D. G. Truhlar and J. T. Muckermann. Reactive scattering cross sections: Quasiclassical and semiclassical methods. In R. B. Bernstein, editor, *Atom-Molecule Collision Theory: A Guide for the Experimentalist*, pages 505–566. Plenum Press, New York, 1979.

[119] R. Schinke. *Photodissociation Dynamics.* Cambridge University Press, Cambridge, 1 edition, 1993.

[120] T. Schaupp, J. Albert, and V. Engel. *Correlated electron-nuclear dissociation dynamics: classical versus quantum motion. European Physical Journal D*, 71:1–7, 2017.

[121] T. Bredtmann, D. J. Diestler, L. Si-Dan, J. Manz, J. F. Perez-Torres, W.-J. Tian, Y.-B. Wu, Y. Yang, and H.-J. Zhai. *Quantum theory of concerted electronic and nuclear fluxes associated with adiabatic intramolecular processes. Chem. Phys. Phys. Chem.*, 17:29421–29464, 2015.

[122] I. Barth, H.-C. Hege, H. Ikeda, A. Kenfack, J. Manz, F. Marquardt, G. K. Paramonova, Y. Yang, and H. Zhai. *Concerted quantum effects of electronic and nuclear fluxes in molecules. Chem. Phys. Lett.*, 481:118, 2009.

[123] J. Manz, J. F. Perez-Torres, and Y. Yang. *Vibrating H2+(2+g, JM = 00) Ion as a Pulsating Quantum Bubble in the Laboratory Frame. J. Phys. Chem.*, 118:8411–8425, 2014.

[124] J. F. Perez-Torres. *Dissociating H2+(2+g, JM=00) Ion as an Exploding Quantum Bubble. J. Phys. Chem.*, 119:2895–2901, 2015.

[125] D. J. Diestler, A. Kenfack, J. Manz, B. Paulus, J. F. Perez-Torres, and V. Pohl. *Computation of the Electronic Flux Density in the Born-Oppenheimer Approximation. J. Phys. Chem. A*, 117:8519–8527, 2013.

[126] G. Herzberg. *Spectra of Diatomic Molecules.* Van Nostrand, New York, 2 edition, 1950.

[127] J. Tellinguisen. The franck-condon principle in bound-free transitions. In K. P. Lawley, editor, *Advances in Chemicl Physics: Photodissociation and Photoionization*, pages 299–369. Wiley, New York, 1985.

[128] R. Schinke. *The rotational reflection principle in the direct photodissociation of triatomic molecules. Close-coupling and classical calculations. J. Chem. Phys.*, 85:5049–5060, 1986.

[129] S. Hennig, V. Engel, and R. Schinke. *Vibrational state distributions following the photodissociation of (collinear) triatomic molecules: the vibrational reflection principle in model calculations for trifluoroiodomethane. J. Chem. Phys.*, 84:5444–5454, 1986.

[130] R. Schinke. *The rotational reflection principle in the direct photodissociation of triatomic molecules. Close-coupling and classical calculations. J. Chem. Phys.*, 85:5049–5060, 1986.

[131] D. R. Yarkony. *Diabolical conical intersections. Rev. Mod. Phys.*, 68:985–1013, 1996.

[132] M. J. Paterson, M. J. Bearpark, M. A. Robb, L. Blancafort, and G. A. Worth. *Conical intersections: A perspective on the computation of spectroscopic Jahn–Teller parameters and the degenerate 'intersection space'. Phys. Chem. Chem. Phys.*, 7:2100, 2005.

[133] W. Domcke and D. R. Yarkony. *Role of conical intersections in molecular spectroscopy and photoinduced chemical dynamics. Annu. Rev. Phys. Chem.*, 63:325, 2012.

[134] W. Domcke, D. R. Yarkony, and H. Köppel. *Conical Intersections: Electronic Structure, Dynamics & Spectroscopy.* World Scientific, Singapore, 15 edition, 2004.

[135] W. Domcke, D. R. Yarkony, and H. Köppel. *Conical intersections: theory, computation and experiment.* World Scientific, Singapore, 15 edition, 2011.

[136] K. Hader, J. Albert, E. K. U. Gross, and V. Engel. *Electron-nuclear wavepacket dynamics through a conical intersection: does the electron care? J. Chem. Phys.*, 146:074304/1–074304/5, 2017.

[137] K. Hader. *Lokalisierungsdynamik unter Berücksichtigung von Molekül-Feld-Wechselwirkung, Kern-Elektron-Kopplung und Exziton-Annihilierung: Localization dynamics considering molecule-field interaction, nuclear-electron coupling and exciton-exciton annihilation.* Dissertation, Julius-Maximilians Universität Würzburg, Department of Chemistry, 2017.

[138] M. V. Berry. *Quantal phase factors accompanying adiabatic changes. Proc. R. Soc. London Ser. A*, 392:45, 1984.

[139] G. Herzberg and H. C. Longuet-Higgins. *Intersection of potential energy surfaces in polyatomic molecules . Discuss. Faraday Soc.*, 35:77, 1963.

[140] S. K. Min, A. Abedi, K. S. Kim, and E. K. U. Gross. *Is the molecular Berry phase an artifact of the Born-Oppenheimer approximation? Phys. Rev. Lett.*, 113:263004, 2014.

[141] D. M. Bischop. *Group Theory and Chemistry.* Dover Publications, Inc., New York, 1 edition, 1993.

[142] J. W. Zwanziger and E. R. Grant. *Topological phase in molecular bound states: Application to the E⊗e system. J. Chem. Phys.*, 87:2954, 1987.

[143] R. G. Gordon. *Correlation Functions for Molecular Motion. Adv. Magn. Reson.*, 3:1–42, 1968.

[144] E. J. Heller. *The semiclassical way to molecular spectroscopy. Acc. Chem. Res.*, 14:368–375, 1981.

Acknowledgment

Foremost, I would like to thank Prof. Dr. Volker Engel, my advisor, for the opportunity to prepare my PhD thesis in his work group and for his continuous support. I am thankful for his patience, knowledge and helpful discussions. I really thank him for supporting my research and for allowing me to grow as a research scientist. I also enjoyed taking part in the scientific group seminars.

Additionally, I want to thank Prof. Dr. Christoph Meier for his supervising activity during my stay at the LCAR Université Paul Sabatier, Toulouse, France.

Moreover, I want to thank Dr. Burkhard Schmidt for his invitation to Berlin and his supervising activity during my stay at the Freie Universität Berlin and his helpful advise on scientific questions.

I also enjoyed the scientific conversation with Dr. Burkhard Schmidt, Prof. Dr. Ágnes Vibók and Gábor, her husband, with Prof. Dr. Christoph Meier and Dr. Klaus Renziehausen about exciting mathematical and quantum-dynamical topics during the MOLEC2016 conference in Toledo.

Furthermore, I want to thank Johannes Wehner, Dr. Mirjam Falge, Dr. Christoph Brüning, Dr. Martin Kess and Dr. Alexander Schubert for their extraordinary support in technical and scientific problems.

I want especially to thank Dr. Kilian Hader, my office colleague, for the exciting mathematical and philosophical discussions and the nice working atmosphere.

Finally, I want to thank Uschi Rüppel for the organization, Eva Renziehausen for proofreading, and the DFG FOR 1809 for the financial support.